Orientation of short steel fibres in concrete: measuring and modelling

Marika Eik

Aalto University

Orientation of short steel fibres in concrete: measuring and modelling

Marika Eik

Aalto University
School of Engineering

Tallinn University of Technology

Supervising professor

Professor Jari Puttonen, Aalto University, Finland

Thesis advisor

Dr. rer. nat. Heiko Herrmann, Tallinn University of Technology, Estonia

Preliminary examiners

Professor Holm Altenbach, Faculty of Mechanical Engineering, Otto-von Guericke-Universität Magdeburg, Germany

Professor Kenneth Runesson, Department of Applied Mechanics, Chalmers University of Technology, Sweden

Opponent

Professor Karin Lundgren, Department of Civil and Environmental Engineering, Chalmers University of Technology, Sweden

NORDIC ECOLABEL
441   697
Printed matter

Orientation of short steel fibres in concrete: measuring and modelling

MARIKA EIK

TALLINN UNIVERSITY OF TECHNOLOGY
Faculty of Civil Engineering
Institute of Cybernetics
Mechanics and Applied Mathematics Department

This dissertation was accepted for the defense of the degree of Doctor of Philosophy in Engineering on March 3rd, 2014.

Supervisor: Heiko Herrmann, Dr. rer. nat.
Mechanics and Applied Mathematics Department, Institute of Cybernetics,
Tallinn University of Technology, Tallinn, Estonia

Co-Supervisor: Jari Puttonen, Professor
Department of Civil and Structural Engineering ,
Aalto University School of Engineering, Espoo, Finland

Opponents: Holm Altenbach, Professor
Faculty of Mechanical Engineering,
Otto-von Guericke-Universität Magdeburg, Germany

Karin Lundgren, Professor
Opponent on the behalf of Aalto University

Defense of the thesis: April 4th, 2014

Declaration:
Hereby I declare that this doctoral thesis, my original investigation and achievement, submitted for the doctoral degree at Tallinn University of Technology and at Aalto University School of Engineering has not been submitted for doctoral or equivalent academic degree.

_____

Marika Eik

Metallist lühikiudude orientatsioon betoonis: mõõtmine ja modelleerimine

MARIKA EIK

Author
Marika Eik

Name of the doctoral dissertation
Orientation of short steel fibres in concrete: measuring and modelling

Abstract

  This research focuses on a cementitious composite formed by mixing of concrete matrix with short steel fibres, SFRC. This composite is quite extensively employed in the construction industry, for example in floors resting on soil and even in some load-bearing structures, such as floor-slabs. The complexity of SFRC is the presence of the anisotropic behaviour occurring due to different alignments of short fibres.

The examinations performed comprise two research branches: measuring of fibre orientations from the hardened concrete matrix and modelling of composite properties considering the orientation distribution of fibres. Two methods of measuring fibre orientations are developed: slicing method and X-ray micro-tomography. Parts extracted from the full-size floor-slabs are used as samples. The slicing with photometry approach is improved by DC-conductivity testing joined with image analysis. X-ray micro-tomography is performed on sufficiently large samples and the orientation of fibres is specified by the analysis of 3D voxel images of scanned fibres. The received measuring results proved that both DC-conductivity testing combined with photometry and X-ray micro-tomography have high accuracy and they can be applied in defining fibre orientations from real concrete samples reliably.

The material model developed for one meso-volume element of SFRC is based on an orthotropic hyperelastic material model where the second-order terms of the strain energy function are employed resulting in orthotropic St. Venant-Kirchhoff model. The orthotropic meso-symmetry of the composite is modelled by the structural tensors based on the eigenvectors of the second-order alignment tensor, which represent the dominating alignment of fibres. The material model developed for SFRC consists of an isotropic part presenting the concrete and the orthotropic part including the influence of short steel fibres. The orientation distribution function of fibres is utilized to evaluate the orthotropic effect in the defined material symmetry directions. The advantage of the material model developed is that it uses the full orientation information of fibres and employs tensor quantities, which are independent of any reference frame. Finally, the implementation of the model is demonstrated by examples based on fibre orientations measured from test samples.

Tiivistelmä

Tutkimuksessa tarkastellaan betonin ja lyhyiden teräskuitujen muodostamaa yhdistelmämateriaalia, jota on laajasti käytetty rakennusalalla esimerkiksi maanvaraisissa lattioissa ja Suomen ulkopuolella myös kantavissa välipohjalaatoissa. Tämän yhdistelmämateriaalin toiminnan arvioinnissa haasteet liittyvät materiaalin anisotrooppisuuteen, joka aiheutuu kuitujen suuntautuneisuuden ja määrän vaihteluista betonissa.

Tutkimus jakaantui kahteen pääosaan, joista ensimmäisessä tarkasteltiin kuitujen suuntaisuuden määrittämistä kovettuneesta betonista ja toisessa kehitettiin menetelmä kuitujen orientaation huomioon ottamiseksi materiaalimallissa. Kuitujen suunnan määritykseen työssä syntyi kaksi menettelyä, jotka perustuivat joko näytekappaleen viipalointiin tai röntgensädettä hyödyntävään mikrotomografiaan. Menetelmiä kehitettiin testikappaleilla, jotka oli otettu mitoiltaan ja valmistustavaltaan todellisia välipohjalaattoja vastaavista koerakenteista. Viipaleiden fotometrista tarkastelua parannettiin testaamalla pisteittäin viipaleiden pintojen välistä sähkönjohtavuutta robottiohjatulla tasasähkölähteellä. Mikrotomografiamittaus suoritettiin riittävän suurilla koekappaleilla, joista kuitujen suuntautuneisuus määritettiin analysoimalla kolmiulotteisia kuvamatriiseja. Saadut mittaustulokset osoittivat sekä fotometrian yhdistettynä tasasähkön johtavuuteen että mikrotomografian olevan tarkkoja menetelmiä, joita voidaan luotettavasti soveltaa kuitujen suuntautuneisuuden määrittämiseen todellisista betonikappaleista.

Kehitetty materiaalimalli kuitubetonin mesotilavuutta kuvaavalle osuudelle perustuu hyperelastiseen materiaaliin, jossa sovelletaan muodonmuutosenergian toisen kertaluvun termejä. Yhdistelmämateriaalin symmetria on kuvattu toisen kertaluvun suuntautuneisuustensorin ominaisvektoreilla, jolloin isotrooppinen St. Venat-Kirchhoff-malli voidaan täydentää ominaisvektoreista muodostetuilla rakennetensoreilla. Tuloksena saadaan ortotrooppinen St. Venant-Kirchhoff-materiaali, jonka isotrooppinen osa kuvaa betonia ortotropian kuvatessa kuitujen vaikutusta. Kuitujen suuntautuneisuuden tiheysfunktiota hyödynnetään laskettaessa suunnasta riippuvien kimmovakioiden vaikutusta määrättyihin symmetriasuuntiin. Johdetun materiaalimallin etuna on, että siinä hyödynnetään kaikki tieto kuitujen suuntautuneisuudesta soveltaen tensorisuureita, jotka ovat valitusta koordinaatistosta riippumattomia. Lopuksi mallin soveltamista on havainnollistettu esimerkeillä, joissa on hyödynnetty koekappaleista mitattuja tietoja kuitujen suuntautuneisuudesta.

Kokkuvõte

Käesolev väitekiri käsitleb tsemendipõhist komposiitmaterjali, mis on moodustatud betoonmassi (matriitsi) ja lühikeste teraskiudude kokku segamisega, mille tulemuseks on teraskiudbetoon. See komposiitmaterjal on juba laialdaselt kasutusel ehituskonstruktsioonides, näiteks tööstuspõrandates ning isegi mõnedes kandekonstruktsioonides nagu näiteks vahelaeplaadid. Teraskiudbetooni keerulisus seisneb tema anisotroopsetes omadustes, mis tulenevad lühikiudude erineva orientatsiooni jaotusest matriitsis.

Teostatud uuringud hõlmavad kahte teadusharu: lühikeste teraskiudude orientatsiooni jaotuse mõõtmise kivistunud betoonmatriitsis ning komposiidi omaduste modelleerimist võttes arvesse kiudude orientatsiooni jaotust. Uurimistöö käigus on arendatud kahte meetodit lühikiudude orientatsiooni jaotuse mõõtmiseks: viilutamine ja mikro-kompuutertomograafia. Katsekehadeks on kasutatud konstruktsiooni osasid, mis olid eraldatud täismõõtmelistest vahelaeplaatidest. Viilutamise ja fotomeetria lähenemine on täiustatud alalisvoolu juhtivuse mõõtmisega, mis omaette on kombineeritud fotoanalüüsiga. Mikro-kompuutertomograafia on teostatud piisavalt suurtel katsekehadel ning lühikiudude orientatsioon on määratud analüüsides 3D voksel pilte skanneeritud kiududest. Saadud mõõtmistulemused on tõestanud, et mõlemad mõõtmismeetodid, st alalisvoolu juhtivuse mõõtmine kombineerituna fotoanalüüsiga ning mikro-kompuutertomograafia, omavad kõrget täpsust mõõtmistel ja neid saab usaldusväärselt kasutada terasest lühikiudude orientatsiooni jaotuse määramisel reaalsetes katsekehades.

Teadustöö käigus välja töötatud materjalimudel ühe teraskiudbetooni meso-ruumelemendi jaoks baseerub ortotroopsel hüperelastsel materjalimudelil, kus deformatsioonienergia funktsioonis kasutatakse teist järku liikmeid, mille tulemuseks on ortotroopne St. Venant-Kirchhoff'i mudel. Komposiidi ortotroopne meso-sümmeetria on modelleeritud struktuursete tensorite abil, mis on moodustatud teist järku joonduvustensori omavektoritest, sest joonduvustensor esitab

lühikiudude domineerivate orientatasioonide suundi. Ortotroopset St. Venant-Kirchhoff'i mudelit saab kasutada isotroopse juhtumi jaoks, kuna suunast sõltuvad struktuursed tensorid taanduvad erisuuna puudumisel. Sellest tulenevalt koosneb materjalimudel ühe teraskiudbetooni meso-ruumelemendi jaoks isotroopsest osast, mis kirjeldab betoonmatriitsi ning ortotroopsest osast, mis kirjeldab terasest lühikiudude mõju. Lühikiudude orientatsiooni jaotusfunktsioon on rakendatud komposiidi ortotroopse meso-elastsuse hindamisel meso-sümmeetria suunades. Formuleeritud materjalimudeli eeliseks on asjaolu, et ta rakendab täieliku infot lühikiu orientatsiooni kohta (sfäärilised koordinaadid) ning kasutab tensorsuurusi, mis ei sõltu koordinatsüsteemi valikust. Viimaks, formuleeritud mudeli rakendamine on esitatud näidetega, mis baseeruvad katsekehades mõõdetud lühikiudude orientatsiooni jaotusel.

Preface

This doctoral thesis is conducted under a convention for the joint supervision of thesis at Aalto University (Finland) and Tallinn University of Technology (Estonia). In Aalto University the research work was carried out at the School of Engineering, Department of Civil and Structural Engineering and in Tallinn University of Technology (TUT) at the Faculty of Civil Engineering, Institute of Cybernetics. The doctoral study at TUT was commenced in the year of 2007 and at Aalto in 2009. The experimental part of the work was implemented in the Testing Hall of Structural Engineering in Aalto University, in the X-ray micro-tomography laboratory, Department of Physics in Helsinki University, and in the Centre of Biorobotics in TUT. The tested real-size floor-slabs were cast and provided for the research by `Rudus Oy`. This research work was possible due to the support of the Doctoral Programme of the Built Environment (RYM-TO) funded through the Academy of Finland and due to the funding from the European Regional Development Fund, in particular through funding for the "Centre for Nonlinear Studies" as an Estonian national centre of excellence. In addition, the research has received funding from Estonian Ministry of Education. Furthermore, Jaanus Otsa doctoral Scholarship of TUT Development Foundation and TUT Alumni Association is gratefully appreciated.

I cordially thank my supervisors Professor Jari Puttonen and Dr. Heiko Herrmann, who believed in me and gave me a real opportunity to plunge into the world of science and to achieve positive results. Through the discussions with my supervisors and with the knowledge obtained during the study, I realised that the science is a key enabling a person to discover and understand the world around. This scientific work is a path that I overcame together with my supervisors and on which I have met so many good people. I express my gratitude to the pre-examiners Professor Kenneth Runesson and Professor Holm Altenbach for their professionality, useful comments and objectivity in the evaluation of my thesis. I appreciate the opponent Professor Karin

Contents

List of Publications

This thesis consists of an overview and of the following publications which are referred to in the text by their Roman numerals.

I M. Eik and J. Puttonen. Challenges of steel fibre reinforced concrete in load bearing structures. *Rakenteiden mekaniikka (Journal of Structural Mechanics)*, 44, 1, 44-64, http://rmseura.tkk.fi/rmlehti/2011/nro1/, June 2011.

II H. Herrmann and M. Eik. Some comments on the theory of short fibre reinforced materials. *Proceedings of the Estonian Academy of Sciences*, 60, 3, 179-183, http://dx.doi.org/10.3176/proc.2011.3.06, June 2011.

III M. Eik and H. Herrmann. Raytraced images for testing the reconstruction of fibre orientation distributions. *Proceedings of the Estonian Academy of Sciences*, 61, 2, 128-136, http://dx.doi.org/10.3176/proc.2012.2.05, June 2012.

IV J.-P. Suuronen, A. Kallonen, M. Eik, J. Puttonen, R. Serimaa and H. Herrmann. Analysis of short fibres orientation in steel fibre reinforced concrete (SFRC) using X-ray tomography. *Journal of Materials Science*, 48, 3, 1358-1367, http://dx.doi.org/10.1007/s10853-012-6882-4, February 2013.

V M. Eik, K. Lõhmus, M. Tigasson, M. Listak, J. Puttonen and H. Herrmann. DC-conductivity testing combined with photometry for measuring fibre orientations in SFRC. *Journal of Materials Science*, 48, 10, 3745-3759, http://dx.doi.org/10.1007/s10853-013-7174-3, May 2013.

VI M. Eik, J. Puttonen and H. Herrmann. Fibre orientation phenomenon in concrete composites: measuring and theoretical modelling. 7th *In-*

ternational Conference FIBRE CONCRETE 2013, Technology, Design, Application; Conference Proceedings, 1-4, September 2013.

Author's Contribution

Publication I: "Challenges of steel fibre reinforced concrete in load bearing structures"

The author provided the ideas and wrote the paper with input from the coauthor.

Publication II: "Some comments on the theory of short fibre reinforced materials"

The author identified some of the weak points in present theories, provided knowledge within the field of civil engineering and wrote the paper together with the coauthor.

Publication III: "Raytraced images for testing the reconstruction of fibre orientation distributions"

The author provided knowledge within the field of civil engineering, performed image analysis and wrote paper together with the coauthor.

Publication IV: "Analysis of short fibres orientation in steel fibre reinforced concrete (SFRC) using X-ray tomography"

The author performed image analysis and statistics, provided knowledge within the field of civil engineering and wrote the paper together with the coauthors.

Publication V: "DC-conductivity testing combined with photometry for measuring fibre orientations in SFRC"

The author performed image processing, analysis and statistics, provided knowledge within the field of civil engineering and wrote the paper together with the coauthors.

Publication VI: "Fibre orientation phenomenon in concrete composites: measuring and theoretical modelling"

The author provided some of the ideas—in particular the idea for orthotropy based on eigenvectors (together with HH) and the idea and reasoning for linear elasticity (together with JP)—provided knowledge within the field of civil engineering and wrote the paper together with the coauthors.

List of Conference Presentations

I M. Eik and H. Herrmann; **Measuring Fibre Orientation in Steel Fibre Reinforced Concrete**; 16th International Conference on Composite Structures (ICCS16), Porto, Portugal, June 28 - 30, 2011

II M. Eik, J. Puttonen and H. Herrmann; **Orientation distribution of fibres in short fibre reinforced concrete: evaluation and introduction to constitutive relations**; 8th European Solid Mechanics Conference (ESMC16), Graz, Austria, July 9 - 13, 2012

III M. Eik, J. Puttonen and H. Herrmann; **Fibre orientation phenomenon in concrete composites: measuring and theoretical modelling**; 7th International Conference FIBRE CONCRETE 2013 Technology, Design, Application, Prague, Czech Republic, September 12 - 13, 2013

List of Figures

List of Tables

Notations and definitions

Vectors and tensors are either denoted by bold letters or using index-notation for components with respect to an arbitrary fixed basis, for shortness the basis vectors will be omitted from the equations. Explicit calculations are performed in Cartesian coordinates. In index-notations, the Einstein summation convention is used.

A vector (bold small letters):

$$\mathbf{v} \;=\; v_i \mathbf{g}_i \;,$$

A 2nd order tensor (bold capital letters):

$$\mathbf{A} \;=\; A_{ij} \mathbf{g}_i \otimes \mathbf{g}_j \;.$$

A 4th order tensor:

$$^{<4>}\mathbf{D} \;=\; D_{ijkl} \mathbf{g}_i \otimes \mathbf{g}_j \otimes \mathbf{g}_k \otimes \mathbf{g}_l \;.$$

An l-order tensor:

$$^{<l>}\mathbf{A} \;=\; A_{\mu_1 \ldots \mu_l} \mathbf{g}_{\mu_1} \otimes \cdots \otimes \mathbf{g}_{\mu_l} \;.$$

The 2nd- and 4th order identity tensors, respectively:

$$\mathbf{I} \;=\; \mathbf{g}_i \otimes \mathbf{g}_i \quad , \qquad ^{<4>}\mathbf{I} = \mathbf{g}_i \otimes \mathbf{g}_j \otimes \mathbf{g}_k \otimes \mathbf{g}_l \;.$$

An outer product of two vectors (forming a second order tensor):

$$\mathbf{v} \otimes \mathbf{n} \;=\; v_i \mathbf{g}_i \otimes n_j \mathbf{g}_j \;.$$

An l-order symmetric irreducible (traceless) part of an l-order symmetric tensor formed by the l-order outer products of a vector $\mathbf{n}$ with itself:

$$\overline{\underbrace{\mathbf{n} \otimes \ldots \otimes \mathbf{n}}_{\text{l-times}}} \quad , \quad \overline{n_{\mu_1} \otimes \ldots \otimes n_{\mu_l}} \quad .$$

An inner product (also called scalar- or dot-product) of two second-order tensors:

$$\mathbf{AB} \quad = \quad \mathbf{A} \cdot \mathbf{B} \quad = \quad A_{ik}\mathbf{g}_i \otimes \mathbf{g}_k \cdot B_{kj}\mathbf{g}_k \otimes \mathbf{g}_j \ ,$$

$$\text{if} \quad \mathbf{B} \quad = \quad \mathbf{A} \ , \quad \text{then} \quad \mathbf{A}^2 = \mathbf{A} \cdot \mathbf{A} \ .$$

A double inner product of two second-order tensors:

$$\mathbf{A} : \mathbf{B} \quad = \quad A_{ik}\mathbf{g}_i \otimes \mathbf{g}_k : B_{ki}\mathbf{g}_k \otimes \mathbf{g}_i \ .$$

An outer product of two second-order tensors:

$$\mathbf{A} \otimes \mathbf{B} = A_{ij}\mathbf{g}_i \otimes \mathbf{g}_j \otimes B_{kl}\mathbf{g}_k \otimes \mathbf{g}_l \quad = \quad C_{ijkl}\mathbf{g}_i \otimes \mathbf{g}_j \otimes \mathbf{g}_k \otimes \mathbf{g}_l \ .$$

A modified outer product of two second-order tensors:

$$\mathbf{A} \,\tilde{\otimes}\, \mathbf{B} = A_{ij}\mathbf{g}_i \otimes \mathbf{g}_j \,\tilde{\otimes}\, B_{kl}\mathbf{g}_k \otimes \mathbf{g}_l \quad = \quad C_{iklj}\mathbf{g}_i \otimes \mathbf{g}_k \otimes \mathbf{g}_l \otimes \mathbf{g}_j \ ,$$

$$\text{an example:} \quad A_{14}\mathbf{g}_1 \otimes \mathbf{g}_4 \,\tilde{\otimes}\, B_{23}\mathbf{g}_2 \otimes \mathbf{g}_3 \quad = \quad C_{1234}\mathbf{g}_1 \otimes \mathbf{g}_2 \otimes \mathbf{g}_3 \otimes \mathbf{g}_4 \ .$$

Kelvin-Mandel variant of the Voigt notation preserving the tensor properties, especially regarding coordinate transformations [3]:

$$C_{\alpha\beta}^{\mathrm{K-M}} \quad = \quad \begin{pmatrix} C_{1111} & C_{1122} & C_{1133} & \sqrt{2}C_{1123} & \sqrt{2}C_{1131} & \sqrt{2}C_{1112} \\ C_{1122} & C_{2222} & C_{2233} & \sqrt{2}C_{2223} & \sqrt{2}C_{2231} & \sqrt{2}C_{2212} \\ C_{1133} & C_{2233} & C_{3333} & \sqrt{2}C_{3323} & \sqrt{2}C_{3331} & \sqrt{2}C_{3312} \\ \sqrt{2}C_{1123} & \sqrt{2}C_{2223} & \sqrt{2}C_{3323} & 2C_{2323} & 2C_{2331} & 2C_{2312} \\ \sqrt{2}C_{1131} & \sqrt{2}C_{2231} & \sqrt{2}C_{3331} & 2C_{2331} & 2C_{3131} & 2C_{3112} \\ \sqrt{2}C_{1112} & \sqrt{2}C_{2212} & \sqrt{2}C_{3312} & 2C_{2312} & 2C_{3112} & 2C_{1212} \end{pmatrix}$$

$$\alpha, \beta = 1, ..., 6 \ .$$

Some notations of continuum mechanics [4, 5]:

$\mathbf{Lin}$ – a set of all linear mappings of a three-dimensional vector space $\mathbb{R}^3$ over real numbers into itself.

$\mathbf{Orth} = \{\mathbf{Q} \in \mathbf{Lin} : \mathbf{Q} = \mathbf{Q}^{-T}\}$ – the symmetry group of orthogonal transformations, where $\mathbf{Q}$ is an orthogonal transformation matrix (rotations).

$W = W(\mathbf{F})$ – strain-energy density function.

$\mathbf{X}$, X_K – coordinates associated with the undeformed state; defined as *material* or *Lagrangian coordinates*. The undeformed state is chosen as a reference configuration.

$\mathbf{x}$, x_k – coordinates associated with the deformed state; defined as *spatial* or *Eulerian coordinates*.

$\mathbf{F} = \frac{\partial \mathbf{x}}{\partial \mathbf{X}}$, $F_{kK} = \frac{\partial x_k}{\partial X_K} = x_{k,K}$ – deformation gradient.

$\mathbf{C} = \mathbf{F}^T \cdot \mathbf{F} = \mathbf{C}^T$, $C_{KL} = \sum_k \frac{\partial x_k}{\partial X_K} \frac{\partial x_k}{\partial X_L} = x_{k,K} x_{k,L}$ – *Green* deformation tensor.

$\mathbf{E} = \frac{1}{2}(\mathbf{C} - \mathbf{I}) = \mathbf{E}^T = \frac{1}{2}(\nabla_{\mathbf{X}}\mathbf{U} + (\nabla_{\mathbf{X}}\mathbf{U})^T + (\nabla_{\mathbf{X}}\mathbf{U})^T \cdot \nabla_{\mathbf{X}}\mathbf{U}) = \frac{1}{2}(U_{K,L} + U_{L,K} + U_{M,K}U_{M,L})$ – *Lagrangian* strain tensor, where $U_{K,L}, U_{L,K}, U_{M,K}, U_{M,L}$ are displacement gradients. The term $U_{M,K}U_{M,L}$ refers to geometrical non-linearity. If $U_{M,K}U_{M,L} \ll 1$, then:

$$\mathbf{E} \approx \boldsymbol{\varepsilon} = \boldsymbol{\varepsilon}^T = \frac{1}{2}(\nabla_{\mathbf{x}}\mathbf{u} + (\nabla_{\mathbf{x}}\mathbf{u})^T) \, ,$$

where $\boldsymbol{\varepsilon}$ is an infinitesimal strain tensor and $\mathbf{x}$ represents undeformed position. A benefit of using *Lagrangian* strain tensor is that *Lagrange strain*, ε_L, can be measured based on experimental data, i.e.
$\varepsilon_L = \frac{l^2 - l_0^2}{2l_0^2} = \frac{1}{2}(\beta^2 - 1)$,
where l_0, l are sample lengths in the beginning and end of a test, respectively and $\beta = \frac{l}{l_0}$ is a stretch ratio.
An infinitesimal strain—*engineering strain*, ε_e—may be experimentally defined as following:
$\varepsilon_e = \frac{l - l_0}{l_0} = (\beta - 1)$.

$\mathbf{S} = 2\frac{\partial W}{\partial \mathbf{C}} = \frac{\partial W}{\partial \mathbf{E}}$ – second *Piola-Kirchhoff pseudo-stress* tensor, expresses the stress with respect to the original (undeformed) surface area. Second Piola-Kirchhoff pseudo-stress tensor presents the stress at the material point X.

(c), (m), (f), (s) – refer to the composite, matrix, fibres, steel, respectively.
ij, i, j, $i, j = 1, 2, 3$ – upper indices refer to material symmetry axes.
(f_{ms}), (f_{str}) – refer to orientation-weighted fibres in material meso-symmetry and structural coordinates, respectively.
S – refers to a symmetric part of a tensor (minor symmetry within last 2 indices).

1. Introduction

In the last decades the development of composites is connected with the need to improve the efficiency and economy of materials. A possibility to increase the strength of the base material or matrix is the addition of short fibres. Concrete-matrix composites are an example of short fibre-reinforced materials. They usually consist of a cement-based matrix and different types of short fibres: glass [6], polypropylene [7], carbon [8], and steel [9], Fig. 1.1. The short steel fibres are made of cold-drawn steel, which has a high strength, but insignificant deformation capacity compared to the ductility of common hot-rolled construction steels. The shapes of steel fibres depend on manufacturers as shown in Fig. 1.1(b).

(a) Upper: carbon nanofibres [8]. Lower: polypropylene fibres.

(b) Steel fibres with varying geometry.
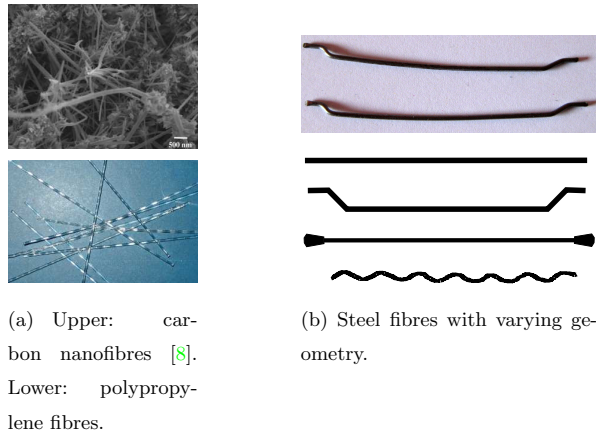
Figure 1.1. Short fibres used for the reinforcement of concrete matrix.

The motivation to study concrete composites comes from the demand for using them in load-bearing structures to reduce the construction time and improve quality of structures. The addition of fibres may help to decrease brittle failure characteristics of concrete. The major role of fibres is to carry tensile stresses, while the concrete matrix carries compression as well as distributes and transfers the internal tensile forces to the fibres.

The present research concentrates on the study of the properties and the use of concrete reinforced by short hooked-end steel fibres (steel fibre reinforced concrete, SFRC). In contrast to concrete reinforced with steel bars, short steel fibres are added to the concrete mass at the mixing stage, Fig. 1.2.
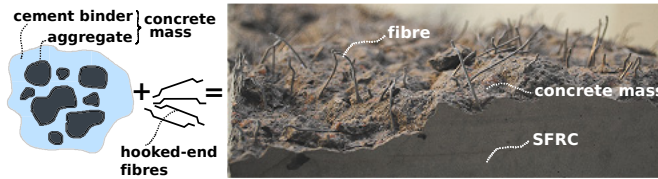
Figure 1.2. Cross-section of a cast SFRC structure. Concrete reinforced by short hooked-end steel fibres, SFRC.

Although the properties of SFRC have not been thoroughly explored, it is widely used in the construction industry and even for providing the load-bearing capacity of structures, Fig. 1.3. In recent years many scientists have

(a) Cast SFRC floor-slabs in Rocca Tower, Tallinn, Estonia.

(b) Cast SFRC floor-slabs in the office building on Kotkapoja street, Tallinn, Estonia.

Figure 1.3. Buildings where SFRC was used for load-bearing structures.

devoted their research to the study of steel fibre reinforced concrete. For example, in the references [9, 10] the authors summarized both theoretical and experimental knowledges developed during the last 20-30 years of research. The studies such as [11, 12] were focused on constitutive mappings. In some recent works [13, 14, 15, 16, 17, 18, 16, 19] the authors utilised several advanced methods and approaches, such as computer-tomography, electrical and magnetic surveys, and image analysis, to investigate the mechanical properties of SFRC. The bearing capacity of SFRC largely depends on the orientation distribution of fibres. Fig. 1.4 demonstrates a basic difference between concrete beams reinforced with steel bars and short steel fibres. In a conventionally

reinforced concrete beam, the predicted tension coincides with the actual re-inforcement. From Fig. 1.4, it is possible to conclude that the determination and further the quantification of fibre orientations play an important role in the specification of the bearing capacity of SFRC.
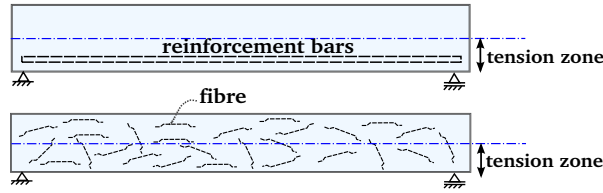
Figure 1.4. The comparison between a reinforced concrete and a SFRC beam. In the SFRC beam the orientation distribution of fibres is not specified.

1.1 Unknowns and open questions with SFRC

The development of any composite system requires to study its deformation and fracture mechanics. The adding of short steel fibres to the matrix leads to an anisotropic behaviour, i.e. direction dependent properties. SFRC exhibits anisotropic properties in accordance with the orientation distribution of fibres. When the alignment of fibres coincides with a principal stress in a structure, the contribution of fibres to the material strength is more pronounced than otherwise. Many empirical measuring techniques enable us to determine the orientation of short steel fibres [17, 20, 21]. Though, the main limitation of these methods is that they may define only the tendencies such as a measured average orientation of fibres and some degree of alignment [20, 21] instead of the attempt to evaluate the orientation of each fibre. In the earlier studies the casting of specimens is usually carried out under well defined and controlled laboratory conditions. These conditions may clearly differ from those at a construction site, where the casting depends on the technological process and is typically site-specific.

The behaviour of any material is determined by its properties, which are con-sidered by constitutive equation (material model). This equation establishes the linkage between stresses and deformations. As the properties of the studied composite depend on the orientation of short steel fibres, a reliable material model for SFRC shall include the quantities, which give a representative de-scription of fibre orientations.

The material models available for composites reinforced by short fibres usually either consider the orientation of fibres utilizing only a single one-dimensional

case with aligned fibres [22, 23] or assume a mean orientation with respect to a predefined axis and use one orientation angle as a parameter [11, 12]. One approach is the orientation number (ON), which is defined as an average projected length of fibres in a cross-section onto the normal of the cross-section divided by the fibre length [12]. Another approach is the orientation profile (OP) [11], which extends the concept of the orientation number counting the amount of fibres (out of the total number of fibres given) within different inclination intervals assuming a pre-defined statistical distribution.

An alternative would be the use of full orientation information of fibres and tensor quantities. In spherical coordinates the position of a point is specified by three numbers: radial distance, inclination angle θ, azimuth (in-plane) angle ϕ. For the description of the orientation of a fibre two angles are necessary and the radius is not needed, Fig. 1.5.
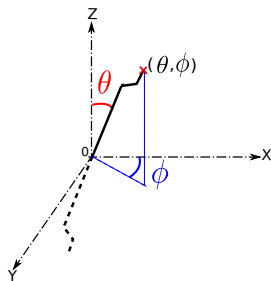
Figure 1.5. Representation of a fibre in spherical coordinate system.

Recently, a plastic approach (based on the formation of plastic hinges) has found a wide application in the design of load-bearing structures made of SFRC [24, 25, 26, 27]. This approach assumes a plastic dependence between the stress and strain and also redistribution of stresses in statically indeterminate structures [28]. Thereby, in a bended conventionally reinforced concrete member, the area of large local plastic deformations, called a plastic hinge, is assumed to be developed. This area includes the compressed concrete zone and tensioned steel bars. However, the behaviour of a bended SFRC member can be taken rather brittle than ductile, since the cracks in a tension zone are not gradually developing and, as a consequence, the failure may occur suddenly. In the case of SFRC, it is not possible to assume any yielding of short steel fibres since they are made of cold-drawn high-strength steel and their anchoring capacity is limited. These issues suggest to start the constitutive mappings for SFRC from the linear-elastic state, meaning that the cracking can be excluded from the material model.

The lack of an objective material model for SFRC, which includes the ori-

entation distribution of fibres required for predicting the bearing capacity of SFRC, suggests that a more fundamental, both theoretical and experimental, research is needed. In addition, the intention to use SFRC as a load-bearing component in concrete structures requires numerical simulations using the material models, which are independent of any reference frame.

The shortcomings of present theories for fibre reinforced materials and their limitations for the design of load-bearing structures made of SFRC are highlighted and presented in Publication I.

1.2   Research goals and implementations

The mechanical properties of SFRC are directly dependent on the orientation distribution of short steel fibres. Only by knowing fibre orientations it is possible to determine the bearing capacity of this composite. The ability to measure the orientation of fibres may also provide a ground to monitor, track and influence on the orientation during the production or cast process. Thus, the main goals of this study can be classified as follows:

experimental: determination of fibre orientations in specimens

theoretical: development of an anisotropic linear-elastic material model, which includes the orientation distribution of fibres

The outcomes of the study can be used for developing the production process of SFRC structures, since the existing principles of casting concrete structures are not originally designed for SFRC and new technological solutions optimising the fibre orientations in the composite are needed.

In developing the methodology for measuring fibre orientations in SFRC products two methods are under elaboration: slicing and X-ray micro-tomography. For both methods the parts extracted from the real-size structures were employed as specimens. The target of the slicing method developed is the intention to combine two approaches, i.e. the photometric image analysis and DC-conductivity measurements by a special robot. As an output, it is expected to obtain the full orientation information of each measured fibre in spherical coordinates. X-ray micro tomography (μCT) is an advanced method for measuring the orientation distribution of fibres from hardened concrete samples. With this method, it is planned to obtain a voxel image of fibres directly in 3D and, later on, the orientation of each individual fibre can be calculated based on a skeletonized (centre line) representation of 3D image received.

The possible applicability of the developed methods for measuring fibre orientations, their precision, and feasibility are highlighted in Publication IV, Publication V.

The presence of short fibres in SFRC and the relevance of their orientation to the bearing capacity of the composite makes it necessary to consider these factors in governing equations. Besides, the brittle behaviour of the concrete matrix, the restricted anchoring of short steel fibres and small range of plastic deformations of high strength steel used for fibres justify the assumption of linear-elastic dependence between stress and deformation. Regarding to this, *the research includes the formulation of the orthotropic linear-elastic constitutive relation for one representative volume element of steel fibre reinforced concrete taking into account the orientation distribution of fibres.*

The approach is based on the use of the orientation distribution function and the alignment tensors [29, 30, 31]. These quantities have been successfully employed in e.g. liquid crystals (LCs) [29, 30], short fibre polymer composites [31], and penny shaped micro-cracks in brittle materials [32], where the orientation distribution of rod-like particles is relevant. The approach rests on the concepts of mesoscopic continuum theory, which is between a microscopic description, which uses the statistical methods, and macroscopic description, which usually does not take into account any micro-structure. Mesoscopic continuum theory introduces new variables as, for example, the mesoscopic distribution function, which in our case is a statistical orientation distribution function. It was developed about 50 years ago for LCs (rod-like particles) [33, 34, 35]. The orientation distribution function (ODF) defines a probability of finding a rod-like particle between the given angles on a sphere. Each point of this sphere is associated with the direction of a rod-like particle (LC molecule, fibre) represented by a unit vector. Thereby, all possible directions of a unit vector form a unit sphere (radius $r = 1$) [30]. Here, it is useful to introduce the l-order orientation tensor (OT), which is symmetric and can be composed by dyadic products of a unit vector with itself, then integrating the result with the ODF over the whole unit sphere [31]. The irreducible—symmetric traceless—part of the l-order OT, called the l-order alignment tensor (AT) [29, 30, 36], can recover the ODF. The orientation distribution function defined on a unit sphere can be expanded into the series of main spherical harmonics forming a complete orthonormal basis. The l-order symmetric tensorial product of a unit vector from which the trace is removed gives an l-order symmetric irreducible tensor, which is a spherical harmonic function [30]. The latter allows to decompose the ODF in a series by basis

formed by symmetric irreducible tensors and the ATs are acting as the expansion coefficients. This implies that if the expansion coefficients–ATs–in a complete orthonormal basis are known the original function–ODF–can also be considered as known [37].

The clear advantage of using the tools of mesoscopic continuum theory in the present research is achieved by the potential to describe the orientation state of short fibres in space employing the tensorial quantities: orientation and alignment tensors. The latter are able to include the complete data of fibre orientations (two angles in spherical coordinates) needed for specifying the position of a point in space. Moreover, the described mesoscopic orientation characteristics can be used in the material model for SFRC.

The main tasks that will be solved during the research are presented in Fig. 1.6. From the figure we may conclude that the concept of the whole work is the consolidation of theoretical and experimental branches. This is needed for enhancing the design and manufacturing in order to obtain the most favourable orientation of fibres in a structure.

The constitutive modelling of anisotropic material properties of SFRC employing the concepts of mesoscopic continuum theory is highlighted in Publication VI.

Fibre orientation phenomenon in concrete composites: measuring and theoretical modelling

theoretical research

experimental research

Task 1t. Analysis of existing theories for short fibre reinforced materials

Task 1e. Overview of possible measuring techniques. Examination of methods planned to be used in the research

Task 2t. The role of the orientation of rod-like particles in other materials, e.g. liquid crystals, short fibre composites

Introduction of new characteristics: the alignment tensors and the orientation distribution function

Task 2e. Measuring fibre orientations using:
- slicing: photometric measurements
- slicing: DC-conductivity testing combined to photometry
- X-ray micro-tomography

Task 3t. Formulation of the orthotropic linear-elastic material model for one representative volume element of SFRC employing the alignment tensors and the ODF

Task 3e. Statistics of the orientation distribution of fibres received by:
- slicing: photometric measurements
- slicing: DC-conductivity testing combined to photometry
- X-ray micro-tomography

Task 4t. Calculation of the alignment tensors and the orientation distribution functions of fibres based on X-ray micro-tomography data

Task 4e. Comparison and analysis of the orientation distribution of fibres obtained by:
- photometric measurements versus micro computed tomography
- DC-conductivity testing versus photometric measurements

Consolidation of theoretical and experimental parts:
application of formulated material model for the description of the elastic properties of SFRC specimens with measured fiber orientations

Results

Developed measuring methods can be utilised in the production technology

Constitutive model considering fibre orientation distributions for numerical simulation of SFRC structures

Figure 1.6. Graphical representation of the basic objectives during the research.

2. Methodology for measuring fibre orientations

The bearing capacity of SFRC has an anisotropic nature, and the level of anisotropy originates primarily from the orientation state of fibres. Thus, an experimental problem is the determination of the orientation distribution of fibres. In this Chapter, an overview of methods for measuring fibre orientations in SFRC precedes a detailed description of the methods elaborated and realized in the research work.

The measuring techniques developed and implemented in the research are highlighted in Publication IV and Publication V.

2.1   Overview of measuring techniques

In recent years, various techniques have been utilised to investigate the orientation of short steel fibres in hardened concrete. These methods include photometric analysis [11, 12, 14, 15, 38, 39], X-ray computed tomography [16, 40, 41, 42] or they are based on different physical phenomena such as electrical conductivity and magnetism [20, 21, 43, 44].

Slicing with photometric analysis

The idea to utilize the photos of cut specimens—slices—to specify fibre orientations in fibre reinforced composites has already been widely used, e.g. by P. Stroeven and J.Hu, L.Ferrara *et al.*, P. Purnell *et al.* [14, 18, 45], by C.Redon *et al.* [17], who used a Fourier transform and by C. Redon *et al.*, P.Stroeven [43, 46], who used image analysis on 2D X-ray transmission images. Fourier image transform is an automatic method to assess fibre orientations. It involves the application of the Fourier transform depending on the orientation of a mask on a grey-level image and, further, the detection of the portions of fibres oriented into the defined direction. 2D X-ray images may be employed to trace manually the fibres on transparent films representing them by a num-

ber of distinguishable lines. Therein the precision of outcomes depends on the resolution of images, as the estimation of fibre orientations is based on the geometry of cut fibres. The shape detection of cut fibres may be performed using an image analysis software. Employing this method it is possible to define the orientation of a fibre in spherical coordinates, by the inclination θ and in-plane ϕ angles, Fig. 1.5. However, the in-plane angle can be measured only within the interval from $[0°, 180°]$ instead of the $[0°, 360°]$ and this leads to an ambiguity in the direction of a fibre, Fig. 2.1.
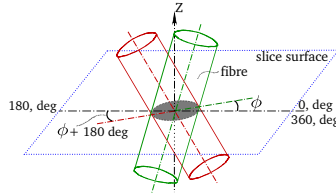
Figure 2.1. Ambiguity in the direction of a fibre in case of photometric analysis.

This is not a problem of the image analysis software employed, but fundamental to the analysis of 2D images, which can only contain limited information.

X-ray computed tomography

X-ray computed tomography (CT) has emerged as a powerful technique for non-destructive 3D visualization of the micro-structural features of objects [13, 47, 48, 49]. The method has also been used to study fibre and steel fibre reinforced concrete [16, 42, 50, 51]. The X-ray micro-tomography (μCT) basically works on the same principle as conventional CT, except that in μCT the sample is rotated instead of the X-ray source and detector. The main benefit of μCT method is that it allows to determine the orientation of individual fibres in a sample based on their spatial (3D) representation. The major steps of μCT are:

– scanning of composite sample;

– segmentation into constituent material phases and visualization as 3D image;

– application of skeletonization (centre line) algorithms;

– analysis of skeletonized objects, e.g fibres;

– determination of the inclination θ and in-plane ϕ angles of each individual fibre.

10

Indirect methods for conductive steel fibre reinforced composites

Indirect methods mainly rely on the electro-magnetic properties of steel fibres. Two recently used methods are a magnetic one, and another is based on the alternating current impedance. An advantage of these methods is their non-destructive nature. A drawback is the ability to asses only general tendencies, such as the average orientation of fibres and some order of their alignment, instead of the evaluation of the orientation of a single fibre.

A magnetic method

A magnetic method is one of those developed within last 3 years. It is a non-destructive method, based on monitoring the specimen surface and detecting or measuring the variation of the inductance of a probe [20]. The main idea of the method is that the presence of steel fibres within a specimen can modify the flux linked by the winding of a probe resulting in the variation of impedance. A magnetic permeability of cement-based matrix is much lower than that of fibres. Thereby, the macroscopic magnetic properties of the matrix material and the effective magnetic permeability dyad of the composite can be defined. The effective magnetic permeability depends on the volume fraction of fibres, on their orientation and aspect ratio (ratio of length to diameter), but it does not depend on their size. Therefore, the measuring of a parameter influenced by the effective permeability of SFRC element may allow to asses both the concentration and orientation of steel fibres.

Alternating Current Impedance Spectroscopy

Alternating Current Impedance Spectroscopy (AC-IS) is an electrical characterization method, which allows to study the various features of micro-structural materials [21]. AC-IS can also be utilised to obtain fibre dispersion parameters of conductive fibre reinforced composites owing to its unique dual-arc behaviour. The latter means that, due to the existence of a small portion of conductive fibres in a composite of finite matrix conductivity, one matrix impedance arc is divided into two separate low and high frequency arcs in the complex impedance plane. This effect is more pronounced when the fibres are highly conductive compared to the matrix material. The dual-arc mode is caused by the frequency dependent behaviour of conductive fibres, which are insulating under the low frequencies (Hz), but are conductive under the high frequencies (MHz). Thus, the idea of applying the AC-IS method on SFRC includes the impact of an alternating voltage on specimens (concrete and SFRC) and the measurement of a current responses. For this purpose,

the electrodes are positioned on the specimens and further the matrix and composite resistances are measured. Later on, it is possible to calculate the conductivities of the matrix and composite. The measurements result in normalized conductivity profiles of specimens.

2.2 Selection of measuring methods

Within the research work, slicing and X-ray micro-tomography methods are chosen as basic approaches for measuring fibre orientations in SFRC samples. Such selection is made by the following criteria:

The slicing method does not require any special or expensive devices: which makes it attractive for industrial applications too. X-ray micro-tomography (µCT) is based on expensive devices operated by highly educated personal. In spite of this, its accuracy and clarity are greater than other methods for measuring of fibre orientations: thus, it sets a baseline for the calibration of the methods. µCT method is also interesting as the integration of some, perhaps not so sophisticated, CT systems into the manufacturing process of SFRC may be feasible in the future.

2.3 Slicing method as a combination of DC-conductivity testing with photometry

Compared to those earlier studies, the slicing method developed in this research is based on the structural parts extracted from the full-size members (floor-slabs) and the use of multiple slices close to each other, which are analysed to improve the statistics, in contrast to the single-picture approach that is found in the literature [15]. In addition, the experimental full-size members are prepared not in controlled laboratory conditions, but following the site-specific casting. The slices are analysed utilizing approaches that are joined together: the coordinates received in the image analysis are employed as an input for a special robot measuring DC (direct current) conductivity.

The first phase of the slicing method presented includes the extraction of sample cuboids from the full-size floor-slabs, cutting them into the slices and taking the photos of slice surfaces. In the photos the fibres cut are visible as ellipses and circles. The image processing and analysis including the detection of the shapes of cut fibres are performed using the public domain software ImageJ [52]. Identification of the geometry of cut fibres makes it possible to measure the inclination θ and in-plane ϕ angles. As it was mentioned above,

the measurement of the in-plane angle ϕ by photometry is possible within the range of $[0°, 180°]$, which results in the ambiguity of the direction of a fibre. The measured orientation distribution of fibres by photometry needs to be adjusted/checked by some additional approaches in slicing. Therefore, the slicing with photometry is improved by a prototype of a special robot measuring DC-conductivity by scanning the slice surfaces and measuring the electrical conductivity between the cut ends of steel fibres. If the cross-sections of a cut fibre on the opposite slice surfaces belong to the same fibre, the current flows and the robot detects the electrical conductivity and saves the coordinates. The measurements by a robot are combined with photometric data and thus this approach is considered as an extension of slicing with photometry. The coordinates of cut fibres on both sides of a slice are known from the image analysis and one can use these as the input for a robot. The outcome received by combining two analysing approaches in slicing, i.e. photometry and DC-conductivity, improves the results of photometry. The main advantage by adding the DC-conductivity testing to the procedure is that it removes the ambiguity related to the in-plane ϕ angle.

2.3.1 Experimental set up

A horizontal structure was chosen to study the orientation distribution of fibres since the structure makes possible to observe both the compressive and tensile stresses as well as the features of fibre behaviour in the vicinity of the formwork and in the bulk. Thereby, six experimental full-size floor-slabs were cast in a factory using a bucket according to the scheme presented in Fig. 2.2(a). The concrete class was C30/37 and concrete was self-compacting, which means no vibration was needed. The fibres used had hooked-ends, the length of a fibre l_f was 50 mm and the diameter d_f was 1 mm, Fig. 2.2(b). The material for fibres was rod wire of types C4D or C7D steel according to standard EN 10016-2 and their amount per cubic meter of concrete was 80 kg, resulting in about 250 fibres per dm^3.
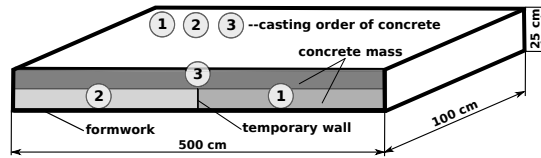
(a) Casting order of a full-size floor-slab.   (b) Hooked-end steel fibres with the aspect ratio of $l_f/d_f = 50$.
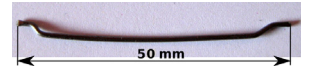
Figure 2.2. The casting order and the fibre types used.

The extraction of sample cuboids from the full-size floor-slabs has started on the 30th of September 2010 and was implemented in the Department of Civil and Structural Engineering in Aalto University (Finland). Before the extraction of cuboids, 28 days old slabs were tested using a three point bending test. During these tests three slabs have shown approximately the same capacity (slabs 1, 2, 3) and the capacity of the remaining three ones (slabs 4, 5, 6) was lower, Fig. 2.3. This behaviour could be explained either by different fibre orientations or by variations in matrix quality such as the existence of air pores. The tested slabs with sample cuboids are presented in Fig. 2.4.
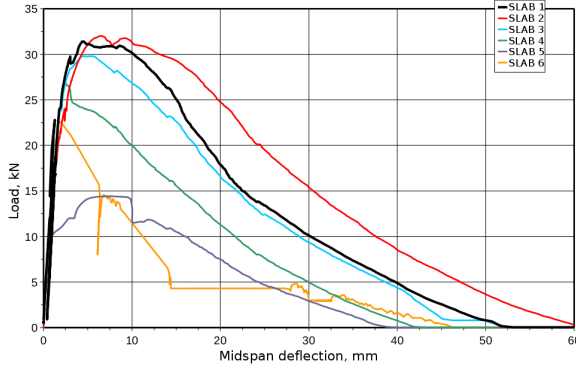
Figure 2.3. Load-deflection diagram of tested floor-slabs during the bending test.
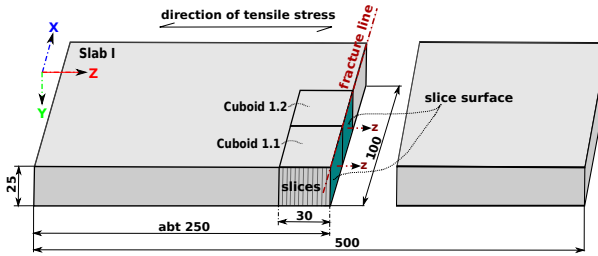
Figure 2.4. Representation of a floor-slab and sample cuboids. Dimensions in (cm).

The sample cuboids ($H \times W \times L : 25\,\text{cm} \times 30\,\text{cm} \times 30\,\text{cm}$) were extracted from the slabs using a diamond saw, Fig. 2.5(a). Each sample cuboid was numbered according to the number of a slab from which it was cut, Fig. 2.4. In addition, all cuboids were marked on a top by milled cross and on one edge by blue water-resistant colour, Fig. 2.5(b). Altogether twelve cuboids were taken. Six of them were sawn from the central part and the others were taken from the side of the slabs, Fig. 2.4. This was done to detect the influence of the formwork moulds on the arrangement of fibres in the matrix, i.e. the tendency of fibres to align themselves in the vicinity of a formwork. Onwards, the sample cuboids were cut into the slices. The cutting of slices has began on

(a) The process of cutting the sample cuboids using a diamond saw.

(b) The marking of cuboids by a milled cross and water resistant blue colour.

Figure 2.5. The cutting and marking of sample cuboids.

the 8th of October 2010. The sample cuboids were transported to a company specializing in the cutting of hard stones. As the sample cuboids had the height of 25 cm, a special stationary diamond saw was needed, Fig. 2.6. Due to the cutting method, the material was lost in the range of $5 - 10$ mm in each cut section.

(a) The disc of a saw with diamond incisors.

(b) The measuring of a slice.

Figure 2.6. The diamond saw used.

It was planned to cut each sample cuboid into 15 slices with the thickness of 2 cm and, hence, to produce 180 slices. However, the cutting of the cuboids into the slices by a diamond saw has caused a considerable loss of the material and instead of the expected 15 slices there were only 11 or 12 slices. Consequently, approximately 60 mm of the material were lost during the cutting process if the number of slices was 12 and in the case with 11 slices the material lost was 80 mm. The numbers of slices received from the sample cuboids were:

– Slab 1: Cuboid 1 – 12 slices, Cuboid 2 – 12 slices;

– Slab 2: Cuboid 1 – 11 slices, Cuboid 2 – 11 slices;

– Slab 3: Cuboid 1 – 11 slices, Cuboid 2 – 11 slices;

– Slab 4: Cuboid 1 – 11 slices, Cuboid 2 – 12 slices;

– Slab 5: Cuboid 1 – 11 slices, Cuboid 2 – 11 slices;

– Slab 6: Cuboid 1 – 11 slices, Cuboid 2 – 11 slices.

2.3.2 Slicing with photometry

The process of photometry has began on the 25th of October 2010. When the sample cuboids had been cut into the slices the photos were taken from each slice surface. Fig. 2.7(a) represents a platform used for taking the pictures. A tripod for the photo-camera was fixed on the platform, Fig. 2.7(b). In order to place the slice surface to the centre of the platform, the central lines were marked as shown in Fig. 2.7(a). The central lines of the platform coincided

Fixed tripod for
the camera

Central lines
marked on a platform

(a) The platform for taking a picture of slice surface.

(b) The tripod fixed on a platform.
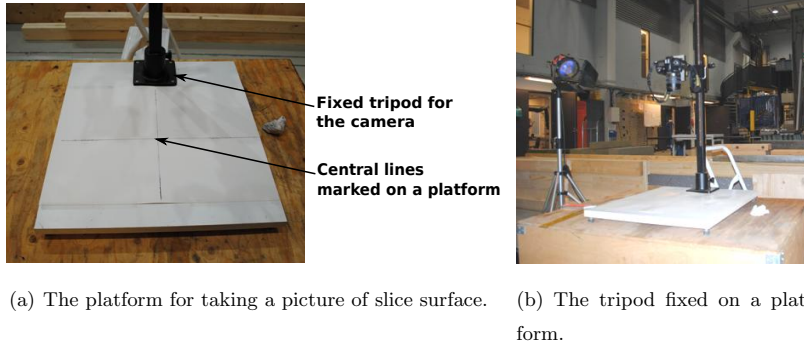
Figure 2.7. The tools used for photographing slice surfaces.

with the central lines of the camera lens. Middle points were marked on two edges of each slice, which further have been merged with the central lines on the platform. To avoid the loss of the correct position of a slice in a cuboid, a corner of each slice was denoted by the red colour. The marked red corner was on the left surface from the blue butt-end of a slice, Fig. 2.8(a). Taking the photos of slice surfaces required a correct lighting. By wetting the slice surface the concrete matrix was made non-reflective and the steel fibres started to reflect the light like a mirror. However, if the slice surface became too wet, the concrete matrix started to reflect the light as well, and it was necessary to wait a moment till the concrete surface had dried a little and become opaque. Taking the photos of slice surfaces in a cuboid were started from the last left slice in a reference to the blue butt-end of a cuboid, Fig. 2.8(b). At first, the photos of the left surface of a slice were taken and then the photos of the right surface, Fig. 2.8(b). In photos, the indication of the left or right surface of a slice was made by the colour of a ruler. The left slice surface was identified by a yellow-red and the right one by a red ruler, Fig. 2.9. The graphical representation of a sample cuboid with slices is shown in Fig. 2.10.
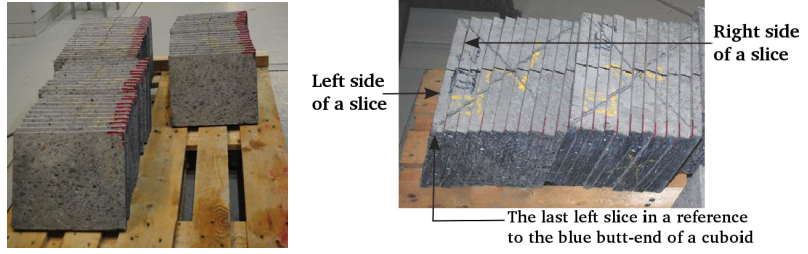
(a) The marked red corners of slices.

(b) The order of taking the photos of slice surfaces in a cuboid.

Figure 2.8. The positioning and marking of slices.
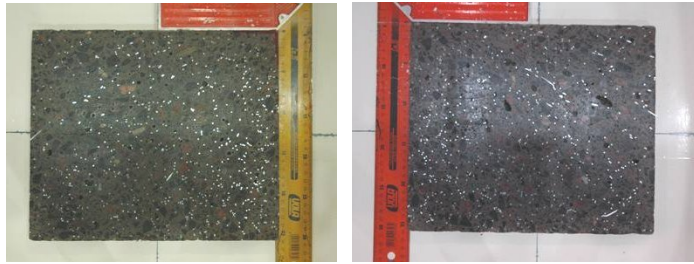
(a) The left surface of a slice and a yellow-red ruler.

(b) The right surface of a slice and a red ruler.

Figure 2.9. The identification of the left or right surface of a slice by the colour of a ruler.
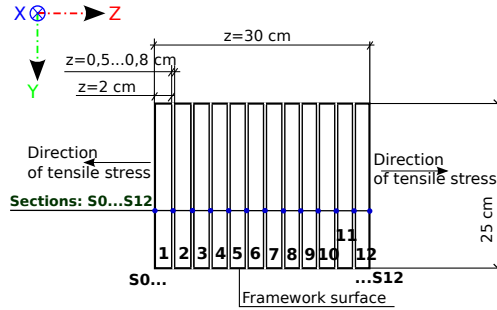
Figure 2.10. Representation of a sample cuboid with slices, see also Fig. 2.8(b).

The photos were saved in two formats at a time: RAW–nef and JPG–basic. The image processing and analysis was done on the RAW images because of their higher resolution and using the public domain software `ImageJ` [52]. A photo of a slice after its filtering with pseudo-flat-field filter [53] and cleaning in binary format is presented in Fig. 2.11. As the fibres are cylindrical, which is a degenerated cone, the intersection of a cone with a plane gives an ellipse as a closed curve. Hence, the bright inclusions in Fig. 2.11(a) are the cut cross-

(a) Filtered image of a slice

(b) Processed image of a slice in binary format
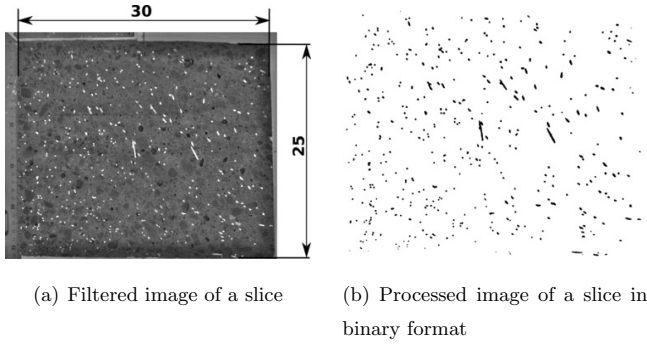
Figure 2.11. Image of a slice.

sections of fibres. The data obtained after the analysis of slice surface include: the coordinates X_i, Y_i determining the position of the centre of fitted ellipses from the origin, the major and minor axes of the ellipses and the in-plane ϕ angle, Figs. 2.12(a), 2.12(b). The shape of an ellipse can give an assessment of the inclination angle θ as the ratio of minor and major axis, Fig. 2.12(a),

$$\theta = \arccos\left(\frac{\text{Ellipse Minor axis}}{\text{Ellipse Major axis}}\right) . \tag{2.1}$$

(a) The inclination θ and in-plane ϕ angles.

(b) The in-plane angle ϕ.

(c) The ambiguity in the direction of fibres.
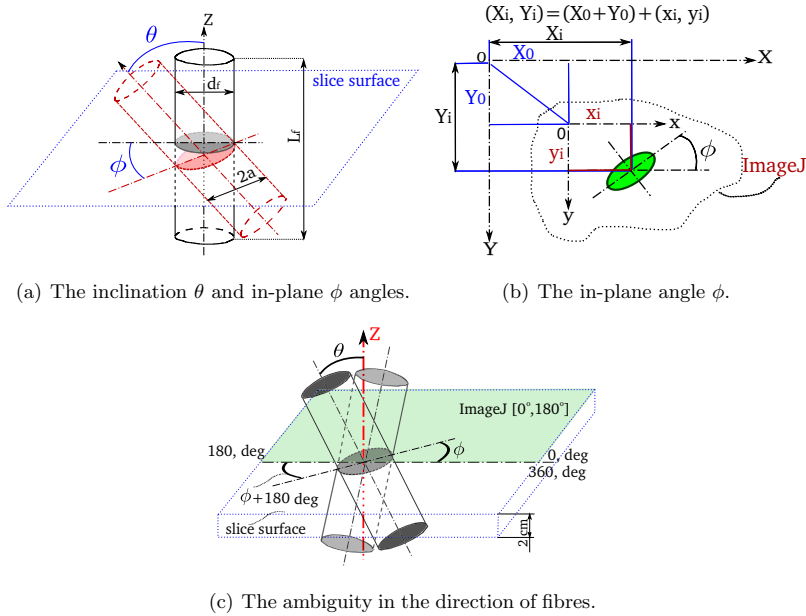
Figure 2.12. Definition of the orientation angles applying the image analysis.

If a fibre is aligned parallel with the normal Z of the slice surface, then the cross section of a cut fibre is a circle with a diameter d_f and the ratio

$$1 = \lim_{\theta \to 0} cos(\theta) = \lim_{2a \to d_f} \frac{d_f}{2a} , \tag{2.2}$$

which implies, that the inclination angle θ is equal to $0°$. On the contrary, if a fibre is perpendicular to the normal Z, then the ratio

$$0 \quad = \quad \lim_{\theta \to 90°} cos(\theta) \quad \approx \quad \lim_{2a \to L_f} \frac{d_f}{2a} \; , \tag{2.3}$$

what means, that the inclination angle θ is $90°$. The in-plane angle ϕ is measured between the orientation of the major axis of an ellipse and the horizontal coordinate axis, Fig. 2.12(b).

As Fig. 2.12(c) illustrates, the in-plane angle determines the direction of a fibre. This direction can be counted from $0°$ up to $180°$ degrees, which leads to an ambiguity in the direction of a fibre. In more detail this ambiguity can be formulated as follows: if the direction of a fibre has the ϕ angle of $45°$, this cannot be distinguished from the fibre at the ϕ angle of $45° + 180°$, since for both cases the shape of cut fibre on slice surface will be the same, Fig. 2.12(c).

2.3.3 Slicing with DC-conductivity joined with photometry

As it was noted in Section 2.3.2, the measurement of the in-plane angle ϕ by photometry is possible within the interval from $[0°, 180°]$ only. Thus, the measured orientation distribution of fibres needs to be checked by some additional approaches in slicing or by another measuring method. DC-conductivity testing was concluded to be an appropriate extension of slicing with photometry, as it can utilize the coordinates of cut fibres defined in the image analysis. Since the fibres are of steel, they have a good electrical conductivity. The robot scans the opposite surfaces of a slice and measures electrical conductivity between the endpoints of cut fibres. If the cut cross-sections of a fibre on the opposite slice surfaces belong to the same fibre, the current flows and the coordinates (in Cartesian system) are recorded to a '.txt' file. The next step is to process the coordinates measured by the robot to get the directions of cut fibres. This can be implemented by the subtraction of the coordinates on one slice surface from those on the opposite surface:

$$d \quad = \quad \begin{pmatrix} X \\ Y \\ 0 \end{pmatrix} - \begin{pmatrix} U \\ V \\ 20 \end{pmatrix} \; , \tag{2.4}$$

where 20 is a slice thickness in mm. The limit inclination angle measured by a robot depends on the thickness of a slice and the length of used fibres. For example, the 20 mm thick slice and 50 mm long fibres give the limit inclination angle of $\theta_c = \arccos(\frac{20 \text{ mm}}{50 \text{ mm}}) = 1.159 = 66.4°$. The in-plane ϕ angle is measured in the interval $[0°, 360°]$, there is no ambiguity here.

The scanning robot was built in cooperation with the Centre of Biorobotics at Tallinn University of Technology (TUT). This robot has four linear axis and

two probes, Figs. 2.13, 2.14(b), 2.14(c). Each axis has a separate drive, so that the probes can be moved independently on a 2D plane: one probe on one side and the other on the opposite side of a slice, see Figs. 2.13, 2.14(a), 2.14(b).
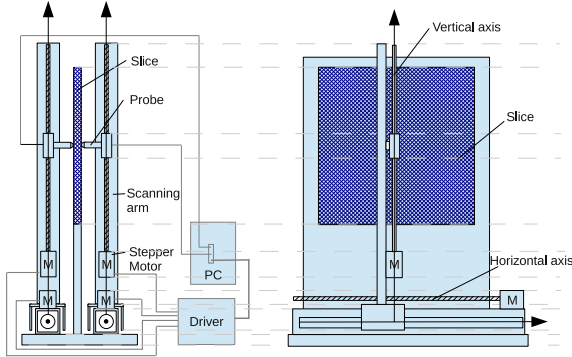
Figure 2.13. The scanning robot (side and front view).
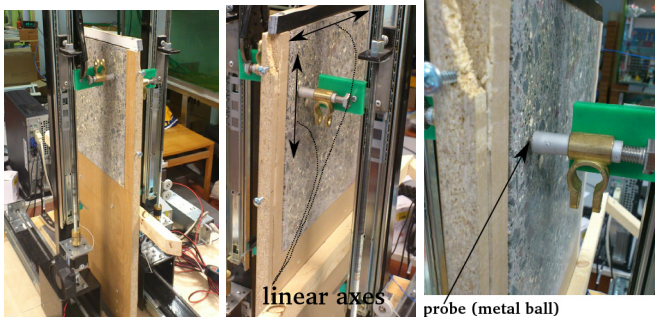
(a) Scanning of one side of a slice.

(b) Scanning of the opposite side of a slice.

(c) A probe.

Figure 2.14. The scanning robot in use.

Each probe is made of a spring, tube and a steel ball, Fig. 2.14(c). The input data were the coordinates of the cross-sections of cut fibres on the both sides of a slice and the output data should be the coordinates of connected cross-sections. The `Emc2` (Enhanced Machine controller) software [54] was selected to control the scanning robot. It is a free Linux program for computer control of different machines. The program was configured to control 4 linear axes at the speed of 10 mm per second. Two methods were considered for scanning the slice surface. One was to scan the whole surface area (step 0.9 mm), which would take about 5 years with the present prototype. The other method was to check only the coordinates of the cross-sections of cut fibres defined in image analysis. The second method was selected as it reduced the scanning time remarkably. The algorithm for the movement of axis was made using

the G-code (DIN 66025/ISO 6983), which is widely used in the automation telling the computerized machines where, how fast, and which path to move. The G-code algorithm included about 25000 different combinations consisting about 180 000 lines. Therefore, another simple program was written in the C-language. This program calculates the range, where the cross-section of a cut fibre may locate on the opposite slice surface and accordingly generates the G-code.

2.4 X-ray micro-tomography method (µCT)

The cylinder samples (sufficiently large in size) extracted from the same full-size floor-slabs as the sliced cuboids were scanned using µCT equipment. With this method, the fibres in a samples were represented directly in 3D and, further, the application of 3D skeleton (centre line) processing algorithm made possible to specify the orientation of each individual fibre.

2.4.1 Procedure set up

SFRC cylinders were extracted from the floor-slabs according to Fig. 2.15. Two cylinder samples from each floor-slab: one from the central ("B"-samples) and one from the side ("A"-samples) region. As with the slicing method, the samples were taken also near the mould to investigate its effect on the orientation of fibres. Altogether twelve cylinder samples with a diameter of 10 cm each were
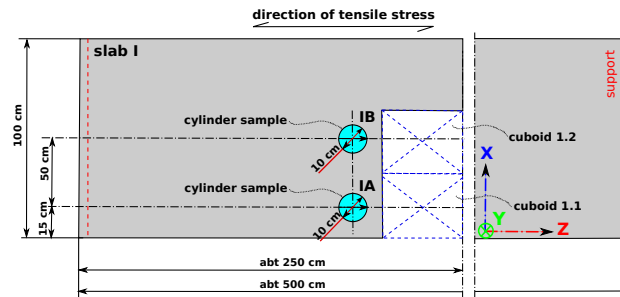
Figure 2.15. The position of an analysed cylinder in the floor-slab.

extracted. The cylinder samples were scanned in the Department of Physics in Helsinki University (Finland) using the experience of micro-tomography group, i.e. Jussi-Petteri Suuronen, Aki Kallonen and Prof. Ritva Serimaa. The X-ray Micro-tomography Laboratory is built around a state-of-the-art µCT scanner Nanotom 180 NF supplied by phoenix| xray Systems + Services GmbH (Wunstorf, Germany), Fig. 2.16. The circumference of a cylinder sam-

(a) A cylinder sample in the µCT scanner.

(b) The room with the µCT scanner.
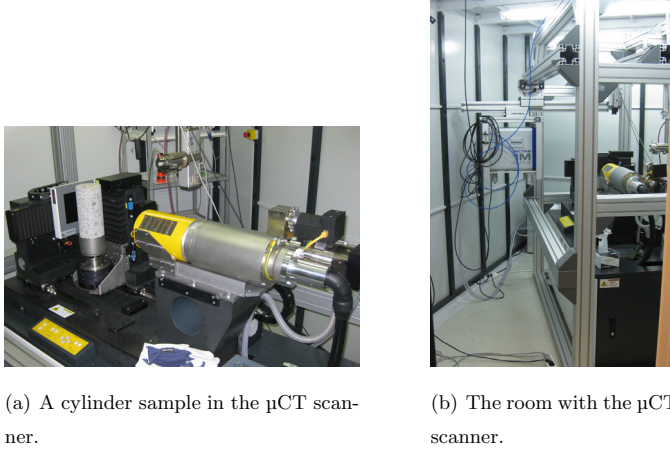
Figure 2.16. The scanner nanotom supplied by Phoenix|x-ray Systems.

ple was scanned with an angular step of 1 deg leading to 360 projection images made. The scanning of a sample took approximately three hours. Within the first phase of scanning, the middle part of the cylinder samples was scanned, Fig. 2.17(a). The height of the middle part was about 7 cm. The second phase included the scanning of the top and bottom parts of four cylinder samples. The choice of the scanning area was connected with the technical capabilities
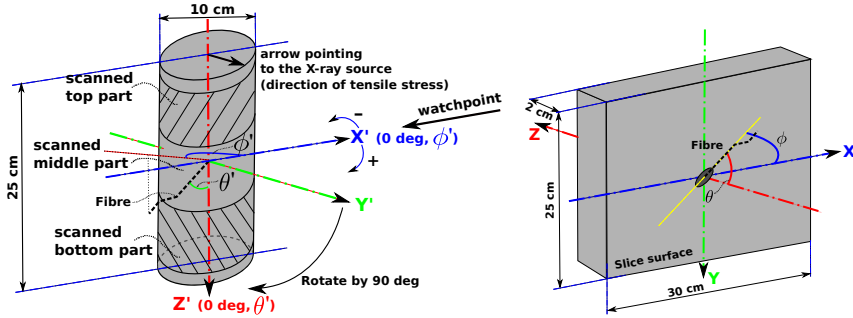
(a) Definition of the orientation angles θ' and ϕ' measured from the µCT data. The position of the scanned top, middle and bottom parts. The coordinate system in Avizo Fire.

(b) The slicing coordinate system, considered as structural coordinates.

Figure 2.17. The representation of µCT and slicing coordinate systems.

of the used scanning machine, i.e. the size of the detector (LCD screen) and with the intention to investigate the differences of fibre orientations in the bulk and close to formwork or free surface. Besides, the chosen scanning order made it possible to analyse fibre orientation distributions in compressed and tensioned cross-sectional areas.

To improve the quality of projection images, a median filter (implemented

in `ImageJ`) was applied prior to reconstruction. The reconstruction from the projection images was implemented using an FDK-algorithm-based [55] reconstruction software 'datos| x rec' supplied by the manufacturer. Within the reconstruction procedure 'highEdge' filtering was used to intensify the contrast between the fibres and concrete matrix. A 3D edge preserving smoothing algorithm [56], followed by a dual threshold binarisation (function hysteresis in Avizo Fire), was applied for enhancing the purity of images. A 3D volume image obtained by µCT scanning provided a picture of actual fibre orientations in the concrete matrix, Fig. 2.18.
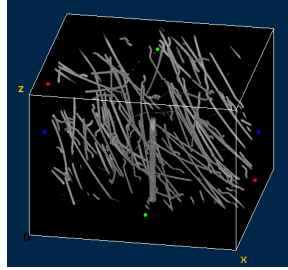
Figure 2.18. Thresholded volume image of a middle part of a cylinder sample scanned by µCT. Still showing an artefact in the middle (data courtesy of Aki Kallonen [1]).

2.4.2 Fibre orientation analysis

Before analysing the orientation of fibres, a skeletonised representation (centre lines) of the fibres was calculated using Avizo Fire 6.2 software (VSG, France). The centre lines of the fibres were received as a thinning of binarised data using the XSkeleton pack extension to Avizo. However, as many fibres in the data were touching each other, the skeleton also contained the connections between the fibres. To solve this problem, the skeleton processing algorithm was applied as a function in Matlab software (Mathworks Inc., USA), which can be called directly from Avizo Fire. After the application of skeleton processing algorithm, the 3D-orientation (the inclination θ' and in-plane ϕ' angles) of fibres was calculated using Avizo. From Fig. 2.17 it is clear, that the coordinate system in Avizo Fire does not coincide with the slicing system. In order to match the coordinates from Avizo Fire with those of the slicing, it is necessary to rotate the Y' and Z' about the X' axis by 90 degrees anticlockwise, Fig. 2.17(a). Since the position of each skeleton-object—fibre—in Avizo Fire is defined in spherical coordinates, it is transformed into Cartesian coordinates and rotated by 90 degrees anticlockwise around the X'-axis using the rotation matrix. Afterwards, the rotated Cartesian coordinates should be again

transformed to spherical ones. Finally, Avizo Fire coordinates considered as laboratory ones are adjusted to the slicing coordinates which are regarded as the structural ones.

2.5 Summary of developed and implemented measuring methods

During the research two methods for measuring fibre orientations have been developed and implemented: coupled measuring approach in slicing—DC-conductivity testing combined with image analysis— and µCT scanning.

The slicing method is obviously suitable for straight and hooked-end fibres. In the case of corrugated fibres this method probably will not give good results, since the reconstruction or tracking of the whole length of a fibre will be a tricky task. When applying the slicing method, one should take into account the ratio between the thickness of a slice and the length of a fibre. The shorter the fibres are, the thinner the slices should be. But the minimum thickness of a slice will still depend on a type of used equipment, i.e. cutting method (diamond saw, water jet cutting, laser etc.). The maximum thickness of a slice depends on a method for the reconstruction of fibre orientations. While using the slicing with photometry, the maximum thickness of a slice is conditioned by the length of an aligned fibre added by some increment to guarantee that the trace of a fibre appears only on one slice surface. In the case of the 'tracking the trace' of a fibre, the slice should be as thin as allowed by machine tooling. In the inclined state the fibre should leave two traces, i.e. one trace per slice surface, Fig. 2.19(a). The precision of the results in photometric analysis depends

(a) The idea of tracking the trace of a cut fibre.

(b) The maximum error in the measurement of θ angle by DC-conductivity testing depending on slice thickness.
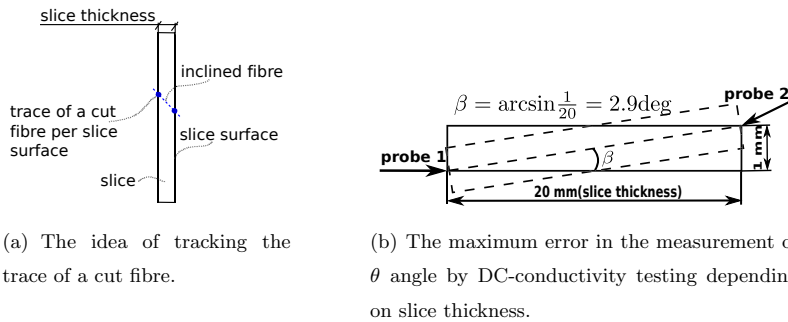
Figure 2.19. The influence of slice thickness on results while tracking the trace of a cut fibre.

a lot on the resolution of the image. The higher the resolution, the more accurately the shape of a cut fibre can be detected. In addition, the accuracy of photometric analysis can be increased by the polishing of slice surface [15].

The biggest drawback of the slicing with photometry is the inability to measure the in-plane angle ϕ in the range from $[0°, 360°]$. Thus, the application of this method is not sufficient for the analysis of the spatial orientation of fibres. DC-conductivity testing utilizing the coordinates received in the image analysis acts as an extension of photometry and solves the ambiguity in the direction of a fibre as it measures the in-plane angle within the interval from $[0°, 360°]$. The possible sources for the errors while utilizing DC-conductivity testing are:

– input coordinates from photometry: accuracy of fibre coordinates is about 1 px, drift after correction up to ± 0.5 mm;

– probe not in the centre of the fibre trace: the maximum error in the measurement of θ angle can be 2.9°, Fig. 2.19(b);

– step size of a step motor. The full step size of a motor can be received as the division of a circle, i.e. 360°, by the amount of steps in a motor. The latter data comes from the technical characteristics of a motor. An error from one step size of a probe has a minor influence on the precision of measurements while the influence of an error arising from the conversion of coordinates, i.e. from pixels to millimetres has the main impact;

– touching fibres: if the fibres are touching, then it is possible to have the conductivity, even if the traces on opposite surfaces belong to different fibres. This seems to be a rare event, as the statistics from the photometry and DC-conductivity testing have similar tendencies;

– hooked-ends of the fibres: if one cut appears to be within the hooked-end of a fibre, this can lead to an error of max 10° ($\arctan \frac{\text{hook-height}}{\text{slice thickness}}$) in the orientation of this fibre, depending on the thickness of a slice and angle of the fibre, Fig. 2.20(a);

– slightly curved middle part of a fibre, Fig. 2.20(b). This can lead to an error below 2°–3° in the fibre orientation ($\arctan \frac{a}{\text{min obj.length}}$).

(a) Maximum error due to only part of fibre being in scanned volume.

(b) Maximum error due to curvature of fibre.
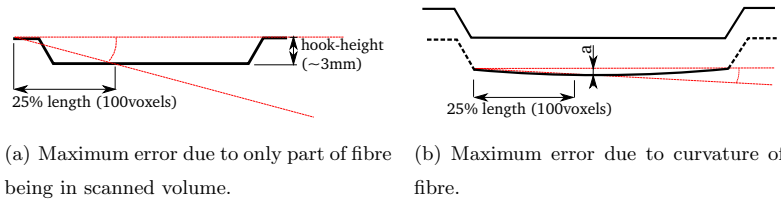
Figure 2.20. Errors connected with the geometry of a fibre.

There is one more factor affecting the accuracy of DC-conductivity measurements: the probability of measuring a fibre is θ-dependent and large inclination angles are underestimated. The probability for one fibre to "leave a trace" on the second surface, under the condition that it "left a trace" on the first surface, is

$$p = \max\left\{\cos\theta - \frac{\text{slice thickness}}{\text{fibre length}}, 0\right\} .$$
(2.5)

X-ray micro-tomography (µCT) method allows to look inside a robust material such as concrete and obtain 3D data about the spatial orientation distribution of fibres. With the equipment used in the research, the actual scanning time was 2–2.5 hours, depending on the imaging parameters, and the reconstruction of a series of the scans into 3D map of a sample took a few minutes. It should be emphasized, that the used µCT equipment is primarily for scanning millimetre-sized samples at sub-micrometer resolution, (i.e. three orders of magnitude higher than the 128.3 µm per voxel) and lacks the beam power necessary to image large samples of highly absorbing materials like concrete. The CT systems which are more suitable for scanning SFRC have a lower precision and higher beam power. The time required for the image processing and statistical analysis is largely dependent on the available computer hardware. The measuring results received by µCT scanning are incomparable in accuracy to other methods. The main sources of error while applying µCT scanning to SFRC are:

– only one of the hooked-ends is within the scanning area, max. error is 13°, from $\Delta\alpha = \arctan\frac{\text{hook-height}}{\text{min obj.length}}$, Fig. 2.20(a). This error could be reduced or eliminated by cutting the hooks away with the kink-detection algorithm;

– resolution of the scan, error about 1 px (0.1283 mm), max error is $\Delta\alpha = \arctan\frac{0.1283\text{mm}}{12.83\text{mm}} = 0.6°$ (1 px off the correct position and 100 px length of object);

– the middle part of the fibres is not exactly straight, but slightly curved, Fig. 2.20(b);

– manual setting of the thresholds;

– skeleton processing: touching fibres and corresponding automatic splitting by the self-written program.

Having reviewed the sources of errors in both measuring methods, it can be stated, that the precision of DC-conductivity testing is close to the one of µCT. The last two error points in DC-conductivity (hooked-ends of the fibres and slightly curved middle part of a fibre) are of the same magnitude as in µCT scanning.

3. Fibre orientation distributions in tested floor-slabs

Numerical estimates of the distribution parameters of fibre orientations in the samples taken from the tested slabs were calculated using the R-programming language [57] and several packages for statistical computing and graphics [2, 58, 59, 60, 61, 62, 63, 64, 65]. The statistical outcomes revealed the variations of fibre orientation distributions along the all axes of the tested slabs: along the X-axis between the side and centre samples, along the Y-axis between the top, middle and bottom parts of the cylinder samples and along the Z-axis between the cuboids and cylinder samples, Fig. 3.1.
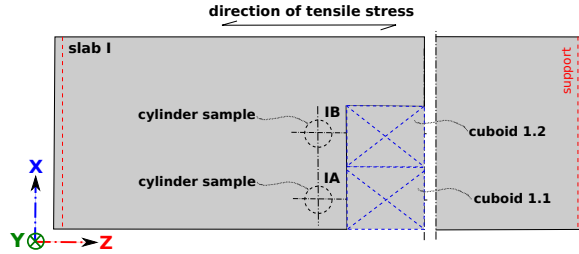
Figure 3.1. The coordinate system in the tested slabs and the location of samples.

These features indicate that a theory capable to consider the spacial—three-dimensional—nature of SFRC material properties is needed. The floor slabs tested were cast applying a casting (site-specific) technology, which can be used in actual construction works. The observed three-dimensional nature of fibre orientations confirms the need to elaborate the manufacturing and the casting processes for SFRC, which will allow to track and control the orientation distribution of fibres.

3.1 Density distribution of the inclination angle θ

The problem with the photometry approach is the ambiguity in the direction of a fibre as the measurement of the in-plane angle ϕ covers only the range

from $[0°, 180°]$. Accordingly, DC-conductivity measurements acting as the improvement of the photometry were performed on the surfaces of the slice nr 11, which belongs to the cuboid 1.1, Fig. 2.10. This choice was done in order to examine the statistics of fibre orientations in the slab with the highest bending capacity, Fig. 2.3.

Fig. 3.2 represents the statistics received by DC-conductivity measurements from the slice 11 (cuboid 1.1). Fig. 3.2(d) actually demonstrates the optimal orientation distribution of fibres since the alignment of fibres almost coincides with the direction of the tensile stress in the slab, Fig. 3.1.

(a) Orientation in scatter plot.

(b) Inclination angle θ.   (c) In-plane angle ϕ.   (d) Scatter plot.
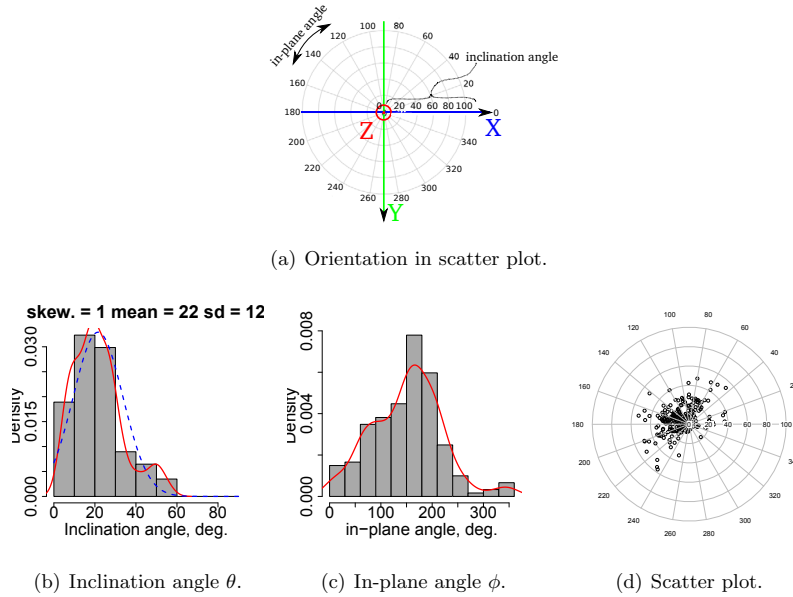
Figure 3.2. Statistics of fibre orientations measured by DC-conductivity testing on slice 11 belonging to the cuboid 1.1. Figs. (b), (c) represent the density distribution–solid line–of the inclination angle θ and in-plane angle ϕ respectively. In Fig. (b) the skewness is compared with the Normal distribution–dashed line. In (a) the radius represents the inclination angle θ and in-plane angle ϕ is on circumference.

The influence of DC-conductivity testing on the results of photometry is presented in Fig. 3.3, where a quite similar behaviour in the density histograms of the inclination angle θ can be noticed. Both analysing approaches gave a positive skewness for the probability density distribution of the θ angle. The density histogram of the in-plane angle ϕ measured by DC-conductivity testing covers the whole range from $[0°, 360°]$, which makes DC-conductivity more preferable to photometry.

(a) Inclination angle θ. (b) In-plane angle $\phi \in (0°, 360°)$.
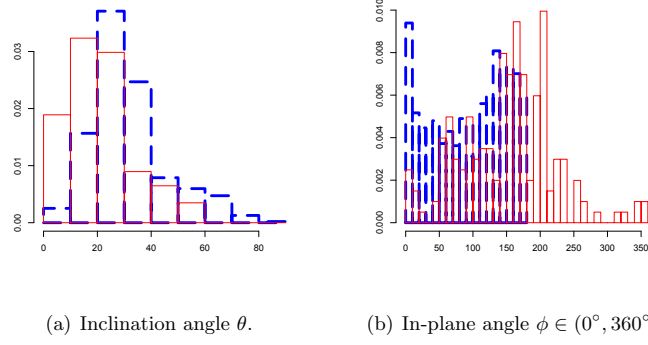
Figure 3.3. The effect of the measuring approaches on the probability density distribution of the inclination angle θ and in-plane angle ϕ. A dashed line represents the results received by photometry (cuboid 1.1) and a solid line the results of DC-conductivity testing (slice 11 from cuboid 1.1).

The photos of slice surfaces were utilised to check the compliance of the density distributions received for the inclination angle θ. Checking was made by the two-sample bootstrap Kolmogorow-Smirnow-test (K-S test, function `ks.boot` from [2]) with a significance level of $\alpha = 5\%$ as threshold. The density distributions for the inclination angle θ are obtained considering every fourth slice surface in a cuboid to account each fibre only once within a given volume. According to the results given in Table 3.1, only the distribution functions of the central cuboids have received higher p-values. In the cuboid 1.2 the p-value received for the inclination angle θ with the null hypothesis of Gumbel distribution was 0.04, which is close but still below the acceptance threshold of 5%.

Table 3.1. Results of the two-sample bootstrap Kolmogorov-Smirnov test (function `ks.boot` from [2]) applied on the density distribution of the inclination angle θ in the slab 1. Reduced cuboid refer to the cuboid, where only every fourth slice surface is taken into account.

	Cuboid 1.1 (side of a slab)				**Cuboid 1.2** (centre of a slab)			
	Inclination angle θ							
	whole cuboid		reduced cuboid		whole cuboid		reduced cuboid	
Distribution	D	p-value	D	p-value	D	p-value	D	p-value
Gaussian	0.114	e-16	0.125	e-16	0.076	e-16	0.078	e-09
Gamma	0.061	e-16	0.066	e-10	0.044	e-10	0.044	0.0033
Gumbel	0.069	e-16	0.065	e-09	0.035	1.7e-06	0.035	**0.0374**
Weibull	0.098	e-16	0.116	e-16	0.075	e-16	0.059	1.9e-05
Log-normal	0.049	e-16	0.058	**1.7e-07**	0.038	2.5e-07	0.040	0.0108

None of the distribution functions of the side cuboids have passed the testing and hence all null hypotheses should be rejected [66].

The most important conclusion of the performed statistical tests is that the

distribution of the inclination angle θ in the central cuboids (in a bulk) does not obey the Gaussian (Normal) distribution, in contrast to the results received earlier [11]. The results of the two-sample bootstrap Kolmogorow-Smirnow-tests in other cuboids are presented in Appendix A.2.

3.2 Variations of fibre orientation distributions along the X- and Y-axes of the slabs

The statistical analysis included the definition of fibre orientation distributions in the side and centre cylinder samples scanned by µCT. In addition, fibre orientation distributions were specified in the top, middle and bottom parts of the cylinder samples. The top and bottom sections were scanned in four cylinders: 1A, 1B, 4A, 4B, but the middle sections were scanned in all cylinder samples. Each section covers about 7 cm of the height of a cylinder, Fig. 2.17(a). The inclination θ and in-plane ϕ angles for each fibre are defined according to Fig. 2.17(b).

Fig. 3.4 demonstrates fibre orientation distributions in the side and centre cylinders and along the height of the whole cylinder samples 1A and 1B. In the bottom section of a cylinder 1A, Fig. 3.4(f), the orientation of fibres is the most optimal since it has the best coincidence with the direction of principal tensile stress of a floor-slab, Fig. 3.1. The fibre orientation distributions are different between the side, Fig. 3.4 (b),(d),(f), and centre, Fig. 3.4 (c),(e),(g), cylinders, and also along the height of the whole cylinder sample, Figs. 3.4(b), 3.4(d), 3.4(f). This indicates the locality of fibre orientation distributions meaning that this phenomenon may exist through the volume of the whole structure. Fig. 3.5 represents probability density histograms of the inclination angle θ and in-plane angle ϕ in the cylinder sample 1A. The outcomes belong to the top, middle and bottom parts of a cylinder. Fig. 3.5(g) demonstrates concentration of fibre alignments on smaller inclination angles. This can be explained by the influence of the formwork whereas the scatter of the inclination angles in Fig. 3.5(a) indicates a free surface.

The statistics of fibre orientation distributions for the other cylinder samples scanned by µCT are presented in Appendix A.3.
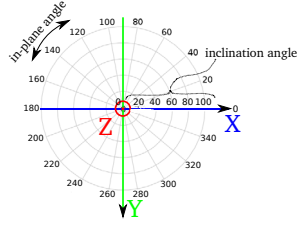
(a) Orientation in scatter plots.
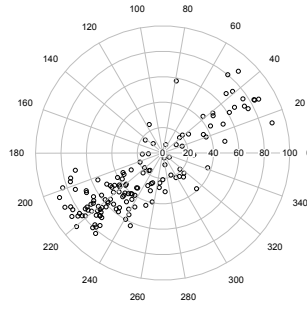
(b) **Top part.** Cylinder 1A.
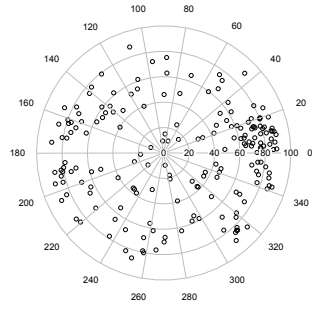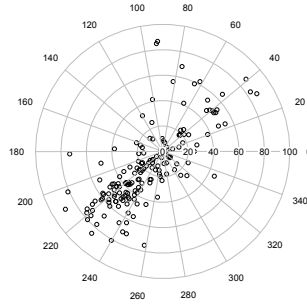
(c) Cylinder 1B.

(d) **Middle part.** Cylinder 1A.
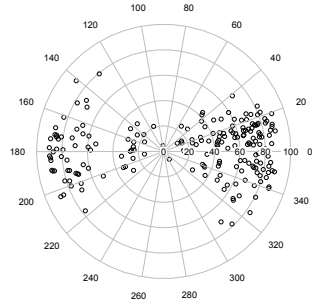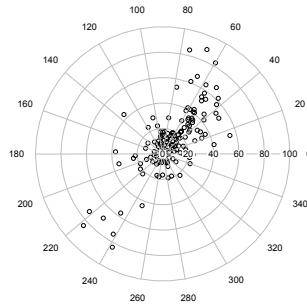
(e) Cylinder 1B.

(f) **Bottom part.** Cylinder 1A.
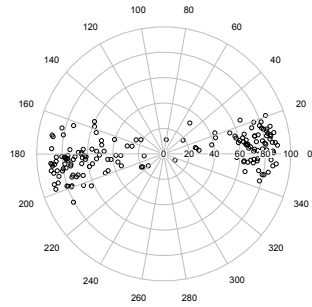
(g) Cylinder 1B.

Figure 3.4. Scatter plots of fibre orientation variations measured by μCT between the side (cylinder 1A) and centre (cylinder 1B), and along the height of the whole cylinder samples. In (a) the radius represents the inclination angle θ and in-plane angle ϕ is on circumference. Z-axis corresponds to the direction of the tensile stress in a slab, Fig. 3.1.

(a) **Top part.** Inclination angle θ.

(b) In-plane angle ϕ.

(c) Bivariate densities.

(d) **Middle part.** Inclination angle θ.

(e) In-plane angle ϕ.

(f) Bivariate densities.

(g) **Bottom part.** Inclination angle θ.

(h) In-plane angle ϕ.

(i) Bivariate densities.
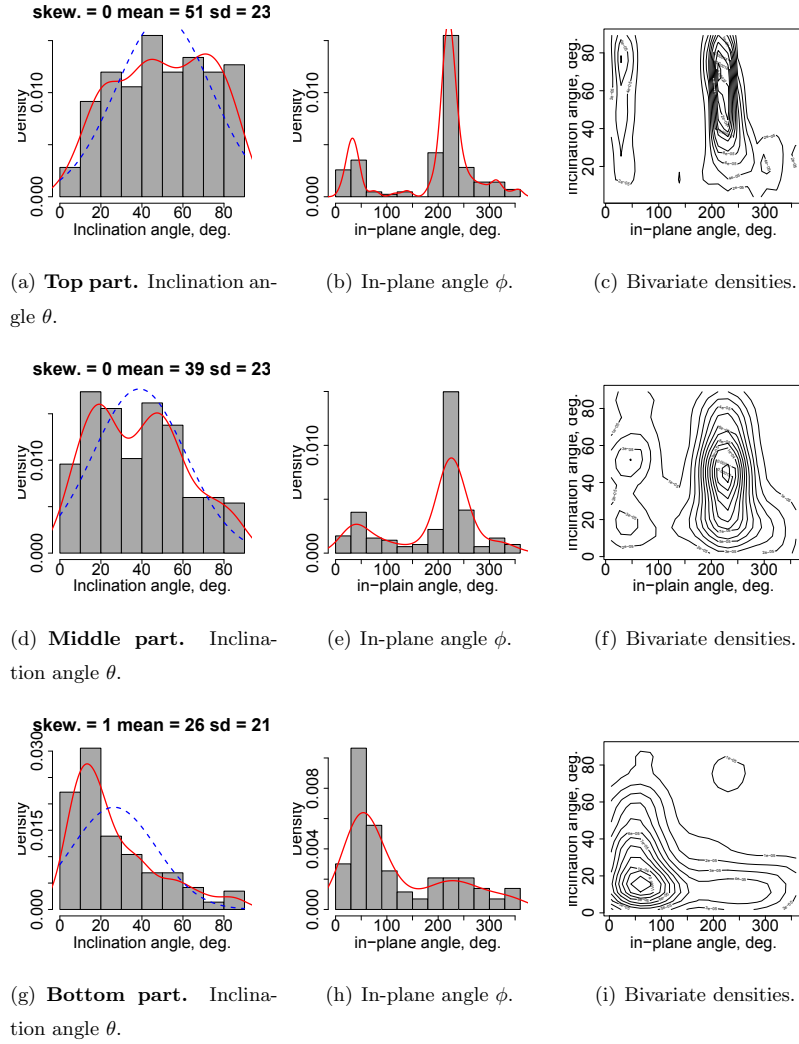
Figure 3.5. Fibre orientation variations measured by µCT along the height of the whole cylinder sample 1A. Figs. (a),(b),(c) represent the statistics for the top; (d),(e),(f) for the middle and (g),(h),(i) for the bottom parts of the cylinder. Figs. (a),(b), (d),(e), (g),(h) represent the density distribution–solid line–of the inclination angle θ and in-plane angle ϕ. In Figs. (a),(d),(g) the skewness is compared with the Normal distribution–dashed blue line. Figs. (c),(f),(i) represent the bivariate densities of the inclination angle θ and in-plane angle ϕ.

3.3 Variations of fibre orientation distributions along the Z-axis of the slabs

Comparison of the outcomes of fibre orientation distributions in the samples taken from the different places along the Z-axis of the slabs, Fig. 3.1 (cuboids and cylinders), revealed the dissimilarity in the density distribution of the in-

clination angle θ, Figs. 3.6, 3.7. In cuboids, measured by slicing with photometry, the density distribution of the inclination angle θ had a positive skewness while in the cylinders, measured by µCT, it was a negative one. Such location dependent variations of fibre orientation distributions point out a strong locality of fibre orientations in the studied structures.

(a) Cuboid 1.1 and Cylinder 1A

(b) Cuboid 1.2 and Cylinder 1B

(c) Cuboid 2.1 and Cylinder 2A

(d) Cuboid 2.2 and Cylinder 2B

(e) Cuboid 3.1 and Cylinder 3A

(f) Cuboid 3.2 and Cylinder 3B
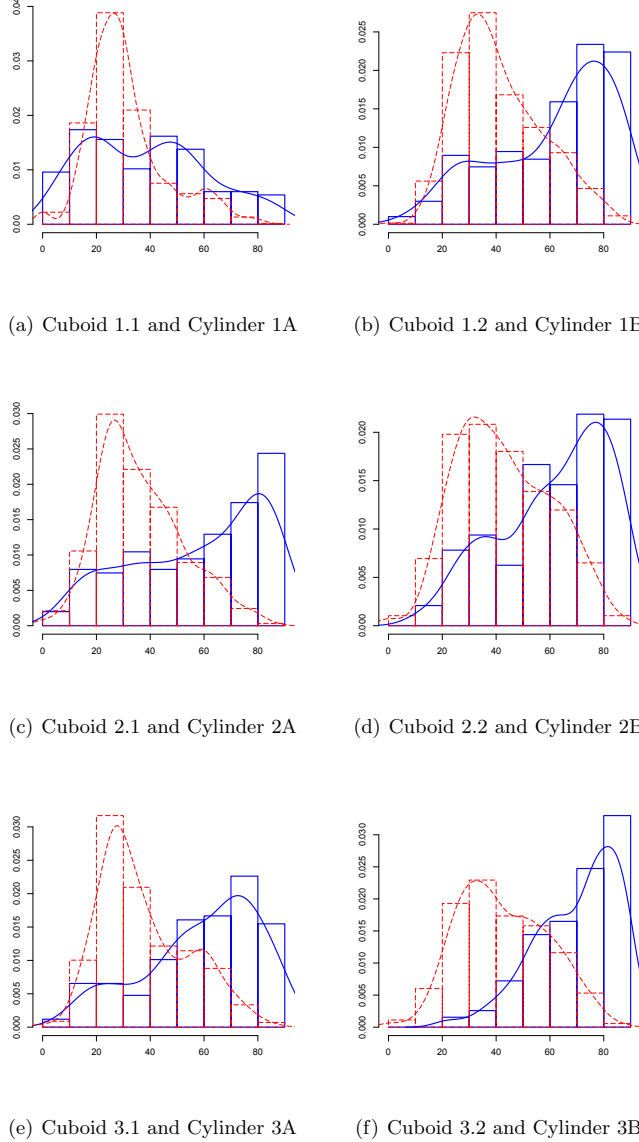
Figure 3.6. Differences in the probability density histograms of the inclination angle θ according to the location along the Z axis of the slabs, Fig. 3.1, in the middle sections of the cuboids 1.1–3.2 and cylinder samples 1A–3B. A dashed line represents the results of cuboids measured by photometry and a solid line the results of cylinder samples measured by µCT.
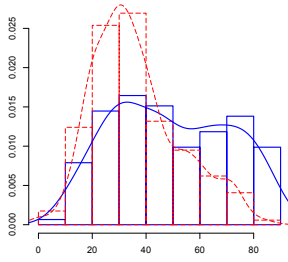
(a) Cuboid 4.1 and Cylinder 4A
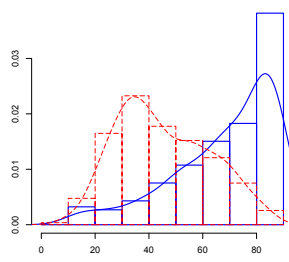
(b) Cuboid 4.2 and Cylinder 4B
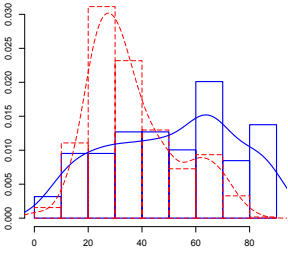
(c) Cuboid 5.1 and Cylinder 5A
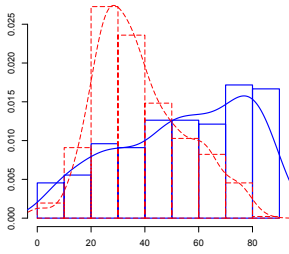
(d) Cuboid 5.2 and Cylinder 5B
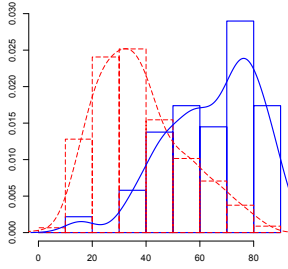
(e) Cuboid 6.1 and Cylinder 6A
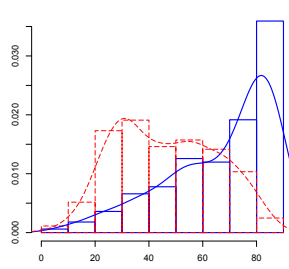
(f) Cuboid 6.2 and Cylinder 6B

Figure 3.7. Differences in the probability density histograms of the inclination angle θ according to the location along the Z axis of the slabs, Fig. 3.1, in the middle sections of the cuboids 4.1–6.2 and cylinder samples 4A–6B. A dashed line represents the results of cuboids measured by photometry and a solid line the results of cylinder samples measured by µCT.

4. Constitutive mappings

4.1 General terms and conditions for material models

The balance equations [67] are formed of basic and constitutive fields. The basic fields such as the mass density, momentum density and energy density are not linked to material properties. The constitutive fields depend on the thermodynamic process and on the material [29]. The constitutive equation establishes the linkage between the stress tensor $\mathbf{S}$ and deformation tensor $\mathbf{E}$. The constitutive equations must hold material objectivity conditions implying two statements [29]:

All corresponding quantities of the domain and of the range of the constitutive mappings are objective meaning that they shall transform under changing of the reference frame by an Euclidean transformation rules (e.g. orthogonal transformation).

The analytical form of a constitutive function must be the same in any frame of reference meaning its invariance from the coordinate system.

The first statement specifies the type of the state space variables to be tensors. The second statement defines the type of functions satisfying coordinate invariance. Such functions are isotropic tensor functions meaning that a tensor function is isotropic if and only if the forms of its component functions are the same for all orthogonal bases [68, 69, 70].

4.2 Behaviour of SFRC

The tensile strength of SFRC depends on the alignment of fibres in the concrete matrix. In a tensioned SFRC member, where all fibres are aligned with

each other, as well as with the principal tensile stress, the fibres have the op-
timal orientation and thus contribute to structural tensile capacity with the
highest efficiency. In an actual situation, the fibres can be oriented not only
in one direction, but an amount of fibres may also be aligned along several
directions or almost randomly. The existence of this phenomenon has been
proven by the measuring of fibre orientations performed in this research, Pub-
lication IV. The measurement results demonstrate that a part of fibres tends
to align along some preferred direction, which may however be different in
the samples taken from the same structural members. In a typical concrete
member, which is reinforced by steel bars in the direction of expected tensile
stresses, the stress behaviour would have an orthotropic character. A similar
situation may be present in a SFRC member and the problem is to identify
and model the directions of fibre alignments. Thus, the constitutive relation
for SFRC is justified to be developed based on an orthotropic material model.
In addition, a linear dependence between stresses and deformations is assumed.
Let us examine a bended concrete member. In general, a compressed concrete
is an elasto-plastic material, where simultaneously both the elastic and plas-
tic deformations are developing. As a consequence, the relation between the
stress and deformation should be non-linear. In a bended concrete, until the
first cracks have appeared in the tension zone of a cross-section the relation
between the stress and deformation can be considered as linear, Fig. 4.1. As
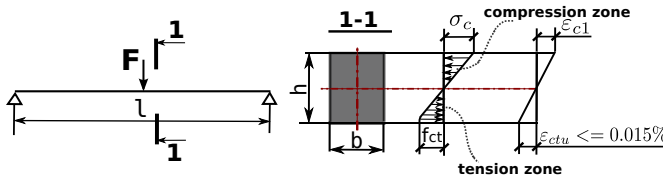
Figure 4.1. A bended concrete member. The stage at the very beginning of the formation
of cracks in the tension zone. f^{ct} denotes the tension strength of concrete,
σ^c is the concrete stress in compression zone, ε^{c1} is the concrete strain in
compression, and ε^{ctu} is the concrete ultimate strain in tension.

soon as cracks are occurring in the tension zone, the deformations start to
grow rapidly and, as a result, the member breaks suddenly in a brittle man-
ner. Drawing a parallel with SFRC it can be stated, that the properties of
this material have a similar brittle character as it was pointed out by the be-
haviour of the full-size floor slabs tested. According to the diagrams of the
bending test, Section 2.3.1 Fig. 2.3, the modes of the load-deformation curves
were linear at the beginning and dropped sharply without any occurrence of
plateaus (plasticity) in three out of six slabs. Essentially, the brittle failure of
SFRC is a consequence from a relative low volume percentage (concentration)

of fibres, which typically, for example, in an elevated floor-slab is $1\% - 2\%$ per cubic meter of concrete. Increasing the concentration of fibres is economically not reasonable since the volume percentage of common reinforcement in the elevated floor-slab is usually between $1.25\% - 1.5\%$. Besides, the high concentration of fibres will induce the clumping (clustering) of fibres, which will cause difficulties in the manufacturing of SFRC. The only difference between the behaviour of a bended concrete and SFRC member can be the appearance of the first cracks at a higher load in SFRC. In this regard, the preferred physically linear-elastic range is an appropriate way to approximate the behaviour of SFRC as also in load-bearing structures based on SFRC the cracking caused by loading should not be allowed.

4.3 Orthotropic elasticity of one meso-volume element of SFRC

The effective elasticity of one meso-volume element of SFRC, Fig. 4.2, can involve two basic terms: concrete matrix and short steel fibres.
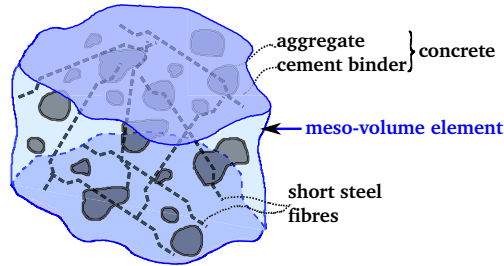
Figure 4.2. One meso-volume element of SFRC.

The fibres are assumed to contribute orthotropicly and the concrete matrix is an isotropic part, such as:

$$^{<4>}\mathbf{C}^{(c)} \quad = \quad \underbrace{\cdots\cdots}_{\text{isotropic concrete matrix}} \quad + \quad \underbrace{\cdots\cdots}_{\text{orthotropic influence of fibres}} \quad , \qquad (4.1)$$

where $^{<4>}\mathbf{C}^{(c)}$ is the orthotropic meso-elasticity of the composite. The choice of a meso-scale for a characteristic volume (representative volume element, RVE) of SFRC is related to measured fibre orientations in the tested floor slabs, Section 3. The measurements revealed that the orientation of fibres has a local character and can vary in three-dimensions.

In the following, the energy approach is used for the constitutive mappings. The reasoning is based on assuming a hyperelastic material. The strain-energy density function W of the hyperelastic material depends on a deformation gra-

dient $\mathbf{F}$ and is a potential function for the stress tensor [68],

$$\mathbf{S}(\mathbf{F}) = \frac{\partial}{\partial \mathbf{F}} W(\mathbf{F}) \ , \quad {}^{<4>}\mathbf{C}(\mathbf{F}) \quad = \quad \frac{\partial \mathbf{S}}{\partial \mathbf{F}} = \frac{\partial^2}{\partial \mathbf{F} \partial \mathbf{F}} W(\mathbf{F}) \ , \qquad (4.2)$$

where ${}^{<4>}\mathbf{C}$ is the Lagrangian elastic modulus or 4th order elasticity tensor.

4.3.1 Modelling of isotropic concrete matrix and orthotropic influence of short steel fibres

The independence of the material from the reference frame means that its strain-energy density is invariant upon orthogonal transformations. This implies that a strain-energy density function of a hyperelastic material can be expressed as a function of the *Lagrangian* strain tensor $\mathbf{E}$ [68], such as

$$W(\mathbf{F}) = W_E(\mathbf{E}) \ . \qquad (4.3)$$

The anisotropic properties of materials are characterised by their symmetry group [69]. The anisotropic influence of short steel fibres may be described by the orthotropic material model, which is symmetric with respect to three mutually orthogonal planes meaning that the material properties remain unchanged by the reflections from these planes. The normal of a plane is called the principal material direction (material symmetry axis). Generally, an orthotropic material has three orthogonal planes and three principal material directions, $\{\mathbf{m}^i\}_{i=1,2,3}$, Fig. 4.3. Choosing a unit vector $\mathbf{l}^1$ directed in one of
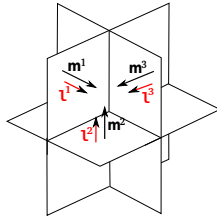
Figure 4.3. Orthotropic material with three principal materal directions $\mathbf{m}^1, \mathbf{m}^2, \mathbf{m}^3$ called as material symmetry axes. $\mathbf{l}^1, \mathbf{l}^2, \mathbf{l}^3$ are the unit vectors along the symmetry axes.

the principal material directions, the following term can be defined [69]:

$$\mathbf{Q}\mathbf{l}^1 \quad = \quad \pm \mathbf{l}^1 \ , \quad \forall \mathbf{Q} \in \mathbf{Orth}^3 \ . \qquad (4.4)$$

Implementing an outer product of the unit vector $\mathbf{l}^1$ with itself, leads to a structural tensor $\mathbf{L}^1$:

$$\mathbf{L}^1 = \mathbf{l}^1 \otimes \mathbf{l}^1 \ , \quad \mathbf{Q}\mathbf{L}^1\mathbf{Q}^T = \mathbf{L}^1 \ , \quad \forall \mathbf{Q} \in \mathbf{Orth}^3 \ . \qquad (4.5)$$

The tensor $\mathbf{L}^1$ is called the structural tensor since it lays down the material or structural symmetry [69]. Thereafter, the structural tensors $\mathbf{L}^2$ and $\mathbf{L}^3$

directed in two other principal material directions $\mathbf{l}^2$ and $\mathbf{l}^3$ may be composed in the same way as in Eq. (4.5). The structural tensors have the following features [69]:

$$\mathbf{L}^i : \mathbf{L}^j = (\mathbf{l}^i \otimes \mathbf{l}^i) : (\mathbf{l}^j \otimes \mathbf{l}^j) = 0 , \quad i \neq j , \tag{4.6}$$

$$(\mathbf{L}^i)^2 = \mathbf{L}^i , \quad \sum_i^3 (\mathbf{L}^i) = \mathbf{I} , \quad \mathrm{tr}(\mathbf{L}^i) = 1 .$$

The strain-energy density function for orthotropic material symmetry with three principal material directions can be defined as:

$$W_{E,\mathrm{ortho}}(\mathbf{Q}\mathbf{E}\mathbf{Q}^T, \mathbf{Q}\mathbf{L}^i\mathbf{Q}^T) = W_{E,\mathrm{ortho}}(\mathbf{E}, \mathbf{L}^i) , \quad \forall \mathbf{Q} \in \mathbf{Orth}^3 , \tag{4.7}$$

$$\mathbf{L}^i = \mathbf{l}^i \otimes \mathbf{l}^i , \quad i = 1, 2, 3 ,$$

where $\mathbf{Orth}^3$ is the symmetry group, which includes all orthogonal transformations in three-dimensional space. In the case of isotropic material the distinctly directed structural tensors $\mathbf{L}^i$ are simplified to arbitrarily chosen ones resulting in direction independent deformation and, consequently, the condition for material symmetry of isotropic material takes the following form:

$$W_{E,\mathrm{iso}}(\mathbf{Q}\mathbf{E}\mathbf{Q}^T) = W_{E,\mathrm{iso}}(\mathbf{E}) , \quad \forall \mathbf{Q} \in \mathbf{Orth}^3 . \tag{4.8}$$

From Eq. (4.7) follows that the isotropy is a special case of orthotropy. Hence, the concrete matrix is considered to be isotropic.

The condition Eq. (4.7) is satisfied if the strain-energy density function is represented as an isotropic tensor function. The isotropic tensor function can be represented as a function of its principal traces $\{\mathrm{tr}(\mathbf{E}^n)\}_{n=1,2,3}$, as the latter ones are uniquely defined by the eigenvalues of the characteristic polynomial [69]. Accordingly, the system of principal traces (or eigenvalues) forms the irreducible basis, the elements of which are independent, i.e. they cannot be expressed in a unique form in terms of the others. Taking into account the properties of the structural tensors Eq. (4.6), the strain-energy density function for orthotropic material symmetry can be represented by the isotropic tensor function of the arguments among which are the structural tensors:

$$W_{E,\mathrm{ortho}}(\mathbf{E}, \mathbf{L}^i) = \hat{W}_{E,\mathrm{ortho}}\Bigg(\underbrace{\mathrm{tr}(\mathbf{E}), \mathrm{tr}(\mathbf{E}^2), \mathrm{tr}(\mathbf{E}^3)}_{\text{for isotropy}}, \underbrace{\mathrm{tr}(\mathbf{L}^i), \mathrm{tr}((\mathbf{L}^i)^2), \mathrm{tr}((\mathbf{L}^i)^3)}_{\mathrm{tr}(\mathbf{L}^i)=1},$$

$$\underbrace{\mathrm{tr}(\mathbf{E}\mathbf{L}^i), \mathrm{tr}(\mathbf{E}^2\mathbf{L}^i)}_{\mathrm{tr}(\mathbf{E}), \mathrm{tr}(\mathbf{E}^2) \text{ if isotropic}}, \underbrace{\mathrm{tr}(\mathbf{E}(\mathbf{L}^i)^2)}_{\mathrm{tr}(\mathbf{E}\mathbf{L}^i)}, \underbrace{\mathrm{tr}(\mathbf{E}^2(\mathbf{L}^i)^2)}_{\mathrm{tr}(\mathbf{E}^2\mathbf{L}^i)} \Bigg)$$

$$= \hat{W}_{E,\mathrm{ortho}}\Bigg(\mathrm{tr}(\mathbf{E}\mathbf{L}^i), \mathrm{tr}(\mathbf{E}^2\mathbf{L}^i), \mathrm{tr}(\mathbf{E}^3) \Bigg) . \tag{4.9}$$

Ten irreducible invariants in Eq. (4.9) are explained by the symmetry of the tensor-arguments, which reduces the number of permutations. The representation of an isotropic tensor function by the system of irreducible invariants, which depend on the amount and properties of tensor-arguments can be found in [71, 72]. Eq. (4.9) explicitly demonstrates that the traces $\mathrm{tr}(\mathbf{E}\mathbf{L}^i)$, $\mathrm{tr}(\mathbf{E}^2\mathbf{L}^i)$ can be utilised for the isotropic case since if $\mathbf{L}^i$ are arbitrarily chosen, then $\mathrm{tr}(\mathbf{E}\mathbf{L}^i) = \mathrm{tr}(\mathbf{E})$, $\mathrm{tr}(\mathbf{E}^2\mathbf{L}^i) = \mathrm{tr}(\mathbf{E}^2)$. The 1st order term in Eq. (4.9) vanishes in order to satisfy the deformation and stress-free natural state. The trace $\mathrm{tr}(\mathbf{E}^3)$ represents the non-linear isotropic matrix. Thereby, dropping the 1st order as well as 3rd order terms and considering that the 2nd order term $\mathrm{tr}(\mathbf{E}^2\mathbf{L}^i)$ can be equivalently presented as [70]:

$$\mathrm{tr}(\mathbf{E}^2\mathbf{L}^i) = \mathrm{tr}(\mathbf{E}\mathbf{L}^i\mathbf{E}\mathbf{L}^j), \quad i > j \ , \tag{4.10}$$

the strain-energy density function for the orthotropic elastic material with three symmetry axes can be specified by the combination of mixed traces of Eq. (4.9), such as:

$$\hat{W}^{(2)}_{E,\mathrm{ortho}}(\mathbf{E}, \mathbf{L}^i) = \frac{1}{2}\sum_{i,j=1}^{3}\gamma^{ij}\,\mathrm{tr}(\mathbf{E}\mathbf{L}^i)\,\mathrm{tr}(\mathbf{E}\mathbf{L}^j) + \sum_{i,j\neq i}^{3}G^{ij}\,\mathrm{tr}(\mathbf{E}\mathbf{L}^i\mathbf{E}\mathbf{L}^j) \ . \tag{4.11}$$

The latter model is known as the orthotropic St. Venant-Kirchhoff material [70]. The constants γ^{ij}, G^{ij} in Eq. (4.11) are the Lamé constants, which are given in terms of Young's modulus Y and Poisson's ratio ν, but here they are direction dependent, i.e. they refer to the material symmetry axes and planes, respectively. The values of γ^{ij}, G^{ij} define if the material is orthotropic or transversely isotropic. For isotropic case the elastic constants will be equal for all directions, i.e. $\gamma^{ij} = \gamma$, $G^{ij} = G$. The differentiation of the strain-energy function Eq. (4.11) with respect to $\mathbf{E}$ leads to the orthotropic 2nd Piola-Kirchhoff stress tensor $\mathbf{S}_{E,\mathrm{ortho}}$ [68]:

$$\mathbf{S}_{E,\mathrm{ortho}} = \frac{\partial}{\partial \mathbf{E}}\hat{W}^{(2)}_{E,\mathrm{ortho}}(\mathbf{E}, \mathbf{L}^i) = \sum_{i,j=1}^{3}\gamma^{ij}\,\mathrm{tr}(\mathbf{E}\mathbf{L}^j)\mathbf{L}^i + 2\sum_{i,j\neq i}^{3}G^{ij}\mathbf{L}^i\mathbf{E}\mathbf{L}^j \ , \tag{4.12}$$

which is linear with respect to $\mathbf{E}$. For isotropic material Eq. (4.12) is as follows:

$$\mathbf{S}_{E,\mathrm{iso}} = \frac{\partial}{\partial \mathbf{E}}\hat{W}^{(2)}_{E,\mathrm{iso}}(\mathbf{E}) = \gamma\mathbf{I}\,\mathrm{tr}(\mathbf{E}) + 2G\mathbf{E} \ , \tag{4.13}$$

which is common form of Hooke's law.

Hereinafter, in Eqs. (4.11-4.13) the linearised hyperelasticity $\mathbf{E} \approx \boldsymbol{\varepsilon}$ implying the insignificant difference between the spatial and material coordinates of a material point in space, is utilised. Thus, the 2nd Piola-Kirchhoff stress tensor $\mathbf{S}$, usually used for finite deformations, is employed for the case of linear elasticity. The advantage of the 2nd Piola-Kirchhoff stress tensor is its symmetry

and the differentiation gives the *second* elasticity tensor (4th order elasticity tensor), which has minor and major symmetries. Essentially, by assuming $\frac{\partial}{\partial x} \approx \frac{\partial}{\partial X}$ the different stress measures shall give the same result.

The material symmetry axes of one meso-volume element of SFRC and, consequently, the direction dependent elasticity constants γ^{ij}, G^{ij} are identified utilising the orientation state of fibres, which is quantified by the orientation tensors and the orientation distribution function [29, 31].

In theory, the orientation distribution function (ODF) $f(\mathbf{n})$, where $\mathbf{n}(\theta, \phi)$ is a unit vector associated with the orientation of a rod-like particle (fibre) in space as e.g. in Fig. 4.4, is defined as the probability of finding a fibre between the angles θ_1 and $\theta_1 + \mathrm{d}\theta$ and ϕ_1 and $\phi_1 + \mathrm{d}\phi$, such as:

$$P(\theta_1 \le \theta \le \theta_1 + \mathrm{d}\theta, \phi_1 \le \phi \le \phi_1 + \mathrm{d}\phi) = f(\theta_1, \phi_1) \sin \theta_1 \mathrm{d}\theta \mathrm{d}\phi . \quad (4.14)$$

All possible directions of a fibre comply with a unit sphere S^2 (radius $r = 1$).
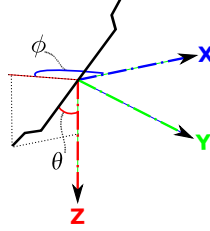
Figure 4.4. The orientation of a fibre (rod-like particle) in space. θ is the inclination angle, $\theta \in (0°, 180°)$, ϕ is the in-plane angle, $\phi \in (0°, 360°)$. In μCT scanning the ranges of definitions $\theta \in (0°, 90°)$ and $\phi \in (0°, 360°)$ are used.

The l-order symmetric orientation tensor $O_{\mu_1 \dots \mu_l}$ can be composed by l-order outer products of a unit vector $\mathbf{n}$ with itself and then integrating the result with the ODF, $f(\mathbf{n})$, over all possible directions:

$$O_{\mu_1 \dots \mu_l} = \oint_{S^2} f(\mathbf{n}) n_{\mu_1} \otimes \dots \otimes n_{\mu_l} \mathrm{d}^2 n . \quad (4.15)$$

The l-order orientation tensor contains the information about the lower order tensors. For example, the 4th order orientation tensor includes the information of the 2nd order orientation tensor. The symmetric traceless or irreducible part of the l-order orientation tensor, in the mesoscopic continuum theory called the l-order alignment tensor (AT) $A_{\mu_1 \dots \mu_l}$ [29], does not contain the information about the lower order tensors. The ATs are able to account for the anisotropy of the system, for example, the 2nd order alignment tensor represents the deviation of the orientation tensor from isotropy. Hence, in

the case of the isotropic distribution the ATs just vanish. In the mesoscopic continuum theory the l-order AT is defined as follows:

$$A_{\mu_1 \ldots \mu_l} \;=\; \oint_{S^2} f(\mathbf{n}) \; \overline{n_{\mu_1} \otimes \ldots \otimes n_{\mu_l}} \; \mathrm{d}^2 n \;, \qquad (4.16)$$

where $\overline{n_{\mu_1} \otimes \ldots \otimes n_{\mu_l}}$ is the l-order symmetric tensorial product of a vector $\mathbf{n}$ (in Cartesian coordinates) from which the trace is removed and which gives an l-order symmetric irreducible tensor. The symmetric irreducible tensors are spherical harmonics [30], which belong to square-integrable functions L^2 and form, in case of a unit sphere, a complete orthonormal basis on L^2, Appendix A.1. Any square-integrable function on a unit sphere can be expanded into the series of $(2l+1)$ main spherical harmonics. The ODF $f(\mathbf{n})$ is quadratically integrable function and it is defined on a unit sphere, and thus it may be decomposed into the series of symmetric irreducible tensors $\overline{n_{\mu_1} \otimes \ldots \otimes n_{\mu_l}}$ forming a complete orthonormal basis, and the ATs are acting as the expansion coefficients:

$$f(\mathbf{n}) \;=\; \underbrace{\frac{1}{4\pi} \cdot f_0}_{\hat{f}(\mathbf{n})} + \frac{1}{4\pi} \sum_{l=1}^{\mathbb{N}} \frac{(2l+1)!!}{l!} A_{\mu_1 \ldots \mu_l} \; \overline{n_{\mu_1} \otimes \ldots \otimes n_{\mu_l}} \;, \quad (4.17)$$

$$f_0 \;=\; \oint_{S^2} f(\mathbf{n}) \; \mathrm{d}^2 n = 1 \;,$$

where $l!$ is the factorial $l! = l \cdot (l-1) \cdots 2 \cdot 1$ and $(2l+1)!! = (2l+1) \cdot (2l-1) \cdots 3 \cdot 1$ denotes the "factorial with double steps" [29, 30, 73]. The first term in Eq. (4.17) represents the zero harmonic, which is a constant equal to the mean integral value $\hat{f}(\mathbf{n})$ (can be interpreted as a mathematical expectation) of the original function $f(\mathbf{n})$ on a sphere. All other harmonics starting from $l = 1$ approximate the deviation $(f(\mathbf{n}) - \hat{f}(\mathbf{n}))$ of the original function $f(\mathbf{n})$ from its mean value (can be interpreted as variance). If the expansion coefficients in a complete orthonormal basis are known then the original function may also be considered as known since the sum of the squares of all expansion coefficients equals to the mean square of the function given on a sphere [37], Appendix A.1. This can be used to approximate the ODF from the experimental data, e.g. measuring of fibre orientations using X-ray micro-tomography scanning (µCT). The ODF satisfies the following conditions:

ODF is even, i.e. $f(\mathbf{n}) = f(-\mathbf{n})$,

ODF is normalised, i.e. $\int_{\theta=0}^{\pi} \int_{\phi=0}^{2\pi} f(\theta, \phi) \sin \theta \mathrm{d}\theta \mathrm{d}\phi = \oint_{S^2} f(\mathbf{n}) \mathrm{d}^2 \mathbf{n} = 1$.

Accordingly, as the ODF is even in $\mathbf{n}$, the odd-order alignment tensors (as well as the orientation tensors) in Eq. (4.17) vanish.

The eigenvalues λ^i ($|\lambda^1| \geq |\lambda^2| \geq |\lambda^3|$) of the 2nd order alignment tensor can be used to introduce a scalar order-parameter S needed to evaluate how well the rod-like particles are aligned with each other [74, 75]. The parameters can be determined by firstly defining the order parameter tensor as $\mathbf{P} = \frac{3}{2}\mathbf{A}$ (the reason for the $\frac{3}{2}$ becomes clear later) with S being its according-to-amount largest eigenvalue:

$$S = \mathbf{d}^1 \cdot \underbrace{\mathbf{P}}_{:=\frac{3}{2}\mathbf{A}} \cdot \mathbf{d}^1 \ , \quad \mathbf{d}^1 \cdot \mathbf{d}^1 = 1 \ . \tag{4.18}$$

Inserting the definition of the alignment tensor Eq. (4.16) combined with the exchange of scalar products and integration leads to

$$S = \oint_{S^2} \left(\frac{1}{2}(3(\mathbf{d}^1 \cdot \mathbf{n})^2 - 1) \right) f(\mathbf{n}) \mathrm{d}^2\mathbf{n} = \left\langle \frac{1}{2}(3(\mathbf{d}^1 \cdot \mathbf{n})^2 - 1) \right\rangle \ , \tag{4.19}$$

which is the average of the second Legendre polynomial $P_2(\mathbf{d}^1 \cdot \mathbf{n})$ and can be further rewritten by introducing $\mathbf{d}^1 \cdot \mathbf{n} =: x$ or $\alpha = \sphericalangle(\mathbf{n}, \mathbf{d}^1)$ into

$$S = \left\langle P_2(\mathbf{d}^1 \cdot \mathbf{n}) \right\rangle \tag{4.20}$$

$$= \left\langle P_2(x) \right\rangle \tag{4.21}$$

$$= \left\langle P_2(\cos\alpha) \right\rangle \ , \tag{4.22}$$

where the meaning of $\alpha = \sphericalangle(\mathbf{n}, \mathbf{d}^1)$ or $\mathbf{d}^1 \cdot \mathbf{n}$ is presented in Fig. 4.5. The values
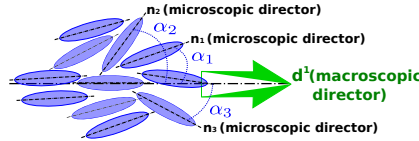
Figure 4.5. A macroscopic director $\mathbf{d}^1$, i.e. the direction of average orientation of particles, corresponds to the eigenvector of the eigenvalue λ^1

of the scalar order-parameter are assumed in the range $S \in [-\frac{1}{2}, 1]$, where the following values correspond to special configurations: $S = 1$ corresponds to the transversely isotropic material symmetry with well aligned fibres, $S = 0$ to the isotropy and $S = -\frac{1}{2}$ describes the plane transversely isotropic case. Here one can see, that the choice of the factor $\frac{3}{2}$ leads directly to the correct coefficients in the Legendre polynomial and to have $S = 0$ for isotropy (no order) [76].

In addition, a biaxiality parameter, which measures the non-symmetry of the distribution with respect to $\mathbf{d}^1$, Fig. 4.6, can be introduced in the following way (compare Eq. (4.18)):

$$\frac{2}{3}S \;=\; \lambda^1 \qquad\qquad (4.23)$$

$$-\frac{1}{3}S - b_S \;=\; \lambda^2 \qquad\qquad (4.24)$$

$$-\frac{1}{3}S + b_S \;=\; \lambda^3 \;, \qquad\qquad (4.25)$$

where $b_S = \frac{1}{2}(\lambda^3 - \lambda^2) = \text{sign}(S)b$ and the biaxiality $b \in \left[0, \frac{1}{3}|S|\right]$ [74, 75, 77]. The limits follow from the ordering of the eigenvalues, and $b_S = 0$ means, that the distribution is rotation symmetric around $\mathbf{d}^1$. As the tensor is traceless, the sum of the eigenvalues λ^i vanishes, and so the sum of the left-hand sides of Eqs. (4.23), (4.24), (4.25) needs to vanish.
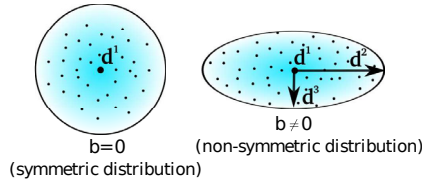
Figure 4.6. Biaxiality. $\mathbf{d}^1, \mathbf{d}^2, \mathbf{d}^3$ are the eigenvectors of the 2nd order alignment tensor.

The 2nd order alignment tensor is used to define the material symmetry axes of one meso-volume element of SFRC. The unit vectors $\mathbf{l}^i$ (Fig. 4.3, Eq. (4.7)) pointing to the principal material directions are chosen to be the normalised eigenvectors $\mathbf{d}^1, \mathbf{d}^2, \mathbf{d}^3$ of the 2nd order alignment tensor. The orientation distribution function $f(\mathbf{n})$ is utilised to estimate the contributions of fibres in the directions of the eigenvectors thus defining the direction dependent meso-elasticity constants of the composite, i.e. γ^{ij}, G^{ij}.

4.3.2   State space for SFRC

As the constitutive equations are different for different materials, the introduction of the concept of the state space is necessary. The variables to be included to the state space depend on the physical problem and on the material [29]. The mechanical properties of the studied composite depend on the orientation of short steel fibres and thus the state space for SFRC shall include the variables associated with the orientation distribution of fibres in a volume element. As it was stated in the previous section, the normalized eigenvectors $\mathbf{d}^i$ of the 2nd order alignment tensor $\mathbf{A}$ are utilised to assign the material meso-symmetry. The orientation distribution function $f(\mathbf{n})$ is weighting the amount of fibres together with their elastic properties in the direction of the considered material meso-symmetry axis.

Hence, a possible state space for one meso-volume element of SFRC:

$$Z : = \left(Y^{(m)}, Y^{(f)}, \nu^{(m)}, V^{(m)}, V^{(f)}, \boldsymbol{\varepsilon}^{(c)}, \mathbf{d}^i(\mathbf{A}), f(\mathbf{n}) \right) , \qquad (4.26)$$
$$\text{with} \quad V^{(m)} = 1 - V^{(f)} ,$$

where $Y^{(m)}$, $Y^{(f)}$ are the Young's modulus of the concrete and steel fibres respectively, $\nu^{(m)}$ is the Poisson's ratio of the concrete, $V^{(m)}$, $V^{(f)}$ are the volume fractions of the concrete and fibres, $\boldsymbol{\varepsilon}^{(c)}$ is the average infinitesimal strain of the composite as long as the bond acts between the steel fibres and the concrete. The average strain is an equivalent strain, which includes the strains of both concrete and steel fibres since a complete bond is assumed between concrete and steel. This is usually justified by some identical physical and mechanical properties of concrete and steel, such as:

– while hardening the concrete adheres to the steel, and thus in a structure the relative deformations of both materials are equal;

– thermal expansion coefficients of concrete and steel are approximately the same, and thus the changes in the ambient temperature do not cause internal stresses in SRFC structures.

4.3.3 Orientation-weighted meso-elasticity of fibres in material meso-symmetry axes

Essentially, the system of eigenvectors, $\mathbf{d}^1, \mathbf{d}^2, \mathbf{d}^3$ forms the new orthonormal coordinate system—material meso-symmetry coordinates, which define the meso-scale of the composite, Fig. 4.7.
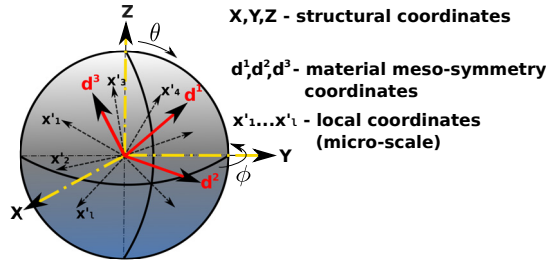
Figure 4.7. The position of the unit vectors—fibres—$x'_1 \ldots x'_l$ relative to structural X, Y, Z and material meso-symmetry $\mathbf{d}^1, \mathbf{d}^2, \mathbf{d}^3$ coordinates.

In order to estimate the contribution of fibres to the directions of the meso-symmetry axes, it is necessary to transform the fibres from their local or micro-scale coordinates into the coordinates characterised by the structural reference frame, Fig. 4.8. Since only the tensile strength of the composite is under consideration, the stretching ability of an individual fibre can be characterised solely by its Young's modulus along its longitudinal axis. Elasticity of a fibre
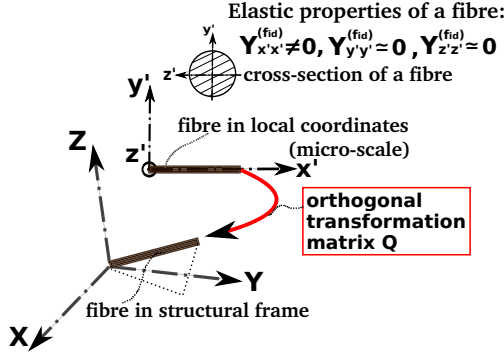
Figure 4.8. Transformation of a fibre from local to structural coordinates. $Y_{x'x'}^{(f_{id})}$ is the Young's modulus of a fibre along the longest axis in local coordinates. $Y^{(m)}$ is the Young's modulus of the matrix.

in its radial direction is assumed to be insignificant, Fig. 4.8. Applying the orthogonal transformation matrices $\mathbf{Q(n)}$, describing a rotation of the coordinate system, to the fourth-order-elasticity-tensor of a single fibre with one non-zero elasticity modulus $^{<4>}\mathbf{C}^{(f_{id})}$, and weighting with the given orientation distribution function $f(\mathbf{n})$, the orientation-weighted orthotropic meso-elasticity of fibres in the structural reference frame is obtained. The following step is to perform one more orthogonal transformation to get the orientation-weighted orthotropic meso-elasticity of fibres in material meso-symmetry coordinates determined by the eigenvectors of the 2nd order alignment tensor, Fig. 4.7. In the mathematical formulation the described steps can be written as follows:

$$C_{ijkl}^{(f_{str})} \quad = \quad \oint_{S^2} Q_{im}(\mathbf{n})Q_{jn}(\mathbf{n})Q_{ko}(\mathbf{n})Q_{lp}(\mathbf{n})C_{mnop}^{(f_{id})}f(\mathbf{n})\mathrm{d}^2\mathbf{n} \ , \quad (4.27)$$

where $C_{ijkl}^{(f_{str})}$ is the orientation-weighted orthotropic meso-elasticity tensor of fibres in structural coordinates, $Q_{im}(\mathbf{n})$ is the transformation matrix per one index of the 4th order elasticity tensor of an individual fibre $C_{mnop}^{(f_{id})}$, and $f(\mathbf{n})$ is the considered orientation distribution function. The transformation matrices in Eq. (4.27) are identical and composed as a dot product (scalar multiplication) of two rotation matrices $\mathbf{R}^z(\phi)$, $\mathbf{R}^y(\theta)$, Fig. 4.9 and Eq. (4.28).
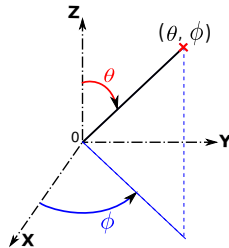
Figure 4.9. Definition of the inclination angle θ and in-plane angle ϕ.

$$\mathbf{Q(n)} \;=\; \mathbf{R}^z(\phi) \cdot \mathbf{R}^y(\theta) \;, \quad \text{where} \;\; \theta \in [0, \pi], \;\; \phi \in [0, 2\pi] \qquad (4.28)$$

$$R^z_{ij}(\phi) \;=\; \begin{pmatrix} \cos\phi & -\sin\phi & 0 \\ \sin\phi & \cos\phi & 0 \\ 0 & 0 & 1 \end{pmatrix}, \; R^y_{ij}(\theta) = \begin{pmatrix} \cos\theta & 0 & -\sin\theta \\ 0 & 1 & 0 \\ \sin\theta & 0 & \cos\theta \end{pmatrix}$$

The further transformation of $C^{(f_{str})}_{ijkl}$, which reads as:

$$C^{(f_{ms})}_{mnop} \;=\; \hat{Q}_{mi}\hat{Q}_{nj}\hat{Q}_{ok}\hat{Q}_{pl}C^{(f_{str})}_{ijkl} \;\;, \qquad (4.29)$$

gives the orientation-weighted orthotropic meso-elasticity tensor of fibres in material meso-symmetry coordinates. The transformations in Eq. (4.29) diagonalize the tensor $C^{(f_{str})}_{ijkl}$ since the transformation matrices are composed of the eigenvectors of the 2nd order alignment tensor, such as:

$$\hat{Q}_{mi} \;=\; \begin{pmatrix} d_{11} & d_{12} & d_{13} \\ d_{21} & d_{22} & d_{23} \\ d_{31} & d_{32} & d_{33} \end{pmatrix} \;, \quad \text{where} \qquad (4.30)$$

$$\mathbf{d}^1 = (d_{11}, d_{21}, d_{31}) \;, \quad \mathbf{d}^2 \;=\; (d_{12}, d_{22}, d_{32}) \;, \quad \mathbf{d}^3 = (d_{13}, d_{23}, d_{33}) \;.$$

An important property of the orientation-weighted orthotropic meso-elasticity of fibres is that it averages out the heterogeneities—orientations of individual fibres—between the three meso-symmetry axes. From Eq. (4.29) one may specify the orientation-weighted orthotropic elasticity constants for fibres γ^{ij} $(i, j = 1, 2, 3)$ and G^{ij} $(i, j = 1, 2, 3; i \neq j)$ referring to the material meso-symmetry directions and planes. The latter constants are utilised in the orthotropic material model for one meso-volume element of SFRC.

$$\gamma^{11} = C^{(f_{ms})}_{1111} \quad , \quad \gamma^{22} = C^{(f_{ms})}_{2222} \quad , \quad \gamma^{33} = C^{(f_{ms})}_{3333}$$

$$\gamma^{23} = C^{(f_{ms})}_{2233} \quad , \quad \gamma^{13} = C^{(f_{ms})}_{1133} \quad , \quad \gamma^{12} = C^{(f_{ms})}_{1122}$$

$$G^{23} = C^{(f_{ms})}_{2323} \quad , \quad G^{13} = C^{(f_{ms})}_{3131} \quad , \quad G^{12} = C^{(f_{ms})}_{1212}$$

$$\gamma^{32} = \gamma^{23} \quad , \quad \gamma^{31} = \gamma^{13} \quad , \quad \gamma^{21} = \gamma^{12}$$

$$(4.31)$$

4.4 Constitutive relation for one meso-volume element of SFRC

A complete bond between the concrete and steel fibres results in the Taylor assumption [78], which assumes no fluctuations (equivalent deformations) within the characteristic volume element of a composite. The chosen linear-elastic

range and a small volume fraction (concentration) of fibres allow to employ the mean-field homogenisation approach to formulate the constitutive relation for SFRC [23, 79, 80]. Essentially, the concrete is a heterogeneous material consisting of cement binder and aggregate of different fractions, Fig. 4.10(a). Although, the elasticity parameters of the hardened concrete, found, for example, in Eurocode 2 [81], are homogenised since they characterise the concrete strength in general. Accordingly, the mean-field homogenisation, which uses the meso-volume element to specify the meso-symmetry axes, Fig. 4.10(b), can be utilised to approximate the structure and behaviour of SFRC on the macro-scale.

(a) Homogenisation of pure concrete.

(b) Homogenised meso-volume element of SFRC specifying the meso-symmetry axes $\mathbf{d}^1, \mathbf{d}^2, \mathbf{d}^3$.
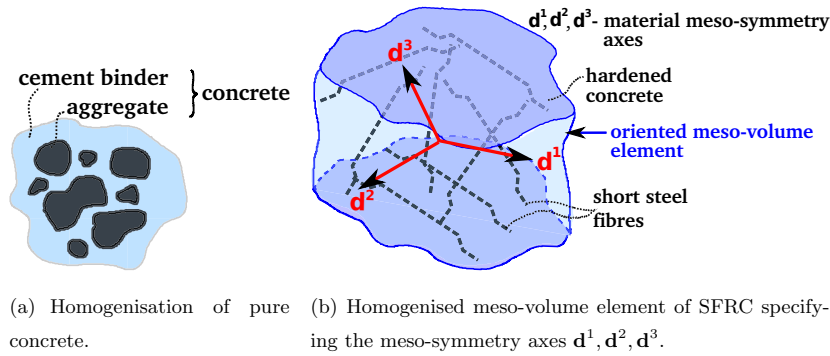
Figure 4.10. The mean-filed homogenisations.

Physically, non-linearity induced by the cracking of SFRC implies the loss of bond between the concrete and steel fibres, which further activates the anchoring of fibres. This also indicates the difference in stresses and strains of the concrete matrix and steel fibres. Such fluctuations within the meso-volume element shall be considered while modelling the fracture mechanism of SFRC. The approaches, which could be helpful for considering these differences are presented in [23, 79, 82, 83]. The proposed linear-elastic material model is valid in the case of microcracks.

The orthotropic linear-elastic material model developed for the description of anisotropic behaviour of one meso-volume element of SFRC is established employing the isotropic and orthotropic St. Venant-Kirchhoff models with three symmetry directions. The strain-energy density function in material symmetry axes for one representative volume element of SFRC can be composed by the superposition of the isotropic concrete matrix and orthotropic influence of short steel fibres (Section 4.3.1) resulting in the homogenisation of the composite on the meso-scale , Fig. 4.10(b), such as:

$$W(\boldsymbol{\varepsilon}^{(c)}) \;\; = \;\; \underbrace{V^{(m)}\left(\frac{1}{2}\gamma(\mathrm{tr}(\boldsymbol{\varepsilon}^{(c)})\,\mathrm{tr}(\boldsymbol{\varepsilon}^{(c)})) + G\,\mathrm{tr}((\boldsymbol{\varepsilon}^{(c)})^2)\right)}_{\text{concrete, isotropic}} + \tag{4.32}$$

$$+ \underbrace{V^{(f)}\left(\frac{1}{2}\sum_{i,j=1}^{3}\gamma^{ij}\,\mathrm{tr}(\boldsymbol{\varepsilon}^{(c)}\mathbf{L}^i)\,\mathrm{tr}(\boldsymbol{\varepsilon}^{(c)}\mathbf{L}^j) + \sum_{i,j\neq i}^{3}G^{ij}\,\mathrm{tr}(\boldsymbol{\varepsilon}^{(c)}\mathbf{L}^i\boldsymbol{\varepsilon}^{(c)}\mathbf{L}^j)\right)}_{\text{fibres, orthotropic}} \;.$$

The differentiation of $W(\boldsymbol{\varepsilon}^{(c)})$ leads to a constitutive relation, which has the following form:

$$\mathbf{S}^{(c)} \;\; = \;\; \frac{\partial}{\partial \boldsymbol{\varepsilon}^{(c)}} W(\boldsymbol{\varepsilon}^{(c)}) \tag{4.33}$$

$$= \;\; \underbrace{V^{(m)}\left(\gamma\mathbf{I}\,\mathrm{tr}(\boldsymbol{\varepsilon}^{(c)}) + 2G\boldsymbol{\varepsilon}^{(c)}\right)}_{\text{concrete, isotropic}} + \underbrace{V^{(f)}\left(\sum_{i,j=1}^{3}\gamma^{ij}\,\mathrm{tr}(\boldsymbol{\varepsilon}^{(c)}\mathbf{L}^j)\mathbf{L}^i + 2\sum_{i,j\neq i}^{3}G^{ij}\mathbf{L}^i\boldsymbol{\varepsilon}^{(c)}\mathbf{L}^j\right)}_{\text{fibres, orthotropic}} \;.$$

$$\tag{4.34}$$

The further differentiation of Eq. (4.34) gives the orientation-weighted orthotropic meso-elasticity of the composite, which reads as:

$$C^{(c)}_{mnkl} \;\; = \;\; \frac{\partial S^{(c)}_{mn}}{\partial \varepsilon^{(c)}_{kl}} \;\; = \;\; \frac{\partial^2}{\partial \varepsilon^{(c)}_{mn}\partial \varepsilon^{(c)}_{kl}} W(\varepsilon^{(c)}_{op}) \;; \tag{4.35}$$

$$^{<4>}\mathbf{C}^{(c)} \;\; = \;\; \underbrace{V^{(m)}\left(\gamma\mathbf{I}\otimes\mathbf{I} + 2G\,^{<4>}\mathbf{I}^S\right)}_{\text{concrete, isotropic}} + \underbrace{V^{(f)}\left(\sum_{i,j}^{3}\gamma^{ij}\mathbf{L}^i\otimes\mathbf{L}^j + \sum_{i,j\neq i}^{3}2G^{ij}(\mathbf{L}^i\,\tilde{\otimes}\,\mathbf{L}^j)^S\right)}_{\text{fibres, orthotropic}} \;.$$

$$\tag{4.36}$$

The term of fibres in Eq. (4.36) can be written in explicit form as follows:

$$\sum_{i,j}^{3}\gamma^{ij}L^i_{mn}\otimes L^j_{kl} + \sum_{i,j\neq i}^{3}2G^{ij}(L^i_{mn}\,\tilde{\otimes}\,L^j_{kl})^S =$$

$$= \left(\gamma^{11}L^1_{mn}L^1_{kl} + \gamma^{22}L^2_{mn}L^2_{kl} + \gamma^{33}L^3_{mn}L^3_{kl} + \gamma^{23}L^2_{mn}L^3_{kl} + \gamma^{13}L^1_{mn}L^3_{kl} + \gamma^{12}L^1_{mn}L^2_{kl} + \right.$$

$$\left. +\gamma^{32}L^3_{mn}L^2_{kl} + \gamma^{31}L^3_{mn}L^1_{kl} + \gamma^{21}L^2_{mn}L^1_{kl}\right) +$$

$$+ \left(G^{23}\frac{1}{2}(L^2_{ml}L^3_{kn} + L^2_{mk}L^3_{ln}) + G^{13}\frac{1}{2}(L^1_{ml}L^3_{kn} + L^1_{mk}L^3_{ln}) + G^{12}\frac{1}{2}(L^1_{ml}L^2_{kn} + L^1_{mk}L^2_{ln})\right)$$

4.5 Example calculations of orientation-weighted 4th order meso-elasticity tensors based on experimental data

In this research the ODF is approximated employing the experimental data (Section 4.3.1). The sum expression of the alignment tensors based on the fibre orientations measured by µCT reads as follows:

$$A_{i_1\ldots i_l} \;\; = \;\; \frac{1}{N}\sum_{k=1}^{N}\overline{v^{(k)}_{i_1}\otimes\ldots\otimes v^{(k)}_{i_l}} \;, \tag{4.37}$$

where $v_i^{(k)}$ is the orientation of each fibre (in Cartesian coordinates) and N is the amount of fibres measured by µCT. In Eq. (4.17) the infinite series for the function $f(\mathbf{n})$ is replaced by a partial sum of finite terms, whereas the M-th partial sum of the series contains $(M+1)^2$ coefficients [37]. The sum expression for the approximation of the ODF reads:

$$f(\mathbf{v}) = \frac{1}{4\pi}\left(1 + \sum_{l=1}^{M}\frac{(2l+1)!!}{l!}\left[\frac{1}{N}\sum_{k=1}^{N}\overline{v_{i_1}^{(k)}\otimes\ldots\otimes v_{i_l}^{(k)}}\right]\cdot\overline{v_{i_1}\otimes\ldots\otimes v_{i_l}}\right),$$

(4.38)

where M is the order of approximation, $\overline{v_{i_1}\otimes\ldots\otimes v_{i_l}}$ are the symmetric irreducible tensors considering all possible directions of a fibre, i.e. $\theta\in[0°, 180°]$ and $\phi\in[0°, 360°]$. If $M\to\infty$ the approximation turns to infinite series of spherical harmonics, which converges absolutely and uniformly to the original function $f(\mathbf{n})$. The approximation implemented using the coefficients defined considering a minimum squared error, Eq. (4.37), provides a good accuracy within the sum of the first expansion terms [37], Appendix A.1.

In the following, the ODF is calculated using the 2nd order alignment tensor, A_{ij}, which defines the main material symmetry axes of one meso-volume element of SFRC. The higher-order alignment tensors are correcting the main symmetry axes received, however, the accuracy provided by the 2nd order tensor is assumed to be acceptable for the present needs of building industry [31]. The calculation of the higher rank tensors and the respective approximation of the ODF need more numerical calculations.

The ODF is defined as a probability and thus it should be normalized. The normalization is implemented utilizing the Riemann sum, which is defined e.g. for the three dimensional case as follows:

$$F_{cart} = \sum_{k=1}^{a}\sum_{j=1}^{b}\sum_{i=1}^{c} f\left(x^i, y^j, z^k\right)\Delta x^i\Delta y^j\Delta z^k ,$$

(4.39)

where $f\left(x^i, y^j, z^k\right)$ is the value of approximated function at a given point and $\Delta x^i\Delta y^j\Delta z^k$ are the lengths of intervals (partitions). Since the ODF is defined on a unit sphere, it is necessary to consider the difference between the volume elements in rectangular and spherical coordinates, Fig. 4.11. The Jacobian determinant of the transformation between the volume elements is defined as follows:

$$\frac{\partial(x,y,z)}{\partial(r,\theta,\phi)} = \begin{vmatrix} \sin\theta\,\cos\phi & r\,\cos\theta\,\cos\phi & -r\,\sin\theta\,\sin\phi \\ \sin\theta\,\sin\phi & r\,\cos\theta\,\sin\phi & r\,\sin\theta\,\cos\phi \\ \cos\theta & -r\,\sin\theta & 0 \end{vmatrix} = r^2\sin\theta , \quad (4.40)$$
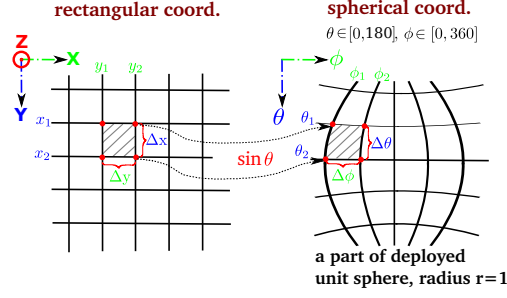
Figure 4.11. The transformation between a rectangular and a spherical volume element.

where $r^2 \sin \theta$ is the actual function that converts a rectangular volume element to spherical coordinates. In the case of a unit sphere $(r^2 = 1)$ only $\sin \theta$ shall be used. The transition of a rectangular volume element to spherical coordinates and calculation of the Riemann sum for the unit sphere reads:

$$F_{sph} = \sin \theta^j \cdot \sum_{j=1}^{b} \sum_{i=1}^{c} f(x^i, y^j) \Delta x^i \Delta y^j \ . \tag{4.41}$$

Eqs. (4.42-4.44), Table 4.1 and Figs. 4.12, A.5.4 present calculated fibre orientation parameters of the middle parts (Fig. 2.17(a)) of two cylinder samples 2A and 2B scanned by µCT. The orientation characteristics include: 2nd order alignment tensor, eigenvalues $\lambda_1, \lambda_2, \lambda_3$, eigenvectors $\mathbf{d}^1, \mathbf{d}^2, \mathbf{d}^3$, scalar order-parameter S, biaxiality b_S, and the approximated orientation distribution functions.

Cylinder 2A   Cylinder 2B

2nd order alignment tensor

$$A_{ij} = \begin{pmatrix} -0.037 & 0.277 & -0.010 \\ 0.277 & 0.038 & -0.013 \\ -0.010 & -0.013 & -0.001 \end{pmatrix}, \quad A_{ij} = \begin{pmatrix} 0.304 & 0.007 & -0.012 \\ 0.007 & -0.244 & -0.070 \\ -0.012 & -0.071 & -0.060 \end{pmatrix} \tag{4.42}$$

Sorted eigenvalues

$$\lambda_1, \ \lambda_2, \ \lambda_3 = 0.28, \ -0.28, \ -0.002 \qquad\qquad \lambda_1, \ \lambda_2, \ \lambda_3 = 0.31, \ -0.27, \ -0.04 \tag{4.43}$$

Eigenvectors of the sorted eigenvalues

$$d_{ij} = \begin{pmatrix} \mathbf{d}^1 & \mathbf{d}^2 & \mathbf{d}^3 \\ -0.656 & 0.753 & 0.042 \\ -0.752 & -0.658 & 0.042 \\ 0.059 & -0.004 & 0.998 \end{pmatrix} \qquad d_{ij} = \begin{pmatrix} \mathbf{d}^1 & \mathbf{d}^2 & \mathbf{d}^3 \\ 0.999 & -0.005 & 0.041 \\ 0.018 & 0.947 & -0.320 \\ -0.037 & 0.321 & 0.946 \end{pmatrix} \tag{4.44}$$

The orientation-weighted orthotropic meso-elasticity of fibres in the material meso-symmetry coordinates specified by the eigenvectors $\mathbf{d}^1, \mathbf{d}^2, \mathbf{d}^3$ are presented by employing the Kelvin-Mandel variant of the Voigt notation in Eq. (4.45).

Cylinder 2A

$C_{\alpha\beta}^{(f_{ms})} = Y^{(f)}.$

$$\begin{pmatrix} 0.44 & 0.07 & 0.11 & 0 & 0 & 0 \\ 0.07 & -0.04 & 0.03 & 0 & 0 & 0 \\ 0.11 & 0.03 & 0.20 & 0 & 0 & 0 \\ 0 & 0 & 0 & 0.05 & 0 & 0 \\ 0 & 0 & 0 & 0 & 0.21 & 0 \\ 0 & 0 & 0 & 0 & 0 & 0.13 \end{pmatrix},$$

Cylinder 2B

$C_{\alpha\beta}^{(f_{ms})} = Y^{(f)}.$

$$\begin{pmatrix} 0.46 & 0.07 & 0.1 & 0 & 0 & 0 \\ 0.07 & -0.03 & 0.02 & 0 & 0 & 0 \\ 0.1 & 0.02 & 0.20 & 0 & 0 & 0 \\ 0 & 0 & 0 & 0.05 & 0 & 0 \\ 0 & 0 & 0 & 0 & 0.21 & 0 \\ 0 & 0 & 0 & 0 & 0 & 0.14 \end{pmatrix}$$

(4.45)

The values of the coefficients in Eq. 4.45 can be called as the probabilities of orientation efficiency. The positive matrix terms describe the optimal fibre orientation from the probabilistic point of view, whereas the negative entry corresponds to a physical case, when the fibres have least effective orientation, and, thus, it can be dealt with by setting it to zero. The situation with negative or zero terms on a main diagonal causes the orientation-weighted orthotropic meso-elasticity tensor of fibres to be indefinite. Nevertheless, the orthotropic elasticity tensor of the composite is still positive definite, since the concrete matrix, being considered as isotropic, compensates the negative–zero–terms of the orthotropic elasticity of fibres, which, from the physical point of view, means the strength of the pure concrete.

Fibre orientation distribution characteristics for the other cylinder samples scanned by µCT are presented in Appendices A.4, A.5.

(a) Orientation.   (b) Cylinder 2A.   (c) Cylinder 2B.
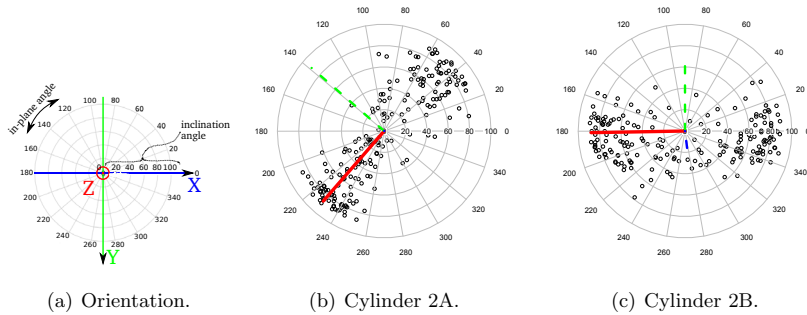
Figure 4.12. Scatter plots of fibre orientations with the triplets of the eigenvectors; $\mathbf{d}^1$-solid red line, $\mathbf{d}^2$-dashed green line, $\mathbf{d}^3$-dot-dashed blue line. $\mathbf{d}^1$ is the director corresponding to according-to-amount-largest eigenvalue. In (a) the radius represents the inclination angle θ and in-plane angle ϕ is on circumference. Z-axis corresponds to the direction of the tensile stress in a slab, Fig. 3.1.

Table 4.1. The scalar-order parameter S and triplet of the eigenvectors from the 2nd order alignment tensor in spherical coordinates. $S = 1$ corresponds to the transversely isotropic material symmetry, $S = 0$ to isotropy and $S = -\frac{1}{2}$ describes the plane isotropic case. The biaxiality b_S shows the non-symmetry of the distribution with respect to $\mathbf{d}^1$.

Cylinder nr.	S	b_S	$\mathbf{d}^1(\theta, \phi)$, deg	$\mathbf{d}^2(\theta, \phi)$, deg	$\mathbf{d}^3(\theta, \phi)$, deg
2A	0.42	0.14	87, 229	90, 139	3, 45
2B	0.46	0.12	88, 181	71, 90	19, 277

(a) Cylinder 2A.

(b) Cylinder 2A.

(c) Cylinder 2B.

(d) Cylinder 2B.
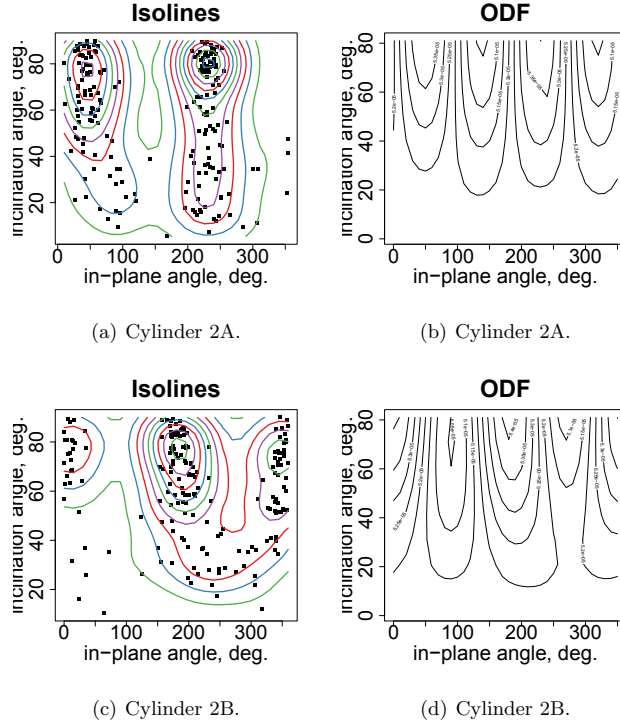
Figure 4.13. The isolines of the measured fibre orientation distributions and the ODFs of fibres approximated using the 2nd order alignment tensor.

4.6 Application areas for the developed material model of SFRC

The application areas of the material model can be utilized by both the numerical computations and the development of SFRC products. The material model developed has a continuous formulation, which makes it attractive for implementing to the finite element programs used in engineering calculations. The results of computer simulations with different fibre orientation distributions may help the manufacturers to better understand the importance of

fibre orientation on the mechanical properties of SFRC and, accordingly, will motivate the development of new technological solutions.

4.6.1 Application in numerical calculations

The orientation tensors (or the alignment tensors) describe the orientation state of fibres compactly not only in a sense of representation, but also in a sense of the number of independent variables needed to characterize the orientation of fibres in each spatial (meso-volume) finite element. For example, the orientation state of fibres in a spatial element using the 2nd order alignment tensor can be specified by 5 independent variables, those are 3 elements above the main diagonal and two elements on the main diagonal. The eigenvectors of the 2nd order alignment tensor show the preferred alignment of fibres in each spatial finite element, Fig. 4.14. As a result one can get a vector field,
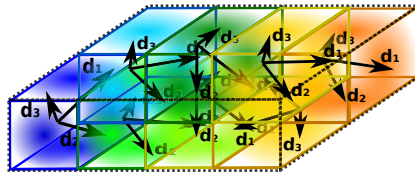
Figure 4.14. SFRC member with a preferred orientation of fibres represented by the triplets of the eigenvectors in each spatial (meso-volume) finite element.

which further may be used to simulate the flow of fibres in a visco-elastic fluid in order to predict fibre orientations.

4.6.2 Application in production technology

A challenge for SFRC manufacturers is to organise the production process to produce a particular orientation of fibres. Ordinary methods for casting concrete structures have not been developed for SFRC and new technological solutions considering the importance of fibre orientations on the mechanical properties of the composite are needed. For example, the optimal fibre orientation can be achieved in a structural member, where only unidirectional principal stress is expected. It may to be realised by utilising of the property of fibres to align along moulds or by the application of some electromagnetic devices. In the case of several principal stresses in a structural member the achievement of the optimal fibre orientation is partially possible and can be fulfilled by the systematic and automated product development as well as by the training of specialised teams for cast-in-place methods. It is expected that the material model encourages the manufacturers by simulating SFRC

properties to develop and evaluate their production technologies.

In general, the material symmetry axes of the composite may not coincide with the load-bearing directions of the structure and thus the information including the symmetry characteristics of the material can be tabularised for different ODFs. These tables may appear to be useful for both the manufacturers and designers as they could reduce the time needed for the analysis of a given ODF. From the industrial point of view, these tables give a tool for manufacturers to optimise production in the respect of composite properties. A designer may select an ODF in accordance with the principal stresses in a structure. To achieve the optimal load-bearing capacity, the selection of the ODF should be based on the expected principal stresses in a structure, which may restrict the approach to cases where load-combinations do not affect the nature of principal stresses.

5. Conclusions and future prospects

During the research two methods, a coupled approach based on sliced samples and μCT scanning, have been developed and implemented for measuring the orientations of short steel fibres from hardened concrete.

The benefit of implemented slicing method is that a coupled approach allows to measure the orientation of individual fibres in the interval from $[0°, 360°]$, which in addition to eliminating the ambiguity of the in-plane angle present in photometry, and also speeds up the scanning time as the coordinates received in image analysis are used as the input for DC-conductivity testing. An important characteristic while using the slicing method is the ratio between the thickness of a slice and the length of used fibres, Section 2.5. The slicing method is beneficial in the case of straight and hooked-end fibres. If fibres are corrugated, the tracking or searching for the opposite end of a cut fibre may cause difficulties. The success of DC-conductivity testing combined with photometry may depend on a price. In the present experiment the direct material costs were below 500 euros. This price is low and not even comparable to the price of μCT equipment. Even an improved robot version may cost only a few thousands euros.

The main advantage of the X-ray micro-tomography (μCT) method is the ability to analyse the orientation of individual fibres based on a 3D voxel representation of a sample. Although the sample size is limited to the order of several dm^3 and the size of structural elements is in the order of m^3, the precision of the measurements is superior to other methods. The most important parameters of the μCT machine are the beam power, acceleration voltage, the scanning resolution of X-ray equipment, and computer hardware resources for the processing of scans.

The study confirmed that the concrete samples require a high beam power and acceleration voltage due to the absorbing nature of concrete. CT systems that are capable of delivering over 1500 W X-ray tube power and greater than

400 kV acceleration voltage, [84, 85], while maintaining sufficient resolution, are readily available as turn-key systems that require only limited knowledge of X-ray methods to operate. The values of the equipment used in this study were 11 W and 160 kV.

In conclusion, the main advantages of the measuring methods developed or tested in the study are:

- Combined work of DC-conductivity with photometry:
  - provides fast scanning time;
  - prevents the ambiguity in the in-plane angle;
  - does not require expensive technical solutions.

- μCT scanning:
  - provides the precision of measurements superior to other methods;
  - offers the availability of CT-systems, which require limited knowledge of X-ray methods.

The outcomes from the measured fibre orientation distributions in the tested floor-slabs revealed a strong spatial heterogeneity in the orientation of fibres, meaning that the alignment of fibres varied along the length (Z-axis), width (X-axis) and the height (Y-axis) of the slabs. Accordingly, the theory that is capable to describe the properties of SFRC in three directions is necessary for the further elaboration of both the production and design of SFRC products.

The result of the modelling part of the research is the formulation of the orthotropic linear-elastic constitutive relation for one meso-volume element of SFRC subjected to small deformations. The approach presented is a mean-field homogenisation utilising a characteristic part of SFRC, i.e. the meso-volume element, which specifies the material symmetry axes on a meso-scale. The model utilises the full orientation information of fibres (two angles in spherical coordinates) and complies with material objectivity conditions. For describing the alignment of short steel fibres, the characteristics of the mesoscopic continuum theory are used: the 2nd order alignment tensor to identify the material meso-symmetry axes and the orientation distribution function to estimate the contribution of fibres to the symmetry axes defined.

The main advantages of the developed orthotropic linear-elastic constitutive model for one meso-volume element of SFRC are:

– the model is invariant under any orthogonal transformations;

– the model is based on dominating directions of the orientation distribution function;

– orthotropic meso-elasticity in the local symmetry axes of the composite are calculated based on the orientation distribution function and the 2nd order alignment tensor.

The future prospect of the material model developed is its implementation into numerical methods, such as finite element or finite volume methods to support the structural design. The material model formulated may also help the manufactures to learn and understand the properties of SFRC to select the most appropriate orientation distribution function for fibres. The adoption of new technologies to manufacturing process of SFRC is perhaps the only way to make the production of this composite controllable. As an outlook for the future research of SFRC, the necessity to study its failure mechanism should be noted. The understanding of SFRC failure may lead to the postulation of an orthotropic non-linear-plastic material model. Besides, the full-size experiments for validation of numerical simulations employing the linear or non-linear constitutive relations are endorsed.

Bibliography

[1] A. Kallonen, J.-P. Suuronen, and R. Serimaa. μ-CT scans of SFRC. private communication, April 2011.

[2] J. S. Sekhon. *Matching: Multivariate and Propensity Score Matching with Balance Optimization*, 2010. URL http://CRAN.R-project.org/package=Matching. R package version 4.7-11.

[3] A. Bertram. *Elasticity and Plasticity of Large Deformations – an Introduction.* Springer, 2005.

[4] A. C. Eringen. *Mechanics of Continua.* Wiley, New York, 1967.

[5] M. N. L. Narasimhan. *Principles of continuum mechanics.* Wiley, New York, 1993.

[6] P. Purnell, A. J. Buchanan, N. R. Short, C. L. Page, and A. J. Majumdar. Determination of bond strength in glass fibre reinforced cement using petrography and image analysis. *Journal of Materials Science*, 35:4653–4659, 2000. DOI: 10.1023/A:1004882419034.

[7] Y. Wang, A.-H. Zureick, B.-S. Cho, and D. E. Scott. Properties of fibre reinforced concrete using recycled fibres from carpet industrial waste. *Journal of Materials Science*, 29:4191–4199, 1994. DOI: 10.1007/BF00414198.

[8] Z. S. Metaxa, M. S. Konsta-Gdoutos, and S. P. Shah. Carbon nanofiber cementitious composites: Effect of debulking procedure on dispersion and reinforcing efficiency. *Cement and Concrete Composites*, 36(0):25 – 32, 2013. DOI: 10.1016/j.cemconcomp.2012.10.009.

[9] R. F. Zollo. Fiber-reinforced concrete: an overview after 30 years of development. *Cement and Concrete Composites*, 19(2):107 – 122, 1997. DOI: 10.1016/S0958-9465(96)00046-7.

[10] J. Tejchman and J. Kozicki. *Experimental and theoretical investigations of steel-fibrous concrete.* Springer series in geomechanics and geoengineering. Springer, 1st edition, 2010.

[11] F. Laranjeira. *Design-oriented constitutive model for steel fiber reinforced concrete.* PhD thesis, Universitat Politecnica de Catalunya, 2010. URL http://www.tdx.cat/TDX-0602110-115910.

[12] S. Grünewald. *Performance-based design of self-compacting fibre reinforced concrete.* PhD thesis, Technische Universiteit

Delft, 2004. URL http://repository.tudelft.nl/view/ir/uuid:07a817aa-cba1-4c93-bbed-40a5645cf0f1/.

[13] J. Schnell, W. Breit, and F. Schuler. Use of computer-tomography for the analysis of fibre reinforced concrete. In Vlastimile Sruma, editor, *Proceedings of the fib Symposium Prague 2011*, pages 583–586, 2011.

[14] P. Stroeven and J. Hu. Review paper – stereology: Historical perspective and applicability to concrete technology. *Materials and Structures*, 39:127–135, 2006. DOI: 10.1617/s11527-005-9031-6.

[15] J. Wuest, E. Denarié, E. Brühwiler, L. Tamarit, M. Kocher, and E. Gallucci. Tomography analysis of fiber distribution and orientation in ultra high-performance fiber-reinforced composites with high-fiber dosages. *Experimental Techniques*, 33 (5):50–55, 2009. DOI: 10.1111/j.1747-1567.2008.00420.x.

[16] S. Barnett, J.-F. Lataste, T. Parry, S. Millard, and M. Soutsos. Assessment of fibre orientation in ultra high performance fibre reinforced concrete and its effect on flexural strength. *Materials and Structures*, 43:1009–1023, 2010. DOI: 10.1617/s11527-009-9562-3.

[17] C. Redon, L. Chermant, J.-L. Chermant, and M. Coster. Assessment of fibre orientation in reinforced concrete using Fourier image transform. *Journal of Microscopy*, 191(3):258–265, 1998. DOI: 10.1046/j.1365-2818.1998.00393.x.

[18] L. Ferrara, N. Ozyurt, and M. di Prisco. High mechanical performance of fibre reinforced cementitious composites: the role of "casting-flow induced" fibre orientation. *Materials and Structures*, 44:109–128, 2011. DOI: 10.1617/s11527-010-9613-9.

[19] B. E. Barragán, R. Gettu, M. A. Martin, and R. L. Zerbino. Uniaxial tension test for steel fibre reinforced concrete – aparametric study. *Cement and Concrete Composites*, 25(7):767–777, 2003. DOI: 10.1016/S0958-9465(02)00096-3.

[20] L. Ferrara, M. Faifer, and S. Toscani. A magnetic method for non destructive monitoring of fiber dispersion and orientation in steel fiber reinforced cementitious composites — Part 1: method calibration. *Materials and Structures*, pages 1–15, 2011. DOI: 10.1617/s11527-011-9793-y.

[21] N. Ozyurt, T. O. Mason, and S. P. Shah. Non-Destructive Monitoring of Fiber Dispersion in FRCS Using AC-Impedance Spectroscopy. In *Measuring, Monitoring and Modeling Concrete Properties*, pages 285–290. Springer, 2007. DOI: 10.1007/978-1-4020-5104-3.

[22] E. Becker and W. Bürger. *Kontinuumsmechanik*. Teubner Studienbücher, Stuttgart, 1975.

[23] M. Taya and R. J. Aresenault. *Metal Matrix Composites: Thermomechanical Behavior*. Pergamon Press, Oxford, 1989.

[24] aci commitee 544 (Stark et al.). Design considerations for steel fiber reinforced concrete. ACI 544.4R-88, 1999.

[25] A. Jansson. *Fibres in reinforced concrete structures-analysis, experiments and design*. PhD thesis, Chalmers University of Technology, 2008. URL http://publications.lib.chalmers.se/records/fulltext/68889.pdf.

[26] L. G. Sorelli, A. Meda, and G. Plizzari. Steel fiber concrete slabs on ground: A structural matter. *ACI Structural Journal*, 103:551–558, 2006.

[27] CNR Advisory Committee on Technical Recommendations for Construction. Guide for the design and construction of fiber-reinforced concrete structures. CNR-DT 204/2006, 2006.

[28] M. Eik and J. Puttonen. Challenges of Steel Fibre Reinforced Concrete in Load Bearing Structures. *Rakenteiden Mekaniikka*, 44(1):44–64, 2011.

[29] W. Muschik, C. Papenfuss, and H. Ehrentraut. *Concepts of Continuum Thermodynamics*. Kielce University of Technology, Technische Universität Berlin, 1996.

[30] H. Ehrentraut and W. Muschik. On Symmetric irreducible tensors in d-dimensions. *ARI - An International Journal for Physical and Engineering Sciences*, 51:149–159, 1998. DOI: 10.1007/s007770050048.

[31] S. G. Advani and C. L. Tucker III. The use of tensors to describe and predict fiber orientation in short fiber composites. *Journal of Rheology*, 31(8):751–784, 1987. DOI: 10.1122/1.549945.

[32] C. Papenfuss, T. Boehme, H. Herrmann, W. Muschik, and J. Verhas. Dynamics of the size and orientation distribution of microcracks and evolution of macroscopic damage parameters. *Journal of Non-Equilibrium Thermodynamics*, 32(2): 129–142, 2007. DOI: 10.1515/JNETDY.2007.005.

[33] L. Waldmann. Kinetische Theorie des Lorentz-Gases aus rotierenden Molekülen. *Zeitschrift für Naturforschung A - A Journal of Physical Sciences*, 18a:1033–1048, 1963.

[34] S. Hess. Fokker–Planck-equation approach to flow alignment in liquid crystals. *Zeitschrift für Naturforschung A - A Journal of Physical Sciences*, 31a:1034–1037, 1976.

[35] S. Hess. Irreversible thermodynamics of nonequilibrium alignment phenomena in molecular liquids and in liquid crystals (1). *Zeitschrift für Naturforschung A - A Journal of Physical Sciences*, 30a:728–738, 1975.

[36] S. G. Advani and C. L. Tucker III. Closure approximations for three-dimensional structure tensors. *Journal of Rheology*, 34(3):367–386, 1990. DOI: 10.1122/1.550133.

[37] J.M Neiman and L.S Sugaipova. Сферические функции и их применение*(Spherical functions and their application)*. Московский государственный университет геодезии и картографии (Moscow State University of Geodesy and Cartography), 2005. URL http://vm.miigaik.ru/kollektiv_kafedr/preppages/neiman_um/.

[38] F. Laranjeira, S. Grünewald, J. Walraven, K. Blom, C. Molins, and A. Aguadoa. Characterization of the orientation profile in fiber reinforced concrete. *Materials and Structures*, 44:1093–1111, 2011. DOI: 10.1617/s11527-010-9686-5.

[39] F. Laranjeira, C. Molins, and A. Aguado. Predicting the pullout response of inclined hooked steel fibers. *Cement and Concrete Research*, 40(10):1471–1487, 2010. DOI: 10.1016/j.cemconres.2010.05.005.

[40] P.J.J. Dumont, S. Le Corre, L. Orgéas, and D. Favier. A numerical analysis of the evolution of bundle orientation in concentrated fibre-bundle suspensions. *Journal of Non-Newtonian Fluid Mechanics*, 160(2–3):76–92, 2009. DOI: 10.1016/j.jnnfm.2009.03.001.

[41] T.-H. Le, P.J.J. Dumont, L. Orgéas, D. Favier, L. Salvo, and E. Boller. X-ray phase contrast microtomography for the analysis of the fibrous microstructure of SMC composites. *Composites Part A: Applied Science and Manufacturing*, 39 (1):91 – 103, 2008. DOI: 10.1016/j.compositesa.2007.08.027.

[42] M. Krause, J. Hausherr, B. Burgeth, C. Herrmann, and W. Krenkel. Determination of the fibre orientation in composites using the structure tensor and local X-ray transform. *Journal of Materials Science*, 45:888–896, 2010. DOI: 10.1007/s10853-009-4016-4.

[43] C. Redon, L. Chermant, J.-L. Chermant, and M. Coster. Automatic image analysis and morphology of fibre reinforced concrete. *Cement and Concrete Composites*, 21(5-6):403 – 412, 1999. DOI: 10.1016/S0958-9465(99)00025-6.

[44] J.F. Lataste, M. Behloul, and D. Breysse. Characterisation of fibres distribution in a steel fibre reinforced concrete with electrical resistivity measurements. *NDT & E International*, 41(8):638 – 647, 2008. DOI: 10.1016/j.ndteint.2008.03.008.

[45] P. Purnell, A. J. Buchanan, N. R. Short, C. L. Page, and A. J. Majumdar. Determination of bond strength in glass fibre reinforced cement using petrography and image analysis. *Journal of Materials Science*, 35:4653–4659, 2000. DOI: 10.1023/A:1004882419034.

[46] P. Stroeven. *Stereology of concrete reinforced with short steel fibres*. PhD thesis, Technische Universiteit Delft, 1986. URL http://repository.tudelft.nl/assets/uuid:fb1416c4-2061-4767-9d5a-925480382d19/Stroeven_1986.pdf.

[47] J. Buffiere, E. Maire, J. Adrien, J. Masse, and E. Boller. In Situ Experiments with X-ray Tomography: an Attractive Tool for Experimental Mechanics. *Experimental Mechanics*, 50:289–305, 2010. DOI: 10.1007/s11340-010-9333-7.

[48] P. Penttilä, J.-P. Suuronen, S. Kirjoranta, M. Peura, K. Jouppila, M. Tenkanen, and R. Serimaa. X-ray characterization of starch-based solid foams. *Journal of Materials Science*, 46:3470–3479, 2011. DOI: 10.1007/s10853-011-5252-y.

[49] K. Leppänen, I. Bjurhager, M. Peura, A. Kallonen, J.-P. Suuronen, P. Penttilä, J. Love, K. Fagerstedt, and R. Serimaa. X-ray scattering and microtomography study on the structural changes of never-dried silver birch, european aspen and hybrid aspen during drying. *Holzforschung*, 65:865–873, Jul 2011. DOI: 10.1515/HF.2011.108.

[50] J.-P. Suuronen, A. Kallonen, M. Eik, J. Puttonen, R. Serimaa, and H. Herrmann. Analysis of short fibres orientation in steel fibre-reinforced concrete (SFRC) by X-ray tomography. *Journal of Materials Science*, 48:1358–1367, 2013. DOI: 10.1007/s10853-012-6882-4.

[51] P. Stähli, R. Custer, and J. van Mier. On flow properties, fibre distribution, fibre orientation and flexural behaviour of FRC. *Materials and Structures*, 41: 189–196, 2008. DOI: 10.1617/s11527-007-9229-x.

[52] M. D. Abràmoff, P. J. Magalhães, and S. J. Ram. Image Processing with ImageJ. *Biophotonics International*, 11(7):36–42, 2004.

[53] T. Collins. Pseudo-flat field filter for ImageJ, 2004. URL http://www.uhnresearch.ca/facilities/wcif/fdownload.html.

[54] EMC2 (Enhanced Machine controller). URL http://www.linuxcnc.org/. Software, http://www.linuxcnc.org/.

[55] L.A. Feldkamp, L.C. Davis, and J.W. Kress. Practical cone-beam algorithm. *Journal of the Optical Society of America*, 1(6):612–619, 1984.

[56] J. Weickert, B. M. Ter Haar Romeney, and M. A. Viergever. Efficient and reliable schemes for nonlinear diffusion filtering. *IEEE Transactions on Image Processing*, 7(3):398–410, 1998.

[57] R Development Core Team. *R: A Language and Environment for Statistical Computing*. R Foundation for Statistical Computing, Vienna, Austria, 2011. URL http://www.R-project.org.

[58] M. L. Delignette-Muller, R. Pouillot, J.-B. Denis, and C. Dutang. *fitdistrplus: help to fit of a parametric distribution to non-censored or censored data*, 2010. R package version 0.1-3.

[59] W. N. Venables and B. D. Ripley. *Modern Applied Statistics with S.* Springer, New York, 4th edition, 2002. URL http://www.stats.ox.ac.uk/pub/MASS4.

[60] A. G. Stephenson. evd: Extreme Value Distributions. *R News*, 2(2):31–32, June 2002. URL http://CRAN.R-project.org/doc/Rnews/.

[61] R. Pouillot and M.-L. Delignette-Muller. Evaluating variability and uncertainty in microbial qunatitative risk assessment using two R packages. *International Journal of Food Microbiology*, 142(3):330–40, 2010. DOI: 10.1016/j.ijfoodmicro.2010.07.011.

[62] D. Adler and D. Murdoch. *rgl: 3D visualization device system (OpenGL)*, 2010. URL http://CRAN.R-project.org/package=rgl. R package version 0.91.

[63] D. Wuertz, many others, and see the SOURCE file. *fMultivar: Multivariate Market Analysis*, 2009. URL http://CRAN.R-project.org/package=fMultivar. R package version 2100.76.

[64] E. Dimitriadou, K. Hornik, F. Leisch, D. Meyer, and A. Weingessel. *e1071: Misc Functions of the Department of Statistics (e1071), TU Wien*, 2011. URL http://CRAN.R-project.org/package=e1071. R package version 1.5-25.

[65] P. Poncet. *modeest: Mode Estimation*, 2010. URL http://CRAN.R-project.org/package=modeest. R package version 1.14.

[66] G. Casella and J. O. Berger. *Statistical Inference.* Duxbury Press, 2nd edition, 2001.

[67] A. J. M. Spencer. *Continuum mechanics.* Dover Pubns, 1980.

[68] C. Truesdell and W. Noll. *The Non-Linear Field Theories of Mechanics, Encyclopedia of Physics.* Springer-Verlag, 1965.

[69] M. Itskov. *Tensor Algebra and Tensor Analysis for Engineers With Applications to Continuum Mechanics.* Springer, 2009.

[70] M. Itskov and N. Aksel. A class of orthotropic and transversely isotropic hyperelastic constitutive models based on a polyconvex strain energy function. *International Journal of Solids and Structures*, 41(14):3833 – 3848, 2004. DOI: 10.1016/j.ijsolstr.2004.02.027.

[71] A.J.M. Spencer and R.S. Rivlin. Isotropic integrity bases for vectors and second-order tensors. *Archive for Rational Mechanics and Analysis*, 9(1):45–63, 1962. ISSN 0003-9527. DOI: http://dx.doi.org/10.1007/BF00253332.

[72] P. P. Teodorescu and N. A. Nicorovici. *Applications of the theory of groups in mechanics and physics*, volume 140 of *Fundamental Theories of Physics*. Springer Netherlands, 2004. DOI: http://dx.doi.org/10.1007/978-1-4020-2047-6.

[73] H. Herrmann and M. Eik. Some comments on the theory of short fibre reinforced material. *Proceedings of the Estonian Academy of Sciences*, 60(3):179–183, 2011. DOI: 10.3176/proc.2011.3.06.

[74] R. Eppenga and D. Frenke. Monte Carlo study of the isotropic and nematic phases of infinitely thin hard platelets. *Molecular Physics*, 52:1303–1334, 1984.

[75] H. Steuer. *Thermodynamical Properties Of A Model Liquid Crystal*. PhD thesis, TU Berlin, 2004. URL http://opus.kobv.de/tuberlin/volltexte/2004/919/.

[76] I. Pardowitz and S. Hess. On the theory of irreversible processes in molecular liquids and liquid crystals, nonequilibrium phenomena associated with the second and fourth rank alignment tensors. *Physica A: Statistical Mechanics and its Applications*, 100(3):540 – 562, 1980. DOI: 10.1016/0378-4371(80)90166-1.

[77] T. J. Jankun-Kelly and K. Mehta. Superellipsoid-based, real symmetric traceless tensor glyphs motivated by nematic liquid crystal alignment visualization. In *IEEE Transactions on Visualization and Computer Graphics (Proceedings Visualization/Information Visualization 2006*, pages 1197–1204, 2006. DOI: 10.1109/TVCG.2006.181.

[78] H. A. Meier, P. Steinmann, and E. Kuhl. Towards multiscale computation of confined granular media: Contact Forces, Stresses and Tangent Operators. *Technische Mechanik*, 28:32–42, 2008. URL http://www.ovgu.de/ifme/zeitschrift_tm/2008_Heft1/04_Meier_Steinmann.pdf.

[79] B. Klusemann and B. Svendsen. Homogenization methods for multi-phase elastic composites: Comparisons and benchmarks. *Technische Mechanik*, 30:374–386, 2010. URL http://www.ovgu.de/ifme/zeitschrift_tm/2010_Heft4/07_Klusemann.html.

[80] L.C. Brinson and W.S. Lin. Comparison of micromechanics methods for effective properties of multiphase viscoelastic composites. *Composite Structures*, 41 (3–4):353 – 367, 1998. ISSN 0263-8223. DOI: http://dx.doi.org/10.1016/S0263-8223(98)00019-1.

[81] European Committee for Standardization. EN 1992-1-1 Eurocode 2: Design of concrete structures - Part 1-1: General ruels and rules for buildings. Brussels, 2005. EN, CEN.

[82] F. Larsson, R. Lillbacka, and K. Runesson. On the adaptive use of the Taylor assumption in computational homogenization of thin metal sheets. *International*

Journal of Material Forming, 2(1):903–906, 2009. DOI: 10.1007/s12289-009-0632-4.

[83] S. Mercier, A. Molinari, S. Berbenni, and M. Berveiller. Comparison of different homogenization approaches for elastic–viscoplastic materials. *Modelling and Simulation in Materials Science and Engineering*, 20(2):1–22, 2012. DOI: http://dx.doi.org/10.1088/0965-0393/20/2/024004.

[84] GE Measurement & Control. phoenix|x-ray v|tome|x l 450, 2013. URL http://www.ge-mcs.com/en/radiography-x-ray/ct-computed-tomography.html. (page visited Oct. 15th 2013).

[85] YXLON International. Y.CT Compact, 2013. URL http://www.yxlon.com/Products/CT-systems/Y-CT-Compact. (page visited Oct. 15th 2013).

[86] V.V Zhuk and G.I Natanson. Тригонометрические ряды Фурье и элементы теории аппроксимации: учебное пособие*(Trigonometric Fourier series and the elements of the theory of approximation)*. Издательство Ленинградского Университета (Leningrad University Publishing), 1983. URL http://books.google.ee/books?id=KlTvAAAAMAAJ.

A. Appendicies

A.1 Orientation distribution function as a spherical harmonic function

Let us consider H_l to be $(2l+1)$ dimensional Hilbert subspace (vector space) spanned by all spherical harmonics of rank l. Then for $l \in \mathbb{N}$:

$$H_l = \operatorname*{span}_{(\mu_1 ... \mu_l) \in \{1,2,3\}^l} h^{(l)}_{\mu_1 ... \mu_l} , \qquad (A.1.1)$$

where $h^{(l)}_{\mu_1 ... \mu_l}$ is a spherical harmonic function. The Hilbert space H of square-integrable functions L^2 can be represented as a direct sum of finite dimensional subspaces H_l, such as:

$$H = \bigoplus_{l=0}^{\infty} H_l , \quad H \in L^2. \qquad (A.1.2)$$

The orientation distribution function $f(\mathbf{n})$, where $\mathbf{n} \in (\theta, \phi)$ is a unit vector, belongs to L^2.

Applying the Laplace operator on $\mathbb{R}^3$, i.e. $\Delta = \left(\frac{\partial^2}{\partial x_1^2} + \frac{\partial^2}{\partial x_2^2} + \frac{\partial^2}{\partial x_3^2} \right)$, on symmetric irreducible (symmetric traceless) tensors, $\overline{n_{\mu_1} \cdots n_{\mu_l}}$, where a unit vector n_μ (radius $r = 1$) can be presented in Cartesian coordinates as $n(\theta, \phi) = \hat{n}(x = \sin\theta \cos\phi, \ y = \sin\theta \sin\phi, \ z = \cos\theta)$, the following can be received:

$$\Delta \ \overline{\hat{n}_{\mu_1} \cdots \hat{n}_{\mu_l}} = 0, \qquad (A.1.3)$$

which explains $\overline{n_{\mu_1} \cdots n_{\mu_l}}$ to be a harmonic function [30]. Applying the Laplace-Beltrami operator, which reads as:

$$\Delta_S = \frac{1}{\sin\theta} \cdot \frac{\partial}{\partial\theta} \left(\sin\theta \cdot \frac{\partial}{\partial\theta} \right) + \frac{1}{\sin^2\theta} \cdot \frac{\partial^2}{\partial\phi^2} , \qquad (A.1.4)$$

the following can be received:

$$\Delta_S \ \overline{n_{\mu_1} \cdots n_{\mu_l}} = -l(l+1) \ \overline{n_{\mu_1} \cdots n_{\mu_l}} , \qquad (A.1.5)$$

which shows that the coordinate functions $\overline{n_{\mu_1}\cdots n_{\mu_l}}$ are the eigenfunctions of the Laplace-Beltrami operator corresponding to eigenvalues $\lambda_l = -l(l+1)$. The eigenfunctions of Laplace-Beltrami operator are called spherical harmonics, which represent the angular portion of a set of orthogonal solutions of the Laplace equation written in spherical coordinates. The eigenfunction with the corresponding eigenvalue $\lambda_l \geq 0$ satisfies:

$$\Delta_S\ \overline{n_{\mu_1}\cdots n_{\mu_l}}\ +\lambda_l\ \overline{n_{\mu_1}\cdots n_{\mu_l}} = 0 \ . \tag{A.1.6}$$

Accordingly, the symmetric irreducible tensors $\overline{n_{\mu_1}\cdots n_{\mu_l}}$ are spherical harmonic functions [30]:

$$h^{(l)}_{\mu_1\ldots\mu_l}(\mathbf{n}) := \overline{n_{\mu_1}\cdots n_{\mu_l}} \ . \tag{A.1.7}$$

Any spherical harmonic function of rank l, $Y_l(\theta,\phi)$, can be represented as a linear combination of $(2l+1)$, Eq. (A.1.5), main spherical functions each depending on either *sines* or *cosines* of the angles θ and ϕ [37]. The main spherical functions may have the following form:

$$P_l^{(0)}(\cos\theta),\ P_l^{(1)}(\cos\theta)\cdot\cos\phi,\ P_l^{(2)}(\cos\theta)\cdot\cos 2\phi,\ \ldots,\ P_l^{(l)}(\cos\theta)\cdot\cos l\phi,$$
$$P_l^{(1)}(\cos\theta)\sin\phi,\ P_l^{(2)}(\cos\theta)\cdot\sin 2\phi,\ \ldots,\ P_l^{(l)}(\cos\theta)\cdot\sin l\phi \ ,$$

where $P_l^{(k)}$ is an l-th rank polynomial of $\cos\theta$ or an $(l-1)$-th rank polynomial of $\cos\theta$ times $\sin\theta$. Accordingly, any arbitrary l-th rank spherical harmonic function can be represented as follows:

$$Y_l(\theta,\phi) = \sum_{k=0}^{l} P_l^{(k)}(\cos\theta)[c_l^k\cdot\cos k\phi + s_l^k\cdot\sin k\phi] = \sum_{m=0}^{2l} a_l^m Y_l^m(\theta,\phi), \tag{A.1.8}$$

where c_l^k, s_l^k are $(2l+1)$ arbitrary constants, $P_l^{(k)}(\cos\theta)$ are: if $k=0$, the Legendre polynomials and if $k = 1, 2, \ldots, l$ the associated Legendre polynomials. The index l is the rank of the main spherical function $Y_l^m(\theta,\phi)$ and the index m is an auxiliary and indicates the order [37]. The index m has the following values:

$$\text{if} \quad m \leq l, \quad Y_l^m(\theta,\phi) \;=\; P_l^{(k)}(\cos\theta)\cdot\cos k\phi, \quad a_l^m = c_l^k, \; k = m \quad \text{(A.1.9)}$$
$$\text{if} \quad m > l, \quad Y_l^m(\theta,\phi) \;=\; P_l^{(k)}(\cos\theta)\cdot\sin k\phi, \quad a_l^m = s_l^k, \; k = m - l \ .$$

The Legendre and the associated Legendre polynomials can be determined using the following recursive formulas, respectively:

$$P_l(\cos\theta) \;=\; \frac{2l-1}{l}\cdot\cos\theta\cdot P_{l-1}(\cos\theta) - \frac{l-1}{l}P_{l-2}(\cos\theta) \ , \tag{A.1.10}$$

$$\text{wherein} \quad P_l(0) = \begin{cases} 0 \ , & \text{if } l \text{ is odd} \\ \frac{l!(-1)^{l/2}}{(\frac{l}{2}!)^2\cdot 2^l} \ , & \text{if } l \text{ is even} \end{cases} \tag{A.1.11}$$

$$P_l^{(k)}(\cos\theta) = \frac{2l-1}{l-k} \cdot \cos\theta \cdot P_{l-1}^{(k)}(\cos\theta) - \frac{l+k-1}{l-k} \cdot P_{l-2}^{(k)}(\cos\theta) ,$$

$$0 \le k \le l-2, \quad l \ge 2 . \tag{A.1.12}$$

The Legendre and the associated Legendre polynomials form an orthogonal system on the interval $[-1, 1]$.

The spherical harmonics belong to square-integrable functions L^2 and form an orthogonal basis on L^2. For the completeness of the basis it is necessary and sufficient that the number of basis vectors coincide with the dimension of the functional space. On a unit sphere S^2 the Legendre and the associated Legendre polynomials form a complete orthonormal basis. Consequently, the same holds true for the tensor family $\{ \overline{n_{\mu_1} \cdots n_{\mu_l}} \}$. On a unit sphere any square-integrable function $g \in L^2$ can be expanded as a series of main spherical harmonics in complete orthonormal basis, such as:

$$g(\theta, \phi) = \sum_{l=0}^{\infty} Y_l(\theta, \phi) = \sum_{l=0}^{\infty} \sum_{m=0}^{2l} a_l^m Y_l^m(\theta, \phi) , \tag{A.1.13}$$

where a_l^m are acting as expansion coefficients [37], such as:

$$a_l^m = \frac{\langle g, Y_l^m \rangle}{||Y_l^m||^2} = \tag{A.1.14}$$

$$\begin{cases} m \le l, \ k = m \\ c_l^k = \frac{(2l+1)}{2\pi \cdot \delta_k} \cdot \frac{(l-k)!}{(l+k)!} \cdot \int_0^{2\pi} \int_0^{\pi} g(\theta, \phi) \cdot \underbrace{P_l^{(k)}(\cos\theta)\cos k\phi}_{Y_l^m} \cdot \underbrace{\sin\theta \cdot d\phi d\theta}_{d\Omega}, \\[2ex] m > l, \ k = l - m \\ s_l^k = \frac{(2l+1)}{2\pi \cdot \delta_k} \cdot \frac{(l-k)!}{(l+k)!} \cdot \int_0^{2\pi} \int_0^{\pi} g(\theta, \phi) \cdot \underbrace{P_l^{(k)}(\cos\theta)\sin k\phi}_{Y_l^m} \cdot \underbrace{\sin\theta \cdot d\phi d\theta}_{d\Omega}, \end{cases}$$

$$\text{where} \ \ \delta_k = 1, \ \text{if} \ k > 0, \ \text{if} \ k = 0, \ \delta_0 = 2 ,$$

$$\sin\theta \cdot d\phi d\theta = d\Omega .$$

$\langle g, Y_l^m \rangle$ in Eq. (A.1.14) means a scalar multiplication defined for any two arbitrary functions p and q on L^2 as:

$$\langle p, q \rangle = \int_a^b p(x)q(x)dx , \tag{A.1.15}$$

$||Y_l^m||^2$ is a square norm of a function and $d\Omega$ comes from the integration over a flat rectangular area $[0, \pi; 0, 2\pi]$ instead of a surface integral $\oint_{S^2}$ on a unit sphere. If in some complete basis system the expansion coefficients a_l^m in Eq. (A.1.13) are known then the function $g(\theta, \phi)$ can be also considered as known and the following identity holds true:

$$\sum_{l=0}^{\infty} \sum_{m=0}^{2l} (\bar{a}_l^m)^2 = \frac{1}{4\pi} \int_{\Omega} g^2(\theta, \phi) d\Omega , \tag{A.1.16}$$

where $\bar{a}_l^m$ is the normalized expansion coefficient:

$$
\begin{aligned}
\bar{a}_l^m &= \sqrt{\frac{\delta_k}{2 \cdot (2l+1)} \cdot \frac{(l+k)!}{(l-k)!}} \cdot a_l^m & \text{(A.1.17)} \\
&= \frac{1}{4\pi} \int_0^{2\pi} \int_0^\pi g(\theta, \phi) \cdot \bar{Y}_l^m \cdot \sin\theta \cdot \mathrm{d}\phi\mathrm{d}\theta \ .
\end{aligned}
$$

The normalization of Y_l^m reads as:

$$
\bar{Y}_l^m(\theta, \phi) = \sqrt{\frac{2 \cdot (2l+1)}{\delta_k} \cdot \frac{(l-k)!}{(l+k)!}} \cdot Y_l^m(\theta, \phi) \ . \qquad \text{(A.1.18)}
$$

The identity Eq. (A.1.16) is called the Parseval's identity. In terms of completely normalized functions Eqs. (A.1.17), (A.1.18), the Eq. (A.1.13) has the following form:

$$
g(\theta, \phi) = \sum_{l=0}^\infty \bar{Y}_l(\theta, \phi) = \sum_{l=0}^\infty \sum_{m=0}^{2l} \bar{a}_l^m \bar{Y}_l^m(\theta, \phi) \ . \qquad \text{(A.1.19)}
$$

The spherical harmonic function of rank l, $Y_l(\theta, \phi)$, in decomposition presented in Eq. (A.1.13) represent the sum of $(l+1)$ terms, which differ from each other by the value of k. Each term having the form as:

$$
P_l^{(k)}(\cos\theta)[c_l^k \cdot \cos k\phi + s_l^k \cdot \sin k\phi], \quad k = 1, 2, 3, \ldots, l \qquad \text{(A.1.20)}
$$

can be considered, similar to the harmonic analysis of one argument function employing the Fourier series, as the l-th harmonic of the original function. If $l = 0$, then:

$$
\bar{Y}_0^{(0)}(\theta, \phi) = Y_0^{(0)}(\theta, \phi) \equiv 1 \quad \text{and} \qquad \text{(A.1.21)}
$$

$$
\bar{a}_{00} = a_{00} = c_{00} = \frac{1}{4\pi} \int_\Omega g(\theta, \phi)\mathrm{d}\Omega = \hat{g} \ , \qquad \text{(A.1.22)}
$$

meaning that the zero harmonic in Eq. (A.1.13) is a constant, which is equal to the mean integral value $\hat{g}$ of the original function $g(\theta, \phi)$ on a sphere. All other harmonics starting from $l = 1$ approximate the deviation $(g - \hat{g})$ of the original function $g(\theta, \phi)$ from its mean value. The series presented in Eq. (A.1.13) are also called Laplace series for the function $g(\theta, \phi)$ and the expansion terms in Eqs. (A.1.13), (A.1.14) are Laplace spherical harmonics. Hence, while decomposing the given function on a unit sphere, $g(\theta, \phi), g \in S^2$, by spherical harmonics, the series terms are always Laplace spherical functions. The values of the coefficients in Eq. (A.1.14) are determined under the least squares method assuming the condition of a minimum squared error σ_n^2, such as:

$$
\sigma_n^2 = \int_\Omega g^2(\theta, \phi)\mathrm{d}\Omega - \sum_{l=0}^n \sum_{m=0}^{2l} \frac{2\pi \cdot \delta_k (l+k)!}{(2l+1)(l-k)!} \cdot (a_l^m)^2 \ . \qquad \text{(A.1.23)}
$$

The infinite Laplace series $l \rightarrow \infty$ converges to the original function absolutely and uniformly and thus the same holds for Eq. (A.1.23) meaning that if $n \rightarrow \infty$ then $\sigma_n^2 \rightarrow 0$ and Eq. (A.1.23) takes the form of the Parseval's identity Eq. (A.1.16). Accordingly, the sum of the squares of all the coefficients of the expansion is closely related to the mean square of the given function on a sphere. The approximation employing the coefficients defined considering a minimum squared error provides a good accuracy within the sum of the first terms of the Laplace series [37].

Spherical harmonics expansion is the modification of the Fourier series decomposing any original function g by an orthogonal basis into the linear combination (sum) of harmonic oscillations with different frequencies. The classical trigonometric Fourier series for the real valued function $g(x)$ integrable on an interval $(x_0, x_0 + T)$, x_0, $T \in \mathbb{R}$ and periodic with a period T outside the interval, for the integers $\mathbb{N} \geq 0$ and $T = 2\pi$ reads as follows:

$$g(x) = \frac{m_0}{2} + \sum_{k=1}^{\mathbb{N}} \left(m_k \cos \frac{2\pi k x}{T} + b_k \sin \frac{2\pi k x}{T} \right) , \qquad (A.1.24)$$

where $m_0, m_k, b_k,\ k = 1, 2 \cdots$ are called the Fourier coefficients of the function g [86].

Let us consider now a function $f(\mathbf{n})$, where $\mathbf{n}$ defines a unit vector on a two-dimensional unit sphere S^2, to be square-integrable, such as: $f(\mathbf{n}) \in L^2(S^2,\ \mathbb{R})$. According to Eqs. (A.1.3) and (A.1.5) the symmetric irreducible tensors $\overline{n_{\mu_1} \cdots n_{\mu_l}}$ are spherical harmonic functions and they form a complete orthonormal basis, since based on Eqs. (A.1.10), (A.1.12) the main spherical harmonics are either Legendre or associated Legendre polynomials. Following Eq. (A.1.21), if $l = 0$ the zero harmonic $Y_0^{(0)}$ can be set to be equal to 1. Consequently, the following representation of $f(\mathbf{n})$ can be obtained:

$$f(\mathbf{n}) \;=\; \alpha_0 \cdot 1 + \sum_{l=1}^{\infty} (2l-1)!! \alpha_{\mu_1 \dots \mu_l} \, \overline{n_{\mu_1} \cdots n_{\mu_l}} , \qquad (A.1.25)$$

where α_0 and $\alpha_{\mu_1 \dots \mu_l}$ are expansion coefficients which read as, see also Eqs. (A.1.19), (A.1.22):

$$\alpha_0 \;=\; \frac{1}{4\pi} \oint_{S^2} f(\mathbf{n}) \cdot 1 \cdot \mathrm{d}^2 n , \qquad (A.1.26)$$

$$\alpha_{\mu_1 \dots \mu_l} \;=\; \frac{1}{4\pi} \frac{(2l+1)}{l!} \oint_{S^2} f(\mathbf{n}) \cdot \overline{n_{\mu_1} \dots n_{\mu_l}} \, \mathrm{d}^2 n , \qquad (A.1.27)$$

where $\mathbf{n} \in (\theta, \phi)$, $\theta \in [0°, 180°]; \phi \in [0°, 360°]$ are the parameters of a current point on a sphere. Thereby, Eq. (A.1.25) is the decomposition of a function

$f(\mathbf{n})$ by an orthonormal system formed by the symmetric irreducible tensors $\overline{n_{\mu_1} \cdots n_{\mu_l}}$, and the expansion coefficients $\alpha_0, \alpha_{\mu_1 \ldots \mu_l}$ in complete basis of $\overline{n_{\mu_1} \cdots n_{\mu_l}}$, according to Eq. (A.1.16), can be used to uniquely reconstruct the original function $f(\mathbf{n})$.

A.2 Density distribution of the inclination angle θ

The results of the bootstrap Kolmogorov-Smirnov tests applied on the density distributions of the inclination angle θ received employing the photos of slice surfaces are presented in Tables A.2.1, A.2.2, A.2.3, A.2.4, A.2.5.

Table A.2.1. Results of the two-sample bootstrap Kolmogorov-Smirnov test (function `ks.boot` from [2]) applied on the density distribution of the inclination angle θ in the slab 2. Reduced cuboid refer to the cuboid, where only every fourth slice surface is taken into account.

	Cuboid 2.1 (side of a slab)				**Cuboid 2.2** (centre of a slab)			
	Inclination angle θ							
	whole cuboid		reduced cuboid		whole cuboid		reduced cuboid	
Distribution	D	p-value	D	p-value	D	p-value	D	p-value
Gaussian	0.104	e-16	0.100	e-16	0.077	e-16	0.066	4.5e-07
Gamma	0.041	e-11	0.051	5.0e-06	0.058	e-16	0.055	5.7e-05
Gumbel	0.038	e-09	0.043	0.0002	0.041	e-09	0.042	**0.0041**
Weibull	0.088	e-16	0.081	e-14	0.067	e-16	0.060	6.6e-06
Log-normal	0.038	e-09	0.036	**0.0031**	0.058	e-16	0.055	5.5e-05

Table A.2.2. Results of the two-sample bootstrap Kolmogorov-Smirnov test (function `ks.boot` from [2]) applied on the density distribution of the inclination angle θ in the slab 3. Reduced cuboid refer to the cuboid, where only every fourth slice surface is taken into account.

	Cuboid 3.1 (side of a slab)				**Cuboid 3.2** (centre of a slab)			
	Inclination angle θ							
	whole cuboid		reduced cuboid		whole cuboid		reduced cuboid	
Distribution	D	p-value	D	p-value	D	p-value	D	p-value
Gaussian	0.099	e-16	0.108	e-16	0.067	e-16	0.072	e-08
Gamma	0.040	e-09	0.048	6.4e-05	0.057	e-16	0.049	0.0003
Gumbel	0.038	e-08	0.045	0.0002	0.042	e-09	0.042	**0.0030**
Weibull	0.087	e-16	0.079	e-12	0.061	e-16	0.069	e-08
Log-normal	0.035	2.6e-07	0.039	**0.0025**	0.053	e-14	0.056	2.4e-05

Table A.2.3. Results of the two-sample bootstrap Kolmogorov-Smirnov test (function `ks.boot` from [2]) applied on the density distribution of the inclination angle θ in the slab 4. Reduced cuboid refer to the cuboid, where only every fourth slice surface is taken into account.

	Cuboid 4.1 (side of a slab)				**Cuboid 4.2** (centre of a slab)			
	Inclination angle θ							
	whole cuboid		reduced cuboid		whole cuboid		reduced cuboid	
Distribution	D	p-value	D	p-value	D	p-value	D	p-value
Gaussian	0.085	e-16	0.087	e-13	0.068	e-16	0.082	e-10
Gamma	0.035	1.0e-06	0.032	0.0381	0.054	e-14	0.058	4.1e-05
Gumbel	0.031	2.4e-05	0.025	**0.1713**	0.044	e-09	0.045	**0.003**
Weibull	0.075	e-16	0.070	e-08	0.061	e-16	0.071	2.3e-07
Log-normal	0.025	0.001	0.031	**0.05177**	0.057	e-15	0.06	1.8e-05

Table A.2.4. Results of the two-sample bootstrap Kolmogorov-Smirnov test (function `ks.boot` from [2]) applied on the density distribution of the inclination angle θ in the slab 5. Reduced cuboid refer to the cuboid, where only every fourth slice surface is taken into account.

	Cuboid 5.1(side of a slab)				**Cuboid 5.2**(centre of a slab)			
	Inclination angle θ							
	whole cuboid		reduced cuboid		whole cuboid		reduced cuboid	
Distribution	D	p-value	D	p-value	D	p-value	D	p-value
Gaussian	0.110	e-16	0.117	e-16	0.078	e-16	0.094	e-15
Gamma	0.052	e-15	0.058	e-06	0.046	e-11	0.044	0.0009
Gumbel	0.047	e-12	0.056	2.9e-06	0.031	1.6e-05	0.036	**0.0103**
Weibull	0.093	e-16	0.099	e-16	0.060	e-16	0.068	e-08
Log-normal	0.040	e-09	0.046	0.0002	0.046	e-11	0.048	**0.0002**

Table A.2.5. Results of the two-sample bootstrap Kolmogorov-Smirnov test (function `ks.boot` from [2]) applied on the density distribution of the inclination angle θ in the slab 6. Reduced cuboid refer to the cuboid, where only every fourth slice surface is taken into account.

	Cuboid 6.1(side of a slab)				**Cuboid 6.2**(centre of a slab)			
	Inclination angle θ							
	whole cuboid		reduced cuboid		whole cuboid		reduced cuboid	
Distribution	D	p-value	D	p-value	D	p-value	D	p-value
Gaussian	0.096	e-16	0.095	e-15	0.082	e-16	0.081	4.3e-07
Gamma	0.037	2.8e-07	0.037	0.013	0.065	e-15	0.073	8.9e-06
Gumbel	0.036	4.7e-07	0.035	0.019	0.053	e-10	0.062	**0.0003**
Weibull	0.075	e-16	0.075	e-09	0.072	e-16	0.068	4.9e-05
Log-normal	0.031	2.7e-05	0.043	**0.002**	0.065	e-15	0.074	7.0e-06

A.3 Variations of fibre orientation distributions along the X- and Y-axes of the slabs

Figs. A.3.1, A.3.2 present the variations of fibre orientation distributions along the height of the whole (i.e. top, middle and bottom parts) cylinder samples 1B, 4A and 4B. The statistical data presented allow to observe the orientation of fibres in the compression (top) and tension (bottom) zones of the tested slabs.

Figs. A.3.3, A.3.4 demonstrate the variations of fibre orientation distributions in the side and centre cylinders.
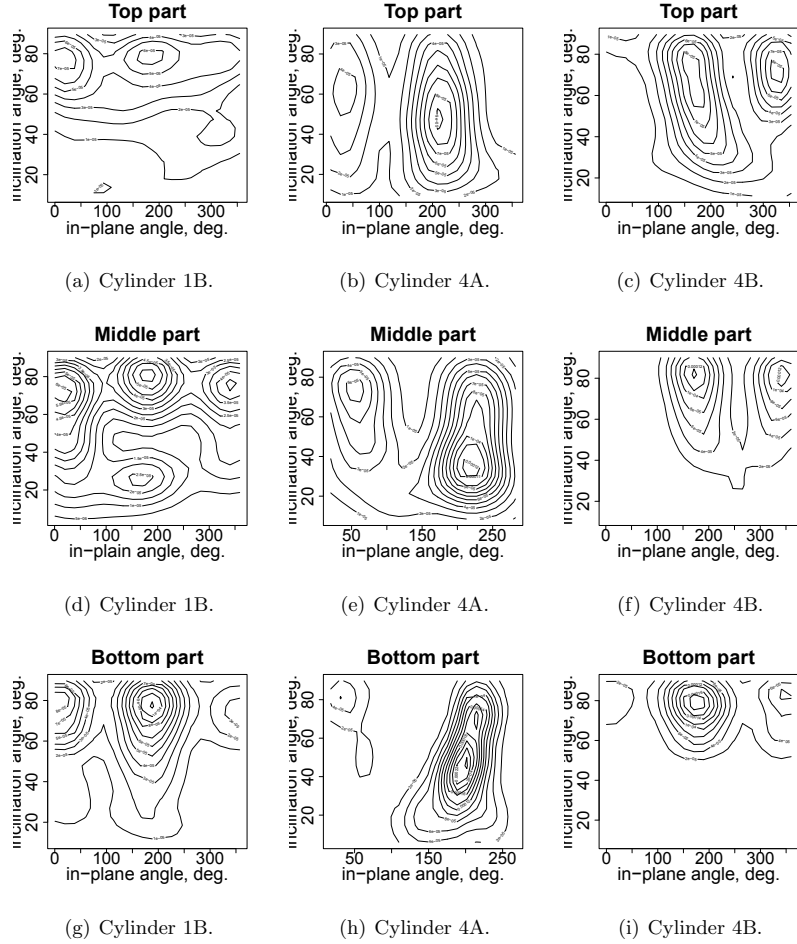
Figure A.3.1. Variations in bivariate densities of the inclination angle θ and in-plane angle ϕ measured by µCT between the side ("Cylinder *.A") and centre ("Cylinder *.B"), and along the height of the whole cylinder samples.
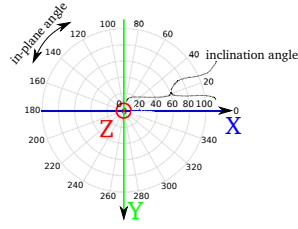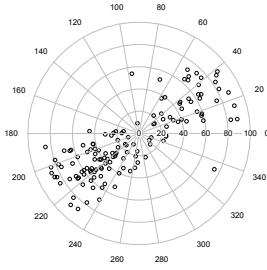
(a) Orientation.

(b) **Top part.** Cylinder 4A.
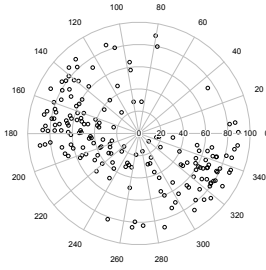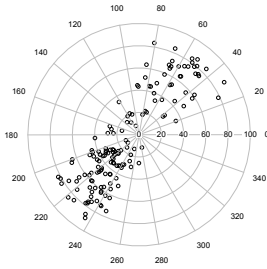
(c) Cylinder 4B.

(d) **Middle part.** Cylinder 4A.
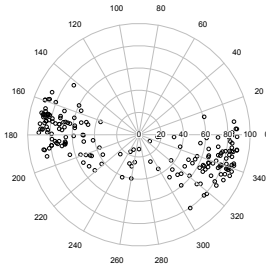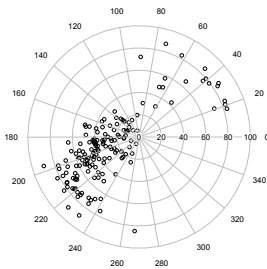
(e) Cylinder 4B.

(f) **Bottom part.** Cylinder 4A.
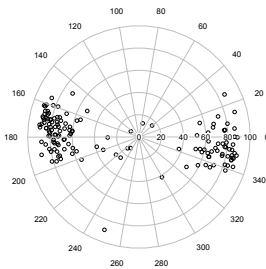
(g) Cylinder 4B.

Figure A.3.2. Scatter plots of fibre orientation variations measured by μCT between the side ("Cylinder *.A") and centre ("Cylinder *.B"), and along the height of the whole cylinder samples. In (a) the radius represents the inclination angle θ and in-plane angle ϕ is on circumference. Z-axis corresponds to the direction of the tensile stress in a slab, Fig. 2.4.
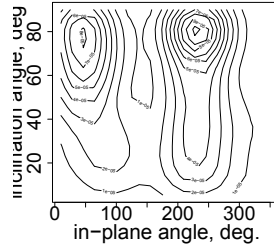
(a) Cylinder 2A.
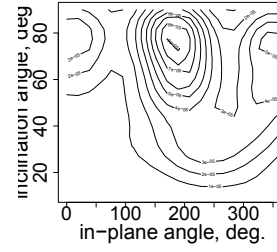
(b) Cylinder 2B.

(c) Cylinder 3A.

(d) Cylinder 3B.

(e) Cylinder 5A.

(f) Cylinder 5B.
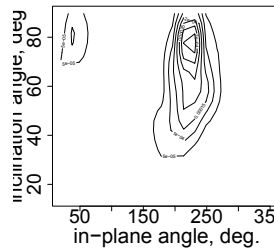
(g) Cylinder 6A.

(h) Cylinder 6B.

Figure A.3.3. Variations in bivariate densities of the inclination angle θ and in-plane angle ϕ measured by µCT between the side ("Cylinder *.A") and centre ("Cylinder *.B") cylinder samples.

(a) Orientation.

(b) Cylinder 2A.

(c) Cylinder 2B.

(d) Cylinder 3A.

(e) Cylinder 3B.

(f) Cylinder 5A.

(g) Cylinder 5B.

(h) Cylinder 6A.
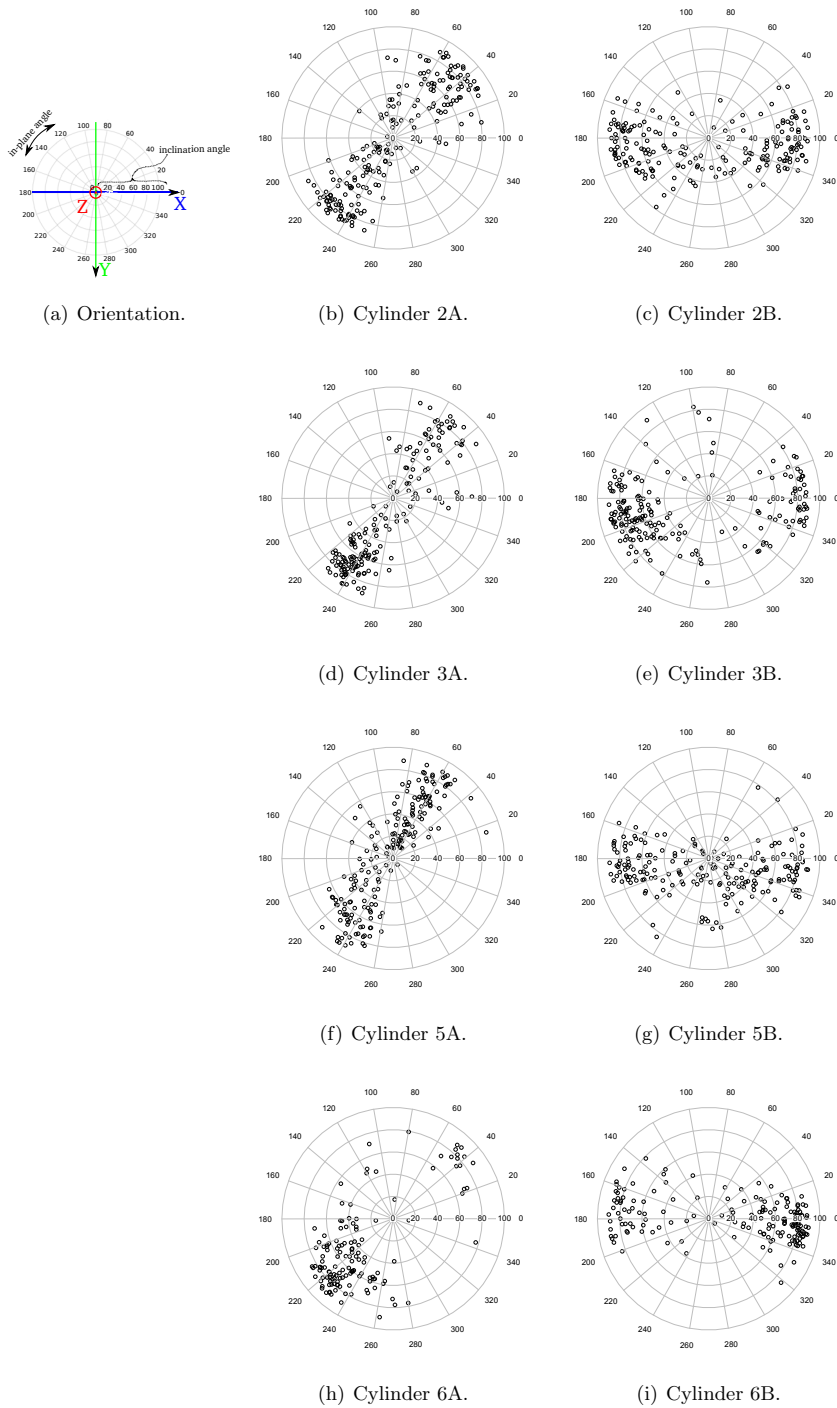
(i) Cylinder 6B.

Figure A.3.4. Scatter plots of fibre orientation variations measured by µCT between the side (Cylinder *.A) and centre ("Cylinder *.B") cylinder samples. In (a) the radius represents the inclination angle θ and in-plane angle ϕ is on circumference. Z-axis corresponds to the direction of the tensile stress in a slab, Fig. 2.4.

A.4 Measured fibre alignments characterized by the eigenvectors of the 2nd order alignment tensor in the tested slabs

Tables A.4.1, A.4.2 and A.4.3 present fibre orientation distribution characteristics for the top, middle and bottom parts of the cylinder samples scanned by µCT, respectively. The orientation characteristics include the scalar-order parameter S and triplet of the eigenvectors $\mathbf{d}^1, \mathbf{d}^2, \mathbf{d}^3$ from the 2nd order alignment tensor in the spherical coordinate system. $S = 1$ corresponds to the transversely isotropic material symmetry, $S = 0$ to isotropy and $S = -\frac{1}{2}$ describes the plane isotropic case. The biaxiality b_S shows the non-symmetry of the distribution with respect to $\mathbf{d}^1$. Figs. A.4.1, A.4.2, A.4.3 demonstrate the location of the eigenvectors $\mathbf{d}^1, \mathbf{d}^2, \mathbf{d}^3$ in all measured cylinder samples. The location of the top, middle and bottom parts is given in Fig. 2.17(a).

Table A.4.1. Fibre orientation distribution characteristics for the top parts of the cylinder samples.

Cylinder nr.	S	b_S	$\mathbf{d}^1(\theta, \phi)$, deg	$\mathbf{d}^2(\theta, \phi)$, deg	$\mathbf{d}^3(\theta, \phi)$, deg
1A	0.49	0.13	53, 222	81, 126	38, 24
1B	0.33	0.009	82, 2	17, 119	75, 269
4A	-0.43	-0.11	87, 122	53, 215	37, 28
4B	0.35	0.11	78, 160	63, 64	30, 272

Table A.4.2. Fibre orientation distribution characteristics for the middle parts of the cylinder samples.

Cylinder nr.	S	b_S	$\mathbf{d}^1(\theta, \phi)$, deg	$\mathbf{d}^2(\theta, \phi)$, deg	$\mathbf{d}^3(\theta, \phi)$, deg
1A	0.52	0.11	28, 227	89, 136	62, 45
1B	0.53	0.09	74, 3	85, 271	17, 163
3A	0.52	0.12	76, 237	85, 145	15, 36
3B	0.59	0.05	79, 190	47, 89	45, 291
4A	-0.44	-0.13	81, 322	51, 224	41, 63
4B	0.62	0.09	89, 169	66, 78	24, 262
5A	-0.44	-0.05	80, 329	77, 61	17, 204
5B	-0.39	-0.06	73, 87	87, 356	18, 256
6A	0.65	0.03	68, 223	64, 324	36, 98
6B	0.63	0.08	81, 356	83, 265	12, 139

Table A.4.3. Fibre orientation distribution characteristics for the bottom parts of the cylinders.

Cylinder nr.	S	b_S	$\mathbf{d}^1(\theta, \phi)$,deg	$\mathbf{d}^2(\theta, \phi)$,deg	$\mathbf{d}^3(\theta, \phi)$,deg
1A	0.70	0.07	14, 52	90, 321	76, 231
1B	0.65	0.09	87, 185	87, 275	4, 57
4A	0.59	0.09	45, 203	73, 311	50, 56
4B	0.72	0.05	86, 175	80, 84	11, 287

(a) Orientation.

(b) **Top part.** Cylinder 1A.

(c) Cylinder 1B.

(d) **Middle part.** Cylinder 1A.

(e) Cylinder 1B.

(f) **Bottom part.** Cylinder 1A.
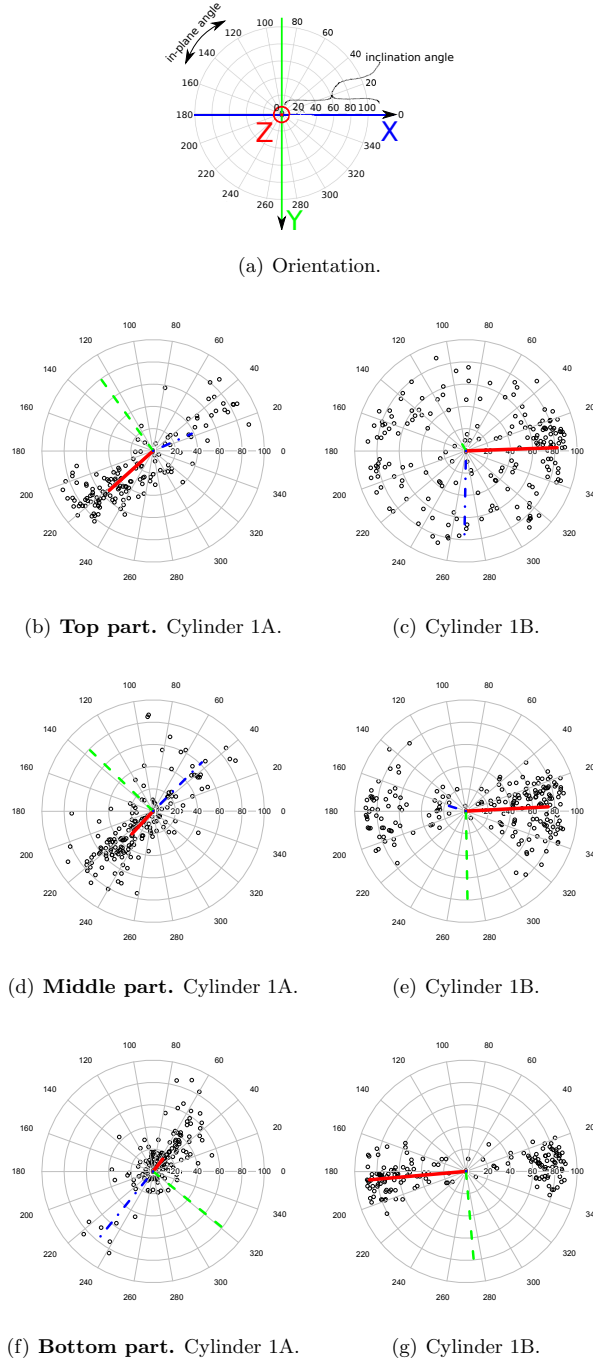
(g) Cylinder 1B.

Figure A.4.1. Fibre orientation distributions with the triplets of the eigenvectors $\mathbf{d}^1, \mathbf{d}^2, \mathbf{d}^3$ for the height of the whole cylinder samples 1A and 1B. $\mathbf{d}^1$-solid red line, $\mathbf{d}^2$-dashed green line, $\mathbf{d}^3$-dot-dashed blue line. $\mathbf{d}^1$ is the director corresponding to according-to-amount-largest eigenvalue. In (a) the radius represents the inclination angle θ and in-plane angle ϕ is on circumference. Z-axis corresponds to the direction of the tensile stress in a slab, Fig. 2.4.

(a) Orientation.

(b) **Top part.** Cylinder 4A.

(c) Cylinder 4B.

(d) **Middle part.** Cylinder 4A.

(e) Cylinder 4B.

(f) **Bottom part.** Cylinder 4A.
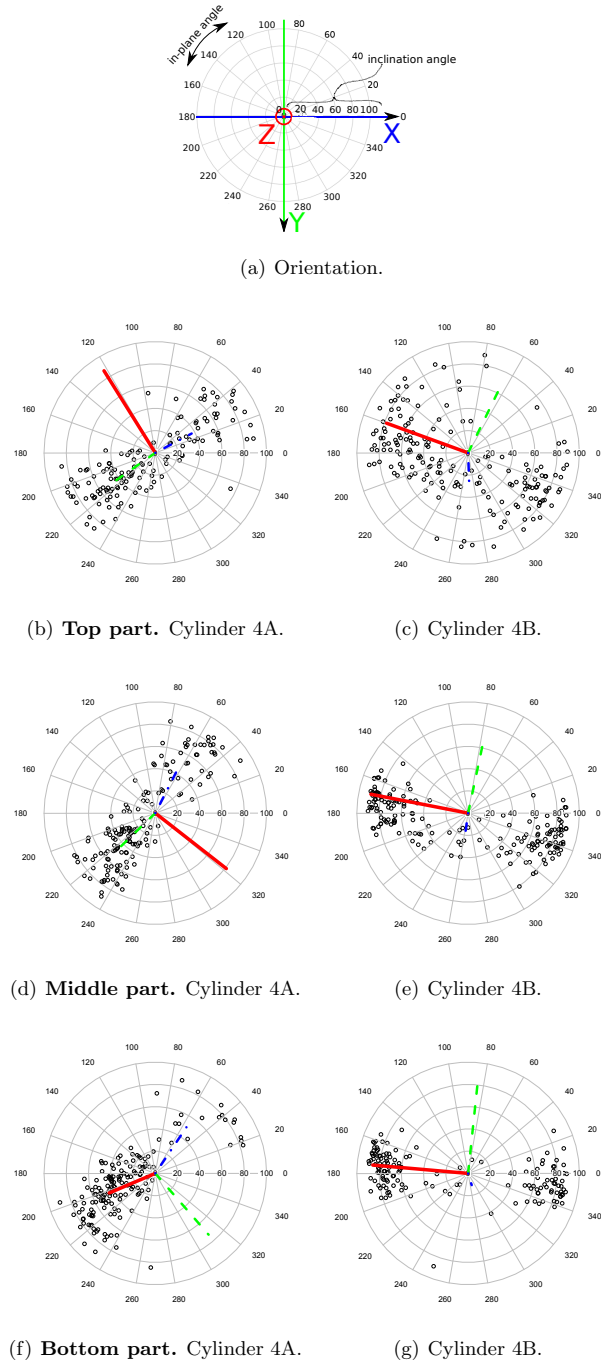
(g) Cylinder 4B.

Figure A.4.2. Fibre orientation distributions with the triplets of the eigenvectors $\mathbf{d}^1, \mathbf{d}^2, \mathbf{d}^3$ for the height of the whole cylinder samples 4A and 4B. $\mathbf{d}^1$-solid red line, $\mathbf{d}^2$-dashed green line, $\mathbf{d}^3$-dot-dashed blue line. $\mathbf{d}^1$ is the director corresponding to according-to-amount-largest eigenvalue. In (a) the radius represents the inclination angle θ and in-plane angle ϕ is on circumference. Z-axis corresponds to the direction of the tensile stress in a slab, Fig. 2.4.

(a) Orientation.

(b) Cylinder 3A.   (c) Cylinder 5A.   (d) Cylinder 6A.

(e) Cylinder 3B.   (f) Cylinder 5B.   (g) Cylinder 6B.
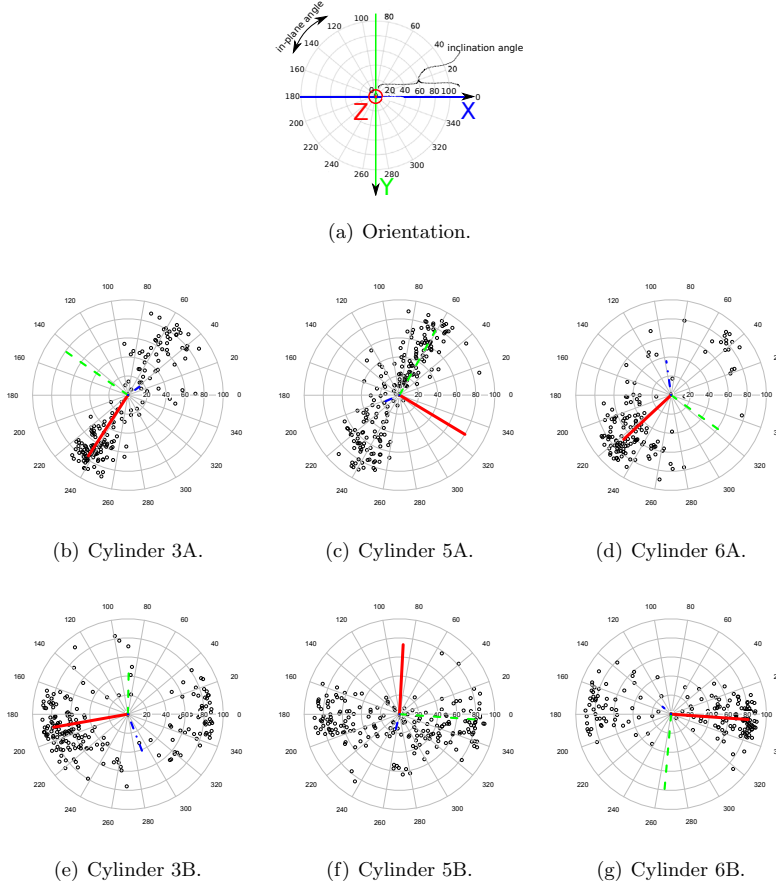
Figure A.4.3. Fibre orientation distributions with the triplets of the eigenvectors $\mathbf{d}^1, \mathbf{d}^2, \mathbf{d}^3$ for the middle parts of the cylinder samples. $\mathbf{d}^1$-solid red line, $\mathbf{d}^2$-dashed green line, $\mathbf{d}^3$-dot-dashed blue line. $\mathbf{d}^1$ is the director corresponding to according-to-amount-largest eigenvalue. In (a) the radius represents the inclination angle θ and in-plane angle ϕ is on circumference. Z-axis corresponds to the direction of the tensile stress in a slab, Fig. 2.4.

A.5   Measured fibre orientation distribution functions in the tested slabs

Figs. A.5.1, A.5.2, A.5.3–A.5.5 present the approximated with the 2nd order alignment tensor ODFs of fibres in the top, bottom and middle parts, respectively. The density values of the approximated ODFs are normalized according to the explanation given in Section 4.5. The orientation-weighted orthotropic elasticity of fibres in material meso-symmetry axes are calculated in the cylinder samples 3A, 3B, 5A, 5B, 6A, 6B and presented in Eqs. (A.5.1-A.5.3) employing the Kelvin-Mandel variant of the Voigt notation.

(a) Cylinder 1A.

(b) Cylinder 1A.

(c) Cylinder 1B.

(d) Cylinder 1B.

(e) Cylinder 4A.

(f) Cylinder 4A.

(g) Cylinder 4B.
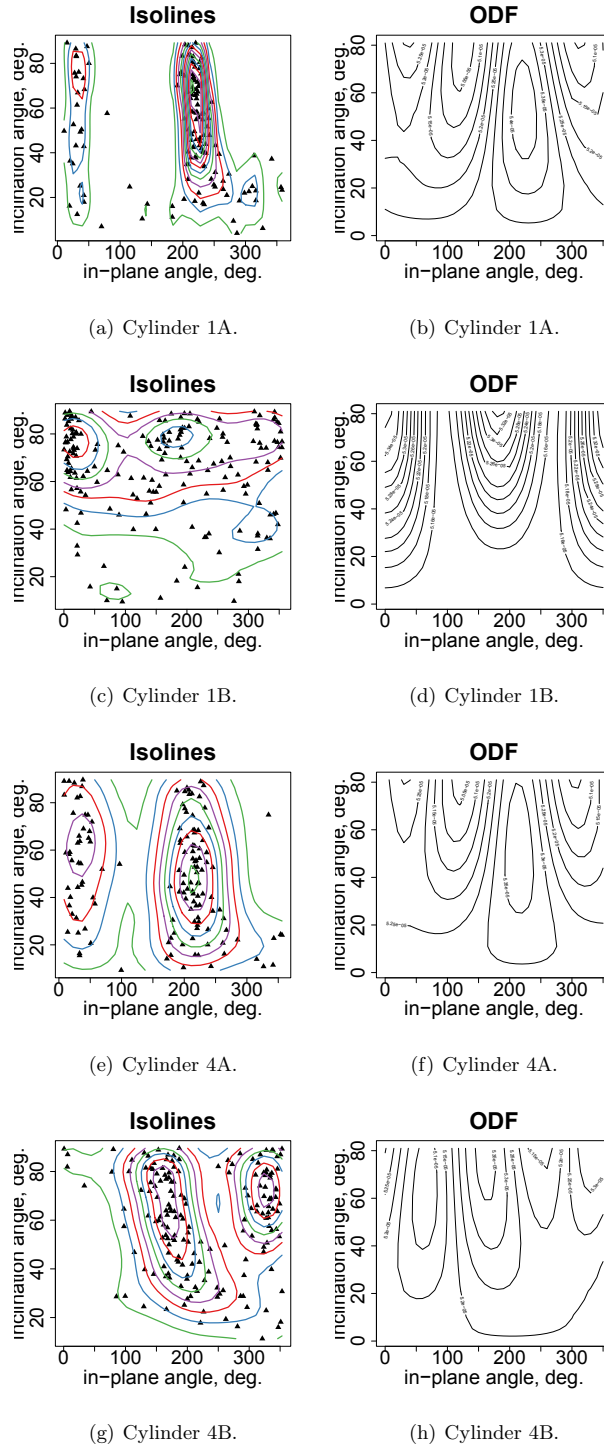
(h) Cylinder 4B.

Figure A.5.1. The top parts of the cylinder samples. The isolines of the measured fibre orientation distributions and the ODFs of fibres approximated using the 2nd order alignment tensor.

(a) Cylinder 1A.

(b) Cylinder 1A.

(c) Cylinder 1B.

(d) Cylinder 1B.

(e) Cylinder 4A.

(f) Cylinder 4A.

(g) Cylinder 4B.
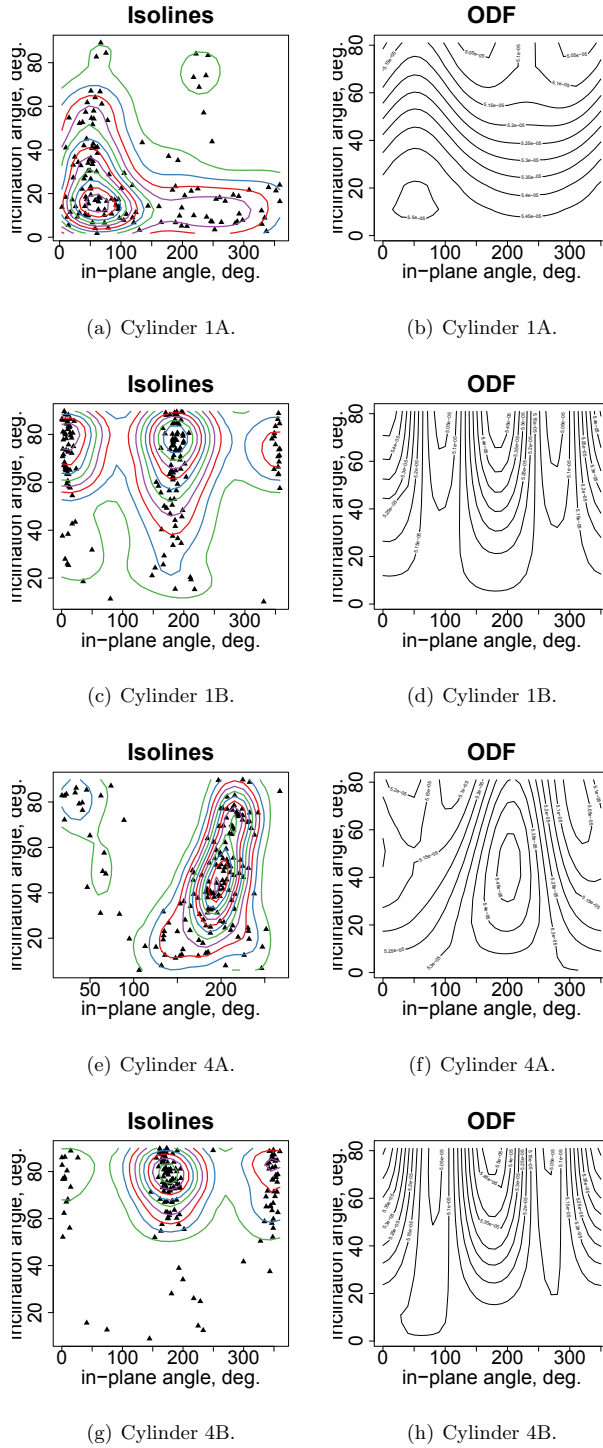
(h) Cylinder 4B.

Figure A.5.2. The bottom parts of the cylinder samples. The isolines of the measured fibre orientation distributions and the ODFs of fibres approximated using the 2nd order alignment tensor.

(a) Cylinder 1A.

(b) Cylinder 1A.

(c) Cylinder 1B.

(d) Cylinder 1B.

(e) Cylinder 3A.

(f) Cylinder 3A.

(g) Cylinder 3B.
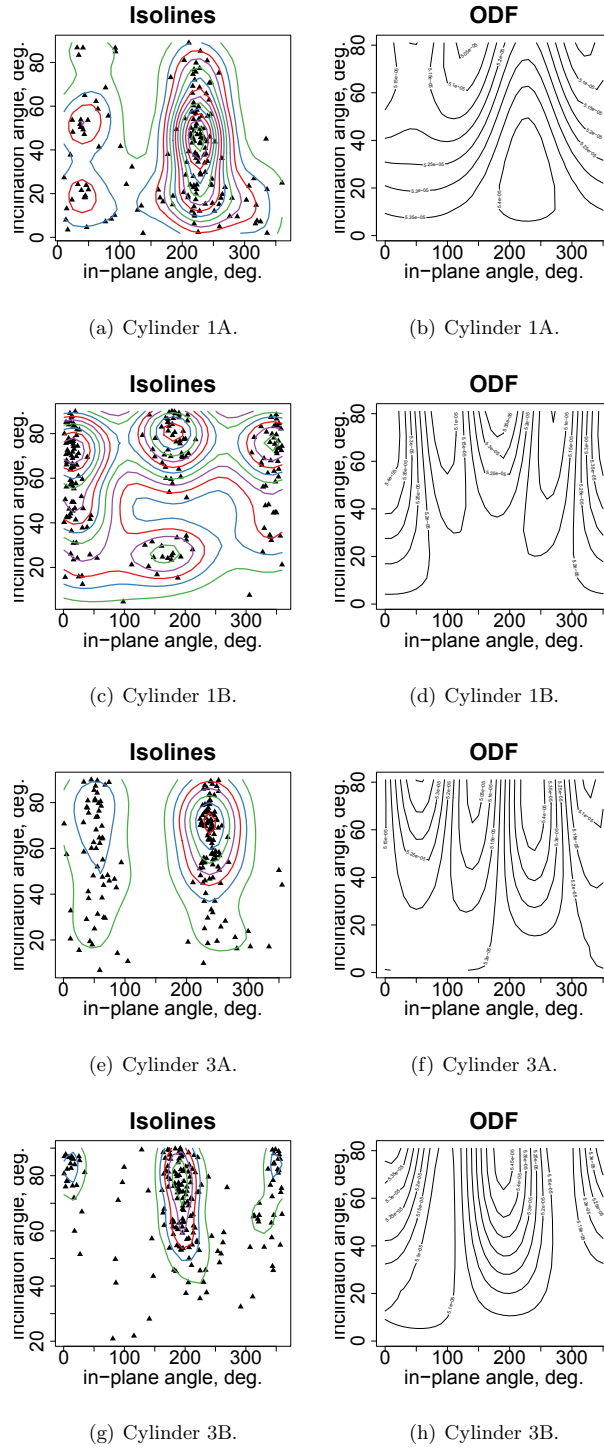
(h) Cylinder 3B.

Figure A.5.3. The middle parts of the cylinder samples 1A–3B. The isolines of the measured fibre orientation distributions and the ODFs of fibres approximated using the 2nd order alignment tensor.

(a) Cylinder 4A.

(b) Cylinder 4A.

(c) Cylinder 4B.

(d) Cylinder 4B.

(e) Cylinder 5A.

(f) Cylinder 5A.

(g) Cylinder 5B.
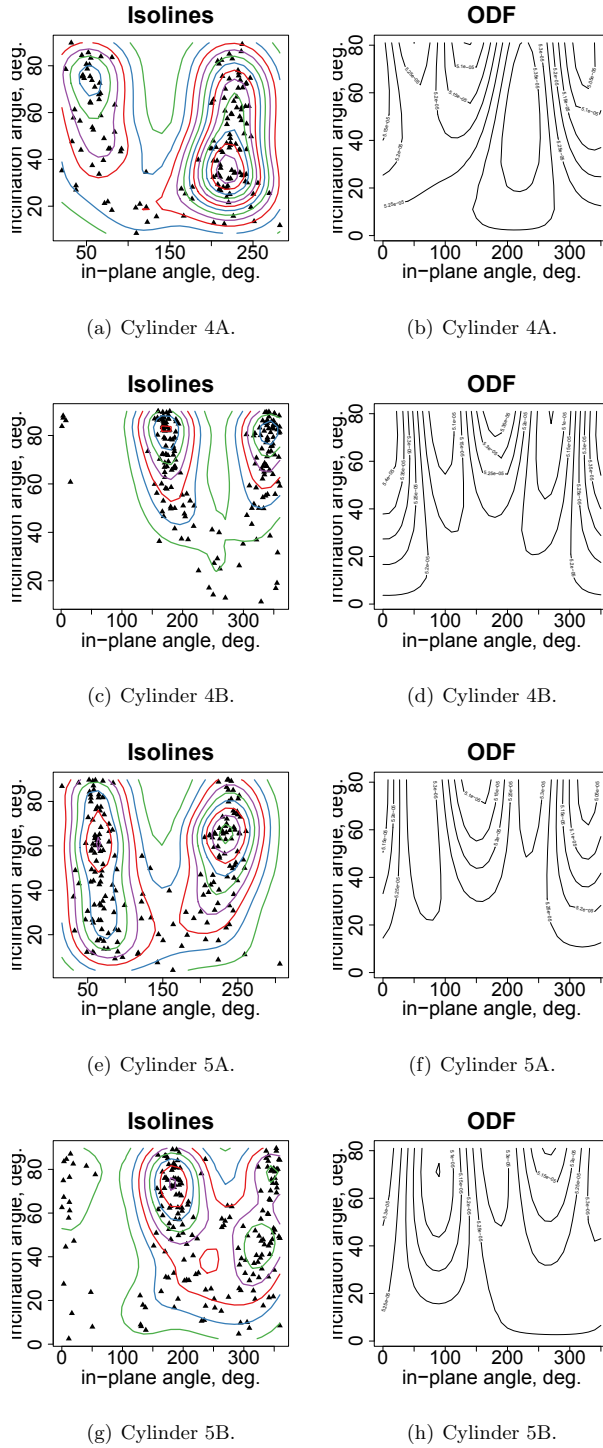
(h) Cylinder 5B.

Figure A.5.4. The middle parts of the cylinder samples 4A–5B. The isolines of the measured fibre orientation distributions and the ODFs of fibres approximated using the 2nd order alignment tensor.
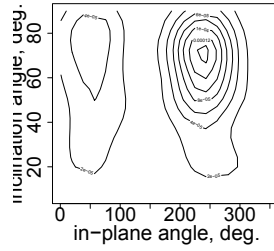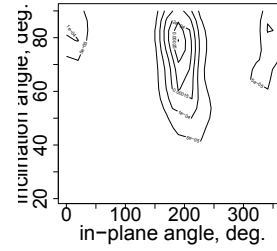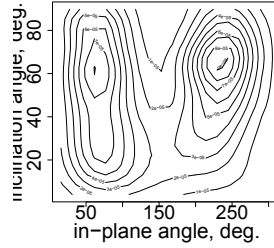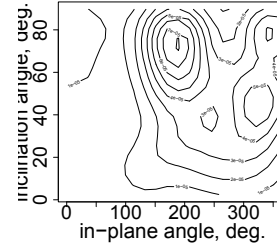
(a) Cylinder 6A.
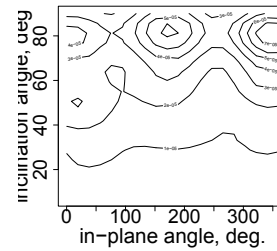
(b) Cylinder 6A.

(c) Cylinder 6B.
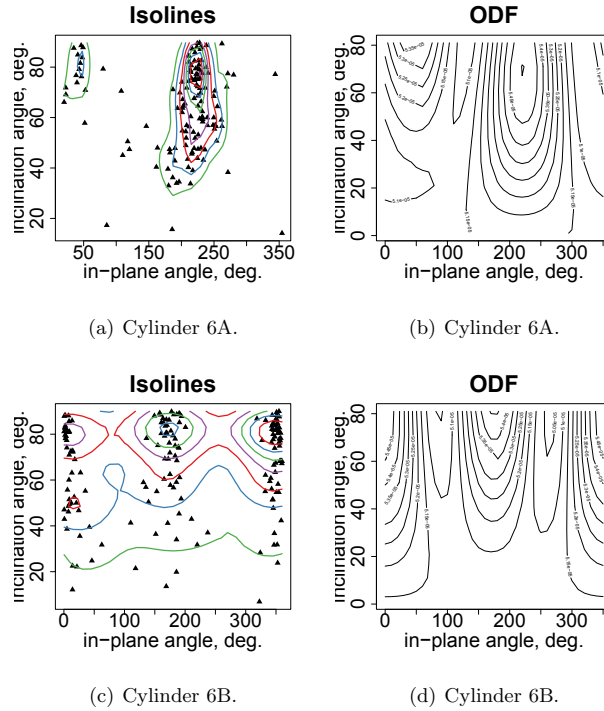
(d) Cylinder 6B.

Figure A.5.5. The middle parts of the cylinder samples 6A–6B. The isolines of the measured fibre orientation distributions and the ODFs of fibres approximated using the 2nd order alignment tensor.

For the middle parts of the cylinder samples 3A and 3B the orientation-weighted orthotropic meso-elasticity of fibres in material meso-symmetry axes are:

$$C^{(f_{ms})}_{\alpha\beta} = Y^{(f)}.$$

$$C^{(f_{ms})}_{\alpha\beta} = Y^{(f)}.$$

$$
\begin{pmatrix}
0.50 & 0.07 & 0.11 & 0 & 0 & 0 \\
0.07 & -0.06 & 0.02 & 0 & 0 & 0 \\
0.11 & 0.02 & 0.16 & 0 & 0 & 0 \\
0 & 0 & 0 & 0.04 & 0 & 0 \\
0 & 0 & 0 & 0 & 0.22 & 0 \\
0 & 0 & 0 & 0 & 0 & 0.15
\end{pmatrix},
\begin{pmatrix}
0.54 & 0.09 & 0.1 & 0 & 0 & 0 \\
0.09 & -0.01 & 0.01 & 0 & 0 & 0 \\
0.1 & 0.01 & 0.07 & 0 & 0 & 0 \\
0 & 0 & 0 & 0.02 & 0 & 0 \\
0 & 0 & 0 & 0 & 0.20 & 0 \\
0 & 0 & 0 & 0 & 0 & 0.18
\end{pmatrix}
$$

$$(A.5.1)$$

For the middle parts of the cylinder samples 5A and 5B they are, respectively:

$$C^{(f_{ms})}_{\alpha\beta} = Y^{(f)}.$$

$$C^{(f_{ms})}_{\alpha\beta} = Y^{(f)}.$$

$$
\begin{pmatrix}
-0.05 & 0.05 & 0.04 & 0 & 0 & 0 \\
0.05 & 0.37 & 0.11 & 0 & 0 & 0 \\
0.04 & 0.11 & 0.28 & 0 & 0 & 0 \\
0 & 0 & 0 & 0.22 & 0 & 0 \\
0 & 0 & 0 & 0 & 0.08 & 0 \\
0 & 0 & 0 & 0 & 0 & 0.11
\end{pmatrix},
\begin{pmatrix}
-0.02 & 0.06 & 0.04 & 0 & 0 & 0 \\
0.06 & 0.36 & 0.1 & 0 & 0 & 0 \\
0.04 & 0.1 & 0.26 & 0 & 0 & 0 \\
0 & 0 & 0 & 0.21 & 0 & 0 \\
0 & 0 & 0 & 0 & 0.08 & 0 \\
0 & 0 & 0 & 0 & 0 & 0.11
\end{pmatrix}
$$

$$(A.5.2)$$

and for the middle parts of the cylinder samples 6A and 6B they are:

$$C_{\alpha\beta}^{(f_{ms})} = Y^{(f)}.$$

$$C_{\alpha\beta}^{(f_{ms})} = Y^{(f)}.$$

$$
\begin{pmatrix}
0.57 & 0.09 & 0.1 & 0 & 0 & 0 \\
0.09 & -0.01 & 0.01 & 0 & 0 & 0 \\
0.1 & 0.01 & 0.04 & 0 & 0 & 0 \\
0 & 0 & 0 & 0.01 & 0 & 0 \\
0 & 0 & 0 & 0 & 0.20 & 0 \\
0 & 0 & 0 & 0 & 0 & 0.19
\end{pmatrix}
,
\begin{pmatrix}
0.56 & 0.09 & 0.11 & 0 & 0 & 0 \\
0.09 & -0.04 & 0.01 & 0 & 0 & 0 \\
0.11 & 0.01 & 0.09 & 0 & 0 & 0 \\
0 & 0 & 0 & 0.01 & 0 & 0 \\
0 & 0 & 0 & 0 & 0.21 & 0 \\
0 & 0 & 0 & 0 & 0 & 0.17
\end{pmatrix}
$$

$$(A.5.3)$$

Curriculum Vitae

Marika Eik

Personal information

Date of Birth	December 11, 1976
Nationality	Estonian
Contact	✉ marika.eik@aalto.fi ☎ +372 555 68712
	✉ me@cens.ioc.ee

Education

2009 − 2014	**Aalto University School of Engineering (AALTO) Department of Civil and Structural Engineering**
	Espoo, Finland
Subject	**D.Sc., Technology**
Thesis	Orientation of short steel fibres in concrete: measuring and modelling
Supervisor	**Prof. Dr. Jari Puttonen**, jari.puttonen@aalto.fi
	Department of Civil and Structural Engineering, AALTO
2007 − 2014	**Tallinn University of Technology (TUT)** Tallinn, Estonia **Faculty of Civil Engineering, Institute of Cybernetics at TUT**
Subject	**Ph.D., Engineering**
Thesis	Orientation of short steel fibres in concrete: measuring and modelling
Supervisor	**Dr. rer. nat. Heiko Herrmann**, hh@cens.ioc.ee
	Mechanics and Applied Mathematics Department, Institute of Cybernetics at TUT
2004 − 2007	**Tallinn University of Technology** Tallinn, Estonia **Faculty of Civil Engineering, Department of Structural Design**
Subject	**M.Sc., Civil Engineering**
Thesis	Post-tensioned roof-ceiling project of Mikkeli's parking house
Supervisor	**Prof. Emeeritus Vello Otsmaa**, vello.otsmaa@ttu.ee
	Faculty of Civil Engineering, Department of Structural Design, TUT
1999 − 2004	**Tallinn University of Technology** Tallinn, Estonia **Faculty of Civil Engineering, Department of Structural Design**
Subject	**Diploma *cum laude*, Civil Engineering**
Thesis	Design of load-bearing structures of `Sammutin Oy` fire engines factory
Supervisor	**Prof. Emeeritus Vello Otsmaa**, vello.otsmaa@ttu.ee
	Faculty of Civil Engineering, Department of Structural Design, TUT
1995–1998	**Tallinn University of Applied Sciences** Tallinn, Estonia
Subject	**Diploma with honours, Civil Engineering**

Research experience

2011 − Present	**Institute of Cybernetics at TUT**	Tallinn, Estonia
	Mechanics and Applied Mathematics Department	
Supervisor	**Dr. rer. nat. Heiko Herrmann**	

The research is focused on the concrete reinforced by short steel fibres, SFRC. The examinations within two research branches: measuring of fibre orientations from the hardened concrete matrix and modelling of composite properties considering the anisotropic behaviour occurring due to different alignments of short steel fibres. The empirical investigations implemented include the following measuring techniques: DC-conductivity testing combined with photometry and X-ray micro-tomography scanning. The material model developed for one meso-volume element of SFRC is orthotropic linear-elastic and is valid in the case of microcracks. The model can be implemented in numerical applications. Doctor-level study project

2010 − Present	**Aalto University School of Engineering**	Espoo, Finland
	Department of Civil and Structural Engineering	
Supervisor	**Prof. Dr. Jari Puttonen**	

The subject of the research is also focused on the concrete reinforced by short steel fibres, SFRC. Doctor-level study project

2004 − 2007	**Tallinn University of Technology**	Tallinn, Estonia
	Faculty of Civil Engineering, Department of Structural Design	
Supervisor	**Prof. Emeeritus Vello Otsmaa**	

The design–strength calculations–of post-tensioned cast concrete slab, simple- and continuous beams employing unbonded stressing tendons. The study of the method based on the load balancing principle, the application of the method to identify the initial necessary stressing force in a structure. Master-level studies

Scholarships and awards

- Jaanus Otsa doctoral Scholarship of TUT Development Foundation and TUT Alumni Association, 2012

Teaching

- Seminars on Structural Mechanics I, TUT 2010
- Geotechnical laboratories, TUT 2008

Work Experience

2011 − Present	**Institute of Cybernetics at TUT**	Tallinn, Estonia
	Mechanics and Applied Mathematics Department	
Position	**Researcher/Ph.D. student**	

2010 − Present	**Aalto University School of Engineering**	Espoo, Finland
	Department of Civil and Structural Engineering	
Position	**Doctoral Candidate**	

| **2007 − 2009** | **Nordecon Betoon OÜ** | Tallinn, Estonia |
| Position | **Project Manager/Designer** | |

Design of load-bearing cast concrete structures

2003 − 2007	**Mittatyö Eesti OÜ**	Tallinn, Estonia
		Yväskülä, Finland
Position	**Project Manager/Designer**	

Design of load-bearing pre-cast concrete structures

| **06/2003–03/2003** | **Neoprojekt OÜ** | Tallinn, Estonia |
| Position | **Designer (Civil Engineering)** | |

| **01/2003–05/2003** | **E–Inseneribüroo OÜ** | Tallinn, Estonia |
| Position | **Designer (Civil Engineering)** | |

| **06/2002–08/2002** | **E–Betoonelement AS** | Tallinn, Estonia |
| Position | **Designer (Civil Engineering)** | |

| **02/1998–08/1999** | **Elisor AS** | Tallinn, Estonia |
| Position | **Assistant of surveying engineer** | |

Preparation and design of topological base-plans.

Languages

Estonian	mother tongue
Russian	mother tongue
English	fluent
Finnish	good
German	basic

Computer Skills

Operating Systems	UNIX/Linux, Windows
Programming	Routine use of `R`, experience with Matlab, Visual Basic
Computer algebra systems	`Maxima`
Text processors	Routine use of `LaTeX`, experience with OpenOffice
Scientific and engineering software	AutoCad, Robot Structural Analysis, `ImageJ`

Publications

- M. Eik, J. Puttonen; **Challenges of steel fibre reinforced concrete in load bearing structures.** *Rakenteiden mekaniikka (Journal of Structural Mechanics)*, 44, 1, 44-64, `http://rmseura.tkk.fi/rmlehti/2011/nro1/`, June 2011

- H. Herrmann, M. Eik; **Some comments on the theory of short fibre reinforced materials.** *Proceedings of the Estonian Academy of Sciences*, 60, 3, 179-183, `http://dx.doi.org/10.3176/proc.2011.3.06`, June 2011

- M. Eik, H. Herrmann; **Raytraced images for testing the reconstruction of fibre orientation distributions.** *Proceedings of the Estonian Academy of Sciences*, 61, 2, 128-136, `http://dx.doi.org/10.3176/proc.2012.2.05`, June 2012

- J.-P. Suuronen, A. Kallonen, M. Eik, J. Puttonen, R. Serimaa, H. Herrmann; **Analysis of short fibres orientation in steel fibre reinforced concrete (SFRC) using X-ray tomography.** *Journal of Materials Science*, 48, 3, 1358-1367, `http://dx.doi.org/10.1007/s10853-012-6882-4`, February 2013

- M. Eik, K. Lõhmus, M. Tigasson, M. Listak, J. Puttonen, H. Herrmann; **DC-conductivity testing combined with photometry for measuring fibre orientations in SFRC.** *Journal of Materials Science*, 48, 10, 3745-3759, `http://dx.doi.org/10.1007/s10853-013-7174-3`, May 2013

- M. Eik, J. Puttonen, H. Herrmann; **Fibre orientation phenomenon in concrete composites: measuring and theoretical modelling.** 7th *International Conference FIBRE CONCRETE 2013, Technology, Design, Application; Conference Proceedings*, 1-4, September 2013

Conference presentations

2011	6th **International Conference on Composite Structures (ICCS16)**
	Porto, Portugal
Oral	M. Eik, H. Herrmann
	Measuring Fibre Orientation in Steel Fibre Reinforced Concrete

2012	8th **European Solid Mechanics Conference (ESMC16)** Graz, Austria
Oral	M. Eik, J. Puttonen, H. Herrmann
	Orientation distribution of fibres in short-fibre reinforced concrete: evaluation and introduction to constitutive relations

2013	7th **International Conference FIBRE CONCRETE 2013 Technology, Design, Application**
	Prague, Czech Republic
Oral	M. Eik, J. Puttonen, H. Herrmann
	Fibre orientation phenomenon in concrete composites: measuring and theoretical modelling

Extras

Licenses	category B driver's license
Interests	dog breeding, photography, yoga, travelling

Marika Eik

Isikuandmed

Sünniaeg	11. Detsember, 1976
Sünnikoht	Tallinn
Kodakondsus	Eesti
Kontakt	✉ marika.eik@aalto.fi ☎ +372 555 68712
	✉ me@cens.ioc.ee

Hariduskäik

2009 − 2014	**Aalto University School of Engineering (AALTO)**
	Ehitusteaduskond Espoo, Soome
Eriala	**D.Sc., Tehnikateadused**
Lõputöö teema	Metallist lühikiudude orientatsioon betoonis: mõõtmine ja modelleerimine
Juhendaja	**Prof. Dr. Jari Puttonen**, jari.puttonen@aalto.fi
	Ehitusteaduskond, AALTO

2007 − 2014	**Tallinna Tehnikaülikool (TTÜ)** Tallinn, Eesti
	Ehitusteaduskond, Küberneetika Instituut
Eriala	**Ph.D., Inseneriteadused**
Lõputöö teema	Metallist lühikiudude orientatsioon betoonis: mõõtmine ja modelleerimine
Juhendaja	**Dr. rer. nat. Heiko Herrmann**, hh@cens.ioc.ee
	Mehaanika ja rakendusmatemaatika osakond, TTÜ Küberneetika Instituut

2004 − 2007	**Tallinna Tehnikaülikool** Tallinn, Eesti
	Ehitusteaduskond, Ehitiste projekteerimise instituut
Eriala	**M.Sc., Ehitustehnika**
Lõputöö teema	Mikkeli autoparkla järeltõmmatud pingearmatuuriga katuslae projekt
Juhendaja	**Prof. Emeeritus Vello Otsmaa**, vello.otsmaa@ttu.ee
	Ehitusteaduskond, Ehitiste projekteerimise instituut, TTÜ

1999 − 2004	**Tallinna Tehnikaülikool** Tallinn, Eesti
	Ehitusteaduskond
Eriala	**Diploma *cum laude*, Ehitusprojekteerimine**
Lõputöö teema	`Sammutin Oy` tuletõrjemasinate tehase kandekonstruktsioonide projekt
Juhendaja	**Prof. Emeeritus Vello Otsmaa**, vello.otsmaa@ttu.ee
	Ehitusteaduskond, Ehitiste projekteerimise instituut, TTÜ

1995–1998	**Tallinna Tehnikakõrgkool** Tallinn, Eesti
Eriala	**Diplom kiitusega, Hoonete ehitus**

Teadustöö kogemus

2011 – ...	**TTÜ Küberneetika Instituut**	Tallinn, Eesti
	Mehaanika ja rakendusmatemaatika osakond	
Juhendaja	**Dr. rer. nat. Heiko Herrmann**	

Teadustöö käsitleb tsemendipõhist komposiitmaterjali, mis on moodustatud betoonmassi (matriitsi) ja lühikeste teraskiudude kokku segamisega, mille tulemuseks on teraskiudbetoon. Uuringud hõlmavad kahte teadusharu: lühikeste teraskiudude orientatsiooni jaotuse mõõtmise kivistunud betoonmatriitsis ning komposiidi omaduste modelleerimist võttes arvesse anisotroopset käitumist, mis tuleneb lühikiudude erinevast orientatsiooni jaotusest matriitsis. Empiiriliste uuringute käigus on arendatud kahte meetodit lühikiudude orientatsiooni jaotuse mõõtmiseks: alalisvoolu juhtivuse mõõtmine kombineerituna fotoanalüüsiga ning mikro-kompuutertomograafia. Teadustöö käigus välja töötatud materjalimudel ühe teraskiudbetooni meso-ruumelemendi jaoks on ortotroopne lineaarne-elastne ning kehtib mikropragude puhul. Antud materjalimudelit saab rakendada numbrilistes arvutustes. Doktoriõpe

2010 – ...	**Aalto University School of Engineering**	Espoo, Soome
	Ehitusteaduskond	
Juhendaja	**Prof. Dr. Jari Puttonen**	

Teadustöö teema on samuti suunatud teraskiudbetooni uurimisele. Doktoriõpe

2004 – 2007	**Tallinna Tehnikaülikool**	Tallinn, Eesti
	Ehitusteaduskond, Ehitiste projekteerimise instituut	
Juhendaja	**Prof. Emeeritus Vello Otsmaa**	

Magistritöö käsitleb järeltõmmatud armatuuriga betoonplaadi, ühe- ja mitmesildelise talade projekteerimist. Nimetatud kandekonstruktsioonid on pingestatud nakketa pingestustrossidega. Lisaks, on uuritud koormuse tasakaalustamise meetodit ja selle rakendamist esialgse algeelpingestusjõu hindamisel. Magistriõpe

Stipendiumid ja autasud

- TTÜ Arengufond, Jaanus Otsa doktoriõppe stipendium, 2012

Õpetustegevus

- Seminarid Ehitusmehaanikas I, TTÜ 2010
- Geotehnikalaborid, TTÜ 2008

Teenistuskäik

2011 – ...	**TTÜ Küberneetika Instituut**	Tallinn, Eesti
	Mehaanika ja rakendusmatemaatika osakond	
Ametikoht	**Teadur/doktorant**	

2010 – ...	**Aalto University School of Engineering**	Espoo, Soome
	Ehitusteaduskond	
Ametikoht	**Doktorant**	

| **2007 − 2009** | **Nordecon Betoon OÜ** | Tallinn, Eesti |
| Aᴍᴇᴛɪᴋᴏʜᴛ | **Projektijuht/Projekteerija** | |

Monoliitraudbetoonist kandekonstruktsioonide projekteerimine

2003 − 2007	**Mittatyö Eesti OÜ**	Tallinn, Eesti
		Yväskülä, Soome
Aᴍᴇᴛɪᴋᴏʜᴛ	**Projektijuht/Projekteerija**	

Kandvate raudbetoonkonstruktsioonide projekteerimine (raudbetoonelemendid)

| **06/2003–03/2003** | **Neoprojekt OÜ** | Tallinn, Eesti |
| Aᴍᴇᴛɪᴋᴏʜᴛ | **Projekteerija (Ehitus)** | |

01/2003–05/2003	**E–Inseneribüroo OÜ**	Tallinn, Eesti
Aᴍᴇᴛɪᴋᴏʜᴛ	**Projekteerija (Ehitus)**	
06/2002–08/2002	**E–Betoonelement AS**	Tallinn, Eesti
Aᴍᴇᴛɪᴋᴏʜᴛ	**Projekteerija (Ehitus)**	

| **02/1998–08/1999** | **Elisor AS** | Tallinn, Eesti |
| Aᴍᴇᴛɪᴋᴏʜᴛ | **Geodeesiainseneri assistent** | |

Geodeetiliste alusplaanide ettevalmistamine ja vormistamine

Kᴇᴇʟᴛᴇᴏꜱᴋᴜꜱ

Eᴇꜱᴛɪ ᴋᴇᴇʟ	emakeel
Vᴇɴᴇ ᴋᴇᴇʟ	emakeel
Iɴɢʟɪꜱᴇ ᴋᴇᴇʟ	kõrgtase
Sᴏᴏᴍᴇ ᴋᴇᴇʟ	kesktase
Sᴀᴋꜱᴀ ᴋᴇᴇʟ	algtase

Aʀᴠᴜᴛɪᴏꜱᴋᴜꜱ

Operatsioonisüsteemid	UNIX/Linux, Windows
Programmeerimine	R, Matlab, Visual Basic
Kompuuteralgebra süsteemid	Maxima
Tekstitöötlus	LaTeX, OpenOffice
Teadus- ja inseneritarkvara	AutoCad, Robot Structural Analysis, ImageJ

Pᴜʙʟɪᴋᴀᴛꜱɪᴏᴏɴɪᴅ

- M. Eik, J. Puttonen; **Challenges of steel fibre reinforced concrete in load bearing structures.** *Rakenteiden mekaniikka (Journal of Structural Mechanics)*, 44, 1, 44-64, http://rmseura.tkk.fi/rmlehti/2011/nro1/, June 2011

- H. Herrmann, M. Eik; **Some comments on the theory of short fibre reinforced materials.** *Proceedings of the Estonian Academy of Sciences*, 60, 3, 179-183, http://dx.doi.org/10.3176/proc.2011.3.06, June 2011

- M. Eik, H. Herrmann; **Raytraced images for testing the reconstruction of fibre orientation distributions.** *Proceedings of the Estonian Academy of Sciences*, 61, 2, 128-136, http://dx.doi.org/10.3176/proc.2012.2.05, June 2012

- J.-P. Suuronen, A. Kallonen, M. Eik, J. Puttonen, R. Serimaa, H. Herrmann; **Analysis of short fibres orientation in steel fibre reinforced concrete (SFRC) using X-ray tomography.** *Journal of Materials Science*, 48, 3, 1358-1367, `http://dx.doi.org/10.1007/s10853-012-6882-4`, February 2013

- M. Eik, K. Lõhmus, M. Tigasson, M. Listak, J. Puttonen, H. Herrmann; **DC-conductivity testing combined with photometry for measuring fibre orientations in SFRC.** *Journal of Materials Science*, 48, 10, 3745-3759, `http://dx.doi.org/10.1007/s10853-013-7174-3`, May 2013

- M. Eik, J. Puttonen, H. Herrmann; **Fibre orientation phenomenon in concrete composites: measuring and theoretical modelling.** 7th *International Conference FIBRE CONCRETE 2013, Technology, Design, Application; Conference Proceedings*, 1-4, September 2013

ETTEKANDED RAHVUSVAHELISTEL KONVERENTSIDEL

2011	6th **International Conference on Composite Structures (ICCS16)**
	Porto, Portugal
SUULINE	M. Eik, H. Herrmann
	Measuring Fibre Orientation in Steel Fibre Reinforced Concrete
2012	8th **European Solid Mechanics Conference (ESMC16)** Graz, Austria
SUULINE	M. Eik, J. Puttonen, H. Herrmann
	Orientation distribution of fibres in short-fibre reinforced concrete: evaluation and introduction to constitutive relations
2013	7th **International Conference FIBRE CONCRETE 2013 Technology, Design, Application**
	Prague, Czech Republic
SUULINE	M. Eik, J. Puttonen, H. Herrmann
	Fibre orientation phenomenon in concrete composites: measuring and theoretical modelling

LISAD

Juhiload	B-kategooria
Hobid	koerte aretus, fotograafia, yoga, reisimine

List of Publications

This thesis consists of an overview and of the following publications which are referred to in the text by their Roman numerals.

Publication I

M. Eik and J. Puttonen. Challenges of steel fibre reinforced concrete in load bearing structures. Rakenteiden mekaniikka (Journal of Structural Mechanics), 44, 1, 44-64, http://rmseura.tkk.fi/rmlehti/2011/nro1/, **June 2011.**

Challenges of steel fibre reinforced concrete in load bearing structures

Marika Eik and Jari Puttonen

Summary. This article focuses on concrete composite reinforced by short metal fibres, where the main role of fibres is to carry the tensile stresses, while the concrete matrix transfers and distributes the loads to the fibres. The efficiency of load transferring from matrix to fibres depends on both the bonding interface between matrix and fibres and the anchorage length of fibres. The effect of fibre orientation in matrix on the strength of composite is also introduced. In the paper the assumptions made in a cross-sectional dimensioning concerning the behaviour of ordinary reinforced or fibre reinforced cross-sections are discussed and compared.

Key words: fibre reinforced composites, orientation of fibres, crack propagation

Description of steel fibre reinforced concrete (SFRC)

Today fibre reinforced concrete is perhaps one of the most realistic possibilities to develop the use of concrete in load bearing structures. Even if the properties of fibre reinforced concrete have not been thoroughly explored, it is already widely used in the construction industry but not usually as a load bearing structure. Its applications are concentrating on floors resting on soil and less extent on floor slabs, walls and foundations. Interest in using fibre reinforced concrete widely in various structural components is high, as its use is expected to improve quality of concrete structures. Its use may also increase the effectiveness of designers' and constructors' work.

Theoretical background in terms of microstructure

Most materials are heterogeneous not only on the microscale but also on the meso- and macroscales due to manufacturing or formation processes. While the properties of such materials vary point-wise in the material space, the concept of nonlocality might be of use to describe the material properties on average. In physical terms, nonlocality means that a field variable at a point X at time t depends on the values of field variables at points of the body other than the point X. Nonlocality in the frame of SFRC can be explained more precisely in the view of the behaviour of a single fibre as follows: if one end of the fibre is influenced by some stress then the other end of the fibre is also affected. In meso-scale nonlocality with SFRC indicates the presence of the interactions between separate constituents of the material (steel fibres, aggregate, binder etc). The SFRC requires an approach, which takes into account the presence of a complex system,

which is composed of parts interrelated in a way, which is challenging to be described. As opposite to nonlocal behaviour, the local behaviour occurs when the stress in one point cannot easily be explained by the deformation occurring at a different point. For instance, the stress near the tip of a crack may not be explained by a global average stress field.

The concept of microstructured materials is quite wide. Examples are media with regular or stochastic distributions of voids (dislocations), fibres (inclusions), cracks (dislocations), etc. Steel fibre reinforced concrete is a kind of microstructured material belonging to cement-matrix composites. This material has a basic matrix made of concrete, which includes embedded short metal fibres. All microstructured materials are characterised by the existence of intrinsic space-scales as the size of grain or a crystallite, the distance between the microcracks, etc. that introduces scale dependence into governing equations.

According to these factors two main questions are under consideration: the first question is heterogeneity / inhomogeneity and respectively the concept of nonlocality; the second question is the distribution of stresses in concrete steel fibre composite.

Start up with the concept of homogeneous solids, which has been successfully applied to many technical problems. Nonlocality is actually introduced to validate a *homogeneous* model for a *heterogeneous* material. This could be explained by a simple example, as follows.

Assuming that a block consists of periodically alternating layers of two different elastic materials, the gross material is elastic in the usual sense, but with the elastic module varying in a discontinuous manner throughout the body. The material can be *homogenized* by describing its gross behaviour with a constitutive equation involving only a single *constant* effective module. This crude homogenization may be acceptable for static problems.

Research hypotheses and methods

The investigation of SFRC might be divided into three stages. The first stage concerns uncracked material in the sense of macrocracks. In this stage a crucial point is to determine orientation distribution function of fibres in a continuum element. This can be done by the mesoscopic theory, where the domain of the field quantities is enlarged by an additional variable characterizing the internal degree of freedom connected to the internal structure of the material [2, 3]. The orientation of fibres in the considered cross section can be characterized by an average vector *n*, which is composed from the respective vector field. The vector field refers to the arrangement of all fibres in considered cross section. The vector *n* should be defined using the spherical coordinate system, as in 3D case the position of the vector *n* can be unambiguously determined only by taking into account both angles, i.e. the inclination angle (between the vector *n* and the surface normal) and the in-plane angle (azimuth angle). This parameter will be taken as an additional variable in the mesoscopic theory. The orientation distribution of fibres is relevant, because only the component of the stress vector parallel to the main orientation vector *n* causes fibres to work, i.e., in a sample where fibres are mostly parallel to

the direction of applied stress, the work of fibres is more pronounced than in a sample where fibres are mostly perpendicular to the stress direction.

Local solution for aligned fibres according to Taya and Arsenault

As a simplification, it can be considered, that all fibres in a volume element are uniformly distributed. In modelling a crucial point is the choice of theory. A possible model can be a simplified description of microstructure (empirical or semi-empirical theories) obtained by assuming that a model developed for a *unit cell* is distributed uniformly throughout the material [1]. This is basis for the shear lag model, which describes the gross behaviour of a composite material consisting of a matrix with embedded short fibres distributed uniformly and aligned in loading direction. The unit cell consists of matrix material with a single representative fibre of length *2l* and diameter *2r*. The width *2R* of the *unit cell* is taken as the mean lateral separation of neighbouring fibres (Figure 1).
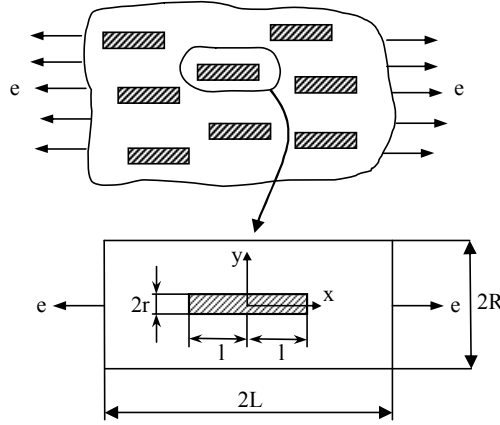
Figure 1. Shear lag model for aligned short fibre after Taya and Arsenault (1989)

If the unit cell is elongated with uniaxial strain *e* along *x* direction, the matrix will exert the shear stress τ_0 or $d\sigma_f/dx$ at the matrix fibre interface, which is proportional to the difference, $(u-v)$, if the axial displacements in the fibre and the matrix on the boundary of the unit cell are denoted by *u* and *v* respectively [1].

$$\frac{d\sigma_f}{dx} = -\frac{4\tau_0}{(2r)} = h \cdot (u-v) \Rightarrow \tau_0 = r \frac{h \cdot (v-u)}{2},$$ (1)

where σ_f is the axial stress in the fibre, h is a constant, which will be determined later, and the local coordinate x is measured from the midpoint of the cell. In the fibre, one dimensional Hooke's law is valid

$$\sigma_f = E_f \frac{du}{dx}, \qquad (2)$$

where E_f denotes elastic modulus of the fibre. The applied composite strain e is equal to dv/dx. Hence, from eqs. (1) and (2) the ordinary differential equation can be obtained

$$\frac{d^2 \sigma_f}{dx^2} = h\left(\frac{du}{dx} - \frac{dv}{dx}\right) = h\left(\frac{\sigma_f}{E_f} - e\right). \qquad (3)$$

The general solution to eq. (3) is given by

$$\sigma_f = E_f e + C_1 \cosh \beta x + C_2 \sinh \beta x, \qquad (4)$$

where

$$\beta = \sqrt{\frac{h}{E_f}}, \qquad (5)$$

and C_1 and C_2 are unknown constants. Applying boundary conditions, $\sigma_f = $ constant (σ_0) at $x = l$ and $d\sigma_f/dx = 0$ at $x = 0$, the stress of the fibre is

$$\sigma_f = E_f e \cdot \left\{ 1 + \frac{\left(\frac{\sigma_0}{E_f e} - 1\right) \cosh \beta x}{\cosh \beta l} \right\}. \qquad (6)$$

It is noted in eq. (6) that $\sigma_0 = 0$ was used in the original derivation by H.L.Cox, implying the absence of additional anchoring at the end of the fibre. σ_0 may not be zero, if anchoring affects around fibre ends are strong as it can be with hooked ends. The value of σ_0 in this case will be proportional to the method of anchoring of fibre ends (mechanical, chemical etc.) and the stress field σ_f in the fibre will not be uniform.

The average fibre stress $\overline{\sigma}_f$ is computed as

$$\overline{\sigma}_f = \frac{1}{l} \int_0^l \sigma_f dx = E_f e \left\{ 1 + \frac{\left(\frac{\sigma_0}{E_f e} - 1\right) \tanh \beta l}{\beta l} \right\}. \qquad (7)$$

Consider next the displacement along x direction at an arbitrary point $(y = y)$ in the matrix, w, where $w(y = r) = u$, and $w(y = R) = v$. Force equilibrium at $y = r$ and arbitrary point $(y = y)$ provides

$$2\pi y\tau = 2\pi r\tau_0 .$$ (8)

The shear strain at $y = y$, γ is related to τ_0 as

$$\gamma = \frac{dw}{dy} = \frac{\tau}{G_m} = \frac{\tau_0}{G_m}\frac{r}{y},$$ (9)

where τ is the shear stress in the matrix at $y = y$, and G_m is the shear modulus of the matrix. Integrating eq. (9) from $y = r$ to $y = R$, it can be obtained

$$v - u = \frac{\tau_0 r}{G_m}\ln\left(\frac{R}{r}\right) \Rightarrow \tau_0 = \frac{G_m \cdot (v - u)}{r \ln(R/r)} .$$ (10)

From eqs. (1) and (10) constant h is solved as

$$h = \frac{2G_m}{r^2 \ln(R/r)} .$$ (11)

From eqs. (5) and (11) β is found as

$$\beta = \frac{\sqrt{2}}{r}\sqrt{\frac{G_m / E_f}{\ln(R/r)}} .$$ (12)

The factor β reflects the relative rigidity of the surrounding matrix in respect to the fibre. With β given by eq. (12) the average stress σ_f in the fibre can be calculated from eq. (7). In order to describe the gross behaviour of the compound material along loading x direction, the mean stress value σ_c can be estimated by using the law of mixtures

$$\sigma_c = \sum_{i=0}^{N} V_i \sigma_i ,$$ (13)

i.e.

$$\sigma_c = \left(1 - V_f\right)\overline{\sigma}_m + V_f \overline{\sigma}_f ,$$ (14)

where $\overline{\sigma}_m$ and $\overline{\sigma}_f$ are interpreted as the average quantities in the relevant domain and V_f is the volume fraction of fibres. For a given applied strain e, one can assume, that

$$\overline{\sigma}_m = E_m e \,, \tag{15}$$

$$\sigma_c = E_c e \,. \tag{16}$$

A substitution of eqs. (7), (16) and (15) into eq. (14) yields Young's modulus of the composite E_c

$$E_c = \left(1 - V_f\right) E_m + V_f E_f \left\{ 1 + \frac{\left(\dfrac{\sigma_0}{E_f} - 1\right) \tanh \beta l}{\beta l} \right\}, \tag{17}$$

where σ_0 can be equal to zero, which means there is no load transfer at the fibre ends. The shear lag model presented by Taya and Arsenault (1989) *excludes nonlocal effects*. It is a usual effective-modulus theory, which describes the composite material by the classical Hooke's law

$$\sigma_c = E_c e \,. \tag{18}$$

The whole theory is about the determination of the effective Young's modulus E_c from the geometric and material data. Certainly, a nonlocal model can be generated using some ideas from Taya and Arsenault's approach, but in the original form it is an example for *localization*.

Nonlocal solution for aligned fibres according to Becker and Bürger

Another approach includes *nonlocality* [4]. Becker and Bürger (1975) have studied a similar problem assuming the fibres being in contact with the matrix at their endpoints only. Consider the uniaxial stretching over elastic material (elastisity modulus E_m) in which parallel elastic fibres (elastisity modulus E_f, cross-section area is A_f, length $2l$) are embedded. X and X^* are, respectively, the position of the cross-section and the right endpoint of the fibre from the origin in the reference configuration. The fibre at position X^* extends from $X^* - 2l$ to X^* (Figure 2).

The number of fibres per volume (number density) n in the cross-section A at X composes the volume fraction, which is equal to following

$$\int\limits_X^{X+2l} n A_f \, dX^* = n A_f \, 2l \,. \tag{19}$$
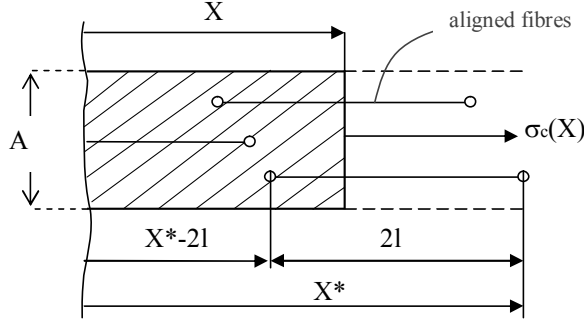
Figure 2. Fibre reinforced material, after Becker and Bürger (1975)

The fibres are glued to the matrix material at their endpoints only. Therefore, the stress in one fibre, which passes through the cross-section at X is equal to $E_f(x(X^*) - x(X^* - 2l) - 2l)/2l$. The relation $x = x(X)$ or $x = x(X^*)$ defines the motion expressed by Lagrangian description according to which the material point X or X^* is transferring to the spatial point x. For the average stress $\sigma_c(X)$ within the whole cross-section area A follows

$$\sigma_c(X)A = A(1 - nA_f 2l)E_m e_x(X) + \int\limits_X^{X+2l} E_f \cdot \frac{x(X^*) - x(X^* - 2l) - 2l}{2l} AnA_f dX^*. \quad (20)$$

From the eq. (20), taking into account the integral (19) and the following substitutions: $(1 - nA_f 2l) \cdot E_m = (1 - V_f)E_m$ and $nA_f 2l \cdot E_f = V_f E_f$ as well as $e_x = dx/dX - 1$, the next expression can be obtained:

$$\sigma_c(X) = \left(1 - V_f\right)E_m\left(\frac{dx}{dX} - 1\right) + V_f E_f \left\{ \frac{1}{(2l)^2} \int\limits_{X-2l}^{X+2l} \left| x(X^*) - x(X) \right| dX^* - 1 \right\} \quad (21)$$

As opposed to eq. (18), Becker and Bürger's eq. (21) exhibits true nonlocal behaviour.

The second stage of investigation of considered material could be concentrated on the analysis of cracked solid. The crucial points of this stage are separation of the whole stress between fibres and matrix and cracks propagation and growth. To solve the problem with stress distribution Becker and Bürger's (1975) approach could be employed.

Cracks propagation and growth

Crack resistance of material (viscosity of fracture) characterizes the ability of material to resist the propagation of pre existing cracks. In case of SFRC propagation of cracks is also under research. In connection with this, it is useful to recall A.A. Griffith's theory about rupture in solids. It is well known, that theoretical strength of solids, calculated by

some atomistic model, is much higher than the real one [6]. A.A. Griffith was the first who suggested that this phenomenon occurs due to the presence of microscopic flaws (discontinuities) in the real material. Griffith's theory gives excellent agreement for brittle materials, but not applicable for ductile ones. A group led by G. R. Irwin assumed, that plasticity should play an important role in the fracture of ductile materials. In such materials, a plastic zone d develops near the tip of a crack (see Figure 3). As the stresses are increasing in the material, the value of plastic zone is increasing as well until the crack is growing and the material behind the crack tip is unloading. The ability of material to resist crack propagation is expressed by the stress intensity factor K (SIF) and the energy release rate G, i.e. the work for plastic deformation per unit of newly created crack surface [6]. Assume an infinite body, uniaxial stress field and the case of plane deformation. In considered instance, the critical value of the stress intensity factor K_{Ic} (fracture toughness) will be equal to following:

$$K_{Ic} = \sigma \sqrt{\pi c} , \qquad (22)$$

where σ denotes a uniform stress field, subscript I denotes mode I loading, i.e. plane strain (a tensile stress is normal to crack plane), c denotes a half of the length of the crack and d denotes the length of the plastic zone in front of the crack (Figures 3, 4).
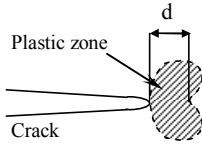
Figure 3. Plastic zone in front of the crack   Figure 4. The length of a crack
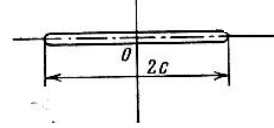
In real materials, the stress near the tip of a crack is very high and exceeds the yield strength of the material, i.e. the local plastic yielding occurs. Hence, plastic yielding plays a significant role in the fracture process of materials.

Dugdale and Barenblatt have offered a model to find the extent of plastic zone. They considered a long, slender plastic zone at the crack tip in plane stress. The strip model is founded on a crack of length $2a = 2c + 2d$, where d is the length of the plastic zone with a closure stress equal to σ_{ys}, applied at each crack tip, see Figure 5. The size of d is chosen that the stress singularity vanishes at the end of the effective crack [11], i.e.

$$K_\sigma + K_d = 0 , \qquad (23)$$

where the definition of K_σ and K_d will be given below.

The estimation of stress intensity due to the closure stress may be implemented assuming a normal force P acting on the crack at a distance x from the centre line of the crack, see Figure 6.
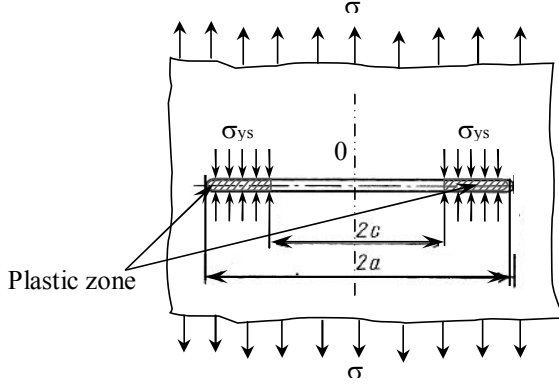
Figure 5. Stresses near the tips of a crack
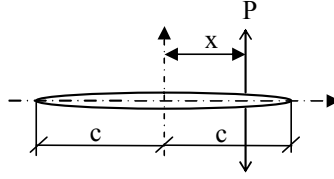
Figure 6. Applied load in a distance x

The resultant stress intensity factors at the right and respectively at the left crack tips are [11]:

$$K_{left} = \frac{P}{\sqrt{\pi c}} \sqrt{\frac{c+x}{c-x}}, \quad K_{right} = \frac{P}{\sqrt{\pi c}} \sqrt{\frac{c-x}{c+x}}, \tag{24}$$

The closure force within the plastic zone is:

$$P = -\sigma_{ys} dx. \tag{25}$$

Hence, the total stress intensity at each crack tip resulting from the closure stress is obtained by replacing c with $c + d = a$ [11], i.e.

$$K_d = \frac{-\sigma_{ys}}{\sqrt{\pi a}} \int_c^a \left\{ \sqrt{\frac{a-x}{a+x}} + \sqrt{\frac{a+x}{a-x}} \right\} dx = \frac{-2\sigma_{ys}a}{\sqrt{\pi}} \int_c^a \frac{dx}{\sqrt{a^2-x^2}} = -\frac{2}{\pi} \sigma_{ys} \sqrt{\pi a} \cos^{-1}\left(\frac{c}{a}\right). \tag{26}$$

The stress intensity from the remote tensile stress is $K_\sigma = \sigma_\infty \sqrt{\pi a}$ and accordingly eq. (23) leads to

$$\frac{c}{a} = \cos\frac{\pi\sigma_\infty}{2\sigma_{ys}}.$$ (27)

The formula (27) allows to determine the length of plastic zone in cases, when linear fracture mechanics is powerless [6]. The value $d = a - c$ can be quite large and it aims to infinity when $\sigma_\infty \to \sigma_{ys}$. On the contrary, for $\sigma_\infty \ll \sigma_{ys}$ neglecting the higher order terms in the series development of the cosine, d is found as [6]

$$d \sim \frac{\pi^2}{8}\frac{\sigma_\infty^2}{\sigma_{ys}^2}c = \frac{\pi}{8}\left(\frac{K_{Ic}}{\sigma_{ys}}\right)^2.$$ (28)

Solution of the singularity at the end of a crack, i.e. J-integral

Consider W to be the strain energy density (the density of elastic energy), which depends on the infinitesimal strain tensor $e_{ij} = \overline{e}_{ij} = u_{(i,j)}$, where $u_{(i,j)} = 1/2\left(u_{i,j} + u_{j,i}\right)$ is the symmetric part of the displacement gradient [6]. It is approved that the integral,

$$J = \int_A^B \left(W dy - \sigma_{ij}\frac{\partial u_i}{\partial x}n_j ds\right),$$ (29)

where

$$W = \int_0^{\overline{e}} \sigma_{ij} d\overline{e}_{ij} ,$$ (30)
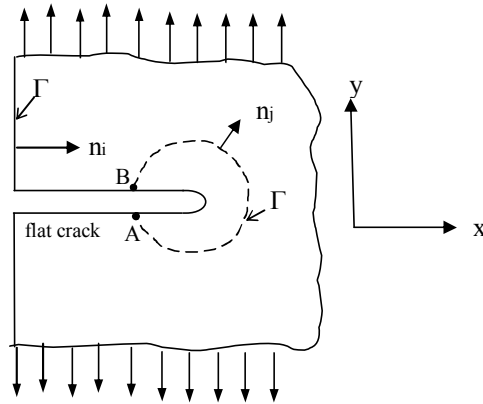
Figure 7. J-integral around a crack in two dimensional deformation field

$\sigma_{ij}n_j = \sigma_i$ is the traction vector defined according to the outward normal n_j along Γ, $\partial u_i / \partial x$ is the displacement vector and ds is an element of arc length along Γ, does not depend on the path of integration between points A and B (Figure 7).

For the proof, it is necessary to show, that integral (29) vanishes for any closed path. On the other hand, it can be proved, that if points A and B are taken on different edges of a crack, then

$$J = -G, \tag{31}$$

where $G = \partial U / \partial \Delta$ is the strain energy release rate, which is equal to the ratio of change in the total elastic energy ∂U, contained in the domain S with boundary Γ, to the propagation of crack end to a distance $\partial \Delta$ [6] (Figure 8).
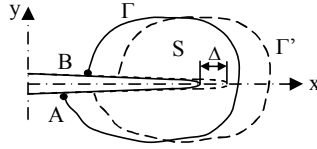
Figure 8. Propagation of a crack

Crack propagation is accompanied by the work of plastic deformation G (strain energy release rate), which is also called resistance force of crack propagation [6]. If G does not reach the critical value of G_c for a given material, the crack is stable. Crack becomes unstable when G reaches or exceeds the critical value of G_c. In case of plane strain (mode I loading), connection between the critical value of strain energy release rate (toughness) and the critical stress intensity factor (fracture toughness) is

$$G_{Ic} = \frac{1-\nu^2}{E_c} K_{Ic}^2, \tag{32}$$

where ν is Poisson's coefficient. In general, to assess the stability of a crack it is possible to compare K (the actual value of stress intensity factor) with K_c (the critical value of stress intensity factor in considered loading mode and material). For stabilized crack $K \le K_c$ must be.

Crack growth begins when crack opening is critical and equal to certain value δ_c [6]. Let's consider $\delta = u^+(c,0) - u^-(c,0)$, where indexes "+" and "–" denote opposite crack surfaces. By choosing the way of integration as in Figure 9, the following can be received: $dy = 0$, $\sigma_{ij}n_jn_i = \sigma_*$ is the stress applied in normal direction, and further

$$G = -J = \sigma_*(u_y^+ - u_y^-) = \sigma_*\delta_c. \tag{33}$$
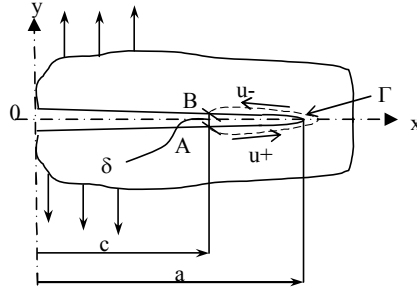
Figure 9. The way of integration

For determination of the critical value of K_{Ic} it is necessary to measure δ_c in a moment when the crack begins to grow

$$\delta_c = \frac{1}{\sigma_*} \cdot \frac{1-v^2}{E_c} K_{Ic}^2 \Rightarrow K_{Ic} = \sqrt{\delta_c \cdot \frac{E_c \sigma_*}{(1-v^2)}} \ . \tag{34}$$

Crack propagation in a composite with aligned fibres

In the researched material crack growth is interrupted by metal fibres, which disturb relative displacements of crack edges. The crack can achieve the value of δ_{ic} when fibres will be broken in some distance ξ from the tip of a crack [6] (Figure 10).
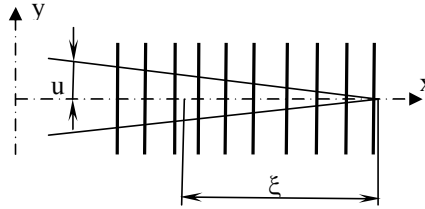
Figure 10. Crack growth in composite with short fibres
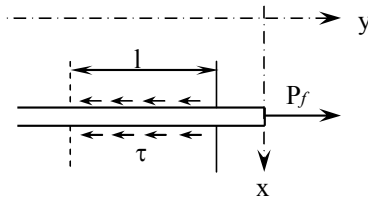
Figure 11. Force applied on a fibre, which is fixed in a matrix

The simplest assumption would be that friction forces τ per unit of surface area balance the tension stresses in fibres and prevent pull out of fibres from the matrix. Let Pf be the force, which is applied to the tip of a fibre with radius r fixed in the matrix. This force is balanced by the uniform shear stress in a segment with length l.

The equation of balance is

$$P_f = 2\pi r l \tau \Rightarrow l = \frac{P_f}{2\pi r \tau}. \tag{35}$$

Hence, the lengthening of fibre segment with length l in y direction considering one half of the crack side (Figure 10) and eq. (35) will be

$$u = \frac{1}{2} \cdot \frac{1}{E_f} \cdot \frac{P_f}{\pi r^2} \cdot l = \frac{1}{4} \cdot \frac{1}{E_f} \cdot \frac{P_f^2}{\pi^2 r^3 \tau}. \tag{36}$$

If σ_c is the average stress of the composite and the crack opening is controlled only by fibres, then

$$\sigma_c = \frac{P_f V_f}{\pi r^2} \Rightarrow P_f = \pi r^2 \sigma_c \cdot \frac{1}{V_f}, \tag{37}$$

where V_f denotes volume density of fibres content in the material. Considering the correlation (36), it can be noticed, that the relationship between the stress in a zone near the tip of a crack and the relative displacements of crack edges will be

$$u = \frac{1}{4} \cdot \frac{r}{E_f \tau V_f^2} \cdot \sigma_c^2 = \alpha \sigma_c^2. \tag{38}$$

Assuming that $\sigma_c = \sigma_{c0} \cdot (\xi / L)^n$ (where σ_{c0} is some stress value, L is some reference length and ξ denotes the distance to the crack tip), $u = \alpha(\sigma_{c0} \cdot (\xi / L)^n)^2$ and calculating the Rice-Cherepanov's integral the following value of the work for plastic deformation can be obtained

$$G_c = \int \sigma_c \frac{\partial u}{\partial \xi} d\xi = \int \sigma_{c0} \cdot \left(\frac{\xi}{L}\right)^n \cdot 2n \frac{\alpha}{L} \sigma_{c0}^2 \left(\frac{\xi}{L}\right)^{2n-1} d\xi =$$
$$= \frac{2}{3} \alpha \cdot \sigma_{c0}^3 \left(\frac{\xi}{L}\right)^{3n} + C = \frac{1}{6} \cdot \frac{r}{E_f \tau V_f^2} \cdot \sigma_c^3 + C \tag{39}$$

It is expected, that the crack begins to grow when σ_f achieves the value of fibre tension strength. Assuming that $\sigma_c = \sigma_f V_f$ and $C = 0$ [6] the following can be obtained

$$G_c = \frac{r}{6E_f\tau}V_f\sigma_f^3. \tag{40}$$

From eq. (40) follows, that resistance of crack propagation increases together with fibre strength and volume density of fibres content in the material. However, it does not mean there is a simple linear relationship. At the same time friction forces, which are equal to matrix shear resistance, should not be too high.

The third stage of researched material could include the identification of fracture mechanics. The main idea here might be to introduce the damage parameter as a macroscopic quantity growing with progressive damage in such a way, that it should be possible to relate reducing effective area of cross section to the growth of the damage parameter [7, 10].

Theoretical background of classical analysis of concrete structures

As it is already known, when considering concrete at microscale, the structure of this material is heterogeneous. But when reinforcement bars are added to the tensioned cross sections of concrete in macroscale it becomes an orthotropic material. The presence of fibres in fibre reinforced concrete makes it necessary to consider this material at meso- and microscales. Regarding to this, a variable characterizing the characteristic length of the inner structure of the material and associated with the orientation of fibres has to be added to the governing equations. Determining the arrangement of fibres in the matrix is the most important starting point for further development of design rules for fibre reinforced concrete structures. Due to different structural scales, theory of reinforced concrete structures cannot directly be applied to the fibre reinforced concrete. However, brittle behaviour of concrete matrix is a common feature for both materials influencing on both the cross-sectional level and on the level of material interfaces. These common features may be possible to utilize in the dimensioning methods for load bearing structures of steel fibre reinforced concrete. For this purpose the dimensioning principles of concrete structures with ordinary reinforcement are introduced in this paragraph.

Experimental basis of the theory of resistance of reinforced concrete and calculation methods of concrete structures

The dimensioning principles of reinforced concrete structures are built up on the experimental data and the principles of mechanics proceeding from the stresses and deformations of members in various loading stages [8].

Three stages of stress and deformation state of reinforced concrete members in case of pure bending

Having loaded reinforced concrete member by gradually increasing loading, it is possible to observe three stages of stresses and deformations:
Stage one (I): uncracked tension zone. In this stage tension stresses are taken both by concrete and reinforcement (Figure 12), where f_{ct}, f_y denotes respectively concrete and
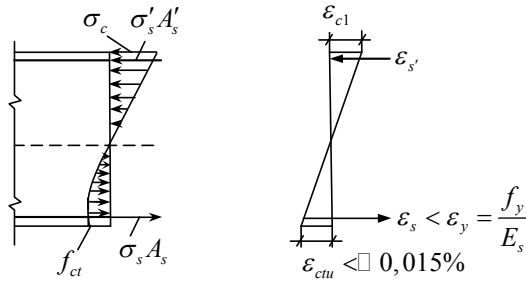
Figure 12. Stage one (I) of stress [σ] deformation [ε] state in reinforced concrete

reinforcement tension strength, σ_c is the concrete stress in compression zone, $\sigma_s A_s$, $\sigma_s' A_s'$ the stress and the cross section area of reinforcement bars respectively in tension and compression zones, E_s is the Young's modulus of the reinforcement, ε_{ctu} is the concrete ultimate strain in tension, ε_{c1} is the concrete maximum strain in compression, ε_s, $\varepsilon_{s'}$ is the reinforcement strain and ε_y is the relative strain of tensioned reinforcement. *Stage two (II)*: cracks in tension zone, but stress in compressed concrete remains under its maximum strength (Figure 13).
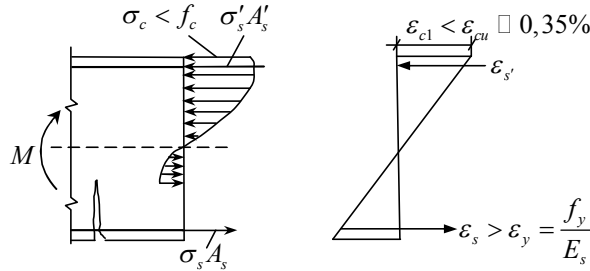
Figure 13. Stage two (II) of stress and deformation state in reinforced concrete, f_c denotes concrete compression strength.

Tension stresses are taken by: a) in cracked sections – by reinforcement and concrete above the crack; b) between cracks – by both concrete and reinforcement.

Stage three (III): the stage of failure. As a result of an increasing external load, the stage two moves to the stage three and, as a consequence, plastic deformations are developing in the compressed concrete zone. The location of the maximum compression stress in concrete moves from the edge of a section to its centre. The reinforcement tension stresses exceed the yield strength. The ultimate strain of concrete ε_{cu} plays a significant role during this stage. Usually it limits plastic deformations that may develop in the reinforcement prior to failure. In design codes the stage three is often divided in to two parts (Figure 14). Case 1. The failure of reinforced concrete begins by yielding of the
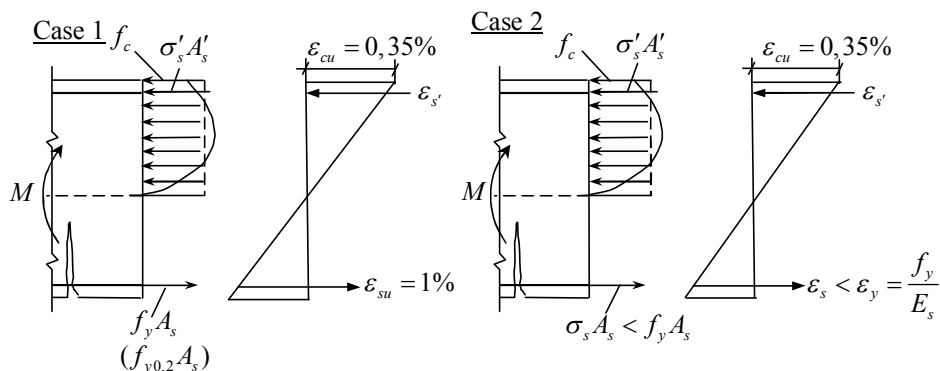
Figure 14. Stage three (III) of stress and deformation state in reinforced concrete

reinforcement in the tension zone and ends by breaking of concrete in the compression zone. This kind of failure has a plastic character. Case 2. The failure of members with excess content of reinforcement or mainly compressed members. The fracture occurs in compression zone before yielding of the steel reinforcement. The failure is brittle.

Stress redistribution in statically indeterminate structures

The essence of the method of stress redistribution in statically indeterminate structures consists of following: under some load value the stresses in tensioned (soft) reinforcement achieve the yield limit. Together with the developing of plastic deformations in bars, the area of large local deformations, called *plastic hinge*, is developing in concrete.

In statically determinate structures, the developing of plastic hinge may cause considerable deflections and decreasing of compressed zone and, as a result, the compression stresses achieve their ultimate value leading to the collapse of the structure. Differently from statically determinate structures, in statically indeterminate structures with the advent of plastic hinge, redundant connections prevent the rotation of parts of structural system in relation of each other and redistribute external loading within the system.

Stage IIa occurs, when stress in tensioned reinforcement achieves the yield limit, but concrete stress does not achieve its ultimate value (Figure 15). At the same time, deformations in plastic hinge are increasing, but the value of bending moment remains unchanged

$$M = f_y A_s z_c,\tag{41}$$

where z_c is the distance (moment arm) between the pair of internal forces. The fracture of the structural member will occur when plastic hinges will be developed in all redundant connections and redistribution of external forces is not possible anymore.
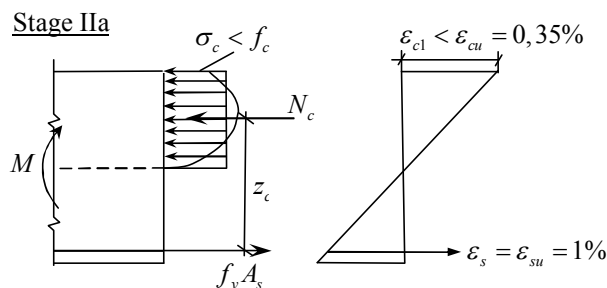
Figure 15. Stage IIa at the section with plastic hinge

Comments

As it was mentioned, concrete with conventional reinforcement behaves like an orthotropic material. The question concerning the orientation of bars is not under consideration, as usually predicted tension in beams or columns coincides with the actual reinforcement. In other words, the principle of determinism can be applied. As a difference from a common reinforced concrete, steel fibre reinforced concrete is anisotropic. The level of anisotropy relies primarily on the degree of fibre orientation. If it would be possible to determine the rule for fibres orientation in the matrix considering reasonably the type of structure, casting method and the rheology of mixture, the calculation of cross-sectional capacities can carried out similarly as done for conventional reinforced concrete cross-sections. However, the issue of anchorage failure must be studied separately. A more precise approach needs to take into account the anchorage length of fibres in the matrix, which depends a lot on the matrix-fibre interface and shape of fibres and, additionally, the work done by the matrix should also be considered. From the latter, the difference between conventional and fibre reinforced concrete rises once again: in common reinforced concrete the tension ability of concrete is simply not taken into account, but reinforcement anchorage is assumed also in tension zone. In general, designing of conventional reinforced concrete structures involves the work of two separate materials: concrete and steel. Each of the materials has its own role for structural capacity: one deals with compression and another with tension. In case of steel fibre reinforced concrete the situation turns to integration of two materials, what finds its explanation in the theory of composites.

Possible solutions

After reviewing the researched material from the point of microstructural material and from the already established theory of analysis of concrete structures, it can be concluded, that a valid, full and objective method, reflecting the behaviour of steel fibre reinforced concrete, does not exist. Fracture mechanics and corresponding calculation methods of steel fibre reinforced concrete are still open questions. The classical theory of reinforced concrete completely ignores the orientation of reinforcement bars. As it was stated above, certain important properties of steel fibre reinforced concrete directly depend on fibres orientation in the matrix. In order to predict the arrangement of fibres in the matrix, certainly both theoretical and practical work must be done. Concerning fibre orientation, a temping approach to this problem could be to employ the theory of probability and implement some initial assumptions about the location of fibres. However, the most valuable and reliable information about the orientation of fibres in the matrix must come from experiments as the orientation is influenced by the manufacturing process of concrete mass with steel fibres.

The diagram, shown in the Figures 16a and 16b may be a conclusion of this article. It shows the formation of composite and the main present ambiguities, which prevent from using SFRC in load-bearing structures safely.

Acknowledgment
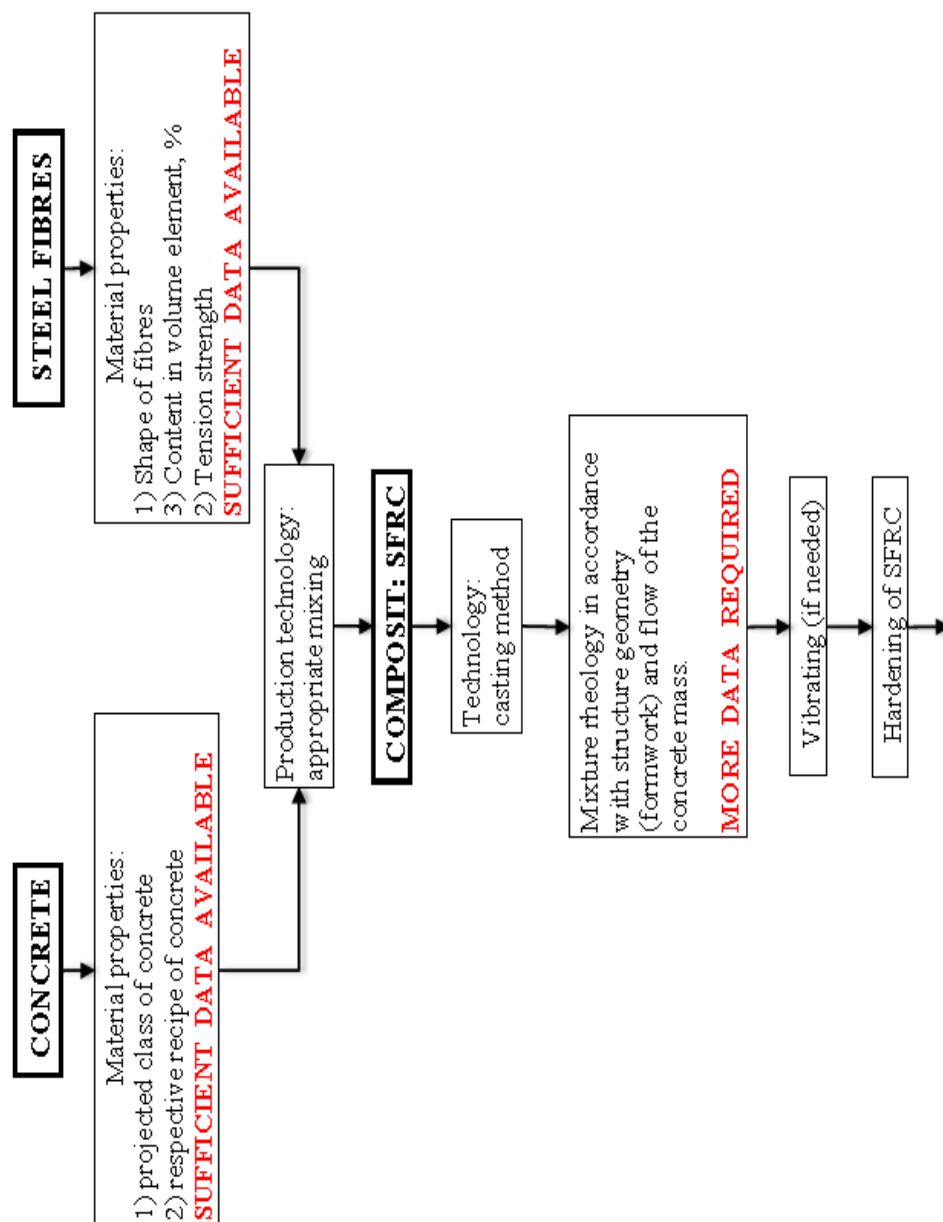
Figure 16. The formation and the main present ambiguities of steel fibre reinforced concrete. (The figure continues on the next page.)

THE STAGE OF RESEARCH

Strength of the matrix - bonding interface between matrix and fibre.

Lack of comprehensive data, but some previous investigations available.
RESEARCH REQUIRED

Anchorage of fibre - the shape of fibre; anchorage length of fibre. Due to the anchorage length there are two ways of loosing tension resistance of SFRC:
1. breakage and pullout of fibres
2. pullout of fibres

Lack of comprehensive data, but some previous investigations available.
RESEARCH REQUIRED

Possible result: constitutive law of SFRC in case of aligned fibres.

Lack of comprehensive data, but some previous investigations available.
RESEARCH REQUIRED

Concrete-matrix

The orientation of fibres - the result of interaction of the parts of complex system, may be predicted.
NO RELIABLE DATA

Possible result: constitutive law of SFRC in case of mesoriented fibres.
NO RELIABLE DATA

Empirical part: Composing orientation of fibres through actual data. Attempt to look inside material.

Analytical part: employing the mesoscopic theory through the inclusion of additional variable representing orientation of fibres. Using alignment tensors for composing orientation distribution function of fibres.

Empirical data processing: Visualization of mesoriented fibres in computer. Data preparation for analytical part.

Figure 16 (continued). The formation and the main present ambiguities of steel fibre reinforced concrete.

63

References

[1] M. Taya and R J. Arsenault, *Metal Matrix Composites,* Pergamon Press, Oxford, 1989.

[2] P. Van, C. Papenfuss, W. Muschik, Mesoscopic dynamics of microcracks, *Physical Review E*, 62(5):6206-6215, 2000.

[3] C. Papenfuss, P. Van, W. Muschik, Mesoscopic theory of microcracks, *Archive of Mechanics*, 55(5-6):481-499, 2003.

[4] E. Becker and W. Bürger, *Kontinuumsmechanik*, B. G. Teubner, Stuttgart, 1975.

[5] A.A. Griffith, The phenomena of rupture and flow in solids, *Philosophical Transactions of the Royal Society A*, 221:163-198, 1920.

[6] J. Rabotnov, *Introduction to Fracture Mechanics (Введение в механику разрушения),* Nauka (Наука), Moscow, 1987.

[7] P. Van, C. Papenfuss, W. Muschik, Griffith cracks in the mesoscopic microcrack theory*, Journal of Physics A*, 37 (20):5315-5328, 2004.

[8] V. Baikov, E. Sigalov, *Reinforced concrete structures: a general course (Железобетонные конструкции: общий курс)***,** Strojizdat (Стройиздат), Moscow, 1991.

[9] Collection of scientific papers edited by Professor G. Hesin and Professor B. Taratorin, *Kinetics and Dynamics of cracks (research by method of photoelasticity) (Статика, кинетика и динамика трещин (исследования методом фотоупругости)***,** Moscow State University of Civil Engineering (МИСИ), Moscow, 1988.

[10] C. Papenfuss, T. Boehme, H. Herrmann, W. Muschik and J. Verhas, Dynamics of the size and orientation distribution of microcracks and evolution of macroscopic damage parameters*, Journal of Non-Equilibrium Thermodynamics*, 32 (2):129-142, 2007.

[11] C. H. Wang, *Introduction to fracture mechanics,* DSTO Aeronautical and Maritime Research Laboratory, Australia, 1996.

Marika Eik, Jari Puttonen
Aalto University, School of Engineering,
Department of Civil and Structural Engineering
PO Box 12100
00076 Aalto
meik@cc.hut.fi, jari.puttonen@aalto.fi

Publication II

MECHANICS

Some comments on the theory of short fibre reinforced materials

Heiko Herrmann[a]* and Marika Eik[b,c]

[a] Centre for Nonlinear Studies, Institute of Cybernetics at Tallinn University of Technology, Akadeemia tee 21, 12618 Tallinn, Estonia
[b] Department of Structural Engineering and Building Technology, Aalto University School of Science and Technology, Rakentajanaukio 4 A, Otaniemi, Espoo, Finland
[c] Department of Structural Design, Tallinn University of Technology, Ehitajate tee 5, 12618 Tallinn, Estonia; meik@cc.hut.fi

Abstract. The orientation of fibres in short fibre reinforced materials is essential for the properties of the composite. It is state of the art to use an orientation number to estimate how many fibres are aligned in the stress direction. This, however, is a very crude approach, as the orientation number is defined by use of the average of the projected length of the fibres. Therefore, the orientation number is not a material property – it depends also on the projection direction. Additionally, a simple number cannot be used to describe anisotropic properties. We introduce a tensorial approach, which is objective and consists of real material properties.

Key words: microstructured solids, constitutive theory, composites, short fibres, alignment tensors.

1. INTRODUCTION

Fibre reinforced materials become increasingly important for constructions of all kinds, from airplanes to buildings. The materials used to form the composite also cover a broad range, including among others glass, carbon or steel for the fibres and metal, plastic or concrete for the matrix. In this paper steel fibre reinforced concrete is chosen as one example. Steel fibre reinforced concrete is a microstructured material, which consists of several homogeneous media (filler, cement, steel fibres), i.e., this material has a basic matrix which includes embedded short metal fibres (see Fig. 1).

Fig. 1. Steel fibre reinforced concrete after a fracture test.

---

* Corresponding author, hh@cens.ioc.ee

Today steel fibre reinforced concrete is perhaps one of the most important new possibilities of developing the use of concrete in load-bearing structures. Despite the fact that the properties of this material have not been thoroughly explored, it is already widely used in the construction industry. Fibre reinforced concrete is widely used in floors resting on soil and to a lesser extent in floor slabs, walls, and foundations, but the request to use it also in various load-bearing structural components is high. The investigation of fibre reinforced concrete as building material is very important for the construction area. Its use increases the effectiveness of the designer's and constructor's work, improving also the quality of the structures. The use of fibre reinforced concrete in construction allows gaining considerable achievement in work performance and of course in time.

Failure mechanisms and corresponding calculation methods are still under development when analysing fibre reinforced concrete. As already known, when considering concrete at microscale, the structure of this material is heterogeneous. But when conventional reinforcement is added to the tensioned structure, in macroscale it becomes an orthotropic material. Due to the presence of short fibres in fibre reinforced concrete, one has to consider this material at meso- and microscales. Thus another variable, characterizing the length of the inner structure of the material and associated with the orientation of fibres, has to be added to the governing equations. Determining the location of fibres in the matrix is one of the most important starting points for further development of design rules. In connection with different structural scales, pure theory of reinforced concrete structures cannot be applied to fibre reinforced concrete. Though, there is very much in common between reinforced and fibre reinforced concrete, which can be used in the integration process of concrete and fibre reinforced concrete.

The fibre orientation is important, because the fibres aligned in the direction of major stresses carry more load than fibres perpendicular to this direction.

The major aspects influencing fibre orientations include the wall-effects introduced by the form-work, geometry of the casting element, the way concrete is poured into the mould, the effect of vibration or, in case of self-compacting concrete, the flow of fresh concrete.

2. THE ORIENTATION NUMBER

The average fibre orientation in a certain direction is generally considered through the so-called orientation number [1–3]. This parameter is frequently applied in experimental investigations to quantify the influence of one of the aforementioned aspects on fibre orientation by isolating it from the others. For instance, the effect of the casting direction has been quantified by considering elements poured in different positions while keeping all the remaining aspects constant.

The orientation number is defined as

$$\eta = \frac{1}{N} \sum_{i=1}^{N} \cos \theta_i, \qquad (1)$$

where N is the number of fibres in the sample and θ is the angle between the fibre and the surface normal (usually parallel to the principal forces). The orientation number corresponds to the average projected length of the fibres in a plane/cross-section onto the normal of the cross-section, divided by the fibre length.

The in-plane angle is not taken into account. Because of this and as the orientation of fibres is 3D, the orientation number does not allow making any statement about the orientation with respect to an axis perpendicular to the cross-section normal.

3. THE ORIENTATION PROFILE

Using an orientation profile [3], the contribution of fibres at different angles to the load direction is introduced into a constitutive function. The orientation profile is based on the mean orientation angle and respective standard deviation (variance) of measured fibre orientations and an *assumed* statistical density distribution function, e.g. normal distribution. From this one can calculate the amount of fibres at any given angle. The in-plane angle is also in this case not taken into account. For this reason and since the orientation of fibres is 3D, also the orientation profile does not allow making any statement about the orientation with respect to an axis perpendicular to the cross-section normal, or any other axis.

An example of the constitutive function is given in [3]:

$$\sigma_{SF}(w) =$$

$$\frac{P_{N,7.5°} + P_{N,22.5°} + P_{N,37.5°} + P_{N,52.5°} + P_{N,67.5°} + P_{N,82.5°}}{A_{sec}},$$
$$(2)$$

where $P_{N,\theta}$ is the pullout response of N fibres in a cross-section A_{sec} under the inclination angle $\theta \in \{7.5°, 22.5°, 37.5°, 52.5°, 67.5°, 82.5°\}$. The partition in $15°$-angles seems to be arbitrary.

4. CRITICISM ON THE ORIENTATION NUMBER AND ORIENTATION PROFILE

Neither the orientation number nor the orientation profile are material properties, as they also depend on the projection direction. The orientation number describes only an average orientation, but many different orientation distributions can produce the same average. Additionally, only the angle with respect to the projection direction is taken into account, while the in-plane angle within the cross-section is neglected. Therefore, also the

orientation profile does not allow making conclusions about differently oriented cross-sections.

It is known from other examples, like electric permittivity, that tensorial quantities are required to describe the behaviour of anisotropic materials. Neither the orientation number nor the orientation profile have tensorial character.

A formulation based on an orientation distribution function and its alignment tensors would be more elegant. It would take into account the 3D character of the fibre orientation and could represent a contiguous distribution.

5. THE ORIENTATION DISTRIBUTION FUNCTION

The orientation distribution function describes the orientation of fibres, using spherical polar coordinates. As the length of the fibres is constant, a unit-sphere (and therefore only the two angular coordinates) is used (see Fig. 2). Each fibre produces two points (opposing each other) on the sphere. The density of the points is normalized, so that the integral over the whole unit sphere is 1; this density is defined as the orientation distribution function. This concept is well known from mesoscopic continuum physics for liquid crystals (where it was first introduced) and micro-cracks [4], [5: sec. 5.4.5], [6], [7].

The advantage of using the orientation distribution function instead of the orientation number and orientation profile is that both angles are taken into account (with their corresponding profiles). However, it is difficult to obtain the precise orientation distribution function and also to include the orientation distribution function into constitutive equations. For this purpose the alignment tensor is a better alternative.

The orientation distribution function is a field, i.e., it is position-dependent. Naturally, the orientation distribution function will be different in the bulk, compared to that close to the wall or corners, where boundary-effects will dominate.
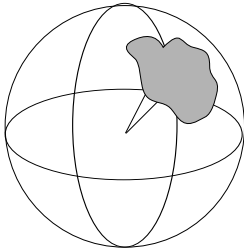
Fig. 2. Orientation distribution function. The symmetric part corresponding to $-\mathbf{n}$ is not shown.

6. THE ALIGNMENT TENSORS

A distribution function can be expanded into a series by using the multipole-expansion. The orientation distribution function is a function $f : S^2 \to \mathbb{R}$. If the orientation distribution function is at least an L^2-function, the expansion is given by [5: sec. 5.4.5]

$$f(\mathbf{n}) = \frac{1}{4\pi}\left(\oint_{S^2} f(\mathbf{n})\,d^2n + \sum_{l=1}^{\infty} \frac{(2l+1)!!}{l!} a_{\mu_1\ldots\mu_l}\, \overline{n_{\mu_1}\cdots n_{\mu_l}} \right), \tag{3}$$

$$a_{\mu_1\ldots\mu_l} = \oint_{S^2} f(\mathbf{n})\, \overline{n_{\mu_1}\cdots n_{\mu_l}}\, d^2n. \tag{4}$$

Here, $l!$ is the factorial $l! = l \cdot (l-1)\cdots 2 \cdot 1$ and $(2l+1)!! = (2l+1) \cdot (2l-1)\cdots 3 \cdot 1$ denotes the "factorial with double steps", and $\overline{n_{\mu_1}\cdots n_{\mu_l}}$ are the components of a tensor obtained by the l-fold symmetric tensorial product of the vector $\mathbf{n} \in S^2$, from which the reducible parts have been removed. The tensor basis is given by $\{ \overline{n_{\mu_1}\cdots n_{\mu_l}} \}_{l\in\mathbf{N}_0}$.

Vice versa, the distribution function can be calculated if all alignment tensors are known. If only some moments are known, an approximation to the distribution density function can be obtained. The accuracy of this approximation depends on the number of known moments.

As the orientation distribution function is position-dependent, also the alignment tensors are fields (position-dependent). The use of alignment tensors to describe the orientation order has been introduced in mesoscopic continuum physics for liquid crystals and microcracks [5: sec. 5.4.5].

If the orientation distribution function is symmetric with respect to $\mathbf{n}$, i.e. $f(-\mathbf{n}) = f(\mathbf{n})$, the alignment tensors of odd order vanish. As the fibres usually have a head-tail symmetry, the orientation distribution function will be symmetric.

Depending on the accuracy with which the orientation distribution function shall be represented, it is sufficient to use only the first (couple) of the alignment tensors, although for the *exact* representation, in general an infinite number of alignment tensors is necessary. Already the use of only the second-order alignment tensor is a huge improvement over the current approaches.

If the orientation distribution function is anisotropic, one can define a *macroscopic director* $\mathbf{d}$, which is a certain average orientation direction of the fibres. The macroscopic director is a unit vector that points into the direction of the eigenvector of the according-to-amount-largest eigenvalue of the second-order alignment tensor. In the case of a uniaxial distribution it is the symmetry axis of the distribution. In addition, it is useful to introduce an (orientational) order parameter $S \in [-\frac{1}{2}, 1]$ to account for the amount of anisotropy, where $S = 1$

corresponds to total alignment and $S = 0$ to isotropy; $S = -\frac{1}{2}$ describes a rare situation, when all fibres are aligned in a plane perpendicular to the eigenvector of the first eigenvalue. In the following, it is assumed that the eigenvalues are sorted according to the amount $|\lambda_1| \geq |\lambda_2| \geq |\lambda_2|$. The order parameter and eigenvalues λ_i are related as follows:

$$\frac{2}{3}S = \lambda_1, \tag{5}$$

$$-\frac{1}{3}S - b_S = \lambda_2, \tag{6}$$

$$-\frac{1}{3}S + b_S = \lambda_3, \tag{7}$$

where $b_S = \text{sign}(S)b$ and the biaxiality $b \in \left[0, \frac{1}{3}|S|\right]$ of the distribution [8].

Although the order parameter is connected to the eigenvalues of the order parameter tensor (second-order alignment tensor), one can calculate it as the average of the second Legendre polynomial $P_2(\cos\alpha)$:

$$S := \langle P_2(\cos\alpha)\rangle, \tag{8}$$

$$S = \left\langle \frac{3}{2}\cos^2\alpha - \frac{1}{2}\right\rangle, \tag{9}$$

where α is the angle between the fibre axis (microscopic director) and the macroscopic director. Legendre polynomials are a special case of spherical harmonics.

In contrast to the orientation number, the order parameter is defined with respect to the average fibre orientation, but each one takes only one angle into account. The alignment tensors, however, take both angles into account and one can calculate the number of fibres aligned in any direction by projecting the alignment tensors.

7. CONSTITUTIVE LAWS USING ALIGNMENT TENSORS

Making use of the previously introduced alignment tensors, one can formulate a general constitutive function for steel fibre reinforced concrete (SFRC):

$$T_{\text{SFRC}}^{ij} = T_{\text{SFRC}}^{ij}(T_{\text{concrete}}^{kl}, \mu, a^{kl}, a^{klmn}, T_{\text{fibres}}^{kl}), \tag{10}$$

where T_{concrete}^{kl} is the stress tensor of concrete without fibres, and T_{fibres}^{kj} is defined to be the stress tensor of an isotropic fibre orientation distribution and independent of the fibre density. It includes the different response of fibres of different inclination angles. The anisotropy is taken into account by the alignment tensors a^{kl} and a^{klmn} and the amount of fibres and spatial inhomogeneities by the volume fraction μ of the fibres. All of these quantities are field functions. Furthermore, properties of the fibres, such as $\frac{d}{l}$, the ratio of diameter to length, and

pull-out resistance, enter either T_{fibres}^{kl} or κ, where κ is a scalar material parameter that is to be determined by experiments.

Two hypothetic examples for constitutive mappings are

$$T_{\text{SFRC}}^{ij} = (1-\mu)T_{\text{concrete}}^{ij} + \mu a^{ik}T_{\text{fibres}}^{kl}a^{lj} \tag{11}$$

and

$$T_{\text{SFRC}}^{ij} = (1-\mu)T_{\text{concrete}}^{ij} + \mu\kappa a^{ij}. \tag{12}$$

Fourth-order alignment tensors could be included in these equations by tracing over two indices.

A thermodynamic consistent constitutive theory for (long) fibre reinforced elastic materials has been developed in [9]. However, this work covers only materials where the length of the fibres is the same as the length of the body that is reinforced. A constitutive theory for short fibre reinforced materials is still a subject of research.

8. CONCLUSIONS

In this paper different methods of describing the orientation of fibres in short fibre reinforced composite were discussed. It was clearly shown that the two commonly used methods for steel fibre reinforced concrete, the orientation number and the orientation profile, are rather approximative and thus insufficient. The newly proposed alignment tensors and corresponding (orientational) order parameter and macroscopic director overcome these limitations. The order parameter has the advantage over the orientation number in being related to the expectation value of the second Legendre polynomial, a special case of spherical harmonics, which are well known in electrodynamics and quantum mechanics. Due to its relation to the alignment tensor, the order parameter is objective and a material property. Especially by use of higher-order alignment tensors, it is possible to describe the orientation distribution of the fibres accurately in three dimensions. In addition, the alignment tensors can be easily used to formulate constitutive equations. These constitutive mappings are tensor equations and contain only objective quantities, especially they are independent of any pre-chosen projection direction. They can be used to calculate the stresses in any direction. Furthermore, all quantities are fields, i.e., they will vary along the material. Although steel fibre reinforced concrete has been chosen as an example, the methods are applicable to all kinds of short fibre reinforced composites.

REFERENCES

1. Grünewald, S. *Performance-Based Design of Self-Compacting Fibre Reinforced Concrete*. PhD thesis, Technische Universiteit Delft, 2004.

2. Lappa, E. S. *High Strength Fibre Reinforced Concrete: Static and Fatigue Behaviour in Bending*. PhD thesis, Technische Universiteit Delft, 2007.

3. Laranjeira de Oliveira, F. *Design-Oriented Constitutive Model for Steel Fiber Reinforced Concrete*. PhD thesis, Universitat Politecnica de Catalunya, 2010.

4. Papenfuss, C., Böhme, T., Herrmann, H., Muschik, W., and Verhás, J. Dynamics of the size and orientation distribution of microcracks and evolution of macro-scopic damage parameters. *J. Non-Equilib. Thermodyn.*, 2007, **32**(2), 1–14.

5. Muschik, W., Papenfuss, C., and Ehrentraut, H. *Concepts of Continuum Thermodynamics*. Kielce University of Technology, Technische Universität Berlin, 1996.

6. Papenfuss, C., Ván, P., and Muschik, W. Mesoscopic theory of microcracks. *Arch. Mech.*, 2003, **55**(5–6), 481–499.

7. Muschik, W., Ehrentraut, H., and Papenfuss, C. Concepts of mesoscopic continuum physics with application to biaxial liquid crystals. *J. Non-Equilib. Thermodyn.*, 2000, **25**, 179–197.

8. Jankun-kelly, T. J. and Mehta, K. Superellipsoid-based, real symmetric traceless tensor glyphs motivated by nematic liquid crystal alignment visualization. In *IEEE Transactions on Visualization and Computer Graphics (Proceedings Visualization/Information Visualization 2006)*. 2006, 1197–1204.

9. Alts, T. *Thermodynamik elastischer Körper mit thermo-kinematischen Zwangsbedingungen: fadenverstärkte Materialien*. Habilitation, TU Berlin, Fachbereich 9, 1979 (in German; Engl. translation of the title: *Thermodynamics of elastic bodies with thermo-kinetic constraints: fibre reinforced materials*).

Kommentaare lühikeste kiududega armeeritud materjalide teooriale

Heiko Herrmann ja Marika Eik

Lühikiududega armeeritud komposiitmaterjalide omadused on tundlikud kiudude orientatsiooni suhtes. Pingete mõjusuunas orienteeritud kiudude arvu hindamiseks kasutatakse orientatsiooni numbrit. See viib väga jämedale hinnangule, sest orientatsiooni number on defineeritud, kasutades pingete mõjusuunale projekteeritud kiudude pikkuste keskmist väärtust. Seega ei ole orientatsiooni number materjali omadus – see sõltub samuti projektsiooni suunast. Lisaks sellele ei piisa materjali anisotroopsete omaduste kirjeldamiseks ühest numbrist. Artiklis on esitatud tensorarvutusel põhinev lähenemisviis vaadeldud materjalide objektiivsete omaduste kirjeldamiseks.

Publication III

M. Eik and H. Herrmann. Raytraced images for testing the reconstruction of fibre orientation distributions. Proceedings of the Estonian Academy of Sciences, 61, 2, 128-136, http://dx.doi.org/10.3176/proc.2012.2.05, **June 2012.**

MECHANICS

Raytraced images for testing the reconstruction of fibre orientation distributions

Marika Eik[a,b,c] and Heiko Herrmann[a*]

[a] Centre for Nonlinear Studies, Department of Mechanics and Applied Mathematics, Institute of Cybernetics at Tallinn University of Technology, Akadeemia tee 21, 12618 Tallinn, Estonia
[b] Department of Civil and Structural Engineering, Aalto University School of Engineering, Rakentajanaukio 4 A, Otaniemi, Espoo Finland
[c] Faculty of Civil Engineering, Tallinn University of Technology, Ehitajate tee 5, 12618 Tallinn, Estonia; me@cens.ioc.ee

Abstract. The orientation distribution of fibres is relevant to the properties of a number of different kinds of fibrous materials from many fields like biology and engineering, including short fibre reinforced composites. The Persistence of Vision Raytracer (PoV-Ray) is a program for creating photorealistic images using raytracing. We discuss a sort of "creative misuse" of this program in science, because it was originally developed as an artistic software. However, the ability to create virtual images of virtual parts, test the image recognition software that is used to measure the fibre orientation distribution, and compare the results with the known distibution is a huge step forward. In this article the focus is on slicing/photometry, but computed-tomography-like images or microscope images could be produced as well and used to test segmentation and skeletonization algorithms.

Key words: image analysis, raytracing, fibre orientation, composite materials.

1. INTRODUCTION

Many composite systems may consist of or contain different types of fibres. Such systems have found application in various fields, from biology to engineering. An example of a composite containing short fibres is fibre reinforced concrete (FRC).

Fibre reinforced concrete has recently become a most popular research subject among civil engineers and scientists. This material is rapidly turning into one of the strongest candidates as a structural material for different load-bearing structures. It belongs to cementitious composites, which are commonly made up of two components, fibres as reinforcement and concrete as a matrix. During production of the composite the fresh concrete mass and the fibres are mixed together, which in turn means that initially this material is composed of individual constituents. For reinforcement of the concrete matrix, both discontinuous (short) and continuous fibres are used. This article considers the problems associated with the use of short steel

fibres (Fig. 1) as reinforcement. The main challenge of adding fibres to fresh concrete is to improve the tensile properties of concrete. Two materials (concrete matrix and steel fibres) that make up the composite are working together, i.e. the fibres take the major part of tensile stresses, while the concrete matrix takes compression and transmits the tensile stresses to the fibres. In the process of joint work, concrete also takes part in the capture of tensile stresses, but not such a significant part as the metal fibres. The stronger the bond between the matrix and the fibres, the greater strength the composite has. The bonding interface between cement matrix and fibres can be improved by mechanical or chemical means. The mechanical properties of the composite reinforced by discontinuos fibres strongly depend on the morphology of the inner structure of the system. Such composites frequently reveal anisotropic features, i.e. the properties depend on the considered direction. Steel fibre reinforced concrete (SFRC) has a strong tendency to anisotropy and the degree of anisotropy is directly connected with the orientation of fibres in the matrix.

---

* Corresponding author, hh@cens.ioc.ee

(a)

(b)
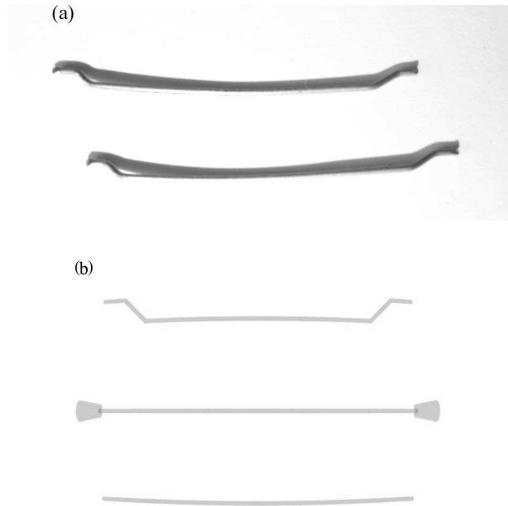
Fig. 1. Different types of fibres used in SFRC. (a) Real photo of hooked fibres. (b) Raytraced image of several kinds of fibres.

2. ESTIMATING THE ORIENTATION DISTRIBUTION FUNCTION USING SLICING AND PHOTOMETRICAL ANALYSIS

One way of identifying the orientation distribution function of fibres is the use of the slicing technique and, further, photometrical analysis. For this method some part of the structure is cut into slices and pictures are taken from both sides of each slice. From the pictures the position and the orientation of the fibres can be measured using specific software, e.g. ImageJ [1]. The advantages of this approach are a quite moderate price, the use of conventional equipment, and the ability to operate with quite large samples. But it has also short-comings, such as the necessity of production of a large number of slices and the uncertainty about the precision of results. The factors that reduce accuracy are related to the cutting method of slices (loss of material and change of the cut-fibre cross section), the type of fibres (shape), and the orientation of fibres within slices. To confirm the outcomes received using the slicing and photometry technique, it is necessary to employ alternative methods such as CT (= computed tomography, 3D X-ray), MRT (= magnetic resonance tomography), AC (= alternating current) impedance spectroscopy, artificial images, etc.

Since the slicing with the photometry technique is the main method used in research work (e.g. by [2]), it is discussed in more detail within this article. The slicing initially started from the procedure of sawing 12 SFRC cubes from six real-size floor slabs. Six of the cubes were

sawn from the edge of the slabs and the rest from the central part of the slabs. This scheme has been chosen to make out the impact of the wall effect on the orientation of fibres within the matrix. The further steps involved taking a photo of each surface of a slice (Fig. 2a) and afterwards the implementation of image processing and analysis. The use of cubes and several slices is a major enhancement with respect to [2], as commonly only a slice is used, which results in a low amount of fibres. The photo of the cleaned and filtered surface of a slice in binary format is presented in Fig. 2.

The cut cross sections of fibres have different shapes: circle, ellipse, and quite elongated ellipse.

(a)
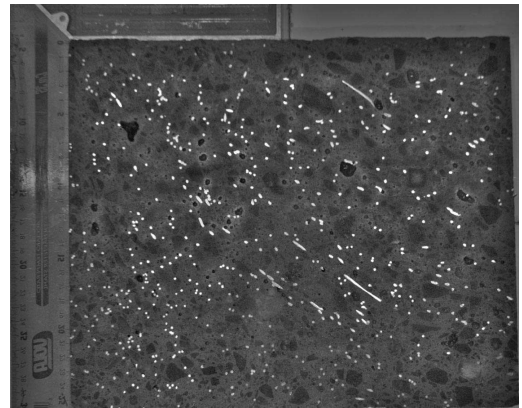
(b)

Fig. 2. Image of a slice. (a) Filtered image of a slice; bright spots are fibres. (b) Processed image of a slice in binary format; black spots are fibres.

2.1. Determining fibre orientation by photometrical analysis

To determine the orientation of a fibre in the matrix, a spherical coordinate system is used (the convention follows [3]). This means that the orientation of a fibre in the matrix is defined by two angles: (1) inclination (out-of-plane) angle ϑ (actually the angle between the surface normal and the fibre) and (2) azimuth angle (in-plane) angle φ.

To determine these angles, an ellipse is fitted to each cut fibre cross section. Fibre cross sections should be ellipses in the photo, because the fibres are cylindrical, which is a degenerated cone, and the intersection of a cone with a plane gives an ellipse as a closed curve. This can be done within the particle analysis of ImageJ. Here, the in-plane angle φ can be directly given by the orientation of the major axis (see Fig. 3). This angle has a 180° ambiguity, as each ellipse is rotation symmetric by 180°.

The inclination angle ϑ can be calculated from the ratio of minor to major axes of the fitted ellipse (Fig. 4):

$$\vartheta = \arccos\left(\frac{\text{ellipse minor axis}}{\text{ellipse major axis}}\right) \qquad (1)$$

or

$$\vartheta = \arccos\left(\frac{d_f}{2a}\right). \qquad (2)$$

If the fibre is aligned orthogonally to the slice, the cut cross section of the fibre is a circle with diameter d_f and the ratio

$$1 = \lim_{\vartheta \to 0}\cos(\vartheta) = \lim_{2a \to d_f}\frac{d_f}{2a}, \qquad (3)$$

which implies that the inclination angle ϑ is equal to 0°.
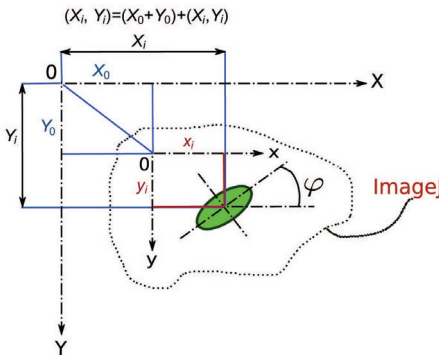
Fig. 3. Definition of the in-plane angle φ. As can be seen, this angle has a 180° ambiguity. This figure is available in colour at http://www.eap.ee.
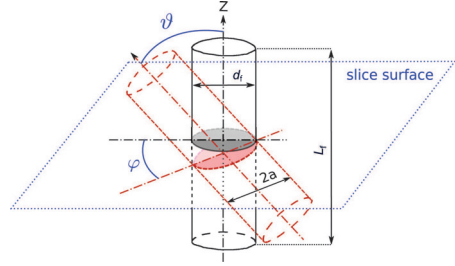
Fig. 4. Definition of the inclination angle ϑ and the in-plane angle φ. This figure is available in colour at http://www.eap.ee.

On the contrary, if the fibre is aligned within the slice surface, the ratio is

$$0 = \lim_{\vartheta \to 90^\circ}\cos(\vartheta) \approx \lim_{2a \to L_f}\frac{d_f}{2a}, \qquad (4)$$

which implies that the inclination angle ϑ is $\approx 90^\circ$.

The inclination angle ϑ determines the deviation of the fibre from the normal Z of the slice surface. The in-plane angle φ determines the direction of the fibre. This direction is measured from 0° up to 180°.

The standard application of the photometry technique only analyses the inclination angle ϑ, although the in-plane angle is easily accessible. The disadvantages of neglecting the in-plane angle and using only the reduced information to characterize the material has been discussed in [4].

The global system of coordinates, which is indicated in Fig. 3 as X_i, Y_i, determines the position of the respective fibre from the origin.

2.2. Measurement errors: similar both in the original and artificial images

During the processing of images, both original and artificial ones, a very interesting error was detected. This error concerns the minor axis of the fitted ellipse. Analytically, the minor axis of the ellipse should always remain constant, i.e. equal to the diameter of a fibre.

In the case of original images, this error was at first attributed to the cutting method of slices. The slices were produced by mechanical cutting using a diamond saw. Within this process there was a slight distortion of the cross section of fibres, due to forming a burr, i.e. spreading fibre material onto concrete. It was assumed that this error arose from the direction of the diamond saw. The error was discovered during the calibration of the scale of images: According to the calibration of the scale of images, there are 6.35 pixels/mm, therefore there should be 6.35 pixels per diameter of a fibre (fibre diameter is 1 mm), but manual counting of the pixels in fibres gave 9 pixels per diameter of a fibre.
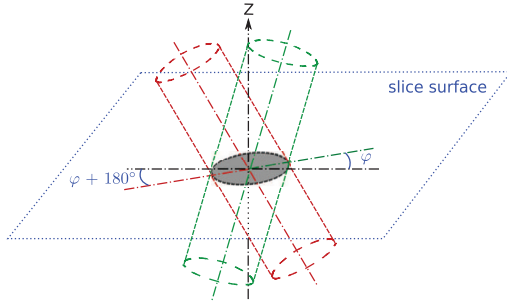
Fig. 5. Two possible orientations of a fibre with the same ϑ angle (inclination) but different φ angles (in-plane), causing the same ellipse (fibre cut cross section). This figure is available in colour at http://www.eap.ee.

Comparing this misfeature with the artificial images, a similar problem could be detected. In the case of artificial images, the minor axes of the fitted ellipses are not constant, varying more largely than could be attributed to the resolution of the images.

An additional systematic error is that the method cannot distinguish between fibres with an in-plane angle φ vs. $\varphi + 180°$ (Fig. 5).

2.3. Distribution parameters of angles ϑ and φ

The statistical distributions of orientation angles ϑ and φ were obtained by means of a specialized statistical program R [5] and several packages [6–14]. Relying on the results obtained by this software, several interesting features can be discovered in the behaviour of density functions of angles ϑ and φ (unpublished data by M. Eik, J. Puttonen, and H. Hermann). Especially, all probability density functions of angle ϑ had a tendency to bimodality, which is often a sign that the distribution is not Gaussian, and maybe a superposition of two density distributions with different maxima.

It is important to choose the slice distance so that each fibre is counted only once in order to avoid a distorted distribution (in contrast to what is needed for the enhanced reconstruction mentioned in Sec. 4.2).

3. ARTIFICIAL IMAGES AS A TESTSUITE

3.1. Why artificial images?

The distribution function of the orientation of fibres in SFRC is difficult to access. The most accurate methods, e.g. micro-computed tomography (μCT), are restricted to small samples. The method proposed by us is applicable to large samples. It is moderately accurate, but has an error that depends on the out-of-plane angle. Furthermore, different fibre types cause

different errors, so the error is expected to be larger for hooked and corrugated (undulating) fibres than for straight ones. The error for hooked-end fibres will depend on the shape/size of the hooked ends compared to fibre length. For undulating fibres the error will depend on the relation between the "amplitude" and the "wavelength" of the undulation, varying from small (comparable to straight fibres) for the small-amplitude–large-wavelength case to so large that the error effectively makes the slicing method unusable for the large-amplitude–short-wavelength case. The error cannot be accurately estimated from real samples (too expensive and time-consuming to make sufficiently many experiments). Using artificial images of the cutting planes, one can compare the reconstructed orientation distribution with the known one, which was used to create the images. From this comparison the error can be accurately given. Different types of errors are caused by different influences, like the resolution or colour/structure of the matrix. In artificial images it is possible to switch the errors on and off, or vary their magnitude, so one can render directly into black-and-white pictures with high contrast, making filtering unnecessary, or use a structured matrix with low contrast to try the effect of filtering.

It is possible to produce also artificial images of slices with fibre orientation distributions estimated from real samples. This enables visual comparison and maybe additional reanalysis of samples and comparison of the measured distributions.

The focus here is on slicing/photometry. However, it is also possible to create CT-like images that can be used to test segmentation and skeletonization algorithms.

3.2. About PoV-Ray

The Persistence of Vision Raytracer [15] (PoV-Ray) is a free and open-source tool to create photorealistic three-dimensional pictures. The scene is described in a human readable text file using constructive solid geometry. The PoV-Ray program supports, e.g. textures, bump maps, and the height field.

From the described scene the raytracer computes an image by following light-rays in the reverse direction, starting from the camera. Reflections and refraction can be taken into account according to prescribed object properties. PoV-Ray uses by default a left-handed Cartesian coordinate system, which should and can be easily changed to a right-handed one. The fact that PoV-Ray uses human readable text files as a scene description makes it easy to create such scenes from scripts or other program output.

PoV-Ray supports a couple of basic objects like

`box`, `sphere`, `cylinder`, `cone`, `torus`, `prism`, `lathe`.

These objects can be combined by using the constructive solid geometry operations

`union`, `intersection`, `difference`, `merge`.
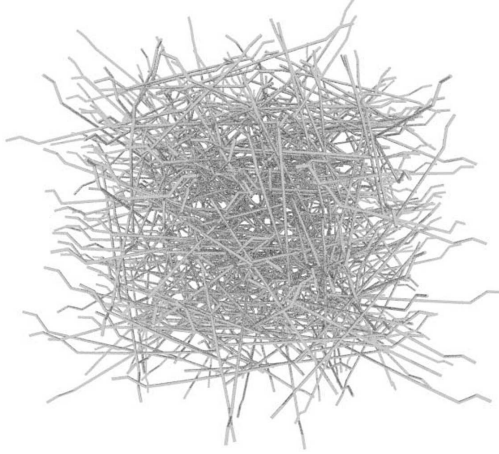
Fig. 6. PoV-Ray image of a bunch of 500 hooked fibres generated with a Python-script.

Furthermore, PoV-Ray supports the object modifiers

`clipped_by`, `material`, `inverse`, `interior`.

Using these, one can construct complicated structures and create astonishing realistic images.

PoV-Ray does not perform any kind of "collision detection", which means that fibres can touch or overlap/penetrate each other. This is not a problem as long as this does not happen within the generated images (slice planes) for which the probability is relatively low for reasonable fibre densities.

The use of constructive solid geometry is the major advantage of PoV-Ray here, as it allows us to first generate the whole structure (or cube) and then "cut" the slices.

In addition to "ordinary photos" (e.g. Fig. 6), standard X-ray transmission or CT images can be simulated. This is possible by using the `interior` modifier and giving the object a `fade_distance` and `fade_power`, thus simulating absorption.

3.3. Other renderers

There are other free and open-source renderers or raytracers besides PoV-Ray: *Blender*, *Art of Illusion*, *Pixie*, *Aqsis*, and *YafaRay*. These have different input (scene description) file formats, notably *Pixie* and *Aqsis* support the RenderMan[TM] language and *Blender* has a Python-scripting interface. The major difference from PoV-Ray is that for these renderers the slices would need to be created *outside* the renderer, which makes the generation of the slices more complicated, as the slice-fibre intersections need to be calculated separately.

4. ANALYSED ORIENTATION DISTRIBUTION AND COMPARISON

To test the reconstruction of fibre orientation distributions by slicing with photometry, three virtual cubes (vcubes) were generated with different fibre orientation distributions. These were "sliced" (Fig. 7) in PoV-Ray and analysed with `ImageJ`'s particle analysis. The distance of the slices was chosen larger than fibre length, to assure that each fibre is only counted once. The fibre orientation distributions were created from (overlapping) bivariate normal distributions. A bivariate normal distribution has the form

$$f(\varphi, \vartheta) = \frac{1}{2\pi\sigma_\varphi\sigma_\vartheta\sqrt{1-\rho^2}} \exp\left(-\frac{1}{2(1-\rho^2)}\right.$$
$$\left.\times\left(\frac{(\varphi-\mu_\varphi)^2}{\sigma_\varphi^2} - 2\rho\frac{\varphi-\mu_\varphi}{\sigma_\varphi}\frac{\vartheta-\mu_\vartheta}{\sigma_\vartheta} + \frac{(\vartheta-\mu_\vartheta)^2}{\sigma_\vartheta^2}\right)\right),$$
$$(5)$$

(a)
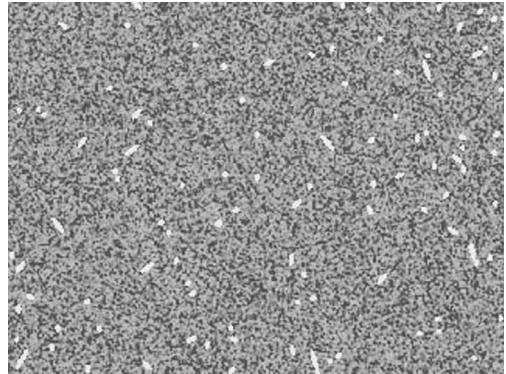
(b)

Fig. 7. PoV-Ray image of a slice of SFRC; two different renderings, one with, one without a structured matrix. (a) Vcube 0 slice 10, (b) vcube 0 slice 10.
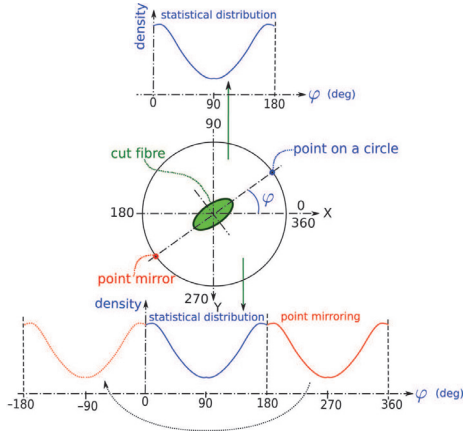
Fig. 8. Point mirroring of the angle φ. This figure is available in colour at http://www.eap.ee.

where μ are the mean values of φ and ϑ and σ are the corresponding standard deviations, and ρ is the correlation – which was chosen as $\rho = 0$ for all above distributions. The generated distributions were:

vcube 0: bivariate normal distribution with
- $\mu_\varphi = 90°$, $\mu_\vartheta = 45°$

vcube 1: superposition of two bivariate normal distributions:
- 70%: $\mu_\varphi = 45°$, $\mu_\vartheta = 45°$
- 30%: $\mu_\varphi = 70°$, $\mu_\vartheta = 45°$

vcube 2: superposition of two bivariate normal distributions:
- 70%: $\mu_\varphi = 45°$, $\mu_\vartheta = 45°$
- 30%: $\mu_\varphi = 250°$, $\mu_\vartheta = 45°$

The latter two distributions have been chosen to generate bimodal distributions, and to test, if the photometry can distinguish between these, as the difference in μ_φ is 180°. It was expected that photometrical analysis cannot distinguish these two bimodal distributions, because the measured direction (angle φ) marks two points on a circle (Fig. 8), one of which is determined by the angle φ and the other is a mirror point. There is no difference between the angles φ and $\varphi + 180°$. The data is just replicated into $[180°, 360°]$. This means the data is periodic with 180° and one can restrict the analysis to an interval with length 180°, e.g. $[0, \pi]$ or $[-\pi/2, \pi/2]$. However, it is important to keep this limitation of the method in mind and look for possibilities of overcoming it (see Sections 4.2 and 4.3).

4.1. Slicing with photometry

The photometrical analysis of the virtual slices was performed without knowledge of the parameters used to produce the images. One can observe that small angles in ϑ are not well represented, probably because of the resolution effect (see Fig. 9). A small deviation from the
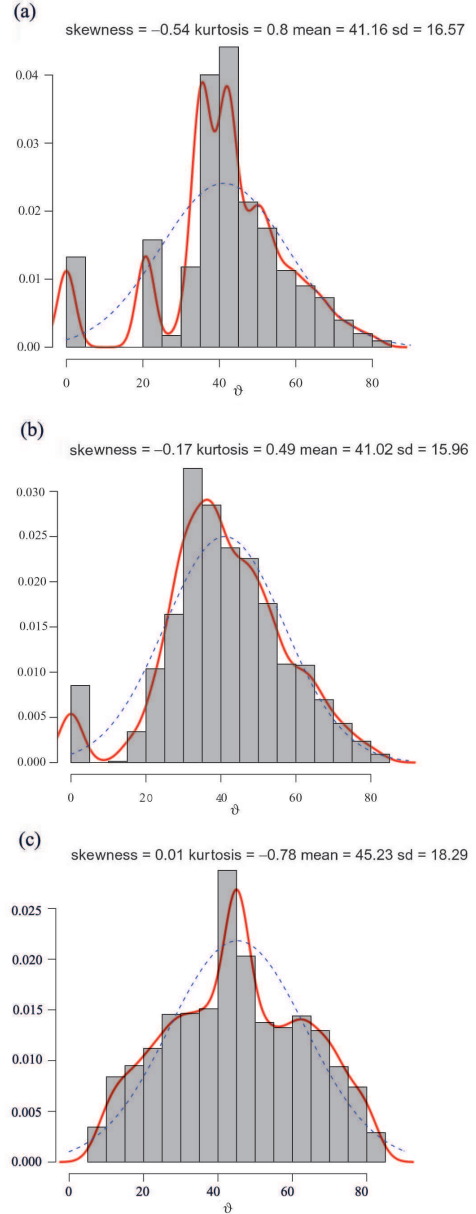
Fig. 9. Histogram plot of the orientation density distributions (inclination angle). The figures with the label "analysed" are the distributions obtained by photometrical analysis of the artificial images, the figures labelled "reference" are the input distributions used to create the images. Comparison of different resolutions. (a) Vcube 0: analysed (low resolution), (b) vcube 0: analysed (higher resolution), (c) vcube 0: reference. This figure is available in colour at http://www.eap.ee.

circle will cause a 1 pixel difference in shape, and the 1 pixel difference has a larger effect for small angles than for large angles.

For the in-plane angle φ, very small angles are over-estimated while the maximum is given accurately (see Fig. 10).

As it was assumed, the distributions of vcubes 1 and 2 cannot be distinguished. For many practical applications it is, however, necessary to determine the full distribution information without disambiguity, as a difference like the one in the two cubes causes different anisotropic effects in the material. In mechanical applications, for example, the stress tensor becomes anisotropic.

Figures 9–11 clearly show an influence of the image resolution. For low resolutions the measured distribution becomes multimodal (has several local maxima).

4.2. Enhancing the reconstruction with optimization methods

It is possible to enhance the reconstructed data by using combined information of several pictures, i.e. trace a single fibre through the slices. By this procedure it is possible to reconstruct the correct φ angle and overcome the φ vs. $\varphi + 180°$ disambiguity. The first test of this method was able to correctly reconstruct 91 fibres; all recognized fibres where correct, however, not all fibres were recognized (see Fig. 12).

This method – or the problem to solve – is similar to tracking temporarily hidden particles. The method does not distinguish whether the pictures are a time or space sequence.

4.3. Enhancing the reconstruction with additional information

Another possibility of removing the uncertainty about the φ-angle is aquiring more information, e.g. through ordinary X-ray transmission scans of the slices. One can then try to combine front, back, and X-ray picture to find the connectivity between points on the front and back of a slice and from that the $\varphi \in [0°, 360°]$ can be given.

These kind of images can also be simulated with PoV-Ray. A simple approach is to use an orthographic camera and a transparent matrix – or remove it entirely. To be more realistic, the matrix should get an interior with fade_distance and fade_power, and the light source should be behind the slice. This will simulate absorption in the matrix.

5. CONCLUSION

The orientation distribution of fibres is relevant for the properties of many different kinds of materials, including natural and man-made ones. To assess the properties of these materials, it is necessary to measure the orientation
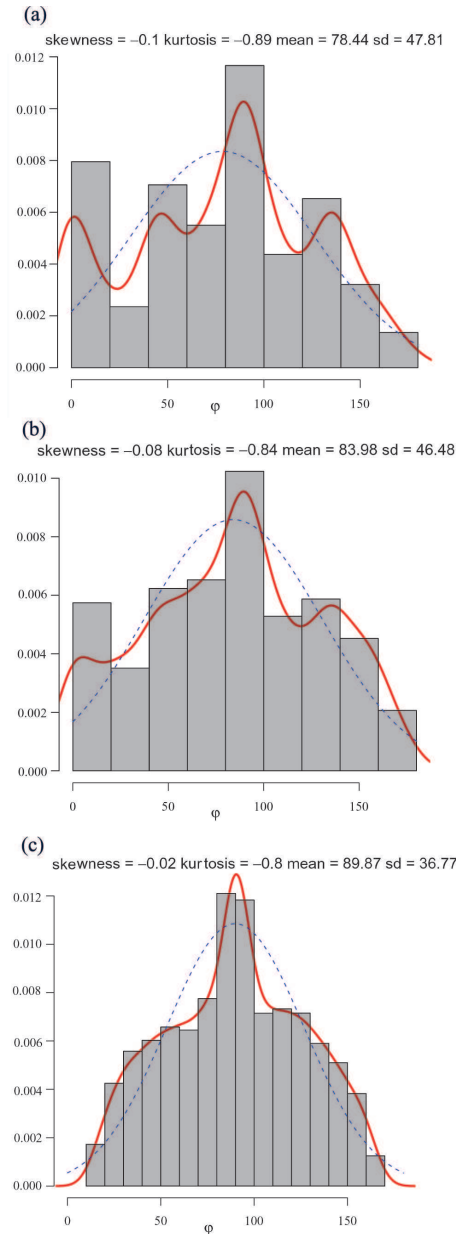
Fig. 10. Histogram plot of the orietation density distributions (in-plane angle). The figures with the label "analysed" are the distributions obtained by photometrical analysis of the artificial images, the figures labelled "reference" are the input distributions used to create the images. Comparison of different resolutions. (a) Vcube 0: analysed (low resolution), (b) vcube 0: analysed (higher resolution), (c) vcube 0: reference. This figure is available in colour at http://www.eap.ee.

(a)

(b)

(c)

Fig. 12. PoV-Ray image of the fibres in the cube and the ones identified by particle tracking (marked in black envelope) (reconstructed data courtesy of A. Fischer, unpublished data).

of fibres. This is often done with methods that include image-analysis (of 2d or 3d images). There are different ways to produce these photos, e.g. CT, microscope, photos of slices.

Testing the accuracy of these methods is important, but often difficult to do on real samples, as the "real" fibre distribution cannot be accessed. It also may be difficult to use different measurement techniques for the same sample, e.g. a CT may not be easy to find.

Slicing with photometry is a method more easily available in civil engineering than, e.g., CT, but the accuracy of this method was unclear, so a procedure to test it was necessary. In this paper a method for testing the accuracy of photometrical analysis for use in fibre orientation distribution measurements was presented. The advantage of the use of raytraced images to try image recognition and fitting software is that different influences which can cause errors can be regulated or switched on and off, like resolution, contrast or background structure. Furthermore, the result can be compared with the input distribution. The slicing with the photometry technique has enabled estimating the parameters of the distribution of angles ϑ and φ and making out features in the respective distributions.

ACKNOWLEDGEMENTS

Fig. 11. Isoline plot of the orietation density distributions. The figures with the label "analysed" are the distributions obtained by photometrical analysis of the artificial images, the figures labelled "reference" are the input distributions used to create the images. Comparison of different resolutions. (a) Vcube 0: analysed (low resolution), (b) vcube 0: analysed (higher resolution), (c) vcube 0: reference.

REFERENCES

1. Abràmoff, M. D., Magalhães, P. J., and Ram, S. J. Image processing with imagej. *Biophotonics International*, 2004, **11**(7), 36–42.

2. Grünewald, S. *Performance-Based Design of Self-Compacting Fibre Reinforced Concrete*. Ph.D. thesis, Technische Universiteit Delft, 2004. URL http://repository.tudelft.nl/view/ir/uuid:07a817aa-cba1-4c93-bbed-40a5645cf0f1/ (accessed 2 Dec. 2011).

3. Bronstein, I. N., Semendjajew, K. A., Musiol, G., and Muehlig, H. *Handbook of Mathematics*. Springer, 5th edition, 2007.

4. Herrmann, H. and Eik, M. Some comments on the theory of short fibre reinforced materials. *Proc. Estonian Acad. Sci.*, 2011, **60**, 179–183.

5. R Development Core Team. *R: A Language and Environment for Statistical Computing*. R Foundation for Statistical Computing, Vienna, Austria, 2011. URL http://www.R-project.org (accessed 2 Dec. 2011).

6. Sekhon, J. S. *Matching: Multivariate and Propensity Score Matching with Balance Optimization*, 2010.

7. Delignette-Muller, M. L., Pouillot, R., Denis, J.-B., and Dutang, C. *Fitdistrplus: Help to Fit of a Parametric Distribution to Non-Censored or Censored Data*, 2010. R package version 0.1-3.

8. Venables, W. N. and Ripley, B. D. *Modern Applied Statistics with S*. Springer, New York, fourth edition, 2002.

9. Stephenson, A. G. evd: Extreme value distributions. *R News*, 2002, **2**(2), 31–32. URL http://CRAN.R-project.org/doc/Rnews/ (accessed 2 Dec. 2011).

10. Pouillot, R. and Delignette-Muller, M.-L. Evaluating variability and uncertainty in microbial quantitative risk assessment using two r packages. *Int. J. Food Microbiol.*, 2010, **142**(3), 330–340.

11. Adler, D. and Murdoch, D. *rgl: 3D Visualization Device System (OpenGL)*, 2010. URL http://CRAN.R-project.org/package=rgl. R package version 0.91 (accessed 2 Dec. 2011).

12. Wuertz, D. et al., and see the SOURCE file. *fMultivar: Multivariate Market Analysis*, 2009. URL http://CRAN.R-project.org/package=fMultivar. R package version 2100.76 (accessed 2 Dec. 2011).

13. Dimitriadou, E., Hornik, K., Leisch, F., Meyer, D., and Weingessel, A. *e1071: Misc Functions of the Department of Statistics (e1071), TU Wien*, 2011. URL http://CRAN.R-project.org/package=e1071. R package version 1.5-25 (accessed 2 Dec. 2011).

14. Poncet, P. *modeest: Mode Estimation*, 2010. URL http://CRAN.R-project.org/package=modeest. R package version 1.14 (accessed 2 Dec. 2011).

15. Persistence of Vision Pty. Ltd. *Persistence of Vision Raytracer (Version 3.6)*. Persistence, Retrieved from http://www.povray.org/download/ (computer software, accessed 2 Dec. 2011).

Fotorealistlikud pildid rekonstrueeritud lühikiudude orientatsiooni jaotuste testimiseks

Marika Eik ja Heiko Herrmann

Paljude kiududega armeeritud materjalide omadused on kiudude orientatsiooni suhtes tundlikud. Lühikiududega armeeritud komposiitides on see asjaolu äärmiselt oluline. PoV-Ray on programm, mis loob fotorealistliku pildi, kasutades kiirte jälitust. Selles artiklis me tutvustame selle programmi n-ö loomingulist kuritarvitamist, sest algselt oli see loodud kunstitarkvarana.

Samas: oskus luua virtuaalseid pilte virtuaalsetest osadest, selleks et testida pildi identifitseerimise tarkvara, mida kasutatakse kiudude jaotamise mõõtmiseks, ja et tulemust oleks võimalik lühikiudude teadaoleva jaotusega võrrelda, on oluline samm edasi. Käesolevas artiklis on keskendutud põhiliselt viilutamisele/fotomeetriale, kuid samuti on võimalik genereerida raaltomograafialaadseid või mikroskoopilte edasiseks segmentimiseks ja skelettalgoritmide testimiseks.

Publication IV

Analysis of short fibres orientation in steel fibre-reinforced concrete (SFRC) by X-ray tomography

**Jussi-Petteri Suuronen · Aki Kallonen ·
Marika Eik · Jari Puttonen · Ritva Serimaa ·
Heiko Herrmann**

Abstract The mechanical properties of fibre composite materials are largely determined by the orientation of fibres within the matrix. Which orientation distribution short fibres follow in different parts of a structural element is still a subject for research and discussions in the scientific community. In this article, we present a modern and advanced method for measuring the orientation of short fibres in steel fibre-reinforced concrete (SFRC) by X-ray microtomography. With this method, a voxel image of the fibres is obtained directly in 3D, and the orientation of each individual fibre is calculated based on a skeletonized representation of this image. Scans of 12 SFRC samples, taken from the central height region of real-size floor slabs, reveal the fibres to be mostly horizontally oriented near the centre of a floor slab and more vertically oriented near the edge; here the alignment with the formwork dominates. The fibre orientation distributions are characterized by several orientation parameters as quantitative measures for the alignment. On the practical side, this method has the potential to be incorporated into the development and production process of SFRC structures to verify how the fibres contribute to capacity.

Introduction

Fibre-reinforced concrete (FRC) is one of the most prominent examples of cementitious composite materials for use in the construction industry. In contrast to concrete reinforcement with steel rebars, the stress-bearing fibres are introduced to the mass already at the mixing stage. Steel is a commonly used fibre material, but e.g. polypropylene [1] and glass [2] are used as well. The fibres can also vary in length, aspect ratio and shape, i.e. corrugated or hooked-end fibres can be used as well as straight ones. The present work concerns the use of short, hooked-end steel fibres (Fig. 1). The presence of the fibres plays an important role in improving the mechanical properties of the concrete mass, bearing some of the tensile stresses, which occur in the matrix, and transferring the remaining part by chemical bonding or mechanical anchorage into stable regions within the matrix. The addition of steel fibres helps to convert the failure characteristics of concrete from brittle to more ductile [3–5].

The performance of short fibre reinforced concrete (mechanical properties) is dependent on a number of factors, such as the shape, aspect ratio, volume fraction, surface characteristics and orientation of the fibers and concrete strength class [6]. Properties of such systems are often anisotropic, due mainly to a non-uniform distribution of fibre orientation within the matrix. The sensitivity of the composite strength on the fibre orientations has been shown in many fibre pull-out tests under different fibre inclination angles, e.g. by [7–11]. The fibre orientation, in turn, depends on the so-called 'wall effect', i.e. the tendency of

J.-P. Suuronen · A. Kallonen · R. Serimaa
Department of Physics, University of Helsinki, PO Box 64,
00014 Helsinki, Finland
e-mail: jussi-petteri.suuronen@helsinki.fi

M. Eik · J. Puttonen
Department of Civil and Structural Engineering, Aalto
University School of Engineering, Rakentajanaukio 4 A,
Otaniemi, Espoo, Finland

M. Eik · H. Herrmann (✉)
Centre for Nonlinear Studies, Institute of Cybernetics at Tallinn
University of Technology, Akadeemia Tee 21, 12618 Tallinn,
Estonia
e-mail: hh@cens.ioc.ee

fibres in the regions near the mold to align themselves with the formwork. One consequence of the wall effect is that different structure types tend to have different orientation distributions of fibres, e.g. the orientation of fibres in a slab may be much different relative to a beam, where the influence of the wall effect is more pronounced. In recent years, there have been many experiments investigating the properties [12–19] of FRC and studies of the orientation of short fibres in concrete [9, 12, 14, 20–28]. However, the conclusions presented in many sources are not expressed by a mathematical formalism (i.e. the functional dependency) or not readily applicable to structural design. Consistent dimensioning rules are also missing, partly due to the lack of sufficient large-scale experiments taking into account the effect of the fibre orientation [3]. The present theory of short fibre-reinforced materials does not take the anisotropy of the system into account very well; e.g. in [29, 30] only a one-dimensional (1D) case with aligned fibres is considered, and other approaches only consider a mean orientation and only one angle [9, 12]. This suggests the need for a more fundamental approach. Recently, a new approach to describe orientation distributions of fibres in short fibre-reinforced materials has been published in [31], who transferred the concepts from (mesoscopic) continuum theory of liquid crystals [32–35]. Comparable methods are used in other short fibre-reinforced materials [22, 23, 36]. Originally, these methods seem to go back to the physics of liquid crystals [37–39] and molecular gases [40, 41]. The main advantage of this tensorial approach is that it is independent of any predetermined direction, and thus able to account for the anisotropy of the material in three dimensions. However, to predict the performance of short fibre-reinforced materials by means of this method requires accurate information about the orientation of the fibres.

In the present article, the authors would like to introduce one of the advanced modern methods—X-ray tomography—to measure the orientation distribution from hardened concrete samples. X-ray microtomography (μCT) is well proven in the study of various microstructured materials [42] and has been previously used to determine the distribution and orientation of fibres in the matrix [14, 22]. Alternative methods that allow to estimate these characteristics include AC-impedance spectrometry [26], a magnetic method [27] and slicing photometry [21, 43, 44]. The main drawback of these methods is that they assess either only tendencies [26, 27] (e.g. average orientation of fibres and some degree of alignment) instead of the evaluation of individual objects (e.g. orientation of each fibre) or are limited to analysing the orientation based on a single slice through the sample [21]. With the method described in this work, both these problems are solved by analysing the orientation of individual fibres based on a 3D voxel representation of the sample. In the present article, the authors

present the results of X-ray tomography scans of sufficiently large (in size) samples, which are parts of the real-scale structures.

Materials and methods

SFRC cylinders

The steel fibre reinforced concrete (SFRC) cylinders used in this study were drilled from six large-scale floor slabs ($H \times W \times L$: 25 cm $\times$ 100 cm $\times$ 500 cm), according to Fig. 2; two cylinders, one from the central ("B"-samples) and one from the edge region ("A"-samples), were extracted from each slab (the number on the sample name refers to the slab it was taken from). This choice of sample location is associated with the wall effect; fibres located in close vicinity to the mould have a tendency to align and concentrate along the formwork. The concrete (concrete class C30/37) was reinforced with 50 mm long, $\varnothing$1 mm hooked-end fibres made of rod wire (C4D or C7D steel according to standard EN 10016-2), see Fig. 1. The length of the hooks was approx. 6 mm with bending angles between 30° and 45°. The fibre content was 80 kg m^{-3}, resulting in approximately 250 fibres per dm^3. The type of concrete was self-compacting, which means no vibration was needed. The slabs were cast in a casting factory using a bucket.

μCT scanning

The centre section of each cylinder was scanned using custom-built μCT equipment Nanotom 180 NF supplied by Phoenix| xray Systems + Services GmbH (Wunstorf, Germany), see Fig. 3. The system consists of a tungsten target nanofocus X-ray source, a high-accuracy computer-controlled translation/rotation sample stage and a CMOS flat panel detector with 2304×2304 square pixels of 50 μm width (Hamamatsu Photonics, Japan). The X-ray tube settings for all scans were 160 kV acceleration voltage and 55–70 μA tube current. Owing to the large sample size and absorbance, the radiation was filtered with a 4 mm Cu slab to reduce beam hardening effects. The effective detector area was doubled for the transmission images by horizontally shifting the detector one detector length for each image, and the detector pixels were binned by a factor
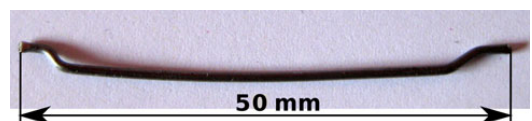
Fig. 1 Hooked-end fibres for slab reinforcement
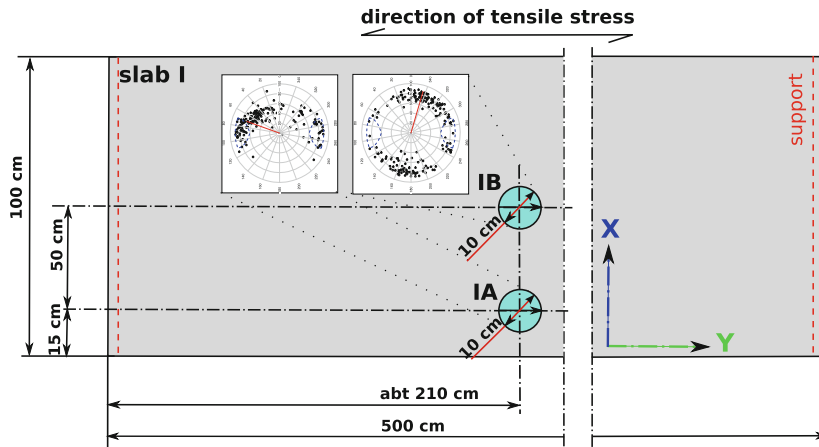
Fig. 2 The positioning of the sample cylinders within a single-span floor slab (dimensions in cm). The position of the supports and the direction of the tensile stress are also *indicated*. In addition, two scatter-plots of the fibre distributions are included to demonstrate inhomogeneities

of 4, resulting in images of 1127 × 576 pixels. In the vertical direction, this resulted in a field-of-view of approximately 7 cm. The projection images used for the reconstruction were composed of an average of 8–10 transmission images from the same angle. The transmission images were acquired with an exposure time of 1000 ms, and a total of 360 projection images were taken from each sample with an angular step of 1°. The measurement geometry resulted in an effective pixel width of 128.3 μm.

Reconstruction from the projection images was performed by an FDK-algorithm-based [45] reconstruction software 'datos| x rec' supplied by the equipment manufacturer. A beam hardening correction module of the reconstruction software was applied. However, owing to the low power of the nanofocus X-ray tube, X-ray intensity transmitted through the center of the sample was too low for the detector to perform optimally. This caused several artifacts to appear in the reconstruction. Firstly, detector

pixels that were completely nonresponsive at low X-ray intensity caused the so-called 'ring artifacts' in the images. These were corrected by filtering the projection images using a 5 × 5 pixel median filter (implemented in ImageJ [46]) before reconstruction. The median filter was also effective in reducing image noise. Secondly, owing to the use of two detector positions, there is a bright cylindrical artifact of high grayvalue in the middle of the reconstruction, and radial streaking artifacts propagating from the central artifact due to undersampling. Together with inhomogeneities in the concrete, this made it difficult to segment the fibres based on the reconstruction (see Fig. 4 (left)). The problem was alleviated by computing the reconstruction by 'highEdge' filtering, which effectively only reconstructs steep density gradients in the sample. In the highEdge-filtered reconstruction (Fig. 4 (right)), the central artifact is greatly reduced in intensity, and only the fibers and the edge of the sample cylinder appear as bright objects (Figs. 5, 6).
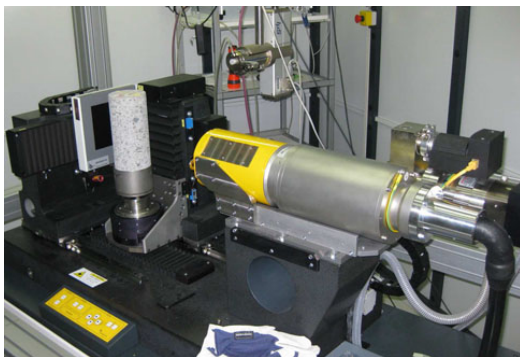
Fig. 3 Photo of an SFRC sample cylinder in the μCT scanner
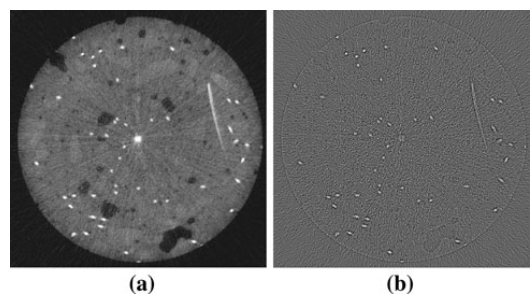
Fig. 4 Comparison of reconstructed *image* without and with applying highEdge filtering
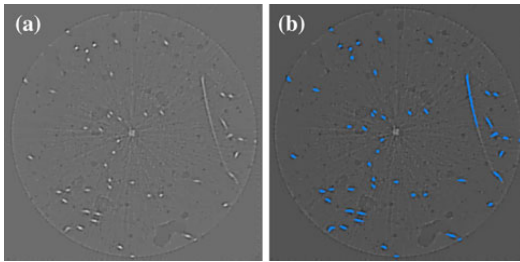
Fig. 5 Comparison of highEdge and nonlinear diffusion filtered reconstruction with segmentation. The nearly horizontal fibre in the right part of the image is connected in the neighbouring slices
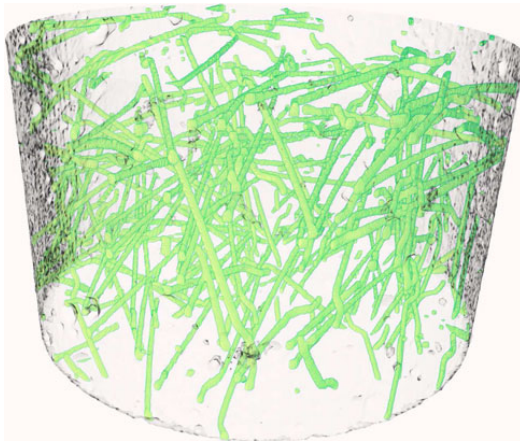
Fig. 6 Thresholded volume image of a μCT scan of SFRC after the removal of the artifact in the middle. The *picture* shows the rendered steel fibres and the outline of the cylinder

Fibre orientation analysis

Before analysing their orientation, a skeletonized representation of the fibres was calculated by Avizo Fire 6.2 software (VSG, France). First, noise was removed from the data by a 3D edge-preserving smoothing algorithm [47], followed by a dual threshold binarisation (function hysteresis in Avizo Fire). In the case of one sample (number 6B), a further morphological closing operation was applied to join fibre segments falsely split in the binarisation phase because of image noise. The central artifact caused by the use of two detector positions, as well as the edge of the SFRC cylinder detected by the highEdge filtering were masked out, i.e. replaced with zeros in the binary data.

Next, the binarised data was thinned by means of the XSkeleton pack extension to Avizo. The result of the thinning is a binary dataset, where only the voxels representing the medial axis of the fibres remain as 1s with the remaining voxels set to zero. However, with many fibres in

the data touching each other, the skeleton also contains connections between fibres, as well as spurious branches associated with noise-related irregularities in the fibre shape. The latter were removed by pruning all branches shorter than 10 voxels from the skeleton and the connected fibres were separated by a skeleton processing algorithm.

The skeleton processing algorithm was implemented as a function in Matlab software (Mathworks Inc., USA), which can be called directly from Avizo Fire. The algorithm begins by separating the voxel skeleton into disconnected objects consisting of one or more connected fibres. Each object is further divided into *lines*, which represent fibre segments and connections between fibres, and *branches*, i.e. areas where three or more lines meet.

The following fibre separation algorithm is then applied to each object in turn:

(1) Isolated lines are firstly checked for length: lines consisting of less than 100 voxels are eliminated, as they necessarily represent less than 25 % of a single fibre. Longer lines are checked for kinks in steps of 50 voxels, starting from one end. If a 50-voxel section forms an angle greater than 45° with the thus-far analysed part, it is identified as a kink and the line is split in two at the beginning of the section. This process is then repeated for the two parts.

(2) In objects with exactly one branch, the line that is least parallel to the others is identified and the voxel connecting that line to the branch is eliminated.

(3) In objects with two or more branches, the shortest line in the object is firstly identified. If that line is connecting two branches, it is eliminated, otherwise criterion 2 is applied to a randomly chosen branch.

(4) For objects in classes 2 and 3, the resulting object is checked for connectivity and the algorithm is recursively called for the remaining object or two objects.

The resulting objects are thus guaranteed to be isolated lines consisting of more than 100 voxels and have no kinks greater than 45°. These are then written to the output dataset as 1s.

After the application of the skeleton processing algorithm, the 3D orientation as well as width and length of the fibres could be calculated by means of Avizo. Since a major proportion of the fibres were only in part inside the sample cylinder, their length data carried little significance, but a large width could be used to identify objects where the fibre separation had failed. In the majority of these cases, however, the correct segmentation was clear on manual inspection, and the error made in the fibres' orientation could be quantified using the 3D angle tool in Avizo. In 20 such cases inspected, there was only one in which the angle between the correctly and falsely separated fibres exceeded 10°. It should be noted that an inaccuracy

of comparable magnitude is produced if one of the fibre's hooked ends lies outside the sample cylinder, see Fig. 11.

Orientation measures and order parameters

As measures to quantify the fibre orientations in the different samples, several parameters are introduced: director, (scalar) order parameter and orientation number. The director is the eigenvector of the according-to-amount-largest eigenvalue of the second order alignment tensor **A**, which is defined as [38, 41]

$$\mathbf{A} = \frac{1}{N} \sum_{i=1}^{N} \overline{\mathbf{n}_i \otimes \mathbf{n}_i} \qquad 1$$

where $\mathbf{n}_i$ is the direction of the i-th fibre, N is the total number of fibres and $\overline{\mathbf{n}_i \otimes \mathbf{n}_i}$ is the symmetric-traceless tensor product.

The order-parameter is given by [31, 37, 39]

$$S := \frac{3}{2} \lambda_1 \qquad (2)$$

or equivalently

$$S := \left\langle \frac{3}{2} \cos^2 \alpha - \frac{1}{2} \right\rangle, \qquad (3)$$

where λ_1 is the according-to-amount-largest eigenvalue of **A** and α is the angle between the director and the individual fibre. In Eq. (3), the order parameter is introduced as the expectation value of the second Legendre polynomial $P_2(\cos \alpha)$ [31, 39]. Additionally, orientation number(s) [12] with respect to a pre-defined axis ξ are introduced as

$$\eta_\xi = \frac{1}{N} \sum_{i=1}^{N} \cos \alpha_i^{(\xi)} \qquad (4)$$

where $\alpha_i^{(\xi)} \in [0°, 90°]$ is the angle between the i-th fibre and the ξ axis (where, e.g. ξ is the Y-, X- or Z-coordinate axis).

Results

The statistical analysis of the scanned data was performed by specialized statistical software [48–52, 55–60] based on the R programming language [53]. This section shows the results of the statistical analysis for fibres located in the middle part of a cylinder, which is about 7 cm in cylinder height. This choice of the scanning area was made to investigate the difference in fibre orientation between the bulk area ("B"-samples) and wall influence of the side walls ("A"-samples); additionally, technical circumstances connected with the secure holding of the samples favored this choice. The inclination angle Θ (diversion from the vertical Z axis) and azimuth (in-plane) angle Φ for each fibre are defined as it is shown on Fig. 7. According to this figure one concludes that the best contribution of the fibres is achieved when Θ is 90° and Φ is 90° or 270° since the Y axis corresponds to the direction of the tensile stress. The arrow that is marked on the top of each cylinder sample coincides with the Y axis, which is pointing towards the X-ray source.

Figures 8, 9 and 10 show the important features of the distributions of the orientation angles Θ and Φ within all scanned cylinders. The properties of the samples are summarized in Table 1.

Discussion

General tendencies of the orientation distributions

It is evident from the scatter plots (Fig. 8) that the orientation distribution of fibres within the edge cylinders is quite different from the central ones. The solid line in the scatter plots (Fig. 8), shows the director of the distribution. The 'director' is the eigenvector of the according-to-amount largest eigenvalue of the second order alignment tensor. The order-parameter-tensor is a second order tensor, calculated from the orientation distribution and connected

Fig. 7 *Left* definition of the orientation angles Θ and Φ measured from the µCT data, where the convention $\Theta \in [0, 90]$ and $\Phi \in [0, 360]$ is used. Therefore, always the orientation of the vector pointing from the 'upper' to the 'lower' end of the fibre is measured. *Right* the case of totally aligned fibres, $\Theta = 90°$, $\Phi = 90°$ or 270°
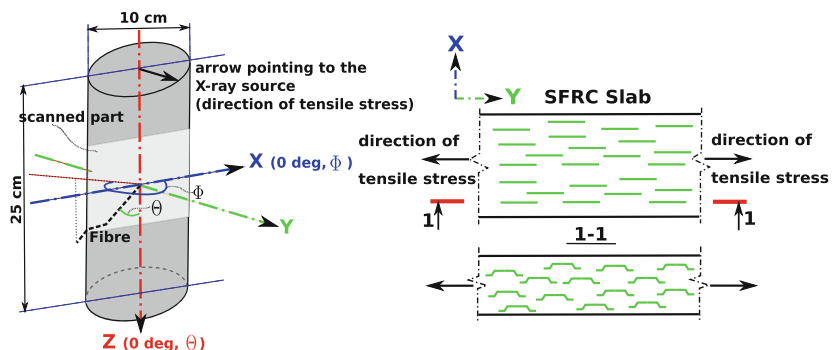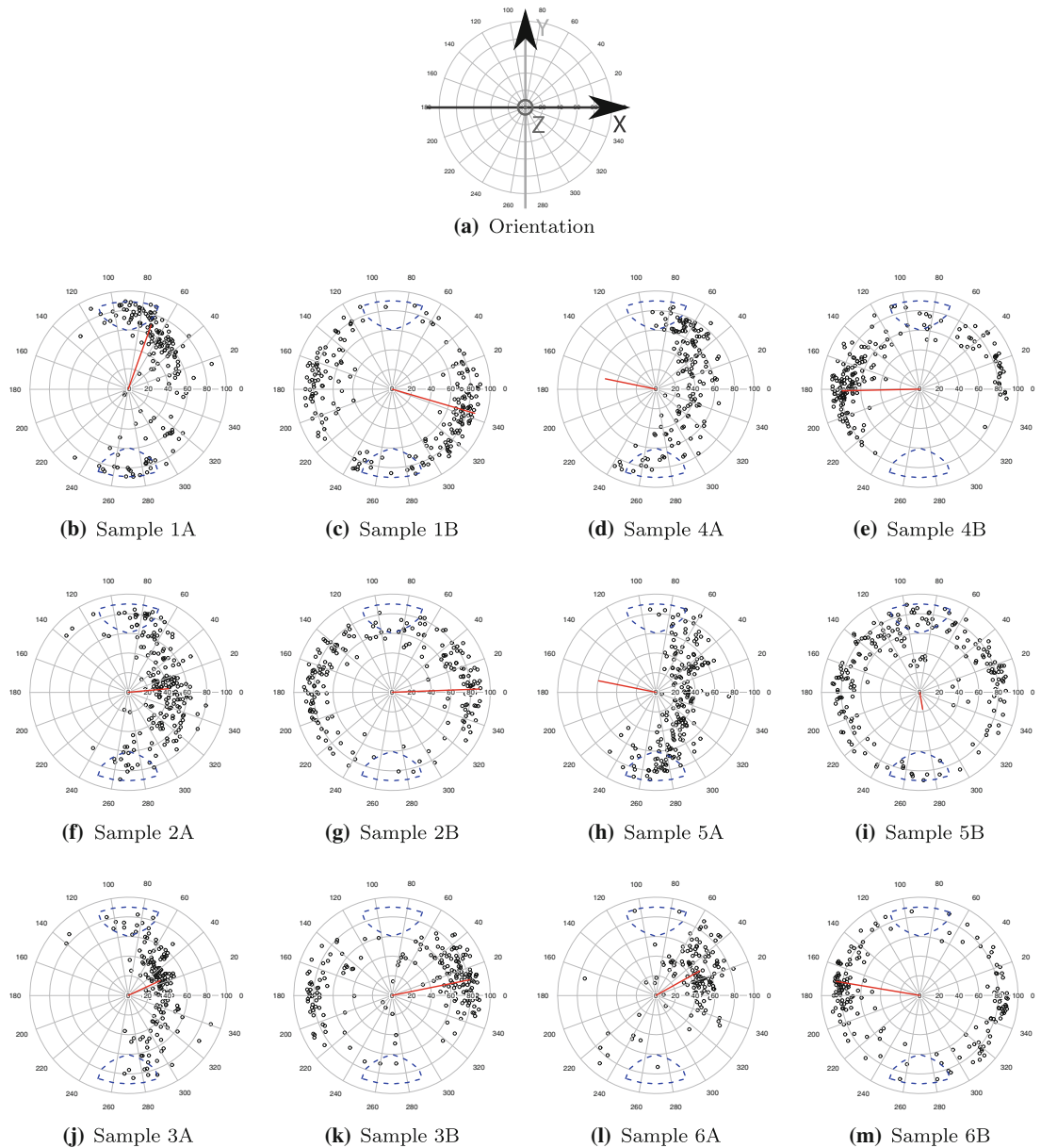
Fig. 8 Scatter plots of fibre orientation, radius is inclination angle Θ in °. View antiparallel to Z axis (from bottom to top of cylinder). The *solid lines* show the director (eigenvector) of the existing distributions. The domains indicated by the *dashed lines* correspond to the case where the fibres are well aligned in direction of the principal stress

with the orientational order [31]. The eigenvectors of this tensor represent the material axes. In case of a transversely isotropic material, the director is the symmetry axis of the material; in case of an orthotropic material, the director corresponds to the 'most reinforced' direction. The edge

cylinders show the tendency of fibres to concentrate in certain sectors of the distribution circle, while the distribution of fibres in the central cylinders is more uniform along the circumference. Similarly, comparing the edge and central cylinders, one can notice that in the edge

Fig. 9 Probability density *histogram* of inclination angle Θ; skewness and kurtosis compared with a normal distribution: *dashed line*

skewness = 0.13 kurtosis = −1.04 mean = 52.13 sd = 19.01

skewness = −1.68 kurtosis = 3.01 mean = 74.74 sd = 12.92

(a) Sample 5A

(b) Sample 5B
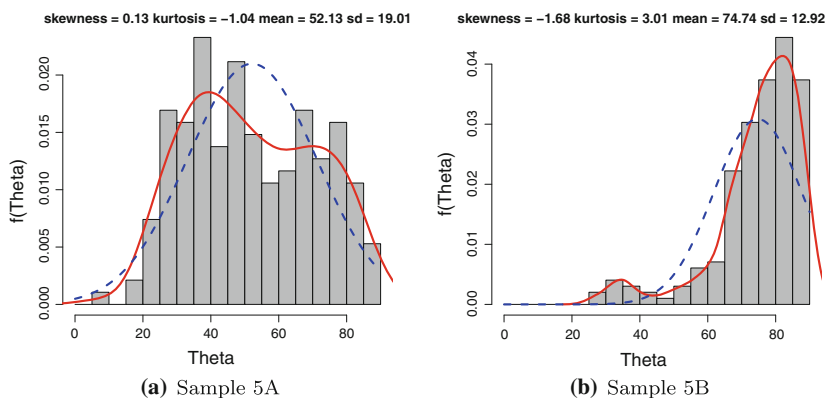
Fig. 10 Probability density *histogram* of in-plane angle Φ

(a) Sample 5A

(b) Sample 5B
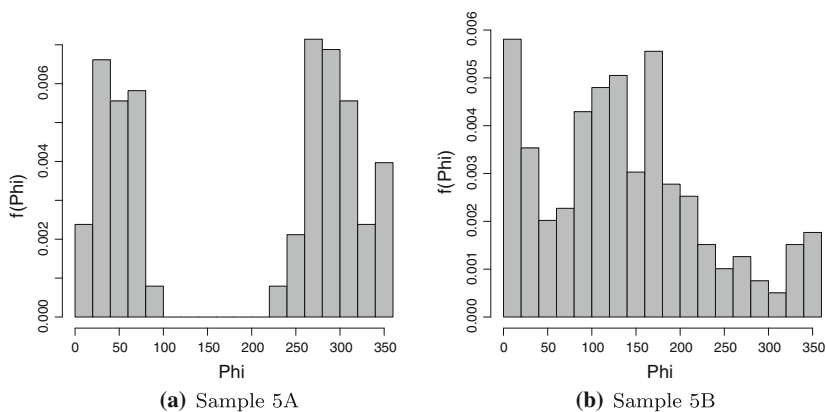
Table 1 Summary of properties of the samples, all samples have been at least 6 month old at the time of scanning

Sample	Location	Batch	# Fibres	Vol.%	$\bar{l}$	$\sigma_{\bar{l}}$	S	$\mathbf{d} = (\Phi, \Theta)$	η_Y	η_X	η_Z
1A	Edge	2	167	0.78	252	97	0.52	(70, 70)	0.72	0.38	0.4
1B	Center	2	201	0.89	239	88	0.53	(344, 88)	0.44	0.77	0.22
2A	Edge	2	201	0.9	242	92	0.42	(5, 41)	0.48	0.49	0.56
2B	Center	2	192	0.83	235	88	0.46	(2, 89)	0.44	0.76	0.25
3A	Edge	2	168	0.77	249	86	0.52	(25, 36)	0.48	0.44	0.64
3B	Center	2	194	0.86	241	90	0.59	(11, 81)	0.33	0.79	0.32
4A	Edge	1	152	0.76	269	89	−0.44	(168, 52)	0.61	0.45	0.51
4B	Center	1	186	0.84	244	90	0.62	(181, 79)	0.34	0.82	0.25
5A	Edge	1	189	0.89	254	93	−0.44	(169, 59)	0.58	0.37	0.58
5B	Center	1	198	0.92	252	95	−0.39	(280, 17)	0.53	0.65	0.25
6A	Edge	1	138	0.7	275	88	0.65	(29, 51)	0.41	0.59	0.57
6B	Center	1	167	0.72	233	90	0.63	(171, 86)	0.36	0.83	0.19

The '# fibres' means parts of fibres longer than 25 % fibre length; the expected number of whole fibres from the real volume fraction would be 143. The volume fraction (vol.%) does not take into account objects of less than 100 voxels (25 % fibre length) and is calculated from the straight end-to-end length received from Avizo Fire, and therefore underestimates the real volume fraction slightly. The average number of fibres per sample is $\bar{n} = 179$ with a standard deviation of $\sigma_{\bar{n}} = 21$, the average fibre volume fraction is $\bar{v} = 0.82$ % and its standard deviation is $\sigma_{\bar{v}} = 0.07$ %. The director is given as a tupel (Φ, Θ), the order-parameter $S \in [-\frac{1}{2}, 1]$ where negative values indicate a flat-isotropic case and the orientation-number in Y-, X- and Z-direction η_Y, η_X and η_Z are also given

cylinders the fibres mostly tend to align in the Y–Z-plane (the inclination angle Θ is mostly between 30° and 70°) and in the central ones the fibres more tend to the X–Y-plane (with Θ between 70° and 90°).

Efficiency of fibre distribution

The domain indicated on the scatter plots corresponds to the case shown on the right-hand side of Fig. 7, where the fibres are well aligned in direction of the tensile stress. This arrangement of fibres corresponds to the most effective one, i.e. all fibers are aligned relative to each other, as well as relative to major tensile stress in the material. In this case, the director of the distribution coincides with the direction of fibres. As evidenced by Fig. 8, this does not hold in the general case. In the case when fibres are well aligned (with each other), e.g. Fig. 8e (sample 4B), the director represents the mean orientation, but in cases where the distribution is more flat-isotropic, e.g. Fig. 8h (sample 5A), the director is perpendicular to the plane in which the fibres are oriented.

Probability density histograms

Probability density histograms of the inclination angle, presented in Fig. 9, may show a slight tendency to bimodality—two local maxima—both in the edge and central cylinders. It is a significant feature that the distribution does not follow a Gaussian distribution. There are interesting features observed in the probability density histograms of the Φ angle as well (Fig. 10), in particular, also these distributions tend to bimodality. This is in contrast to what can be found in other publications, e.g. [9, 24], where a Gaussian distribution is assumed. If the true orientation distribution of the fibres is asymmetric (or bimodal) and for the calculation a Gaussian distribution is assumed, this means that certain fibre orientations are overestimated while others are underestimated. If now the amount of fibres with small inclination angles to the direction of tensile stress is overestimated by the Gauss distribution, this will result in overestimating the strength of the material.

Error estimation

The main sources of error in the orientation distribution are

- only one of the hooked ends is within the scanning area, max. error is 13°, from $\Delta\alpha = \arctan\frac{\text{hook}-\text{height}}{\text{min obj. length}}$ (see Fig. 11);
- resolution of the scan, error about 1 px (0.1283 mm), max error is $\Delta\alpha = \arctan\frac{0.1283\,\text{mm}}{12.83\,\text{mm}} = 0.6°$ (1 px off the correct position and 100 px length of object);
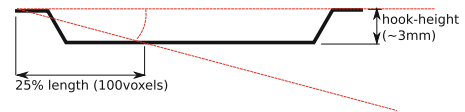
Fig. 11 Maximum error due to only part of fibre being in scanned volume
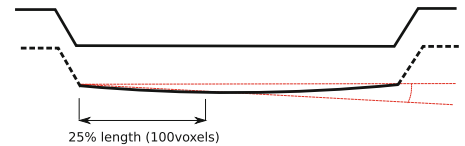
Fig. 12 Maximum error due to curvature of fibre

- the middle part of the fibres is not exactly straight, but slightly curved (see Figs. 1, 12);
- manual setting of the thresholds;
- skeleton processing: touching fibres and corresponding automatic splitting by the self-written program

The errors arising from manual thresholding of the reconstructions was evaluated by repeated analysis of one sample (number 3B). From the inspected fibers, the manual regulation of grayvalue thresholds gave an uncertainty of approximately 2° between the two processed versions. The accuracy of the fibre separation algorithm and the influence of the central artifact were evaluated by performing a manual segmentation of one dataset: using the dual-thresholded image (e.g. Fig. 8e) as a starting point, connections between two fibers were manually removed and disconnected ends of the same fiber manually connected. This eliminated the need for the skeleton processing step, as there were no spurious connections in the skeletonized data. Comparison of scatter plots (Figs. 8l, 13) shows excellent agreement with the automatically processed data.

Conclusions

μCT allows looking inside a robust material such as concrete and obtaining reliable, 3D data about the spatial and orientational distribution of fibres in the matrix. This represents a significant step towards investigating the relationships between fibre orientation and the mechanical characteristics of SFRC and postulating a constitutive relation for concrete reinforced by short fibres. The next task would be defining the orientation distribution function of fibres, which could then be integrated into governing equations [31, 54].
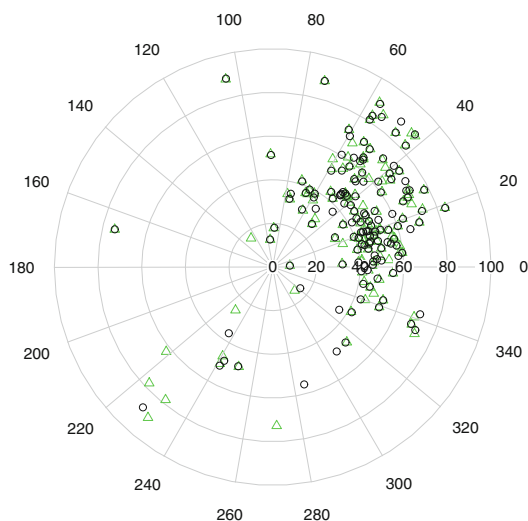
Fig. 13 Comparison of automatic and hand-segmented data for sample 6A. *Scatter plot* of fibre orientation, radius is inclination angle Θ in °. View antiparallel to Z axis (from bottom to top of cylinder). Automatic segmented data is denoted by *triangles* and hand-segmented by *circles*. The director of the distribution changed by less than 1°, $(\Theta, \Phi) = (51, 29)$ in both cases

Another potential application for µCT scanning is in developing production methods for SFRC products. The accurate orientation data could be a valuable asset when attempting to tailor the properties of SFRC by varying the production process. Later, µCT can also be used for quality control. Although the sample size is limited in the order of several dm³ compared to the size of structural elements, which are in the order of m³, the precision of the measurements is unparalleled by other methods and therefore provides valuable information. With the present equipment, the actual CT scan takes 1.5–2 h, depending on the imaging parameters, and the reconstruction a few minutes. The time required for the image processing and statistical analysis is, of course, largely dependent on the available computer hardware: on a single 2.50 GHz Intel Xeon core, the processing takes approximately 3 h per sample. It should be emphasized, however, that this µCT equipment is primarily used for scanning millimeter-sized samples at submicrometre resolution, (i.e. three orders of magnitude higher than the 128.3 µm per voxel used in this study) and lacks the beam power necessary to image large samples of highly absorbing materials like concrete. Without this limitation, most of the time-consuming processing steps (various filters, removal of the central artifact) could most likely be either omitted completely or replaced with less CPU-intensive alternatives. CT systems that are capable of delivering over 1500 W X-ray tube power and greater than

400 kV acceleration voltages (cf. 11 W and 160 kV used in this study), while maintaining sufficient resolution, are readily available as turn-key systems which require only limited knowledge of X-ray methods to operate. Less noisy and artifact-free data might also enable automating the image processing steps (e.g. setting grayvalue thresholds), greatly reducing the level of technical skill required to perform the analysis. Integrating µCT equipment into the quality assurance process of SFRC production is therefore feasible.

References

1. Wang Y, Zureick AH, Cho BS, Scott DE (1994) J Mater Sci 29:4191. doi:10.1007/BF00414198
2. Purnell P, Buchanan AJ, Short NR, Page CL, Majumdar AJ (2000) J Mater Sci 35:4653. doi:10.1023/A:1004882419034
3. Tejchman J, Kozicki J (2010) Experimental and theoretical investigations of steel-fibrous concrete. Springer series in geomechanics and geoengineering, 1st edn. Springer, Berlin
4. Beaumont PWR, Aleszka JC (1978) J Mater Sci 13:1749. doi:10.1007/BF00548738
5. Mangat PS, Motamedi Azari M (1985) Journal of Materials Science, 20:1119.doi:10.1007/BF00585757
6. Zollo RF (1997) Cem Concr Compos 19(2):107. doi:10.1016/S0958-9465(96)00046-7
7. Weiler B, Grosse C (1996) Otto Graf J 7:116. http://www.mpa.uni-stuttgart.de/publikationen/otto_graf_journal/ogj_1996/weiler/index.html. Accessed 5 April 2012
8. Laranjeira F, Molins C, Aguado A (2010) Cem Concr Res 40(10):1471. doi:10.1016/j.cemconres.2010.05.005
9. Laranjeira de Oliveira F (2010) Design-oriented constitutive model for steel fiber reinforced concrete. PhD Thesis, Universitat Politecnica de Catalunya. http://www.tdx.cat/TDX-0602110-115910. Accessed 5 April 2012
10. Pupurs A (2011) Load bearing capacity prediction of steel fiber reinforced concrete elements subjected to bending loads. PhD Thesis, Riga Technical University, Faculty of Civil Engineering, Institute of Structural Engineering and Reconstruction

11. Krasnikovs A, Kononova O, Khabbaz A, Machanovsky E, Machanovsky A (2011) World Acad Sci Eng Technol 59:988
12. Grünewald S (2004) Performance-based design of self-compacting fibre reinforced concrete. PhD Thesis, Technische Universiteit Delft. http://repository.tudelft.nl/view/ir/uuid:07a817aa-cba1-4c93-bbed-40a5645cf0f1. Accessed 5 April 2012
13. Lim D, Oh B (1999) Eng Struct 21(10):937. doi:10.1016/S0141-0296(98)00049-2
14. Schnell J, Breit W, Schuler F (2011) In: Sruma V (ed) Proceedings of the fib symposium Prague 2011, p 583
15. Rao TG, Seshu DR (2005) Cem Concr Compos 27(4):493. doi:10.1016/j.cemconcomp.2004.03.006
16. Ferrara L, Meda A (2006) Mater Struct 39:411. doi:10.1617/s11527-005-9017-4
17. Mohammadi Y, Singh S, Kaushik S (2008) Constr Build Mater 22(5):956. doi:10.1016/j.conbuildmat.2006.12.004
18. Sivakumar A, Santhanam M (2007) Cem Concr Compos 29(7):575. doi:10.1016/j.cemconcomp.2007.03.005
19. Pfyl T (2002) Tragverhalten von stahlfaserbeton. PhD Thesis, Eidgenössische Technische Hochschule Zürich
20. Granju JK, Ringot E (1989) Acta Stereol 8:579
21. Wuest J, Denarié E, Brühwiler E, Tamarit L, Kocher M, Gallucci E (2009) Exp Tech 33(5):50. doi:10.1111/j.1747-1567.2008.00420.x
22. Le TH, Dumont P, Orgéas L, Favier D, Salvo L, Boller E (2008) Composites A 39(1):91. doi:10.1016/j.compositesa.2007.08.027
23. Dumont P, Corre SL, Orgéas L, Favier D (2009) J Non-Newton Fluid Mech 160(2–3):76. doi:10.1016/j.jnnfm.2009.03.001
24. Laranjeira F, Grünewald S, Walraven J, Blom K, Molins C, Aguadoa A (2011) Mater Struct 44:1093. doi:10.1617/s11527-010-9686-5
25. Eiduks M, Krasnikovs A, Dunskis E, Kononova O (2010) Sci J Riga Tech Univ, 33:98. https://ortus.rtu.lv/science/lv/publications/8346. Accessed 5 April 2012
26. Ozyurt N, Mason TO, Shah SP (2007) Measuring, monitoring and modeling concrete properties. Springer, Berlin, p 285. doi:10.1007/978-1-4020-5104-3
27. Ferrara L, Faifer M, Toscani S (2011) J Mater Struct 45(4):575. doi:10.1617/s11527-011-9793-y
28. Barnett S, Lataste JF, Parry T, Millard S, Soutsos M (2010) Mater Struct 43:1009. doi:10.1617/s11527-009-9562-3
29. Taya M, Aresenault RJ (1989) Metal matrix composites: thermomechanical behavior. Pergamon Press, Oxford
30. Becker E, Bürger W (1975) Kontinuumsmechanik. Teubner Studienbücher, Stuttgart
31. Herrmann H, Eik M (2011) Proc Est Acad Sci 60(3):179. doi:10.3176/proc.2011.3.06
32. Papenfuss C (1995) Contribution to a continuum theory of two dimensional liquid crystals. Wissenschaft-und Technik Verlag, Berlin
33. Ehrentraut H (1996) A unified mesoscopic continuum theory of uniaxial and biaxial liquid crystals. Wissenschaft-und Technik Verlag, Berlin
34. Ehrentraut H, Muschik W, Papenfuss C (1996) Concepts of continuum thermodynamics—5 lectures on fundamentals, methods and examples. Sekcja Poligrafi Politechniki Swietokrzyskiej, Kielce
35. Herrmann H, Engelbrecht J (2010) J Non-Equilib Thermodyn 35(3):337. doi:10.1515/JNETDY.2010.021
36. Chalencon F, Orgéas L, Dumont P, Foray G, Cavaillé J, Maire E, Rolland du Roscoat S (2010) Rheol Acta 49:221. doi:10.1007/s00397-009-0393-5
37. Hess S (1976) Z Naturforsch A 31a:1034
38. Pardowitz I, Hess S (1980) Physica A 100(3):540. doi:10.1016/0378-4371(80)90166-1
39. Steuer H (2004) Thermodynamical properties of a model liquid crystal. PhD Thesis, TU Berlin. http://opus.kobv.de/tuberlin/volltexte/2004/919. Accessed 5 April 2012
40. Waldmann L (1963) Z Naturforsch A 18a:1033
41. Hess S (1975) Z Naturforsch A 30a:728
42. Buffiere J, Maire E, Adrien J, Masse J, Boller E (2010) Exp Mech 50:289
43. Stroeven P, Hu J (2006) Mater Struct 39:127. doi:10.1617/s11527-005-9031-6
44. Eik M, Herrmann H (2012) Proc Est Acad Sci 61:128. doi:10.3176/proc.2012.2.05
45. Feldkamp L, Davis L, Kress J (1984) J Opt Soc Am 1(6):612
46. Abràmoff MD, Magalhães PJ, Ram SJ (2004) Biophotonics Int 11(7):36
47. Weickert J, ter Haar Romeney BM, Viergever MA (1998) IEEE Trans Image Process 7(3):398
48. Lemon J (2006) R-News 6(4):8. http://CRAN.R-project.org/doc/Rnews. Accessed 5 April 2012
49. Dimitriadou E, Hornik K, Leisch F, Meyer D, Weingessel A (2011) R package version 1.5-25. e1071: Misc Functions of the Department of Statistics (e1071), TU Wien. http://CRAN.R-project.org/package=e1071. Accessed 5 April 2012
50. Poncet P (2010) R package version 1.14, modeest: mode estimation. http://CRAN.R-project.org/package=modeest. Accessed 5 April 2012
51. Adler D, Murdoch D (2010) rgl: 3D visualization device system, R package version 0.91. http://CRAN.R-project.org/package=rgl. Accessed 5 April 2012
52. Wuertz D, many others, see the SOURCE file (2009) fMultivar: multivariate market analysis, R package version 2100.76. http://CRAN.R-project.org/package=fMultivar. Accessed 5 April 2012
53. R Development Core Team (2011) R: a language and environment for statistical computing. R Foundation for Statistical Computing, Vienna, Austria. http://www.R-project.org. ISBN 3-900051-07-0. Accessed 5 April 2012
54. Herrmann H, Eik M (2011) In: Presented at ICCS 16, 30 Juni 2011, Porto
55. Agostinelli C, Lund U (2011) R package circular: circular statistics (version 0.4-3). CA: Department of Environmental Sciences, Informatics d Statistics, Ca' Foscari University, Venice. UL: Department of Statistics, California Polytechnic State University, San Luis Obispo. https://r-forge.r-project.org/projects/circular. Accessed 5 April 2012
56. Sekhon JS (2010) Matching: multivariate and propensity score matching with balance optimization, R package version 4.7-11. http://CRAN.R-project.org/package=Matching. Accessed 5 April 2012
57. Delignette-Muller ML, Pouillot R, Denis JB, Dutang C (2010) fitdistrplus: help to fit of a parametric distribution to non-censored or censored data. R package version 0.1-3. http://cran.r-project.org/web/packages/fitdistrplus/index.html. Accessed 5 April 2012
58. Venables WN, Ripley BD (2002) Modern applied statistics with S, 4th edn. Springer, New York. http://www.stats.ox.ac.uk/pub/MASS4, ISBN 0-387-95457-0. Accessed 5 April 2012
59. Stephenson AG (2002) R News 2(2):31–32. http://CRAN.R-project.org/doc/Rnews. Accessed 5 April 2012
60. Pouillot R, Delignette-Muller ML (2010) Int J Food Microbiol 142(3):330. doi:10.1016/j.ijfoodmicro.2010.07.011

Publication V

DC-conductivity testing combined with photometry for measuringfibre orientations in SFRC

**Marika Eik · Karl Lõhmus · Martin Tigasson ·
Madis Listak · Jari Puttonen · Heiko Herrmann**

Abstract The orientation distribution of fibres has an important impact on the properties of short-fibre reinforced composites. This article introduces a methodology for defining fibre orientations in steel fibre reinforced concrete (SFRC). The main method under consideration is the slicing, where two approaches are introduced, i.e. the photometric analysis and DC-conductivity measurements by a special robot. The advantage of presented slicing method is the fact that a combined analysing approach is utilized; DC-conductivity testing is joined together with the image analysis. As a result, significant benefits are achieved, e.g. the ability of measuring the orientation of an individual fibre, the measuring of the in-plane angle in the interval [0°, 360°]. An additional important aspect in the presented slicing method is the possible usage of the structural parts extracted from the full-size floor-slabs as specimens, as it is done here. The authors present the statistics of fibre orientations, which are based on the experimental data received by the application of the mentioned
analysing approaches. The presented slicing method with its possible extensions offers possibilities to improve the quality control while producing SFRC products.

Introduction

Nowadays, the use of composites is increasing in various applications. Composites can be considered as innovative/improved materials and, therefore, they hold primacy over the general ones. Cement-matrix composites can be taken as an example of many composite systems. These type of composites usually consist of cement-based matrix and various types of fibres. The main idea of adding fibres to the matrix is to improve its failure characteristics, i.e. turning them from brittle to more ductile. The fibres can be continuous or short, made of various materials [1, 2] (e.g. carbon, polypropylene, glass, steel) and also the geometry, in case of short fibres, may have different shapes (straight, corrugated, hooked-end etc.). The present article focuses on a problem associated with the use of concrete matrix reinforced by short hooked-end steel fibres (steel fibre reinforced concrete, SFRC). Recently, SFRC has become quite popular as a research subject among engineers and scientists [3–8]. This trend is mostly connected with the aspiration to use it in different load bearing structures, which may lead to the reduction of the construction time.

The major role of fibres is to carry tensile stresses while the concrete matrix carries compression and transfers and distributes the load to the fibres. The effectiveness of fibres largely depends on their orientation relative to the principle tensile stress in a structure. The maximum efficiency is achieved, when the alignment of fibres coincides with the direction of relevant tensile stresses. Thus, the mechanical

M. Eik · J. Puttonen
Department of Civil and Structural Engineering, Aalto
University School of Engineering, Rakentajanaukio 4 A,
Otaniemi, Espoo, Finland

M. Eik (✉) · H. Herrmann (✉)
Centre for Nonlinear Studies, Institute of Cybernetics at Tallinn
University of Technology, Akadeemia tee 21,
12618 Tallinn, Estonia
e-mail: me@cens.ioc.ee

H. Herrmann
e-mail: hh@cens.ioc.ee

K. Lõhmus · M. Tigasson · M. Listak (✉)
Centre for Biorobotics, Tallinn University of Technology,
Akadeemia tee 15A-111, 12618 Tallinn, Estonia
e-mail: madis.listak@ttu.ee

properties of SFRC are direction dependent and the latter one is inherent to anisotropic materials.

Within recent years many scientists have devoted their research and experiments to study steel fibre reinforced concrete [3, 4, 5, 7, 8, 9, 10, 11, 12, 13]. A lot of experiments were associated with the definition of composite strength characteristics, e.g. [9, 10, 11, 14]. There were also attempts to determine the orientation of fibres using different evaluation or measuring techniques, e.g. [7, 8, 9, 10, 15, 16] used photometric method, [6, 17, 18, 19] used electrical AC-impedance measurements and a magnetic method, [11, 20, 21, 22] used X-ray computed tomography. The outcomes of these studies have not led to theoretical models, that could give a quantitative assessment of fibre orientations. The missing theory with the lack of full-scale experiments are perhaps the main reason for the absence of consistent design rules for SFRC structures [3]. In the reference [14] the authors emphasize that their samples are not representative for the full-size elements, but have been chosen to emphasize the importance of fibre orientations on the mechanical properties, and that fibre orientations are related to the casting direction. In the earlier studies the casting is usually done under well-defined and controlled laboratory conditions. These differ from a construction site, where the casting depends on the technological process and is typically site-specific. All the mentioned suggests the need for more fundamental both theoretical and experimental research.

In civil engineering the use of SFRC is closely connected with the production technology. The stable technological process is usually linked to quality control. One of the components of such a controllable process in the production of SFRC should be the methodology for measuring fibre orientations. In the present article the authors present a progressive view on the well-known slicing method by introducing DC-conductivity measurements, which are combined with image analysis. The slicing with photometry has been used before for determining the orientation of fibres [8, 10]. Therein the precision of outcomes largely depends on the quality of specimens (e.g. polishing of slice surface) and the resolution of images. In contrast to these, DC-conductivity testing works on a physical phenomenon: as the fibres are made of steel they have a good electrical conduction. One of the problems to solve within this research was to find a possible way to combine the image analysis with DC-conductivity measurements. To accomplish this task, first the sample cubes were taken from the structural elements—full-size single-span floor-slabs—and onwards they were cut into slices. Next, the slices were examined using photometric analysis and afterwards a special robot has scanned the surfaces of one slice employing some data from the photometry. The scanning robot was built in order to measure DC-conductivity between the endpoints of the cut fibres. The outcomes received by both analysing

approaches are interrelated as the photometry acts as the input for DC-conductivity testing while the latter approach improves the results of photometry.

Slicing method

Essentially, the presented method of slicing involves the handling of structural parts, which are cut into the slices. Experimental full-size floor-slabs were cast in a factory using a bucket. The concrete class was C30/37 and concrete was self-compacting, which means no vibration was needed. The fibres used had hooked-ends, the length of a fibre was $l_f = 50$ mm and the diameter was $d_f = 1$ mm (see Fig. 1). The material for fibres was rod wire (C4D or C7D steel according to standard EN 10016-2) and their amount per a cubic metre of concrete was 80 kg, resulting in about 250 fibres per dm^3. Before extracting the sample cubes from the floor-slabs, the slabs were tested using a three point bending test. During these tests three slabs have shown approximately the same capacity (slabs 1, 2, 3) and the capacity of the remaining three ones (slabs 4, 5, 6) was lower (see Fig. 2). This behaviour could be explained either by the orientation of fibres or by the variations in matrix quality (e.g. the existence of air pores).

The dimensions of the tested slabs and sample cubes with the slices are presented in Fig. 3. The sample cubes ($H \times W \times L$: 25 cm $\times$ 30 cm $\times$ 30 cm) were extracted from the slabs using a diamond saw. All together twelve cubes were taken. Six of them were sawn from the central part. The others were taken from the side of the slabs. This was done to detect the influence of the 'wall-effect' on the arrangement of fibres in the matrix, i.e. the tendency of fibres to align themselves with the formwork. Onwards, the sample cubes were cut into slices as shown in Fig. 4.

Spatial orientation of fibres in spherical coordinate system

To determine the orientation of a fibre in the matrix the spherical coordinate system is employed. In spherical
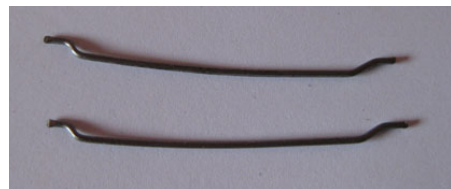
Fig. 1 Hooked steel fibres with aspect ratio of $\frac{l_f}{d_f} = 50$ made of rod wire (C4D or C7D steel according to standard EN 10016-2). The length of the hooks was approx. 6 mm, with bending angles between 30° and 45°
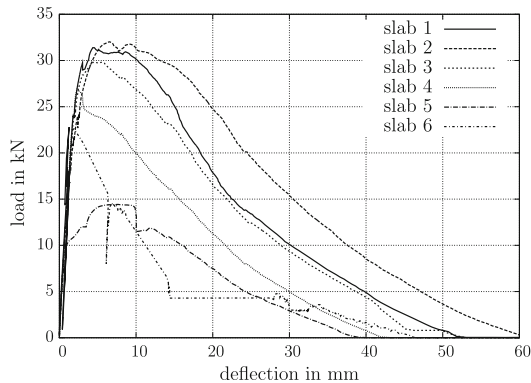
Fig. 2 Load-deflection diagram of tested floor-slabs during the bending test

coordinates the position of a point is specified by three numbers: radial distance, inclination angle ϑ, azimuth (in-plane) angle φ. For the description of the orientation of fibres only two angles are used and the radius is not needed. The graphical representation of the orientation of a fibre based on spherical coordinates can be seen in Fig. 5. The convention follows [23], where also transformation rules to and from Cartesian coordinates can be found. Each fibre carries its own local coordinate system.

Slicing with photometry

When the sample cubes had been cut into slices the photos were taken from both sides of each slice. In the photos the cut fibres are visible as ellipses and circles. According to the geometry of the cut fibres it is possible to estimate their orientational arrangement [7]. The cut fibre's shape detection may be performed using an image analysis software. The idea to utilize the images of cut specimens to analyse fibre orientations in fibre reinforced composites has been used before, e.g. by [2, 7, 13], by [12], who used a Fourier transform, and by [17, 24], who used image analysis on X-ray transmission images. Compared to those earlier studies, the method developed in this study is based on the structural parts extracted from the full-size members

Fig. 4 Representation of a sample *cube* and corresponding slice sections
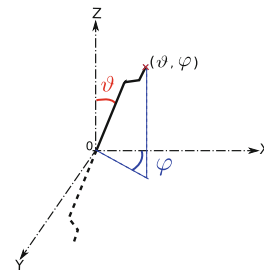
Fig. 5 Representation of a fibre in *spherical* coordinate system

and the use of multiple slices close to each other, which are analysed to improve the statistics, in contrast to the single-picture approach that is found in the literature [8].

In the present research the image analysis was performed using the public domain software ImageJ [25]. A photo of a slice after its filtering with pseudo-flat-field filter [26] and cleaning in binary format is presented in Fig. 6. The bright inclusions in Fig. 6a are the cut cross sections of the fibres. They have different geometry, starting from the circle and ending with elongated ellipse. As the fibres are cylindrical, which is a degenerated cone, then the inter-section of a cone with a plane gives an ellipse as a closed curve. Thus, the shape of an ellipse can give an assessment of the inclination angle ϑ as the ratio of minor and major axis.

Fig. 3 Representation of a floor-slab and sample *cubes* with slices

(a) Filtered image of a slice

(b) Processed image of a slice in binary format
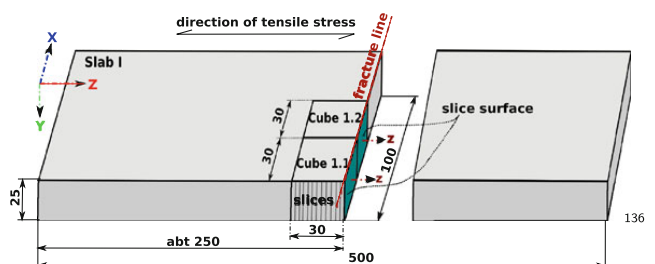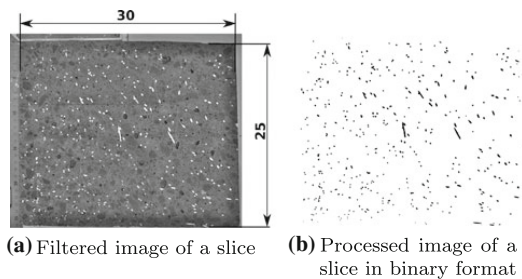
Fig. 6 Image of a slice
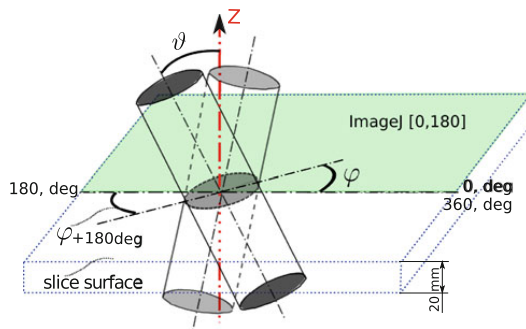
Fig. 7 The ambiguity in the direction of fibres

$$\vartheta = \arccos\left(\frac{\text{Ellipse Minor axis}}{\text{Ellipse Major axis}}\right) \qquad (1)$$

The in-plane angle φ is measured between the orientation of the major axis of an ellipse and the horizontal coordinate axis. This direction is counted from 0° up to 180° degrees, see Fig. 7. A detailed discussion on this theme including the graphical representations can be found e.g. in [27]. The measured direction of the in-plane angle φ marks two points on a circle, one of which is determined by the angle φ and the other is a mirror point. This property can be used in the density function of the angle φ. There is no difference between φ and $\varphi + 180°$ and the data are just replicated from the values for the range of [0°,180°] to the range of [180°,360°]. Subsequently an interval from [− 90°,90°] (resp. [270°,90°]) with a single peak is analysed (shifted in-plane angle φ). More detailed description of the replication procedure is given in [27]. The density distribution function is normalized.

The representation of measured orientation angles ϑ and φ is given in Fig. 7.

Obstacle in slicing with photometry and possible solutions

As it was pointed out in Sect. 2.2, the measurement of the in-plane angle φ is possible within the interval from

[0°, 180°] only, and this leads to an ambiguity in the direction of a fibre. In more detail, this ambiguity can be formulated as follows: if the direction of a fibre has the φ angle of 45°, then this cannot be distinguished from the fibre at the φ angle of 45° + 180°, since for both cases the shape of the cut fibre on the slice surface will be the same, see Fig. 7. This is not a problem of the applied software, but fundamental to the analysis of 2D images, which can only contain limited information. Thus, the measured orientation distribution of fibres by photometric analysis needs to be checked by some additional approaches in slicing or by another measuring method. The authors would like to propose the following slicing extensions and an alternative method:

– Slicing extensions

– DC-conductivity measurements, which is one of the subjects of the present paper (see Sect. 2.4).
– application of optimization algorithms for tracking the traces of a fibre left on the different images of slice surface. A short discission on this method can be found in [27].

– Alternative method

– X-ray computed tomography, especially μCT. This method has emerged as a powerful technique for non-destructive 3D visualization of the microstructural features of objects (see e.g. [5, 28, 29, 30]). The method has also been used to study fibre and steel fibre reinforced concrete, e.g. by [11, 22, 31, 32]. The detailed study of SFRC structural parts employing μCT method is presented in [31].

Slicing with DC-conductivity joined with photometry

The DC-conductivity testing can be used as an extension of slicing with photometry, as it uses the coordinates of the cut fibres on both sides of a slice from the image analysis. Since the fibres are made of metal they have a good electrical conductivity. This phenomenon is taken as a basis for DC-conductivity measurements. To utilize this, a special robot was built by members of the Centre of Biorobotics. This robot scans the opposite surfaces of a slice and measures the electrical conductivity between the endpoints of the cut fibres. If the cross sections of the cut fibre on the opposite slice surfaces belong to the same fibre, then the current can flow and, hence, the coordinates are recorded. This method is conceptually different from the AC impedance measurements (AC impedance spectrometry, AC-IS), e.g. described in [18, 19], which are sometimes also referred to as conductivity measurements. These impedance measurements described there are an indirect
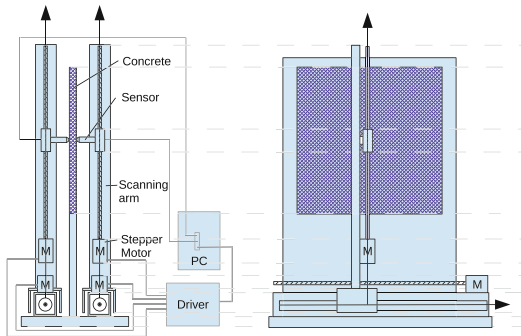
Fig. 8 The scanning robot (*side and front view*)

method by which only the average orientations and tendencies can be measured. In contrast to the referred, DC-conductivity testing delivers the information about the orientation of each individual fibre.

Robot mechanics and set up

The target was to match the cross sections of the same cut fibres. The input data were the coordinates of the cross sections of the cut fibres on both sides of a slice and the output data should be the coordinates of the connected cross sections. The scanning robot has four linear axis and two probes. Each axis has a separate drive, so that the probes can be moved independently on a 2D plane: one probe on one side and the other one on the opposite side of a slice, see Figs. 8 and 9. Each probe is made of a spring, tube and a steel ball.

As the contact area between the ball and slice surface is very small, the positioning accuracy should be at least the

radius of a fibre, i.e. 0.5 mm. The Emc2 (Enhanced Machine controller) software [33] was selected to control the scanning robot. It is a free Linux software for computer control of different machines. The program was configured to control 4 linear axis at the speed of 10 mm per second. Two methods were considered for scanning slice surface. The one method was to scan the whole surface area (step 0.9 mm), which would take about 5 years with the present prototype. This time can be remarkably reduced by the incorporation of the photometry. Hence, the other method was to check only the coordinates of the cross sections of the cut fibres received in image analysis. This approach would take about 17 h with the existing prototype and assuming a constant speed of the probes. The second method was selected.

The scanning procedure has started from the determining of coordinates and choice of a zero point. The zero point was defined as the upper left corner of slice surface, see Fig. 10. The coordinates for scanning were calculated utilizing the transformation from pixels to millimetres, i.e. pixel coordinates in the image of a slice were converted into coordinates in millimetres. The ratio between the pixels and millimetres depends on the distance from the centre of the image. This ratio decreases as the distance increases. If the transformation from the pixels to millimetres would be made linearly, then there would be a drift about +1 mm from the correct coordinate relative to one edge and −1 mm to the other edge of a slice. Using the transformation formula in Eq. (2) the drift was reduced to less than 0.5 mm, which is required to establish the connection between the probe and the cross section of a fibre. Hence, the coordinates were recalculated using the following relation

$$x_1 = c + h \cdot \sin\left[\arctan\left(\frac{x_0 - c}{h}\right)\right], \qquad (2)$$

Fig. 9 The scanning robot at work

(a) One side of a slice. **(b)** Opposite side of a slice.
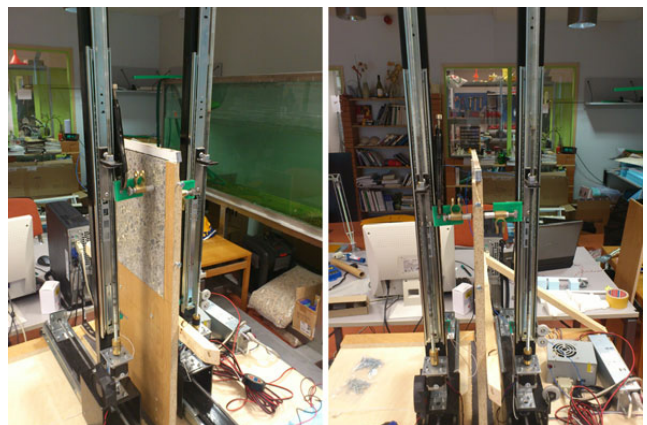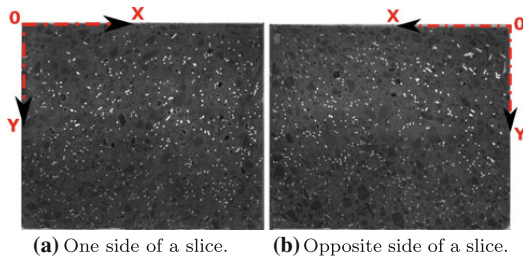
Fig. 10 Zero point for scanning machine on the *opposite sides* of a slice
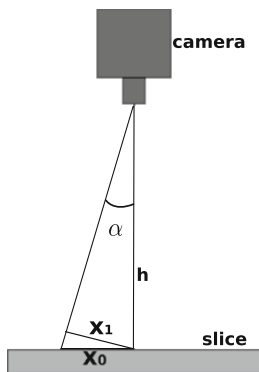
Fig. 11 The transformation of coordinates from the pixels to millimetres

where x_1 is the final abscissa to the cross section of the cut fibre, x_0 is the initial abscissa to the cross section of the cut fibre, c is the abscissa to the centre-point of slice surface, h is a distance between the photo-camera and slice surface, see Fig. 11. The ordinates were calculated following the same outline as in the case of abscissas.

As the scanning arms were fixed only on one end, the drag of a probe caused the arm to bend backwards. During one scanning cycle in order to keep the bending direction unchanged the arms were moved only in one direction. In this way, the accuracy was increased remarkably.

Larger holes/voids in the slice surface, due to air inclusions, have been filled with gypsum to prevent the probe from getting stuck.

Robot programming

The algorithm for the movement includes about 25000 different combinations. The G-code (DIN 66025/ISO 6983) for one combination is shown below:

```
G0 X40.4233 Y133.575 (go to point on one side)
G0 U34.8944 V92.3569 (go to point on other side)
M66 P0 L0            (checks conductivity)
O11720 if[#5399 EQ 1] (if there was connection...)
    G28.1           (save the coordinates...)
    (LOG, X#5161 Y#5162 U#5167 V#5168 )
                    (...and writes to file)
O11720 ENDIF
```

The total G-code consists of about 180000 lines. Therefore, another simple program was written in C. This program calculates the range, where the cross section of the cut fibre may locate on the opposite slice surface and generates the G-code.

Fibre orientation analysis

Conductivity measurements were performed on the slice nr 11 (see Fig. 4), which belongs to the cube 1.1 (see Fig. 3). This choice was done in order to verify the statistics of fibre orientations in the slab, which has shown the highest bending capacity before the first crack appeared (see Fig. 2).

Once the scanning robot measures electrical conductivity between the opposite endpoints of the cut fibre, it saves and writes the coordinates (in Cartesian system) into a '.txt' file. The next step is to process the robot measured coordinates to get the directions of the cut fibres. This can be implemented by the subtraction of the coordinates on one slice surface from those on the opposite surface, the Eq. (3) represents this.

$$d = \begin{pmatrix} X \\ Y \\ 0 \end{pmatrix} - \begin{pmatrix} U \\ V \\ 20 \end{pmatrix}, \tag{3}$$

where 20 is a slice thickness in mm. Further the received directions in Cartesian coordinates are translated into spherical ones, which are used in the photometric analysis. The conversion from Cartesian coordinates to spherical coordinates is done according to [23]. The limit inclination angle is $\vartheta_c = \arccos(\frac{20mm}{50mm}) = 1.159 = 66.4°$, larger angles cannot be measured due to the slice thickness. The in-plane φ angle is measured in the interval [0°, 360°], there is no ambiguity here. The statistics of robot measurements are presented in Sect. 3.

Results

Numerical estimates of the distribution parameters were calculated using specialized software [34–42] based on the R-programming language [43], which is an environment for statistical computing and graphics. The Figs. 12, 13, 14 represent the most interesting features of fibre orientation

Fig. 12 Photometry. Cube 1.1 (*reduced*). Probability density histograms (**a**),(**b**); bivariate density of the inclination ϑ and shifted in-plane φ angles (**c**). In (**a**) *skewness* and *kurtosis* compared with the Normal distribution–*dashed line*

(a) Inclination angle ϑ.

(b) Shifted in-plane angle φ, the interval $(-90°, 90°)$.

(c) Isolines.
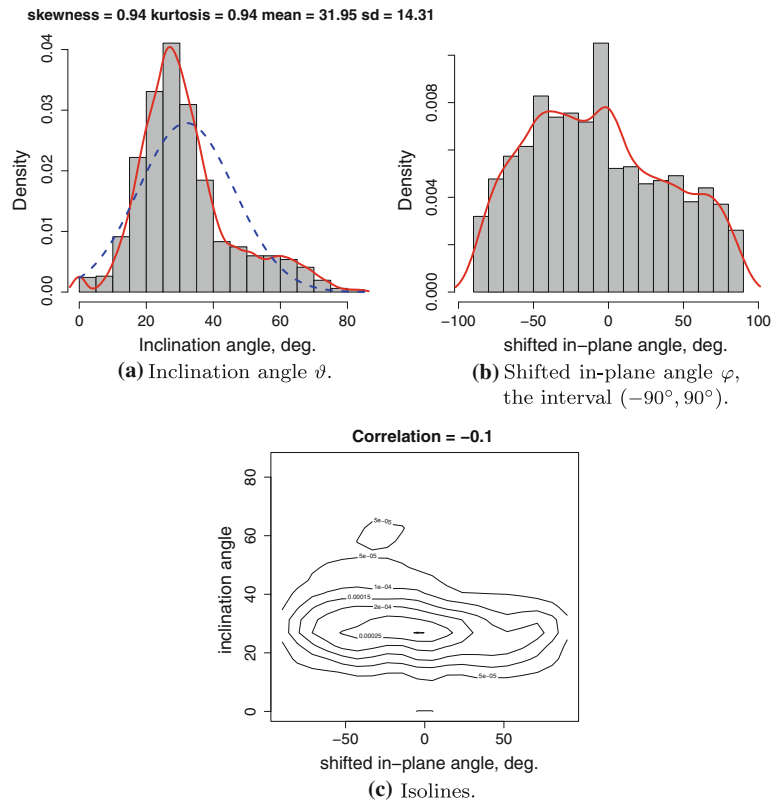
distributions estimated by both photometric analysis and DC-conductivity measurements. Besides, the results obtained by two analysing approaches are compared (see Fig. 20).

Photometry

Based on the results obtained in R, some important features were observed in the density functions of the angles ϑ and φ. Quite interesting results have emerged, when matching the received density functions with common distribution laws. In our study the two-sample bootstrap Kolmogorov-Smirnov test is used for this purpose, see Table 1. More close discussions on this issue are presented in Sect. 4.4.

DC-conductivity testing

In the conductivity measurements by the robot, 201 connections out of 25000 possible combinations were found. The scanning took about 36 h. The time differed from the initially proposed since only the acceleration of a probe was considered. The actual movement of a probe is composed of both acceleration and deceleration. Therefore, the scanning time was longer.

Discussions

Error estimation: photometry

To give a representative evaluation of the distribution parameters of the angles ϑ and φ it is necessary to operate with the number of fibres contained in an element with a given volume. During the slicing process the cubes are cut into 20 mm thick slices, see Fig. 4. This means that a whole single fibre may be cut at least into two parts, as the length of a fibre is 50 mm. If the statistics would take into account the surface of each slice, then the same fibre will be accounted up to 4 times, as the trace/cross section of the cut fibre might appear on 4 surfaces/images, i.e. 20 mm is the thickness of the first slice, 8 mm is the loss of the material during the cutting and 20 mm is the thickness of the next slice. Therefore, in order to account the fibres within the given volume only once, during the statistics only every fourth surface/image is taken into account. In

Fig. 13 Photometry. Cube 1.2 (*reduced*). Probability density histograms (**a**),(**b**); bivariate density of the inclination ϑ and shifted in-plane φ angles (**c**). In (**a**) *skewness* and *kurtosis* compared with the Normal distribution–*dashed line*

skewness = 0.39 kurtosis = −0.48 mean = 42.02 sd = 16.62

(a) Inclination angle ϑ.

(b) Shifted in-plane angle φ, the interval $(-90°, 90°)$.
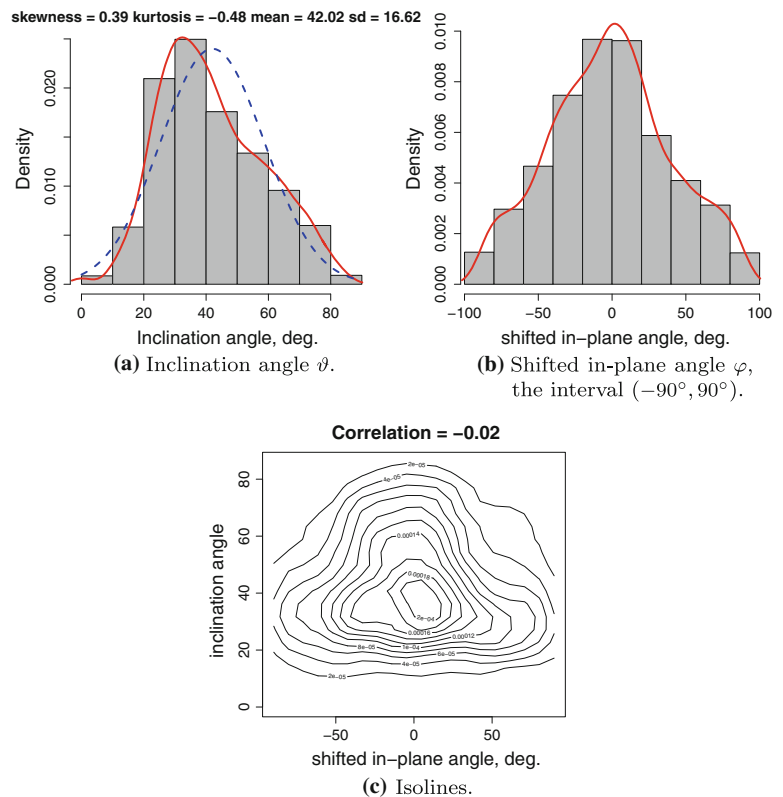
Correlation = −0.02

(c) Isolines.

Fig. 15 there is a comparison of the whole cube versus the reduced cube. As it can be seen, the distributions have the same tendencies. In general, while using the slicing method, the ratio between the thickness of a slice and the length of used fibres should be considered. The shorter the fibres are the thinner the slices should be. But the minimum thickness of a slice will still depend on a type of used equipment, i.e. cutting method (diamond saw, water jet cutting, laser etc.). The maximum thickness of a slice depends on a method of reconstruction of fibre orientations. While using pure slicing (the measurement of the arrangement of fibres utilizing photometry technique only) the maximum thickness of a slice is conditioned by the length of an aligned fibre plus some short distance, which guarantees that the trace of a fibre appears only on one slice surface. In the case of the 'tracking the trace' of a fibre the slice should be as thin as possible, but the maximum will be still proposed by the fibre length. In the inclined state (inclination angle can be conjectural) the fibre should leave at least three traces, i.e. the one trace per slice surface, see Fig. 16. The first two traces are to form the potential straight line and the third one is for checking of the line,

that was just created. DC-conductivity measurement is more close to trace tracking, but here only two traces are enough.

The precision of the results depending on the resolution of the image in photometric analysis is highlighted in [27]. The accuracy of photometric analysis can be raised by the polishing of slice surface. More detailed discussions on this improving method is given in [8].

Error estimation: robot

Possible sources for an error in the measured orientation of an individual fibre are:

– input coordinates from photometry: accuracy of fibre coordinates is about 1 px, drift after correction up to ± 0.5 mm
– probe not in the centre of the fibre trace: the maximum error in the measurement of ϑ angle can be 2.9°, see Fig. 17
– step size of a step motor. The full step size of a motor can be received as the division of a circle, i.e. 360°, by

Fig. 14 DC-conductivity. Probability density histograms (**a**),(**b**),(**c**),(**e**); bivariate density of the inclination ϑ and shifted in-plane φ angles (**f**). In (**a**) *skewness* and *kurtosis* compared with the Normal distribution– *dashed line*. In (**d**) the inclination angle ϑ is radius and in-plane angle φ is on circumference. The marked *circle* (*dashed line*) is the limit angle ϑ_c

(a) Inclination angle ϑ.

(b) In-plane angle φ, the interval $(0°, 360°)$.

(c) Shifted in-plane angle φ, the interval $(-180°, 180°)$.

(d) Scatter plot of fibre orientations.

(e) Shifted in-plane angle φ, the interval $(-90°, 90°)$, calculated by $\varphi \bmod 180°$.

(f) Isolines.
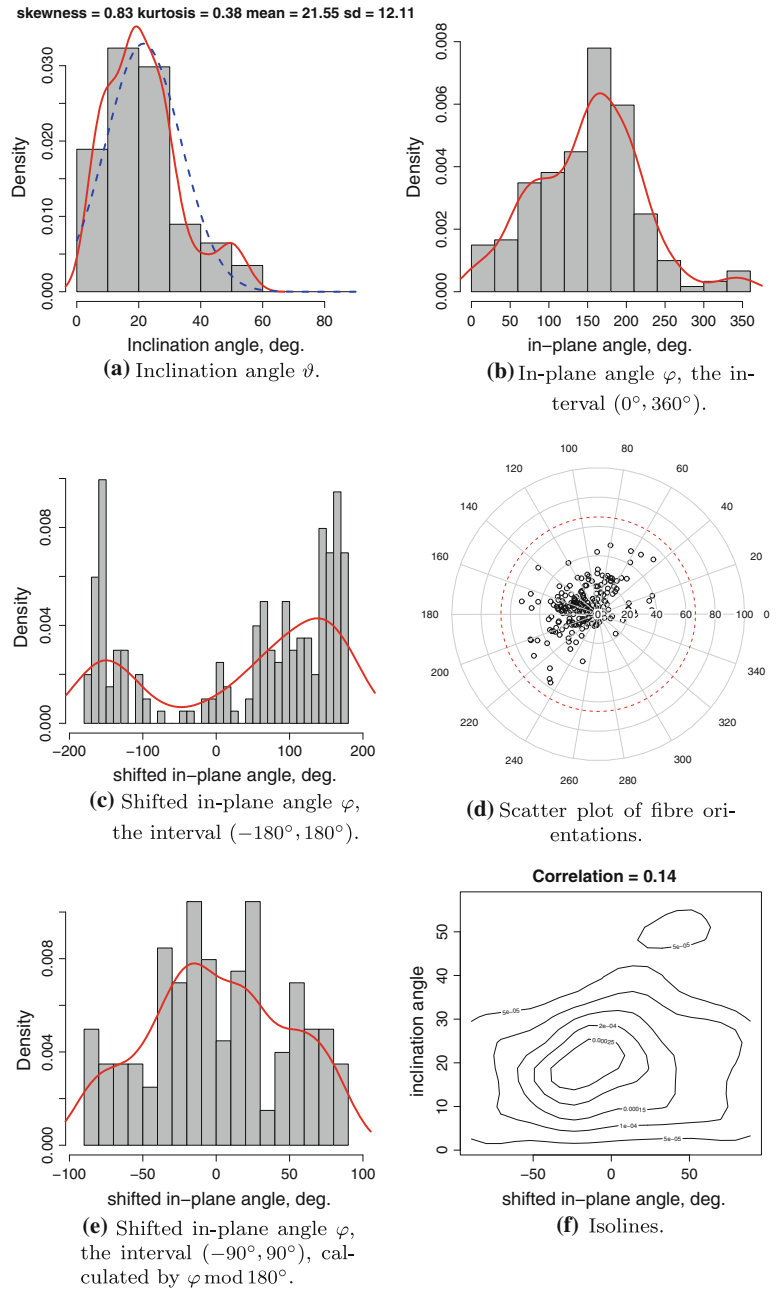
the amount of steps in a motor. The latter data come from the technical characteristics of a motor. Hence, in the present case the full step size was received as $\frac{360}{200} = 1.8°$. In addition to this, the driver used 16 micro-steps, what means that the full step size should be divided by 16. Because of the presence of a friction between the probe and slice surface 16 micro-steps can be reduced to 4. Considering the pitch of a thread in a

Table 1 Results of the two-sample bootstrap Kolmogorov-Smirnov test (function `ks.boot` from [34]) for the slab 1

| Distribution (H_0)	Cube 1.1 (in the side of a slab)				Cube 1.2 (in the centre of a slab)			
	Whole cube		Reduced cube		Whole cube		Reduced cube	
	D	p-value	D	p-value	D	p-value	D	p-value
Inclination angle ϑ								
Normal (Gaussian)	0.1143	e-16	0.1254	e-16	0.0761	e-16	0.0783	e-09
Gamma	0.0613	e-16	0.0658	e-10	0.0443	e-10	0.0439	0.0033
Gumbel	0.0687	e-16	0.0652	e-09	0.0352	1.7e-06	0.0346	**0.0374**
Weibull	0.098	e-16	0.1164	e-16	0.0754	e-16	0.0591	1.9e-05
Log-normal	0.0492	e-16	0.0575	**1.7e-07**	0.0377	2.5e-07	0.0397	0.0108
Shifted in-plane angle φ								
Normal (Gaussian)	0.0527	e-16	0.0527	**2.6e-06**	0.021	0.0142	0.0274	**0.167**
Gamma	0.0715	e-16	0.067	e-10	0.0659	e-16	0.0683	4.1e-07
Gumbel	0.0567	e-16	0.0666	e-10	0.059	e-16	0.0632	3.7e-06
Weibull	0.0454	e-13	0.0548	**9.0e-07**	0.0534	e-14	0.0515	0.00032
Log-normal	0.1086	e-16	0.1043	e-16	0.1497	e-16	0.1285	e-16

p-values printed in bold are those who come closest to the threshold or are above it

Fig. 15 Photometry. Probability density histograms of the inclination angle ϑ in the *cube* 2.2

(a) The whole cube.　　　　　**(b)** The reduced cube.
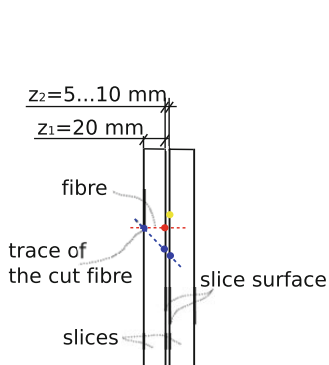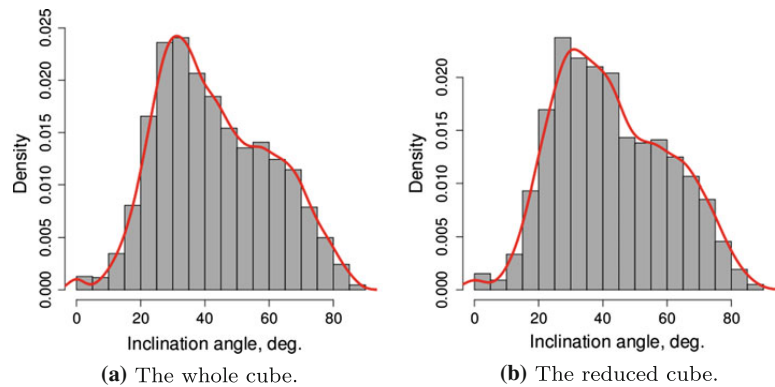
Fig. 16 The idea of tracking the trace of a cut fibre

$$\beta = \arcsin\frac{1}{20} = 2.9\text{deg}$$
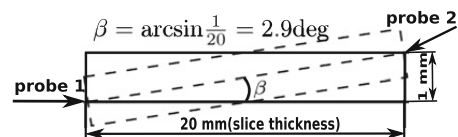
Fig. 17 The maximum error in the measurement of ϑ angle

winding lathe, i.e. 1.25 mm, and 4 micro-steps one step size of a probe should be:

$$\frac{1.25}{200 \cdot 4} = 0.0016\,\text{mm}$$

$$\frac{1.25}{200} = 0.0063\,\text{mm} - \text{for a fullstep}$$

An error from one step size of a probe has a minor influence on the precision of measurements while the influence of an error arising from the conversion of coordinates—pixels ⇒ millimetres—has the main impact.

– touching fibres: if the fibres are touching, then it is possible to have the conductivity, even if the traces on opposite surfaces belong to different fibres. This seems to be a rare event, as the statistics from the photometry and DC-conductivity testing have the similar tendencies.
– hooked-ends of the fibres: if one cut appears to be within the hooked-end of a fibre, this can lead to a <10° error in the orientation of this fibre, depending on the thickness of a slice and angle of the fibre.
– slightly curved middle part of a fibre, see Fig. 1. This can lead to an error below 2°–3° in the fibre orientation.

The last two points are of the same magnitude as for example in μCT measurements (compare [31]), where the orientation is also determined by an end-to-end direction of a fibre segment. Additionally, there is one factor affecting the measured orientation distribution: the probability of measuring a fibre is ϑ-dependent and the large inclination angles are underestimated. The probability for one fibre to "leave a trace" on the second surface, under the condition that it "left a trace" on the first surface, is

$$p = \max\left\{\cos\vartheta - \frac{\text{slice thickness}}{\text{fibre length}}, 0\right\}. \quad (4)$$

The diagrams presented in this paper are not corrected for this.

DC-conductivity robot: limitations and possible improvements

The effectiveness of conductivity measurements can be increased, e.g. by the robot improvement. The robot scanning speed depends on the average moving speed of a probe and the average distance between the cross sections of the cut fibres. If one would use the larger step motors and higher voltage, then the acceleration and the average moving speed will be increased. The average distance between the cross sections of the cut fibres may be minimized by the calculation of an optimal trajectory when creating the G-code. The scanning accuracy can be improved by the adding of a slider and synchronous winding lathe to the other end of the horizontal axes (see also Fig. 8). The latter mean should be done, if an optimal trajectory is used. Another option to decrease the scanning time is to use several probes in parallel, see Fig. 18. Thus, much wider strip can be scanned at once. In principle, one can simply build a more powerful robot or use several
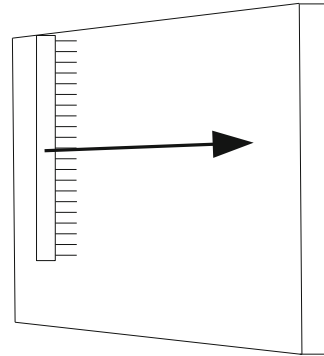

Fig. 18 Several probes in *parallel*

robots at once, which would be able to scan much larger areas, i.e. several metres within comparable or shorter time.

General tendencies in fibre orientation distributions

One of the noticeable tendencies in the distribution of the inclination angle ϑ is the slight bimodal compartment in the density function, see Figs. 12a, 14a, 15. Bimodal or multi-modal distributions have more than one local maximum in contrast to uni-modal distributions[1], see Fig. 19.

Bi-modality of sample distribution is often an indication, that the considered distribution is not Gaussian. Besides, the bi-modality can often show that the sample is not homogeneous and observations are generated by two or more 'overlap' distributions. The tendency of the density function of the inclination angle to bi-modality was noticed among all cubes analysed by photometry and also the same behaviour was observed in the statistics of DC-conductivity.

Based on the diagrams of bivariate density distributions one may see that the side cubes have the elongation of the distribution in the direction of the φ angle (see Figs. 12c, 14f), what means smaller deviations in the ϑ angles. This matter can be caused by the wall effect. Bivariate density distributions of the central cubes have more symmetric shape, i.e. elongated along the ϑ angle as well as along the φ angle (see Fig. 13c). Following from the shapes of bivariate density diagrams the point of maximum densities in the side cubes is located in the lower left sector and in the centre cubes in the middle of the diagram.

For testing, if the measured data follow a common distribution, the Kolmogorow-Smirnow-test (K–S test) with a significance level of $\alpha = 5$ % as threshold was

---

[1] A function $f(x)$ is strictly defined to be uni-modal, if it is monotonic increasing for $x < m$ and monotonic decreasing for $x > m$.

Fig. 19 Comparison of the measured density distribution of the inclination angle with a bimodal density distribution, constructed by a superposition of two normal distributions

(a) Photometry. Probability density histogram of the inclination angle ϑ.

(b) Example of a bimodal distribution which originates as a result of two overlapping distributions.
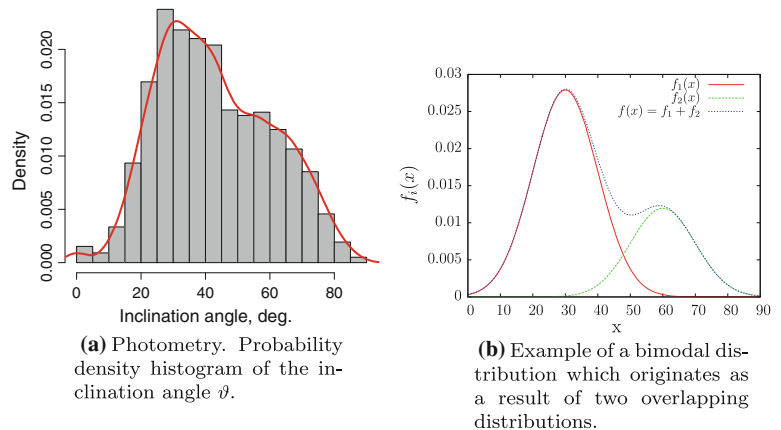
chosen. According to the results of the bootstrap K–S tests (function `ks.boot` from [34]), see Table 1, only the distribution functions of the central cubes have passed the testing; however, a passing of the test is not a confirmation that the data follow this distribution, just that there was not enough evidence to reject it.

The p-values e.g. in the cube 1.2 are:

Inclination angle ϑ: The statistical test with the null hypothesis of Gumbel distribution: p-value = 0.04, which is close but still below the threshold of 5 % ($\Rightarrow$ distribution rejected)

In-plane angle φ : The statistical test with the null hypothesis of Gauss distribution: p-value = 0.17, which is higher than the threshold of 5 % ($\Rightarrow$ distribution not rejected)

None of the distribution functions of the side cubes have passed the testing and hence all null hypotheses (H_0) should be rejected [44], although it should be noted that the Log-normal and Weibull distributions received higher p-values than the other tested distributions. The most important consequence of the performed statistical tests is, therefore, the fact that the distribution of the inclination angle ϑ is not according to the Normal distribution, in contrast to the statement made in [9]. The difference in distributions between the side and central cubes is obviously caused by the wall effect and rheology.

Influence of DC-conductivity testing on the results of photometry

As the slice measured by the robot may be considered as a sample of the population represented by the cube, the distribution parameters of the cube 1.1 and slice 1.1.11 should show the similar tendencies, if the sample is representative. If this is not the case, then it can be concluded that there is a strong locality of the studied material. In this

Section the distribution parameters of the slice and the cube are compared, see Fig. 20.
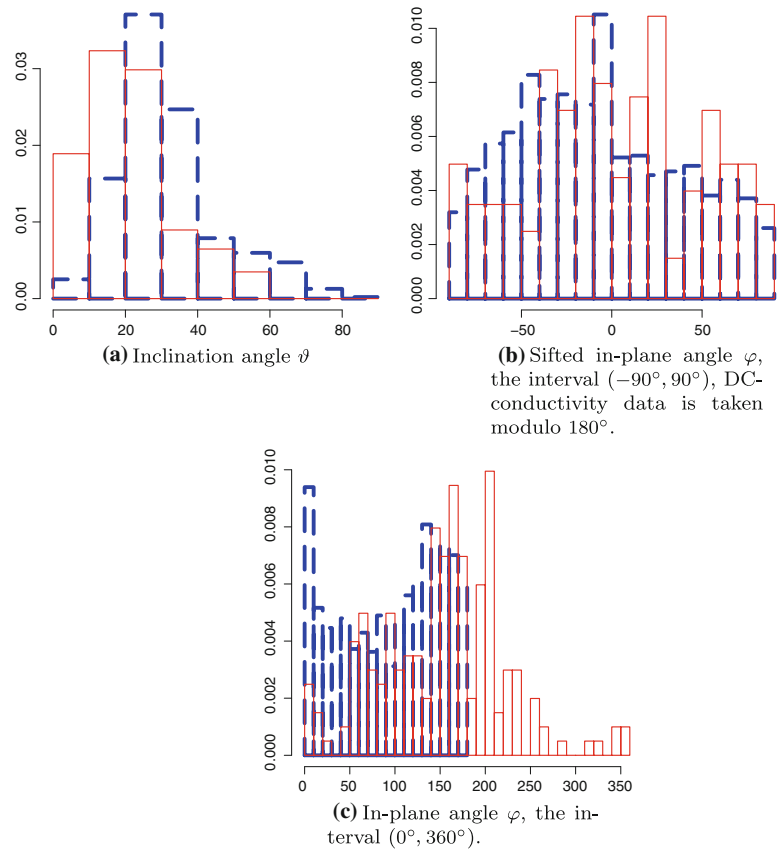
Following from the diagrams of the differences (see Fig. 20), a quite similar behaviour in the density functions can be noticed. Both analysing approaches gave a positive skewness in the probability density function of the ϑ angle. Bivariate density diagrams are also resembling, i.e. elongated along the φ angle, see Figs. 12c, 14f. This can lead to the conclusion that the material properties vary within the slice plane or only on a longer length scale than the cube dimensions.

Concluding remarks

The main idea of presented study is to give the consistent statistical and quantitative (in case of DC-conductivity, see Sect. 2.4) evaluation to fibre orientations, which can further be employed in governing equations, and to introduce feasible measuring methods for fibre orientations in hardened concrete matrix.

As it was noted in Sect. 1, the effectiveness of fibres largely depend on their orientation in the direction of the relevant tensile stress. This orientational component can be modelled mathematically using e.g. some simple trigonometric function [9] or calculating the alignment tensors [31, 45]. In the case of trigonometric function the orientational component may be calculated as the orientation number (ON)—average projected length of fibres in cross section onto the normal of the cross section divided by the fibre length [9]. Another possibility is the use of the orientation profile (OP), which is defined as the frequency of occurrence of the inclination angle in percentage, assuming that it follows the Normal (Gaussian) distribution with respective average and standard deviation. From this one can calculate the amount of fibres at any given inclination

Fig. 20 Differences in the probability density histograms of the inclination ϑ and shifted in-plane φ angles in accordance with the measuring method, i.e. photometry (*dashed line*)– reduced cube 1.1 versus DC-conductivity measurments (*solid line*)–slice 1.1.11

(a) Inclination angle ϑ

(b) Sifted in-plane angle φ, the interval $(-90°, 90°)$, DC-conductivity data is taken modulo $180°$.

(c) In-plane angle φ, the interval $(0°, 360°)$.

angle. Although, both the ON and the OP are inconsistent with material frame indifference and objectivity conditions [46], as they depend on the projection direction and have no tensorial character. Material frame indifference is closely connected with observer-invariance and material properties, which must not depend on the projection direction. Objectivity condition is related to objective quantities, which should transform like tensor components under changing the observer. The use of the alignment tensors for calculation of the orientational order in SFRC is highlighted in [31, 45]. Essentially, the concept of the alignment tensors is widely used in the theory of liquid crystals [46, 47], where the orientation of molecules is also relevant.

The remark made in Sect. 2 that the difference in capacity of the slabs was caused by different fibre orientations did not find a proof, since the distributions of the angles ϑ and φ were roughly the same in all photometrically analysed cubes. This result is significant since it pointed out not only the importance of the orientation of fibres, but also the relevance of the rheology and quality of the fresh concrete mass.

Coupled measuring approaches in slicing method— photometry with DC-conductivity—introduced in this article and μCT scanning are likely to be used in the quality control while producing SFRC products. The presented methodology may be efficiently used in the case of pre-cast structural elements as the production mode in a factory is more controllable and even. The slicing method may be preferably used for straight and hooked-end fibres. In the case of corrugated fibres this method probably will not give good results, since the tracking/reconstruction of the full length of a fibre will be a very tricky task. When applying the slicing method one should surely take into account the ratio between the thickness of a slice and the length of a fibre, see Sect. 4.1. The given article is mostly devoted to the slicing method, where two analysing approaches are joined together. Consequently, the coordinates received in the image analysis were used as the input for DC-conductivity. Such joint work has shown very good results as it allowed to speed up the scanning time and eliminate the ambiguity of the in-plane angle in the case of photometry (see Sect. 2.3). The effectiveness of the alliance of the photometry with DC-

conductivity has been proved by the concepts and results presented in this article. The success of the consolidation of image analysis with robot scanning also lies in the price. In the present experiment, the cost of the robot was about 200 Euro. This price is several orders of magnitude lower than the price of μCT equipment. The improved robot version may cost about 2000–5000 Euro, depending on the implemented improvements.

References

1. Wang Y, Zureick AH, Cho BS, Scott DE (1994) Properties of fibre reinforced concrete using recycled fibres from carpet industrial waste. J Mater Sci, 29:4191–4199. http://dx.doi.org/10.1007/BF00414198. doi: 10.1007/BF00414198

2. Purnell P, Buchanan AJ, Short NR, Page CL, Majumdar AJ (2000) Determination of bond strength in glass fibre reinforced cement using petrography and image analysis. J Mater Sci, 35:4653–4659, doi:10.1023/A:1004882419034. http://dx.doi.org/10.1023/A:1004882419034

3. Tejchman J, Kozicki J (2010) Experimental and theoretical investigations of steel-fibrous concrete. Springer series in geomechanics and geoengineering 3 1st edn. Springer, Dordrecht

4. Weiler B, Grosse C (1996) Otto Graf J 7:116–127. http://www.mpa.uni-stuttgart.de/publikationen/otto_graf_journal/ogj_1996/weiler/index.html

5. Schnell J, Breit W, Schuler F (2011) Use of computer-tomography for the analysis of fibre reinforced concrete. In: Sruma V (ed) Proceedings of the fib Symposium Prague 2011, p 583–586

6. Ferrara L, Faifer M, Toscani S (2011) Mater Struct 1–15. http://dx.doi.org/10.1617/s11527-011-9793-y. 10.1617/s11527-011-9793-y

7. Stroeven P, Hu J (2006) Review paper – stereology: Mater Struct 39:127–135. doi:10.1617/s11527-005-9031-6. http://dx.doi.org/10.1617/s11527-005-9031-6

8. Wuest J, Denarié E, Brühwiler E, Tamarit L, Kocher M, Gallucci E (2009) Exp Tech 33(5):50–55. doi:10.1111/j.1747-1567.2008.00420.x. http://dx.doi.org/10.1111/j.1747-1567.2008.00420.x

9. Laranjeira de Oliveira F (2010) Design-oriented constitutive model for steel fiber reinforced concrete. Ph.D. thesis, Universitat Politecnica de Catalunya, Barcelona. http://www.tdx.cat/TDX-0602110-115910

10. Grünewald S (2004) Performance-based design of self-compacting fibre reinforced concrete. Ph.D. thesis, Technische Universiteit Delft, Delft. http://repository.tudelft.nl/view/ir/uuid:07a817aa-cba1-4c93-bbed-40a5645cf0f1/

11. Barnett S, Lataste JF, Parry T, Millard S, Soutsos M (2010) Mater Struct 43:1009–1023. doi:10.1617/s11527-009-9562-3. http://dx.doi.org/10.1617/s11527-009-9562-3

12. Redon C, Chermant L, Chermant JL, Coster M (1998) J Microsc 191(3):258–265. doi:10.1046/j.1365-2818.1998.00393.x. http://dx.doi.org/10.1046/j.1365-2818.1998.00393.x

13. Ferrara L, Ozyurt N, di Prisco M (2011) Mater Struct 44:109–128. doi:10.1617/s11527-010-9613-9. http://dx.doi.org/10.1617/s11527-010-9613-9

14. Barragán BE, Gettu R, Martin MA, Zerbino RL (2003) Cem Concr Compos 25(7):767–777. doi:10.1016/S0958-9465(02)00096-3. http://www.sciencedirect.com/science/article/pii/S0958946502000963

15. Laranjeira F, Grünewald S, Walraven J, Blom K, Molins C, Aguadoa A (2011) Mater Struct 44:1093–1111. doi:10.1617/s11527-010-9686-5. http://dx.doi.org/10.1617/s11527-010-9686-5

16. Laranjeira F, Molins C, Aguado A (2010) Cem Concr Res 40(10):1471–1487. doi:10.1016/j.cemconres.2010.05.005. http://www.sciencedirect.com/science/article/pii/S0008884610001249

17. Redon C, Chermant L, Chermant JL, Coster M (1999) Cem Concr Compos 21(5-6):403 – 412. doi:10.1016/S0958-9465(99)00025-6. http://www.sciencedirect.com/science/article/pii/S0958946599000256

18. Ozyurt N, Mason TO, Shah SP (2007) Non-destructive monitoring of fiber dispersion in FRCS using ac-impedance spectroscopy. In: Measuring, monitoring and modeling concrete properties, Springer, Dordrecht, p 285–290. doi:10.1007/978-1-4020-5104-3. http://dx.doi.org/10.1007/978-1-4020-5104-3

19. Lataste J, Behloul M, Breysse D (2008) Characterisation of fibres distribution in a steel fibre reinforced concrete with electrical resistivity measurements. NDT& E Int 41(8):638–647. doi:10.1016/j.ndteint.2008.03.008. http://www.sciencedirect.com/science/article/pii/S0963869508000315

20. Dumont P, Corre SL, Orgéas L, Favier D (2009) A numerical analysis of the evolution of bundle orientation in concentrated fibre-bundle suspensions. J Non-Newton Fluid Mech 160(2–3):76–92. doi:10.1016/j.jnnfm.2009.03.001. http://www.sciencedirect.com/science/article/pii/S0377025709000627

21. Le TH, Dumont P, Orgéas L, Favier D, Salvo L, Boller E (2008) X-ray phase contrast microtomography for the analysis of the fibrous microstructure of smc composites. Compos Part A: Appl Sci Manuf 39(1):91–103. doi:10.1016/j.compositesa.2007.08.027. http://www.sciencedirect.com/science/article/pii/S1359835X07001741

22. Krause M, Hausherr J, Burgeth B, Herrmann C, Krenkel W (2010) Determination of the fibre orientation in composites using the structure tensor and local x-ray transform. J Mater Sci 45:888–896. doi:10.1007/s10853-009-4016-4. http://dx.doi.org/10.1007/s10853-009-4016-4

23. Bronstein IN, Semendjajew KA, Musiol G, Muehlig H (2007) Handbook of mathematics 5th edn. Springer, Dordrecht

24. Stroeven P (1986) Stereology of concrete reinforced with short steel fibres. Ph.D. thesis, Technische Universiteit Delft, Delft. http://repository.tudelft.nl/assets/uuid:fb1416c4-2061-4767-9d5a-925480382d19/Stroeven_1986.pdf

25. Abrámoff MD, aes PJM, Ram SJ (2004) Biophotonics Int 11(7):36–42

26. Collins T (2004) Pseudo-flat field filter for imagej. http://www.uhnresearch.ca/facilities/wcif/fdownload.html

27. Eik M, Herrmann H (2012) Proc Est Acad Sci 61:128–136. doi:10.3176/proc.2012.2.05

28. Buffiere J, Maire E, Adrien J, Masse J, Boller E (2010) Exp Mech 50:289–305. http://dx.doi.org/10.1007/s11340-010-9333-7

29. Penttilä P, Suuronen JP, Kirjoranta S, Peura M, Jouppila K, Tenkanen M, Serimaa R (2011) J Mater Sci 46:3470–3479. doi:10.1007/s10853-011-5252-y, http://dx.doi.org/10.1007/s10853-011-5252-y

30. Leppänen K, Bjurhager I, Peura M, Kallonen A, Suuronen JP, Penttilä P, Love J, Fagerstedt K, Serimaa R (2011) X-ray scattering and microtomography study on the structural changes of never-dried silver birch, european aspen and hybrid aspen during drying. Holzforschung, pp. 777–897. doi:10.1515/HF.2011.108. http://www.degruyter.com/view/j/hfsg.2011.65.issue-6/hf.2011.108/hf.2011.108.xml

31. Suuronen JP, Kallonen A, Eik M, Puttonen J, Serimaa R, Herrmann H (2012) J Mater Sci 48(3)4358–4367. doi:10.1007/s10853-012-6882-4.

32. Stähli P, Custer R, van Mier J (2008) Mater Struct 41:189–196. doi:10.1617/s11527-007-9229-x. http://dx.doi.org/10.1617/s11527-007-9229-x

33. Emc2 (enhanced machine controller). http://www.linuxcnc.org/, software. http://www.linuxcnc.org/

34. Sekhon JS (2010) Matching: multivariate and propensity score matching with balance optimization. http://CRAN.R-project.org/package=Matching, r package version 4.7-11

35. Delignette-Muller ML, Pouillot R, Denis JB, Dutang C (2010) Fitdistrplus: help to fit of a parametric distribution to non-censored or censored data. R package version 0.1–3

36. Venables WN, Ripley BD (2002) Modern applied statistics with S. Springer, New York, 4th edn. http://www.stats.ox.ac.uk/pub/MASS4,iSBN 0-387-95457-0

37. Stephenson AG (2002) R News 2(2):31–32. http://CRAN.R-project.org/doc/Rnews/

38. Pouillot R, Delignette-Muller ML (2010) Int J Food Microbiol 142(3):330–40. doi:10.1016/j.ijfoodmicro.2010.07.011

39. Adler D, Murdoch D (2010) rgl: 3D visualization device system (OpenGL). http://CRAN.R-project.org/package=rgl, r package version 0.91

40. Wuertz D (2009) many others, see the SOURCE file fMultivar: multivariate market analysis. http://CRAN.R-project.org/package=fMultivar, r package version2100.76

41. Dimitriadou E, Hornik K, Leisch F, Meyer D, Weingessel A (2011) e1071: Misc functions of the department of statistics (e1071), TU Wien. http://CRAN.R-project.org/package=e1071, r package version 1.5-25

42. Poncet P (2010) Modeest: Mode Estimation. http://CRAN.R-project.org/package=modeest, r package version 1.14

43. Development Core Team R (2011) R: a language and environment for statistical computing. R Foundation for Statistical Computing, Vienna, Austria, http://www.R-project.org, ISBN 3-900051-07-0

44. Casella G, Berger JO (2001) Statistical Inference 2nd edn. Duxbury Press, Belmont

45. Herrmann H, Eik M (2011) Proc Est Acad Sci 60(3):179–183. doi:10.3176/proc.2011.3.06

46. Muschik W, Papenfuss C, Ehrentraut H (1996) Concepts of continuum thermodynamics. Kielce University of Technology, Technische Universität Berlin, Berlin

47. Ehrentraut H, Muschik W (1998) ARI - Int J Phys Eng Sci 51:149–159. doi:10.1007/s007770050048. http://dx.doi.org/10.1007/s007770050048

Publication VI

M. Eik, J. Puttonen and H. Herrmann. Fibre orientation phenomenon in concrete composites: measuring and theoretical modelling. 7th International Conference FIBRE CONCRETE 2013, Technology, Design, Application; Conference Proceedings, 1-4, September 2013.

FIBRE ORIENTATION PHENOMENON IN CONCRETE COMPOSITES: MEASURING AND THEORETICAL MODELLING

EIK Marika[1], PUTTONEN Jari[2], HERRMANN Heiko[3]

Abstract: *The highlight of the paper is the constitutive modelling of anisotropic properties of steel fibre reinforced concrete. The matter of anisotropy arises with the adding of short fibres to the concrete matrix. In the following, the anisotropic influence of short fibres is specified by the alignment tensors and the orientation distribution function. Utilizing the latter characteristics, it is possible to lay down the symmetry axes of the composite and define its elastic properties by employing the orientation distribution function defined as a statistical element.*

Keywords: fibre orientation, constitutive mappings, orthotropic material

1. Introduction

Nowadays composite materials are replacing the general ones since due to the superposition of the constituents of various materials they have improved physical and mechanical properties. So, one of the options to strengthen the base material (matrix) is the addition of fibres, which can be made of glass, polypropylene, steel etc. The investigation of the properties of concrete (as matrix material) reinforced by short hooked-end steel fibres (SFRC) is a subject of the present research. This composite has a history of usage since middle fifties of the 20 century. Despite this, the modelling of mechanical properties of SFRC still remains an open topic for research. Essentially, one of the reasons is that the mixing of short fibres with concrete matrix results in an anisotropic properties depending on the orientation of fibres and the matter of fibre orientations is not taken into account by the existing material models for short fibre composites adequatelly [1, 2, 3]. Although, only by knowing fibre orientations it is possible to determine the bearing capacity of SFRC. Thereby, one of the goals of the research is related to the development of anisotropic material model, which would include the objective description of fibre orientations.

2. Phenomenological assumptions for constitutive mappings for SFRC

Essentially, the assumption for the orthotropic model is based on a comparison of the behaviour of a conventional concrete and SFRC beams, Fig. 1. In a concrete beam the reinforcement bars coincide with the regions of predicted tensile stresses and thus it has an orthotropic behaviour

---

[1],[2]   Eik M., Puttonen J., Aalto University, Finland, e-mail: jari.puttonen, marika.eik@aalto.fi

[2][3]   Herrmann H., Institute of Cybernetics at TUT, Estonia, e-mail: hh@cens.ioc.ee
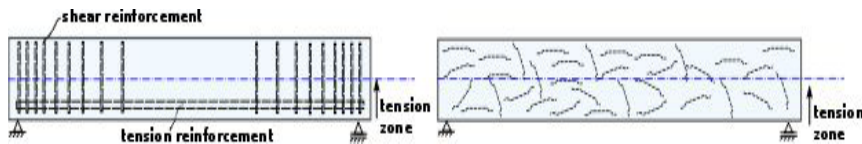
[3]

Figure 1: The comparison of reinforced concrete versus SFRC beam. In SFRC beam the orientation distribution of fibres is not specified.

The arrangement of fibres in SFRC beam may have the similar tendency, i.e. the fibres may be aligned along several preferred directions and the research problem is their identification and modelling. The tendency of fibres to be aligned in distinct directions is justified by X-ray micro-tomography (µCT) measurments conducted during the research [4]. Sufficiently large specimens—cylinders (*H*:25 *cm*, d: 10 *cm*)—were drilled from full-size floor-slabs (*H×W×L*:25 *cm*×100 *cm*×500 *cm*) and were scanned by µCT scanner. The µCT investigations have showed, that the fibers are aligned along some directions and the latter ones can be different within the same structure. These preffered directions can be modelled by the eigenvectors of the   order alignment tensor (AT) [5, 6], which may assign the symmetry axes of the composite, Figs. 2(b), 2(c). The infinite hierarchy of the ATs rebuilts the orientation distribution function (ODF) [5, 6]. The ODF defines a probability of finding a fibre (rod-like particle) between the given angles on a sphere. Thus, the ODF may be used to give a probabilistic assessment of fibre contributions in material symmetry axes and this will result in the orientation-weighted order elsticity tensor of fibres.
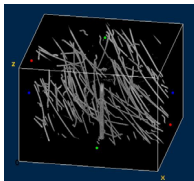
(a) *Thresholded volume image of a cylinder sample scanned by µCT.*
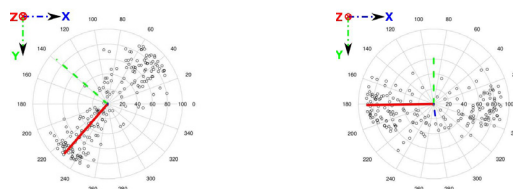
(b) *Scatter plot of fibre orientations in cylinder 2A (side region of a slab).*

(c) *Scatter plot of fibre orientations in cylinder 2B (centre region of a slab).*

Figure 2: Fibre orientations received by µCT scanning. In scatter plots the lines correspond to the directions of the eigenvectors; Z axis points to the direction of principle stress in a floor-slab.

The brittle behaviour of concrete matrix, an incomplete (minor) anchoring of steel fibres and insignificant deformation of high strength steel used for fibres (compared to ductile steel) can serve as a basis for the assumption of linear-elastic dependence between stresses and deformations. In addition, the linear-elastic state is supported by the actual behaviour of experimental SFRC full-size floor-slabs, which were tested for bending and have showed the brittle character of the fracture [7].

2

3.   Formulation of orthotropic linear-elastic material model for SFRC

SFRC material model described below utilizes the full orientation information of a fibre, i.e. the inclination and azimuth (in-plane) angles of spherical coordinates, and uses the tensor quantities, which satisfy the objectivity condition and the principle of material frame indifference [8]. Essentially, the constitutive mappings for SFRC utilize a hyperelastic material model. The assumed isotropic concrete matrix is modelled employing the representation of the strain-energy density as an isotropic tensor function of one argument and expressing only 2nd order invariant. By this the isotropic St. Venant-Kirchhoff model is received [9]. The anisotropic influence of short fibres is characterised employing the mentioned strain-energy density function, but complemented for the orthotropic case by the structural tensors [10]. The structural tensors are the tensors, which lay down the material symmetry and thus may be composed by the eigenvectors of the 2nd order AT. Thereby, the orthotropic St. Venant-Kirchhoff model is received by the representation of the strain-energy density function utilizing the mixed invariants. In the following, the orthotropic liner-elastic material model for SFRC in material symmetry axes is developed by the superposition of the isotropic and orthotropic St. Venant-Kirchhoff material models. The material model for SFRC is given in terms of material constants, which are specified from the orientation-weighted 4th order elsticity tensor calculated using the ODF of fibres.

4.   Conclusion

The material model formulated gives a representative description of composite properties in a physical term since it is observer-independent and uses tensorial description. Orientation order of fibres is quantified by the ATs, which can be used in the evolution equations for estimating the rheological properties of fibre suspensions. Formulated constitutive model provides a groundwork for numerical computation methods since it establishes the relation between the stress and deformation of the composite through the orientation weighted   order elasticity tensor. Postulated material model allow the manufactures to simulate and understand SFRC properties and thus may help them in product development.

References

[1]   Herrmann H, Eik M (2011)Some comments on the theory of short fibre reinforced material. Proceedings of the Estonian Academy of Sciences, 60(3):179–183, 10.3176/proc.2011.3.06

[2]   Taya M, Aresenault RJ (1989)Metal Matrix Composites: Thermomechanical Behavior. Pergamon Press, Oxford

[3]   Laranjeira de Oliveira F (2010)Design-oriented constitutive model for steel fiber reinforced concrete. Ph.D. thesis, Universitat Politecnica de Catalunya, URL `http://www.tdx.cat/TDX-0602110-115910`

[4]   Suuronen JP, Kallonen A, Eik M, Puttonen J, Serimaa R, Herrmann H (2012)Analysis of short fibres orientation in steel fibre-reinforced concrete (sfrc) by x-ray tomography. Journal of Materials Science, 48(3):1358–1367, 10.1007/s10853-012-6882-4

[5]   Advani SG, Tucker III CL (1987)The use of tensors to describe and predict fiber orientation in short fiber composites. Journal of Rheology, 31(8):751–784, 10.1122/1.549945

[6]   Muschik W, Papenfuss C, Ehrentraut H (1996)Concepts of Continuum Thermodynamics. Kielce University of Technology, Technische Universität Berlin

[7]   Eik M, Lõhmus K, Tigasson M, Listak M, Puttonen J, Herrmann H (2013)DC-conductivity testing combined with photometry for measuring fibre orientations in SFRC. Journal of Materials Science, 48(10):3745–3759, 10.1007/s10853-013-7174-3

[8] Muschik W, Restuccia L (2002)Changing the observer and moving materials in continuum physics: Objectivity and frame-indifference. Technische Mechanik, 22(2):152–160

[9] Itskov M (2001)A generalized orthotropic hyperelastic material model with application to incompressible shells. International Journal for Numerical Methods in Engineering, 50(8):1777–1799, 10.1002/nme.86

[10] Itskov M (2009)Tensor Algebra and Tensor Analysis for Engineers With Applications to Continuum Mechanics. Springer

DISSERTATIONS DEFENDED AT
TALLINN UNIVERSITY OF TECHNOLOGY ON
CIVIL ENGINEERING

1. **Heino Mölder**. Cycle of Investigations to Improve the Efficiency and Reliability of Activated Sludge Process in Sewage Treatment Plants. 1992.

2. **Stellian Grabko**. Structure and Properties of Oil-Shale Portland Cement Concrete. 1993.

3. **Kent Arvidsson**. Analysis of Interacting Systems of Shear Walls, Coupled Shear Walls and Frames in Multi-Storey Buildings. 1996.

4. **Andrus Aavik**. Methodical Basis for the Evaluation of Pavement Structural Strength in Estonian Pavement Management System (EPMS). 2003.

5. **Priit Vilba**. Unstiffened Welded Thin-Walled Metal Girder under Uniform Loading. 2003.

6. **Irene Lill.** Evaluation of Labour Management Strategies in Construction. 2004.

7. **Juhan Idnurm**. Discrete Analysis of Cable-Supported Bridges. 2004.

8. **Arvo Iital**. Monitoring of Surface Water Quality in Small Agricultural Watersheds. Methodology and Optimization of monitoring Network. 2005.

9. **Liis Sipelgas**. Application of Satellite Data for Monitoring the Marine Environment. 2006.

10. **Ott Koppel**. Infrastruktuuri arvestus vertikaalselt integreeritud raudtee-ettevõtja korral: hinnakujunduse aspekt (Eesti peamise raudtee-ettevõtja näitel). 2006.

11. **Targo Kalamees**. Hygrothermal Criteria for Design and Simulation of Buildings. 2006.

12. **Raido Puust**. Probabilistic Leak Detection in Pipe Networks Using the SCEM-UA Algorithm. 2007.

13. **Sergei Zub**. Combined Treatment of Sulfate-Rich Molasses Wastewater from Yeast Industry. Technology Optimization. 2007.

14. **Alvina Reihan**. Analysis of Long-Term River Runoff Trends and Climate Change Impact on Water Resources in Estonia. 2008.

15. **Ain Valdmann**. On the Coastal Zone Management of the City of Tallinn under Natural and Anthropogenic Pressure. 2008.

16. **Ira Didenkulova**. Long Wave Dynamics in the Coastal Zone. 2008.

17. **Alvar Toode**. DHW Consumption, Consumption Profiles and Their Influence on Dimensioning of a District Heating Network. 2008.

18. **Annely Kuu**. Biological Diversity of Agricultural Soils in Estonia. 2008.

19. **Andres Tolli**. Hiina konteinerveod läbi Eesti Venemaale ja Hiinasse tagasisaadetavate tühjade konteinerite arvu vähendamise võimalused. 2008.

20. **Heiki Onton**. Investigation of the Causes of Deterioration of Old Reinforced Concrete Constructions and Possibilities of Their Restoration. 2008.

21. **Harri Moora**. Life Cycle Assessment as a Decision Support Tool for System optimisation – the Case of Waste Management in Estonia. 2009.

22. **Andres Kask**. Lithohydrodynamic Processes in the Tallinn Bay Area. 2009.

23. **Loreta Kelpšaitė**. Changing Properties of Wind Waves and Vessel Wakes on the Eastern Coast of the Baltic Sea. 2009.

24. **Dmitry Kurennoy.** Analysis of the Properties of Fast Ferry Wakes in the Context of Coastal Management. 2009.

25. **Egon Kivi**. Structural Behavior of Cable-Stayed Suspension Bridge Structure. 2009.

26. **Madis Ratassepp**. Wave Scattering at Discontinuities in Plates and Pipes. 2010.

27. **Tiia Pedusaar**. Management of Lake Ülemiste, a Drinking Water Reservoir. 2010.

28. **Karin Pachel**. Water Resources, Sustainable Use and Integrated Management in Estonia. 2010.

29. **Andrus Räämet**. Spatio-Temporal Variability of the Baltic Sea Wave Fields. 2010.

30. **Alar Just**. Structural Fire Design of Timber Frame Assemblies Insulated by Glass Wool and Covered by Gypsum Plasterboards. 2010.

31. **Toomas Liiv**. Experimental Analysis of Boundary Layer Dynamics in Plunging Breaking Wave. 2011.

32. **Martti Kiisa**. Discrete Analysis of Single-Pylon Suspension Bridges. 2011.

33. **Ivar Annus**. Development of Accelerating Pipe Flow Starting from Rest. 2011.

34. **Emlyn D. Q. Witt**. Risk Transfer and Construction Project Delivery Efficiency – Implications for Public Private Partnerships. 2012.

35. **Oxana Kurkina**. Nonlinear Dynamics of Internal Gravity Waves in Shallow Seas. 2012.

36. **Allan Hani**. Investigation of Energy Efficiency in Buildings and HVAC Systems. 2012.

37. **Tiina Hain**. Characteristics of Portland Cements for Sulfate and Weather Resistant Concrete. 2012.

38. **Dmitri Loginov**. Autonomous Design Systems (ADS) in HVAC Field. Synergetics-Based Approach. 2012.

39. **Kati Kõrbe Kaare**. Performance Measurement for the Road Network: Conceptual Approach and Technologies for Estonia. 2013.

40. **Viktoria Voronova**. Assessment of Environmental Impacts of Landfilling and Alternatives for Management of Municipal Solid Waste. 2013.

41. **Joonas Vaabel**. Hydraulic Power Capacity of Water Supply Systems. 2013.

42. **Inga Zaitseva-Pärnaste**. Wave Climate and its Decadal Changes in the Baltic Sea Derived from Visual Observations. 2013.

43. **Bert Viikmäe**. Optimising Fairways in the Gulf of Finland Using Patterns of Surface Currents. 2014.

44. **Raili Niine**. Population Equivalence Based Discharge Criteria of Wastewater Treatment Plants in Estonia. 2014.

This doctoral thesis is conducted under a convention for the joint supervision of thesis at Aalto University (Finland) and Tallinn University of Technology (Estonia). The research implemented is concentrated on the concrete reinforced by short steel fibres, SFRC. The examinations performed comprise two research branches: measuring of fibre orientations from the hardened concrete matrix and modelling of composite properties considering the anisotropic behaviour occurring due to different alignments of short fibres.
The outcomes of empirical investigations proved that the elaborated and implemented measuring techniques: DC-conductivity testing combined with photometry and X-ray micro-tomography scanning, offer possibilities to improve and develop the manufacturing process of SFRC products (look into the summary). The advantage of the material model postulated is that it uses the full orientation information of fibres and employs tensor quantities. The model can be implemented in numerical applications.

BUSINESS +
ECONOMY

ART +
DESIGN +
ARCHITECTURE

SCIENCE +
TECHNOLOGY

CROSSOVER

DOCTORAL
DISSERTATIONS